Tracking Detector and Møller Polarimeter for the P2 Experiment

Dissertation

submitted for the award of the title

"Doctor of Natural Sciences"

to the

Faculty of Physics, Mathematics and Computer Science

of Johannes Gutenberg University Mainz

presented by

Michail Kravchenko

born in Minsk, Belarus

Mainz, 10 April 2025

”Feci quod potui, faciant meliora potentes.”
Eng.: ”I have done what I could; let those who can do better.”

Henry Baerlein (attributed)

Abstract

The primary aim of the P2 experiment is to determine the weak mixing angle $\sin^2\theta_w$ precisely. The experiment will take place at the Mainz Energy Recovery Superconducting Accelerator (MESA), which will provide a beam of electrons with alternating longitudinal polarization and energy of 155 MeV and a current of 150 µA. These conditions enable a targeted relative uncertainty of 0.14 % on $\sin^2\theta_w$ at low four-momentum transfer of $Q^2 = 4.5 \times 10^{-3}$ GeV^2. This high precision allows for a sensitive search for physics beyond the Standard Model of Elementary Particle Physics.

In the experiment, the parity-violating asymmetry will be measured by integrating Cherenkov detectors. Additionally, a tracking detector will determine the four-momentum transfer Q^2 of electrons scattered in the liquid hydrogen target and reconstruct individual electron tracks for systematic studies. The tracking detector will employ High Voltage Monolithic Active Pixel Sensors (HV-MAPS), a novel technology designed to minimize the material budget and thus reduce multiple scattering. A major challenge is represented by the high electron scattering rate into the tracking detector acceptance, reaching approximately 100 GHz. This demands additional requirements on the data acquisition system and the radiation hardness of all used materials and components.

The value of the electroweak mixing angle will be extracted from the parity-violating rate asymmetry measured in the experiment. The measured asymmetry is directly proportional to the beam polarization. Long-term scattering asymmetry measurements at the Mainz Microtron MAMI have shown that beam polarization can fluctuate by up to 10 % during a typical run. To ensure the required accuracy in the asymmetry measurements, beam polarization must be monitored regularly, ideally continuously, with a precision of $\leq$0.5 %. Møller polarimetry using a low-density gaseous atomic hydrogen target is the only suitable technique to meet these stringent requirements. A concept for this type of polarimeter, known as the Hydro-Møller polarimeter, was originally proposed by V. Luppov and E. Chudakov. This setup allows for online, non-destructive beam monitoring. However, the gaseous target introduces significant technological challenges that must be addressed. As an interim solution, a Møller polarimeter, which will initially use a conventional solid iron target and operate in discontinuous mode until the hydrogen target is ready, is currently under consideration.

Contents

Part I.

Introduction

1 Introduction

The famous proposal of the nuclear model of the atom by Rutherford in 1911 [1] became a significant boost in the promotion of nuclear and particle physics. Several decades later, in the 1960s–1970s, a theory that describes and unifies the interactions of the fundamental particles was developed. This framework, the Standard Model (SM) of particle physics, has been extensively tested and confirmed in numerous experiments. For example, it predicts the mass of the W boson with a very small uncertainty of less than 0.01% [2], and it stays valid on a distance scale down to 1×10^{-16} cm. The relatively recent discovery of the Higgs boson [3, 4] completed the SM.

Despite the successes, the Standard Model (SM) cannot account for several key phenomena. For instance, it does not explain dark matter, dark energy, the matter-antimatter asymmetry in the Universe, or the oscillations observed between neutrino flavors, and it does not incorporate gravitational forces—the weakest of the four fundamental interactions. Moreover, the SM fails to resolve the hierarchy problem, which refers to the facts that the weak force is 10^{24} times stronger than gravity or that the Higgs boson mass of ($\approx$125 GeV) is unexpectedly light compared to the Planck scale ($\sim 10^{19}$ GeV). Quantum corrections would naturally elevate the Higgs mass to much higher values unless an improbable degree of fine-tuning or *New physics* is invoked to stabilize it. This has motivated extensive experimental searches for *physics beyond the Standard Model (BSM)* to address these shortcomings and develop a more comprehensive theoretical framework.

The weak interaction deserves particular attention because it is the only force violating parity in the SM. This unique feature is particularly interesting as it offers a sensitive probe into the symmetry structure of fundamental interactions and provides a critical testing ground for new physics. Over the past 30 years, the measurement of parity violation in weak interactions has been a well-established experimental technique in atomic, particle, and nuclear physics.

The P2 experiment [5, 6] aims to measure the weak mixing angle, a fundamental parameter of the SM, with very high precision. This angle quantifies the relationship between the electromagnetic and the weak force, and its precise measurement is crucial for testing the SM and searching for BSM physics. In the P2 experiment, an electron beam with alternating polarization scatters off an unpolarized proton target (liquid hydrogen). An integrating Cherenkov detector measures the parity-violating asymmetry in the elastic electron-proton scattering. Additionally, a tracking detector measures the four-momentum transfer of the scattered electrons and reconstructs their individual tracks, enabling systematic studies.

The P2 experiment presents significant technical challenges, primarily due to the precision required in measuring the weak mixing angle at low momentum transfer. Achieving this level of accuracy is essential because it provides a sensitive test of the Standard Model at the given energy scale and could potentially reveal hints of BSM physics. Furthermore, the P2 experiment complements other high-energy experiments searching for BSM physics, contributing to a broader effort to probe fundamental symmetries and deepen understanding of the universe at its most fundamental level.

The structure of this work and the personal contribution in the respective parts are as follows:

- The first part introduces the P2 experiment, outlining the theoretical foundation, main objectives, and general technical requirements.
- The second part of this work details the design of the tracking detector for the P2 setup and provides an overview of recent design updates. Furthermore, it presents the results of laboratory measurements and studies on the tracking detector cooling system carried out in the context of this thesis.
- The third part focuses on the technical design of the Møller polarimeter and presents the results of Geant4 simulations performed in the framework of this thesis. The overall design concept of the polarimeter was comprehensively revised and subsequently optimized based on these studies. A co-authored publication [7], primarily based on the results obtained in this work, is currently in preparation.
- Finally, the thesis concludes by summarizing the results and discussing follow-up plans for the P2 experiment.

2 Theoretical Base for the P2 Experiment

Most planned, running, or already completed experiments in elementary particle physics focus on high-energy probing of the key predictions of the Standard Model and search for new physics. However, these explorations can also be conducted in the low-energy region. The P2 experiment, being one such experiment, aims to precisely measure the weak mixing angle $\sin^2\theta_w$, a fundamental parameter in the electroweak theory, via parity-violating electron-proton scattering. This chapter introduces the most relevant theory aspects, which form the theoretical base for the P2 experiment.

It is important to note that the discussion of the weak mixing angle in this section is restricted to *tree-level* calculations, meaning only the *leading-order* contribution is included in a process without higher-order *loop corrections*. A more precise approach requires accounting for these corrections via *renormalization* of the theory. The necessity of renormalization and its relation to defining the weak mixing angle will be covered in section 2.5.

This section gives the basic theoretical overview essential for introducing the P2 experiment. A more detailed explanation and derivations can be found in the following books, which were used as a basis and framework for the text: [8–14].

2.1. Standard Model

The Standard Model (SM) of particle physics is a self-consistent, renormalizable quantum field theory that describes three of nature's four fundamental forces: electromagnetism, the weak force, and the strong force (only gravity is absent). It is based on gauge symmetries and combines the electroweak $SU(2)_\mathrm{L} \times U(1)_Y$ with strong nuclear force $SU(3)_C$ *gauge groups* [15, 16]. These groups define the local symmetries of a field theory, determining how fields transform under continuous symmetry operations. Further details are briefly given in section 2.4.

The diagram in figure 2.1 gives an overview of the elementary particles of the SM. They are classified based on their quantum numbers and divided into two main groups based on the statistics they follow: fermions and bosons.

Fermions are matter particles with half-integer spin (1/2), which follow Fermi-Dirac statistics and obey the Pauli exclusion principle. They, in turn, are subdivided into the three generations (with no evidence for a fourth) of quarks and leptons. Quarks carry electric and color charges, allowing them to participate in the strong, weak, and electromagnetic interactions. Each generation of quarks consists of one particle with a charge of $2/3$ (like the up quark) and one with a charge of $-1/3$ (like the down quark). Leptons, which do not carry color charge, also come in three generations, each containing a charged lepton (electron, muon, or tau) and a corresponding neutrino (ν_e, ν_μ, ν_τ). While charged leptons interact electromagnetically and weakly, neutrinos only interact weakly as they carry no electric charge.

Bosons are the integer spin particles that describe the interactions between particles through force carriers. Photons (γ) carry the electromagnetic force, gluons (g) mediate the strong force, and $W^\pm$ and Z^0 bosons are responsible for the weak force. The electromagnetic force has an

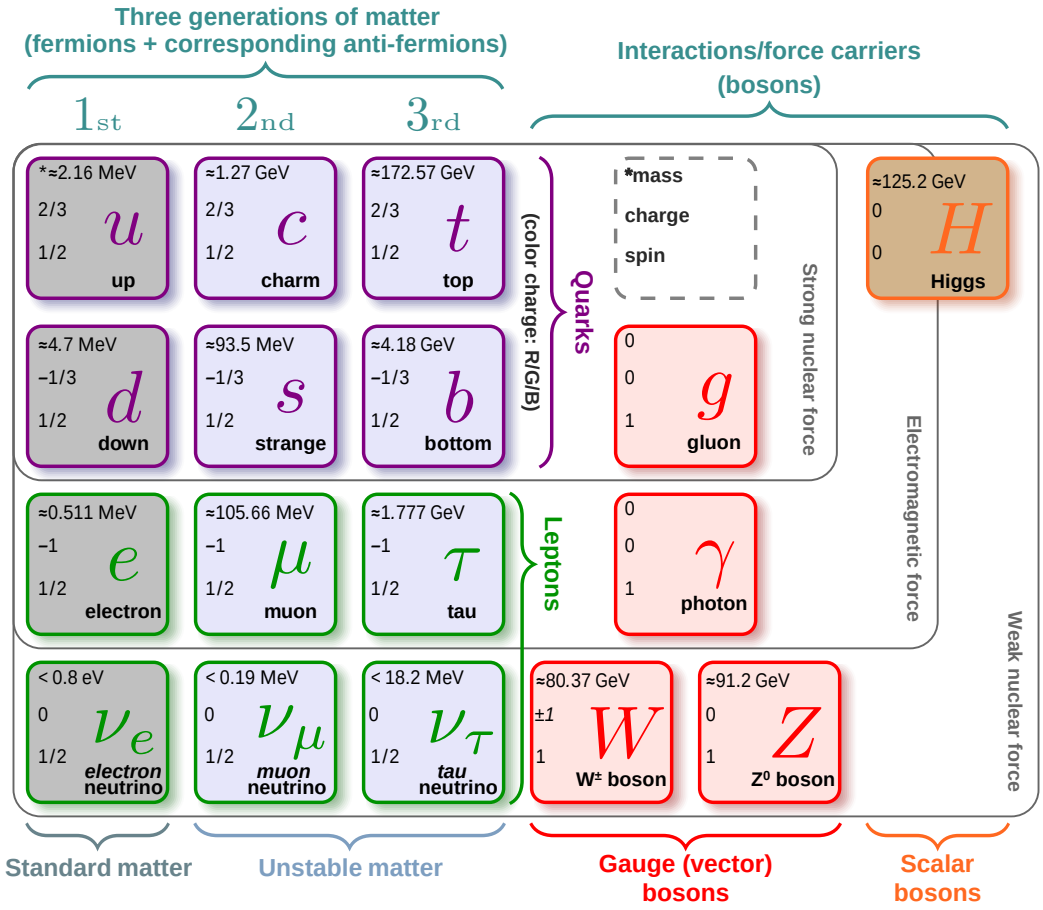

Figure 2.1.: Elementary particles of the Standard Model of particle physics (the up-to-date at the moment of writing values or upper limits of masses are taken from [17]). Reproduced with modifications and updates from [18].

infinite range due to the massless photon. However, its intensity diminishes by the square of the distance. Though much more intense, the strong force only operates at short distances because quarks and gluons are confined in color-neutral bound states (mesons or baryons). This confinement ensures quarks are never observed in isolation. In turn, the exchange bosons of the weak interaction are much heavier with masses of around 100 GeV, which gives the weak interaction a very short range compared to the electromagnetic and strong ones.

The Higgs boson is the only elementary scalar particle (spin-0) in the SM, and it plays a crucial role in generating particle masses through the Higgs mechanism [19–24]. This mechanism, proposed in the 1960s, explains how particles like the W and Z bosons acquire mass by interacting with the Higgs field, which permeates all of space. The experimental confirmation of the Higgs boson at the Large Hadron Collider (LHC) in 2012 [3, 4] provided strong support for this theory.

The masses of the $W^{\pm}$ and Z^0 bosons are predicted by the electroweak theory, a part of the Standard Model, through a spontaneous symmetry-breaking mechanism—the Higgs mechanism. Similarly, the masses of quarks and leptons also originate from the Higgs mechanism via their Yukawa couplings to the Higgs field. However, the values of these masses, as the Higgs boson mass itself, remain empirical parameters that must be determined experimentally. Initially, neutrinos were assumed to be massless. However, experimental evidence for their finite masses was discovered over 20 years ago [25], and the upper limits of their mass are still being refined.

Quarks, as carriers of color charge, cannot exist in isolation due to the phenomenon of color confinement [26–28]. Instead, they combine to form color-neutral composite particles known as hadrons. However, hadrons are not elementary particles, as they consist of multiple quarks bound together by the strong interaction. Hadrons are classified into two main categories: mesons and baryons. Mesons (e.g., pions, kaons) are composed of a quark-antiquark pair, making them bosons with integer spin that follow Bose-Einstein statistics. Baryons (e.g., protons, neutrons) consist of three quarks, making them fermions with half-integer spin that obey the Pauli exclusion principle.

2.2. Symmetries in the Standard Model

Symmetries play an essential role in the Standard Model, providing a profound understanding of the fundamental structure and leading to conservation laws through Noether's theorem [29]. Unlike static symmetries, such as those in crystal lattices, the symmetries of interest in the Standard Model are local (gauge) or spontaneously broken symmetries. These symmetries fundamentally govern interactions and influence the behavior of physical systems. Noether's theorem connects these symmetries and conservation laws, stating that each global dynamical symmetry corresponds to a conserved quantity. For example, invariant systems under Poincaré transformations, including linear and rotational transformations, conserve linear and angular momentum, while time-symmetric systems conserve energy.

Quantum Electrodynamics (QED), the theory that describes the interactions of relativistic charged particles through the electromagnetic force, is a prime example of a quantum field theory governed by such symmetries. In QED, fermions, half-integer spin particles, interact by exchanging a massless spin-1 particle, the photon. The theory can be formulated using the Lagrangian formalism, where the Lagrangian for free fermions is extended by requiring local gauge symmetry. This process serves as a template for constructing other aspects of the Standard Model, such as the electroweak Lagrangian, which, in turn, leads to the definition of the weak mixing angle θ_w, the central quantity in the P2 experiment.

The Dirac equation is a fundamental quantum mechanics and quantum field theory equation that describes the behavior of relativistic fermions. In natural units ($\hbar = c = 1$), for a free particle with mass m it is written as

$$\left(i\,\gamma^\mu \partial_\mu - m\right)\psi = 0, \tag{2.1}$$

where ψ is the Dirac spinor, $\mu = (t, -\bar{x})$ is a Lorentz index, γ^μ are the gamma matrices, and ∂_μ is the four-gradient.

The symmetries in the SM are internal symmetries, meaning that the Lagrangian

$$\mathcal{L} = \overline{\psi}(i\gamma^\mu \partial_\mu - m)\psi \tag{2.2}$$

stays invariant under gauge transformations. These transformations correspond to changes in the *global* phase of the fermion fields θ as

$$\psi \rightarrow e^{-iq\theta}\psi, \tag{2.3}$$

with implied conservation of the electric charge q.

Since QED is a gauge theory with a $U(1)$, which represents complex phase transformations symmetry group, the QED Lagrangian and the derived wave equation must remain invariant

under transformations that involve the local space-time dependent phase factor $\theta(x)$:

$$\psi \rightarrow \psi' = e^{-iq\theta(x)}\psi. \tag{2.4}$$

However, the free Lagrangian, which is given by eq. 2.2, being not constant in the space-time coordinates, is not invariant under these transformations because the ordinary derivatives ∂_μ do not vanish:

$$\partial_\mu\psi' = e^{-iq\theta(x)}[\partial_\mu - -iq(\partial_\mu\theta(x))]\psi. \tag{2.5}$$

It is possible to maintain gauge invariance by introducing the gauge-covariant derivative D_μ, with an associated gauge field A_μ as follows:

$$\partial_\mu \rightarrow D_\mu \equiv \partial_\mu - iqA_\mu. \tag{2.6}$$

Here, the unwanted term in eq. 2.5 vanishes due to transforms of the gauge field A_μ under the local space-time dependent mentioned above:

$$A_\mu \rightarrow A_\mu + \frac{1}{q}\partial_\mu\theta(x). \tag{2.7}$$

As a result, the Lagrangian for free fermion fields, which maintains local gauge invariance, is:

$$\mathcal{L} = i\overline{\psi}\gamma^\mu\partial_\mu\psi - m\overline{\psi}\psi - \left(q\overline{\psi}\gamma^\mu\psi\right)A_\mu = i\overline{\psi}\gamma^\mu\mathcal{D}_\mu\psi - m\overline{\psi}\psi. \tag{2.8}$$

However, introducing gauge fields A_μ introduces electromagnetic interaction, which requires an additional free particle as the mediator. The photon is the only candidate for such a particle in the SM (figure 2.1). Since a photon is a boson, a spin-1 particle, it can be described by the Proca Lagrangian:

$$\mathcal{L} = -\frac{1}{4}F^{\mu\nu}F_{\mu\nu} + \frac{1}{2}m^2A^\nu A_\nu \tag{2.9}$$

with the field tensor $F^{\mu\nu} = (\partial^\mu A^\nu - \partial^\nu A^\mu)$. As seen here, only the first term fulfills the local gauge invariance. The second term disappears since the photon is massless. Finally, the complete gauge invariant QED Lagrangian, which describes fermions in the presence of an electromagnetic field, can be written as

$$\mathcal{L}_{\text{QED}} = i\overline{\psi}\gamma^\mu\mathcal{D}_\mu\psi - m\overline{\psi}\psi - \frac{1}{4}F^{\mu\nu}F_{\mu\nu}. \tag{2.10}$$

Requiring a global symmetry to be valid at a local level is a fundamental aspect of the Standard Model. However, this approach does not explicitly include the mass terms necessary for a complete electroweak theory. These mass terms are introduced through the Higgs mechanism (sections 2.4.2 and 2.4.3).

2.3. Discrete Symmetries. Helicity and Chirality

Symmetries can be classified into two categories: continuous and discrete. Parity, an example of a discrete symmetry, involves the inversion of all spatial coordinates, representing a mirror reflection. For instance, looking into a mirror interchanges right and left hands. This concept is extended to particles by assigning them a specific handedness.

The electromagnetic field interacts with all particles in proportion to their electric charge.

However, to describe processes involving the weak force, it is essential first to introduce the concepts of helicity and chirality. Helicity describes the alignment of the spin vector, $\mathbf{S}$, with the momentum direction, $\mathbf{p}$ (with the notation $\mathbf{p} \equiv |\vec{p}|$), as follows:

$$h \equiv \frac{\mathbf{S} \cdot \mathbf{p}}{p} = \begin{cases} > 0 \rightarrow & \text{positive helicity} \\ < 0 \rightarrow & \text{negative helicity} \end{cases} . \tag{2.11}$$

When $\mathbf{S}$ and $\mathbf{p}$ are parallel, the particle is *right-handed* or has positive helicity. Conversely, the particle is *left-handed* or has negative helicity when they are anti-parallel. In the case of a spin-half particle, the helicity operator has eigenvalues of $\pm\frac{1}{2}$ with positive and negative helicity states, respectively.

It is important to note that, while helicity is well defined for all particles, it is not a Lorentz invariant quantity for massive particles. In the case of massless particles, helicity is equivalent to chirality. Chirality is the Lorentz invariant description used when describing weak interactions.

Any Dirac spinor ψ can be expressed as a sum of its helicity eigenstates:

$$\psi = \mathcal{P}_+ \, \psi + \mathcal{P}_- \, \psi \equiv \psi_+ + \psi_- \, , \tag{2.12}$$

where $\mathcal{P}_\pm = (\mathbb{1}_4 \pm \hat{h})/2$ is the helicity projection operator.

Helicity is an important concept in particle physics. It is a conserved quantity for free particles, as it commutes with the Dirac Hamiltonian. However, helicity is not a Lorentz invariant for massive particles. This is because a Lorentz boost can reverse the particle's momentum direction without changing its spin, thus flipping the helicity eigenvalue.

In contrast, chirality, which defines the handedness of massless particles, is Lorentz invariant and represents an intrinsic property of the particle. Chirality lacks a simple physical interpretation, it is a purely quantum mechanical concept. In Dirac-Pauli representations, the chirality operator can be represented by a matrix as

$$\gamma^5 = i\gamma^0\gamma^1\gamma^2\gamma^3 = \begin{pmatrix} 0 & \mathbb{1}_2 \\ \mathbb{1}_2 & 0 \end{pmatrix}, \tag{2.13}$$

with the eigenvalues of ± 1. Confusingly, particles with negative or positive chirality are also often referred to as left- or right-handed, respectively. Therefore, the following sections will explicitly specify whether handedness is mentioned in terms of chirality or helicity.

For massive particles, the associated Dirac spinor consists of both left-chiral and right-chiral components, meaning that it does not serve as an eigenvector of the chirality operator on its own. However, it is feasible to express the Dirac spinor as a sum of its right- and left-chiral components (R and L indexes, respectively) by employing the chiral projection operators

$$\mathcal{P}_{\mathrm{R,L}} = \frac{1}{2}\left(1 \pm \gamma^5\right) , \tag{2.14}$$

allowing the Dirac spinor ψ be written as

$$\psi = \mathcal{P}_\mathrm{L} \, \psi + \mathcal{P}_\mathrm{R} \, \psi \equiv \psi_\mathrm{L} + \psi_\mathrm{R} \, . \tag{2.15}$$

Helicity and chirality are distinct properties for massive fermions, although they are related. For a spin-half fermion with positive helicity, its Dirac spinor ψ_+ can be expressed in terms of

chiral components ψ_R and ψ_L as follows:

$$\psi_+ \propto \left(\frac{1+\kappa}{2}\right)\psi_R + \left(\frac{1-\kappa}{2}\right)\psi_L\,, \tag{2.16}$$

with $\kappa = p/(E+m)$. The probability of finding this particle left-handed in terms of chirality is proportional to $(1-\kappa)^2$, which vanishes in the ultrarelativistic limit ($E \gg m$). This shows that in the ultrarelativistic limit, positive helicity states become almost entirely right-handed (while negative helicity states become almost entirely left-handed).

Helicity, unlike chirality, can flip with momentum changes. In the case of massless particles, helicity and chirality are equivalent and conserved. However, for massive particles, they are distinct. Interactions with the Higgs field, which gives particles mass, can change chirality by mixing left- and right-handed components in the Dirac equation. Therefore, while crucial for weak interactions, chirality is not conserved like electric charge.

As discussed in the following sections, left- and right-chiral particles interact differently via the weak force. This cannot be directly validated by changing the particle's helicity since, as mentioned above, the chirality state can change. However, in experiments, the probability of a particle being in a particular chiral state can be measured instead of requiring a particle with a defined chirality state. This probability can be determined from the particle's energy, momentum, and helicity, all of which are measurable.

2.4. Electroweak Theory

The electroweak theory, proposed by Glashow, Salam, and Weinberg [30–32] in the late 1960s, and therefore also known as the GWS model, is a gauge theory that unifies electromagnetic and weak interaction into one theoretical framework. Here, the interactions are governed by the symmetry transformations of the gauge group, while the Higgs mechanism is responsible for generating mass for the three heavy gauge bosons. Furthermore, fermions acquire mass through a simple Yukawa coupling with the Higgs field. This coupling is related to the strength of the interaction between the Higgs field and a specific fermion, ensuring the Standard Model remains renormalizable.

The electroweak theory is built on the gauge groups $SU(2)_L$ and $U(1)_Y$. $U(N)$ refers to the group of unitary matrices, and $SU(N)$ refers to the subgroup of unitary matrices with determinant 1. Both $U(N)$ and $SU(N)$ are examples of Lie groups, which are groups of smooth transformations that combine algebraic group structure with smooth geometric properties. The number in brackets indicates the group's order, reflecting the number of independent symmetry transformations. The $SU(2)_L$ group corresponds to weak isospin—a quantum number that groups particles into doublets that interact via the weak force—and is chosen to describe the weak interaction because it naturally accounts for its left-handed nature (reflected in the 'L' subscript). The $U(1)_Y$ group, associated with weak hypercharge—a quantum number related to electric charge and governing interactions with the electroweak force—(denoted by 'Y' subscript), provides a framework for unifying the weak and electromagnetic interactions by ensuring the correct quantum numbers for the electromagnetic force and its corresponding gauge boson.

The $SU(3)$ group describes the strong (mentioned earlier in section 2.1) interaction governing how quarks and gluons interact via the exchange of color charge (denoted by 'C' subscript). It ensures the confinement of quarks and leads to asymptotic freedom at high energies, fundamental Quantum Chromodynamics (QCD) features.

At first glance, one might assume that the electromagnetic and weak interactions are entirely separate, associating $SU(2)_{\mathrm{L}} \equiv SU(2)_W$ and $U(1)_Y \equiv U(1)_{\mathrm{EM}}$, where the subscripts 'W' and 'EM' explicitly refer to the weak and electromagnetic forces, respectively. However, directly identifying these groups with the observed interactions would result in four massless gauge bosons, contradicting experimental evidence. Although adding mass terms manually for these bosons is possible, doing so results in a non-renormalizable theory, thereby eliminating its predictive power.

2.4.1. Electroweak Symmetry. Gauge and Higgs Fields

A more viable solution involves mixing $SU(2)_{\mathrm{L}} \times U(1)_Y$, which, through spontaneous symmetry breaking via the Higgs mechanism, results in the emergence of the electromagnetic gauge symmetry $U(1)_{\mathrm{EM}}$. Here, $SU(2)_{\mathrm{L}}$ corresponds to weak isospin and is associated with three gauge bosons W_1^μ, W_2^μ, W_3^μ, and $U(1)_Y$, in turn, corresponds to weak hypercharge and is associated with one gauge boson B. While the mechanism's details have not been fully introduced, the structure of the electroweak currents can be predicted from their gauge properties.

In QED, the electromagnetic current j^μ_{EM} interacts with the gauge field A_μ as

$$j^\mu_{\mathrm{EM}} A_\mu = (\overline{\psi}\gamma^\mu Q\psi)A_\mu \,, \tag{2.17}$$

where Q is the charge operator. In turn, the $U(1)_Y$ gauge group introduces a hypercharge current j^μ_Y, with coupling g, interacting with the gauge field B_μ, given by:

$$j^\mu_Y B_\mu = -ig\overline{\psi}\gamma^\mu \frac{Y}{2}\psi B_\mu \,. \tag{2.18}$$

For $SU(2)_{\mathrm{L}}$, the weak currents j^μ_a ($a = 1, 2, 3$) couple to the corresponding gauge fields W^μ_a, with generators τ_a (normalized Pauli matrices) and coupling g', as

$$-ig'\; j^\mu_a W^\mu_a = -ig_2\, \overline{\chi}_{\mathrm{L}}\, \gamma^\mu \tau_a W^\mu_a \chi_{\mathrm{L}} \,, \tag{2.19}$$

where χ_{L} are left-handed fermion weak isospin doublets. Only left-handed particles interact this way, while right-handed fermions decouple, acting as weak isosinglets.

The electric charge operator Q is related to the third component of the weak isospin operator I_3 (is relevant for the Z^0 boson interactions), and hypercharge Y by the Gell-Mann–Nishijima relation:

$$Q = I_3 + \frac{Y}{2}. \tag{2.20}$$

In the same way, the electromagnetic current can be expressed using the hypercharge and related weak currents, j^μ_Y (2.18) and j^μ_3 (2.19), respectively, as

$$j^\mu_{\mathrm{EM}} = j^\mu_3 + \frac{1}{2} j^\mu_Y. \tag{2.21}$$

This shows that the electromagnetic interaction is embedded within the larger electroweak structure. Notably, j^μ_3 involves only left-handed components, meaning charged weak interactions only couple left-handed fermions, while neutral currents interact with both left- and right-handed fermions.

2.4.2. Higgs Mechanism. Spontaneous Symmetry Breaking

To generate masses for the weak gauge bosons without breaking gauge invariance explicitly, the Higgs field ϕ is introduced. The Higgs field is a complex scalar field and forms a doublet under $SU(2)_{\mathrm{L}}$ with a hypercharge of $Y = 1$. The components of the Higgs field can be written as

$$\Phi = \begin{pmatrix} \phi^+ \\ \phi^0 \end{pmatrix} = \frac{1}{\sqrt{2}} \begin{pmatrix} \phi_1 + i\phi_2 \\ \phi_3 + i\phi_4 \end{pmatrix}, \tag{2.22}$$

where ϕ^+ and ϕ^0 are the charged and neutral components of the Higgs field, respectively, and ϕ_i (i = 1,2,3,4) are the real scalar components.

The Higgs field interacts with itself through a potential:

$$V(\phi) = \mu^2 \phi^\dagger \phi + \lambda (\phi^\dagger \phi)^2 \tag{2.23}$$

where $\lambda > 0$ is the self-interaction coupling, and μ^2 determines the form of the potential.

Gauge invariance implies that all gauge bosons must be massless. However, this contradicts experimental observations, which reveal that the $W_\pm$ and Z_0 bosons have mass. The Higgs mechanism [19–24] resolves this problem. If $\mu^2 > 0$, the potential acquires a nonzero vacuum expectation value (VEV), leading to spontaneous symmetry breaking.

At the minimum of the potential $V(\phi)$, the Higgs field acquires a VEV given by:

$$\langle \phi \rangle = \frac{v}{\sqrt{2}}, \tag{2.24}$$

where $v = \sqrt{-\mu^2/\lambda} \approx 246\,\mathrm{GeV}$ is determined from the Fermi constant, measured in low-energy weak interactions. The nonzero VEV allows the Higgs field to interact with gauge fields, giving mass to the weak bosons. The choice of a specific direction for the Higgs VEV breaks the symmetry $SU(2)_{\mathrm{L}} \times U(1)_Y$ down to the symmetry of electromagnetism $U(1)_{\mathrm{EM}}$, keeping the photon massless.

The scalar Higgs field (ϕ) includes the standard kinetic and potential terms:

$$\mathcal{L}_{\mathrm{kin}} = (\partial_\mu \phi)^\dagger (\partial^\mu \phi) - V(\phi^\dagger \phi) - \mathcal{L}_{\mathrm{hf}}\,. \tag{2.25}$$

When spontaneous symmetry breaking occurs, the gauge bosons acquire masses. The covariant derivative for the Higgs field is given by:

$$D_\mu \phi = \left(\partial_\mu - i\frac{g_2}{2} W_\mu^a \tau^a - i\frac{g_1}{2} Y B_\mu \right) \phi. \tag{2.26}$$

2.4.3. Gauge Boson Masses. The Weak Mixing Angle

Substituting the VEV of the Higgs field into the kinetic term of the Lagrangian, we obtain the mass terms for the gauge bosons. The relevant terms in the Lagrangian now become:

$$(D_\mu \phi)^\dagger (D_\mu \phi) \to -\frac{v^2}{8} \left[g^2 (W_1^\mu W_{1\mu} + W_2^\mu W_{2\mu}) + (g W_3^\mu - g' B^\mu)^2 \right]. \tag{2.27}$$

This expression generates the masses for the physical gauge bosons. The combination of W_1^μ and W_2^μ produces the charged $W^\pm$ bosons:

$$W_\pm^\mu = \frac{1}{\sqrt{2}}(W_1^\mu \mp iW_2^\mu)\,. \tag{2.28}$$

The mass of the $W^\pm$ bosons is given by:

$$m_{W^\pm} = \frac{gv}{2}\,. \tag{2.29}$$

The neutral bosons $W_3^\mu$and B^μ mix to form the Z^0 boson and the massless photon. The mixing is parametrized by the Weinberg angle (or weak mixing angle) θ_w, defined as

$$\tan(\theta_w) = \frac{g'}{g},\quad \cos\theta_w = \frac{g}{\sqrt{g^2+g'^2}},\quad \sin\theta_w = \frac{g'}{\sqrt{g^2+g'^2}}\,. \tag{2.30}$$

The fields of photon A^μ and the neutral weak boson Z^μ are linear combinations of W_3^μ and B^μ:

$$A^\mu = \cos\theta_w B^\mu + \sin\theta_w W_3^\mu\,; \tag{2.31a}$$
$$Z^\mu = -\sin\theta_w B^\mu + \cos\theta_w W_3^\mu\,. \tag{2.31b}$$

The mass of the Z^0 boson is given by:

$$m_Z = \frac{v}{2}\sqrt{g'^2+g^2}. \tag{2.32}$$

At the tree-level, the weak mixing angle can be expressed in terms of the masses of the weak gauge $W^\pm$ and Z bosons using eqs. 2.29 and 2.32 given above as

$$\sin^2\theta_w = 1 - \left(\frac{m_W}{m_Z}\right)^2\,. \tag{2.33}$$

This relation, derived from the Higgs mechanism, provides an improved theoretical formulation and allows the most accurate determination of the Weinberg angle since the masses of the gauge bosons can be measured with high precision. However, the relations presented so far are limited to tree-level calculations, which exclude higher-order (loop) corrections. A thorough validation of the SM is only possible when factoring in these corrections with a consequent renormalizing of the theory (addressed further in section 2.5).

2.4.4. Neutral Weak Current and Nucleon Weak Charges

The neutral current interaction involves electromagnetic or weak exchanges via photon γ or Z_0 boson, respectively (figure 2.2). Following the derivation of the electromagnetic current j_{EM}^μ in section 2.4.1, the neutral weak exchange can be defined in terms of weak and hypercharge currents (j_3^μ and j_Y^μ, respectively) in proportion according to eq. 2.31b as

$$j_Z^\mu = j_3^\mu \cos\theta_w - j_Y^\mu \cos\theta_w\,. \tag{2.34}$$

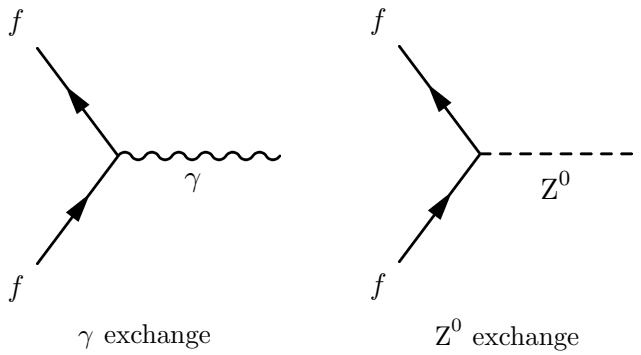

Figure 2.2.: Neutral current exchange diagrams both the electromagnetic and weak exchange.

Then, solving eq. 2.20 for Y and placing eqs. 2.18 and 2.19 for j_Y^μ and j_3^μ and eq. 2.14 for $\mathcal{P}_\mathrm{R}$ and $\mathcal{P}_\mathrm{L}$ in the above gives:

$$j_Z^\mu = \frac{e}{\sin\theta_w \cos\theta_w}[\overline{\psi}_\mathrm{L}(I_3 - 2Q\sin^2\theta_w)\gamma_\mu\psi_\mathrm{L} + (-Q\sin^2\theta_w)\overline{\psi}_\mathrm{R}\gamma_\mu\psi_\mathrm{R}]\,. \tag{2.35}$$

Consider the following definitions of couplings:

$$g_Z = \frac{e}{\sin\theta_w\cos\theta_w} = \frac{g}{\cos\theta_w}\,,\quad g_V = I_3 - 2Q_f\sin^2\theta_w\,,\quad \text{and}\quad g_A = I_3\,. \tag{2.36}$$

Using these definitions, eq. 2.35 converts to

$$j_Z^\mu = g_Z\,\overline{\psi}\gamma_\mu(g_V - g_A\gamma^5)\psi. \tag{2.37}$$

Table 2.1 lists vector and axial-vector couplings for fundamental fermions. The weak interaction, including the neutral current interaction, violates parity since both couplings are non-zero. These components transform differently under parity, and when they are combined in the neutral current, the interaction does not remain invariant under the parity transformation. Parity violation is one of the key features of the weak interaction, distinguishing it from the strong and electromagnetic interactions, which conserve parity.

Fermion	**Charge** Q	**Isospin** I_3	g_V	g_A
ν_e, ν_μ, ν_τ	0	$+1/2$	$+1/2$	$+1/2$
e^-, μ^-, τ^-	-1	$-1/2$	$-1/2 + 2\sin^2\theta_w$	$-1/2$
u, c, t	$+2/3$	$+1/2$	$+1/2 - 4/3\sin^2\theta_w$	$+1/2$
d, s, b	$-1/3$	$-1/2$	$-1/2 + 2/3\sin^2\theta_w$	$-1/2$

Table 2.1.: Neutral vector and axial-vector couplings to the Z^0 boson in the Standard Model.

The electromagnetic and neutral weak charges of composite structures are determined via the coherent sum of charges of the corresponding *valence quarks* listed in table 2.1. For example, in the case of the proton, which consists of *uud* quarks, the electromagnetic charge is

$$Q_\mathrm{EM}^p = \sum_i Q_i = 2Q_u + Q_d = 2\cdot\frac{2}{3} - \frac{1}{3} = 1\,. \tag{2.38}$$

In the experimental context, the weak charge of a fermion is conventionally given as corresponding vector coupling with a normalization factor of 2:

$$Q_{\mathrm{W}} \equiv 2\, g_v \,. \tag{2.39}$$

Thus, the weak charge of the proton at three level is

$$\begin{aligned} Q_{\mathrm{W}}^{p} &= \sum_i Q_{\mathrm{W}}^{i} = (2Q_{\mathrm{W}}^{u} + Q_{\mathrm{W}}^{d}) \\ &= 2\left(1 - \frac{8}{3}\sin^2\theta_w\right) + \left(-1 + \frac{4}{3}\sin^2\theta_w\right) = 1 - 4\sin^2\theta_w \,. \end{aligned} \tag{2.40}$$

Similarly, the neutron (udd) weak charge is $Q_{\mathrm{W}}^{n} = -1$ (at three level).

Given the experimentally determined value of the weak mixing angle, $\sin^2\theta_w \sim 0.23$ [17], the proton weak charge is suppressed, while the neutron weak charge is not. Consequently, the proton weak charge is highly sensitive to the value of $\sin^2\theta_w$.

2.5. Electroweak Radiative Corrections

The results discussed so far have focused on leading-order, or tree-level, processes, where interactions occur with the minimum number of vertices required. However, higher-order corrections involving additional vertices are crucial for accurate theoretical predictions, especially at the sub-percent precision level, as in low-energy parity-violation experiments like the P2 experiment.

These higher-order processes, as shown in figure 2.3, involve virtual particles, where a fermion can emit and reabsorb a virtual particle, leading to loop diagrams such as vacuum polarization. These virtual particles are not constrained by energy or momentum conservation, causing integrals over all possible momenta, which can lead to ultraviolet divergences. A well-known example of this in quantum electrodynamics (QED) is the vacuum polarization correction. In such cases, the infinities must be handled through a procedure known as renormalization, where divergent terms are absorbed into redefined or renormalized parameters.

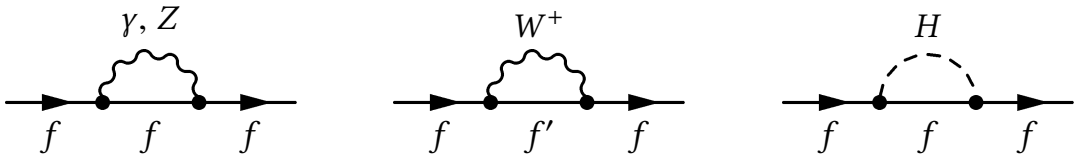

Figure 2.3.: First order loop corrections to the fermion propagation, involving different virtual particles. Taken from [33].

In electroweak theory, the renormalization process ensures that the coupling constants become functions of the momentum transfer Q^2. For instance, the QED coupling the electromagnetic coupling constant α is renormalized to $\alpha(Q^2)$, meaning the strength of interactions depends on the energy scale. This phenomenon, often described as the *running* of the coupling constant, can be experimentally observed, such as in the Lamb shift in the hydrogen atom's hyperfine structure [10, 11].

Thus, the bare parameters from tree-level electroweak theory are replaced by renormalized ones. The Standard Model's predictive accuracy in higher-order, perturbative calculations is possible because it is a renormalizable theory [34–38], allowing these corrections to be systematically accounted for across different energy scales.

The weak mixing angle quantifies the relation between the electromagnetic and the weak force, specifically between the Z boson and the photon (γ).

2.5.1. Scale-Dependence of Weak Mixing Angle

In the Standard Model, parameters like masses, couplings, and mixing angles, including the weak mixing angle $\sin^2\theta_w$, require renormalization to account for higher-order corrections. Particle loops, such as those involving Z propagation and $Z-\gamma$ transitions, affect the weak mixing angle, making its renormalized value dependent on the chosen approach — renormalization scheme.

In the on-shell scheme, $\sin^2\theta_w$ is tied to the gauge boson mass relationship given in eq. 2.33. Therefore, it is directly linked to physical observables. However, this induces radiative corrections to neutral current amplitudes proportional to $O(\alpha m_t^2/m_W^2)$ [39], which makes this approach unfavorable due to the large top quark mass m_t.

In measurements at the Large Electron-Positron Collider (LEP), an effective weak mixing angle was defined at the Z-pole using the ratio of leptonic vector and axial-vector couplings g_V^l and g_A^l [40]:

$$\sin^2\theta_w^{\text{LEP}} = \frac{1}{4}\left(1 - \frac{g_V^l}{g_A^l}\right). \tag{2.41}$$

This definition is practical for Z-pole measurements but requires additional corrections for non-Z-pole applications.

In the *modified minimal subtraction* ($\overline{\text{MS}}$) scheme, the weak mixing angle becomes dependent on an arbitrary mass scale $\mu \equiv \mu_{\overline{\text{MS}}}$. This approach is computationally convenient since it simplifies calculations by efficiently absorbing the divergences from loop calculations into renormalized parameters and allows consistent calculations across different energy scales with minimal complexity. For example, the definitions of the weak mixing angle in the LEP and $\overline{\text{MS}}$ schemes have a slight numerical difference [41]:

$$\sin^2\theta_w^{\text{LEP}} - \sin^2\theta_w(m_Z)_{\overline{\text{MS}}} = 2.8 \times 10^{-4}. \tag{2.42}$$

At the moment of writing, the most precise experimentally determined value of the weak mixing angle is: $\sin^2\theta_w(m_Z)_{\overline{\text{MS}}} = 0.231\,29(4)$ [17]. The scale dependence, or running, of the weak mixing angle in the $\overline{\text{MS}}$ renormalization scheme is shown in figure 2.4.

Radiative corrections, including γ-Z mixing and WW box diagrams, influence the running of the weak mixing angle. Fermion loops tend to screen the weak charge, reducing $\sin^2\theta_w(Q^2)$ at higher energies, while boson loops have the opposite effect, increasing it beyond the W-boson mass. Although poorly measured experimentally, the running weak mixing angle might reveal physics beyond the Standard Model, as undiscovered particles contribute to this dependence. The P2 experiment will contribute by precisely measuring $\sin^2\theta_w$ at low-momentum transfer (Q^2) through parity-violating electron scattering (PVES).

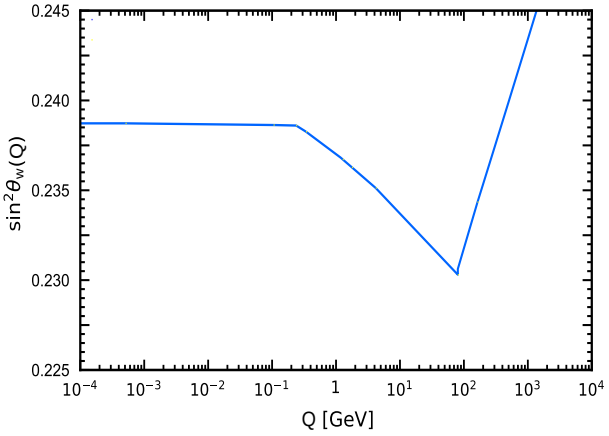

Figure 2.4.: Scale dependence of the weak mixing angle in the $\overline{\text{MS}}$ scheme. Modified from [17].

2.6. Experimental Measurement of Parity Violation

Among the various electron scattering processes employed in PVES experiments, electron-electron (Møller) scattering and electron-proton (ep) scattering are particularly important.

Ep scattering involves the interaction of an electron with a proton—a composite particle made of quarks. This process is sensitive to both electromagnetic and weak interactions. The measured asymmetries can provide information about the proton's internal structure and reveal the interplay of different fundamental forces.

In contrast, Møller scattering involves the collision of two electrons, making it a purely leptonic interaction. The absence of hadronic contributions eliminates complications from the strong force, thus offering a cleaner probe of the electroweak interaction between fundamental leptons. This characteristic is crucial for performing precise tests of the SM.

Depending on the experimental configuration, either Møller or ep scattering can serve as the primary signal, with the other process acting as a background. For instance, experiments like MOLLER and SLAC E158 are designed to study purely leptonic interactions, whereas experiments like P2 and Q_{weak} focus on electron-nucleon interactions. Although all these experiments operate in the low momentum transfer regime (see figure 2.5), the choice of signal and background processes, along with the specific kinematic settings, are carefully optimized to enhance sensitivity to electroweak parameters and to mitigate systematic uncertainties. Table 2.2 gives an overview and compares these experiments, and figure 2.5 illustrates the scale dependence of the weak mixing angle in the $\overline{\text{MS}}$ renormalization scheme compared with experimental data.

In the completed SLAC E158 experiment and the proposed MOLLER experiment, the parity-violating asymmetry is measured via Møller scattering. In this context, the asymmetry is directly sensitive to weak interaction parameters while largely avoiding hadronic uncertainties. Any contribution from ep scattering acts as a background that must be carefully accounted for or minimized.

Conversely, the P2 experiment, similar in approach to the completed Q_{weak} experiment, uses elastic electron-proton scattering as the primary signal. While both experiments have the same goals, the P2 experiment aims to determine the weak mixing angle with higher precision, comparable to that achieved at the Z-pole.

Feature	P2 (MESA)	Q_{weak} (JLAB) [42, 43]	SLAC E158 [44, 45]	MOLLER (JLAB) [46]
Primary physics goal	$\sin^2\theta_w$	Q^p_{W}, $\sin^2\theta_w$	$\sin^2\theta_w$	Q^e_{W}, $\sin^2\theta_w$
Signal process	Møller scattering		Elastic ep scattering	
Beam energy	155 MeV	1.16 GeV	45 − 50 GeV	11 GeV
Beam current, µA	150	180	~2	65
Beam polarization, %	85-90	~89	~85	~85
Target type*	Liquid hydrogen, unpolarized			
Scattering angles (lab)	25 − 45°	4.4 − 7.5°	4.5 − 8 mrad	5 − 19 mrad
Q^2, GeV^2	4.5×10^{-3}	25×10^{-3}	30×10^{-3}	5.6×10^{-3}

*With different lengths and configurations.

Table 2.2.: Overview and comparison of PVES experiments.

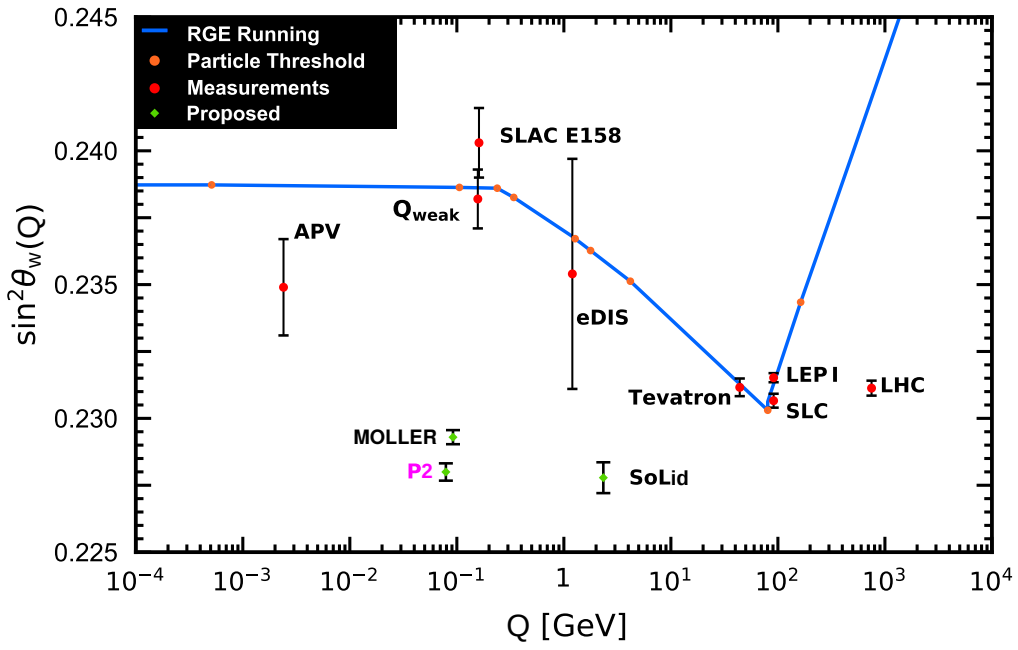

Figure 2.5.: Scale dependence of the weak mixing angle in the $\overline{\text{MS}}$ renormalization scheme compared with experimental data. The points for the proposed experiments are put to arbitrary vertical positions, with the error bars corresponding to the estimated precision. Picture modified from [17].

The following section is devoted to parity violation in ep scattering, representing signal events in the P2 experiment. The theoretical framework for Møller scattering will be discussed in section 7.2.1 (part III and chapter 7) in the context of the Møller polarimetry technique.

2.7. Parity Violation in Electron-Proton Scattering

Electron-proton scattering has been a fundamental method for investigating nuclear structure, and it has a long and successful experimental history. Over the past 50 years, advances in experimental techniques have allowed researchers to map out the distribution of electric charge and magnetization within nuclei [47–49]. Recent technological developments have pushed the boundaries further, enabling electron scattering experiments to probe higher-order processes with unprecedented precision. One key advancement is parity-violating electron scattering, which has provided insights into strangeness contributions in nucleons and served as a crucial test of the Standard Model. These experiments, particularly those involving polarized electron beams, allow for detecting small parity-violating asymmetries, providing a way to examine the V-A structure (combination of vector and axial vector currents) of the weak force.

2.7.1. Cross Section for Electron-Proton Scattering

Elastic electron-proton scattering (figure 2.6) is primarily governed by electromagnetic interaction, with weak interaction effects, such as parity violation from polarized electrons, being negligible for scattering cross-section/in most scattering cross-section measurements. The differential cross section for a relativistic spin-1/2 particle with energy E scattering elastically off a static, spinless, point-like particle is given by the Mott cross section, which incorporates the Rutherford cross section with an additional angular factor that accounts for the electron spin:

$$\left(\frac{d\sigma}{d\Omega}\right)_{\text{Mott}} = \left(\frac{d\sigma}{d\Omega}\right)_{\text{Rutherford}} \cos^2\left(\frac{\theta}{2}\right) = \frac{\alpha^2}{4E^2 \sin^4\left(\frac{\theta}{2}\right)} \cos^2\left(\frac{\theta}{2}\right), \tag{2.43}$$

where α is the fine-structure constant and θ the scattering angle in the lab frame.

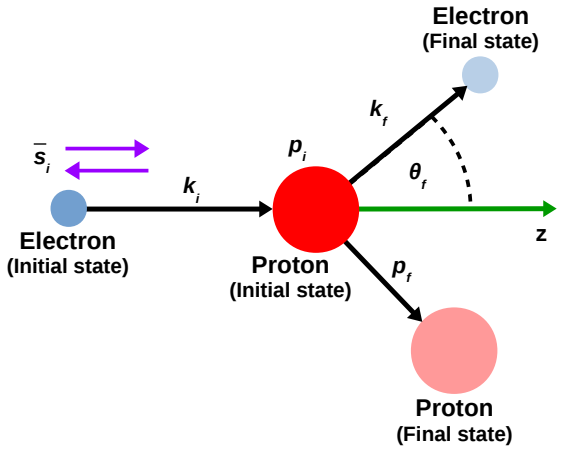

Figure 2.6.: Schematic of elastic electron-proton scattering in the laboratory frame. An incoming electron (blue) with momentum $\mathbf{k_i}$ and spin vector $\bar{\mathbf{s}}_\mathbf{i}$ interacts with a stationary proton (red) with momentum p_i, resulting in a scattered electron (light blue, $\mathbf{k_f}$) and a recoiling proton (pink, $\mathbf{p_f}$). The scattering angle of the electron is denoted as θ_f. Reproduced and modified from [50].

In electron-proton scattering, recoil and proton spin effects must be considered, leading to the cross section:

$$\left(\frac{d\sigma}{d\Omega}\right) = \left(\frac{d\sigma}{d\Omega}\right)_{\text{Mott}} \frac{E}{E'} \left(1 + 2\tau \tan^2\frac{\theta}{2}\right), \tag{2.44}$$

with

$$\tau = \frac{Q^2}{4m_p^2}\,, \tag{2.45}$$

where E' is the electron's final energy after scattering, Q^2 is the four-momentum transfer and m_p is the proton mass. The energy of the electron after scattering is related to the initial energy and the scattering angle θ by:

$$E' = \frac{m_p\, E}{m_p + E\,(1-\cos\theta)}\,, \tag{2.46}$$

with neglected electron mass. Then, the four-momentum transfer squared — one of the key quantities in electron-proton scattering — can be derived from energy and momentum conservation as

$$Q^2 = 4EE'\sin^2\frac{\theta}{2} = \frac{2m_pE^2\,(1-\cos\theta)}{m_p + E\,(1-\cos\theta)}\,. \tag{2.47}$$

Therefore, Q^2, as it can be seen, depends only on the incident electron energy E and the scattering angle θ.

2.7.2. Electromagnetic Form Factors

In the experiments, the Sachs electromagnetic form factors $G_{\mathrm{E}}^{\gamma,p}(Q^2)$ and $G_{\mathrm{M}}^{\gamma,p}(Q^2)$, which account for the finite size of the proton and describe the proton's internal structure, are usually introduced. These form factors modify the cross section, leading to the Rosenbluth formula:

$$\left(\frac{d\sigma}{d\Omega}\right)_{\text{Rosenbluth}} = \left(\frac{d\sigma}{d\Omega}\right)_{\text{Mott}} \frac{E}{E'}\left[\frac{(G_{\mathrm{E}}^{\gamma,p}(Q^2))^2 + \tau(G_{\mathrm{M}}^{\gamma,p}(Q^2))^2}{1+\tau} + 2\tau(G_{\mathrm{M}}^{\gamma,p}(Q^2))^2\tan^2\frac{\theta}{2}\right]. \tag{2.48}$$

At low momentum transfer, when $Q^2 \ll m_p^2$, $\tau \to 0$ and therefore the term in brackets simplifies to $(G_{\mathrm{E}}^{\gamma,p}(Q^2))^2$.

Electroweak scattering amplitudes require considering all contributing processes. In electron-nucleon scattering, while Z^0 boson exchange is generally suppressed due to its mass, it becomes significant in parity-violating scattering. Therefore, accurately describing electron-nucleon interactions requires determining the photon and Z^0 boson exchange vertices (at tree-level).

The electron vertices are related to the electromagnetic and weak currents given by eqs. 2.17 and 2.37. However, the nucleon currents are more complicated since nucleons are composite particles. In the case of the proton, the vertex can be expressed via corresponding currents using Pauli and Dirac form factors $F_{1,2}(Q^2)$ and axial current $G_{\mathrm{A}}^{Z}(Q^2)$, as [51]

$$j_\gamma^\mu = \bar\psi\left(F_1^\gamma(Q^2)\gamma^\mu + F_2^\gamma(Q^2)\frac{i\sigma^{\mu\nu}q_\nu}{2m_p}\right)\psi\,; \tag{2.49a}$$

$$j_Z^\mu = \bar\psi\left(F_1^Z(Q^2)\gamma^\mu + F_2^Z(Q^2)\frac{i\sigma^{\mu\nu}q_\nu}{2m_p} + G_{\mathrm{A}}^Z(Q^2)\gamma^\mu\gamma_5\right)\psi. \tag{2.49b}$$

with $\sigma^{\mu\nu} = i\left[\gamma^\mu, \gamma^\nu\right]$ and q_ν are components of the four-momentum transfer. The axial form factor in the neutral weak proton vertex is introduced due to parity violation by the Z^0 exchange.

The electromagnetic and neutral weak form factors, in turn, can be approximated in terms

of contributing quarks (neglecting the contributions of heavier quarks [52]), weighted by their respective electric or weak charges (table 2.1):

$$F_{1,2}^{\gamma} = \frac{2}{3} F_{1,2}^{u} - \frac{1}{3} \left(F_{1,2}^{d} + F_{1,2}^{s} \right) ; \tag{2.50a}$$

$$F_{1,2}^{Z} = \left(1 - \frac{8}{3} \sin^2\theta_w \right) F_{1,2}^{u} + 2 \left(-1 + \frac{4}{3} \sin^2\theta_w \right) \left(F_{1,2}^{d} + F_{1,2}^{s} \right) ; \tag{2.50b}$$

$$G_{\mathrm{A}}^{Z} = G_{\mathrm{A}}^{u} - G_{\mathrm{A}}^{d} - G_{\mathrm{A}}^{s} . \tag{2.50c}$$

with the conventional normalization factor of 2 for axial coupling g_{A} in G_{A}^{Z}, similarly to eq. 2.39. Though not explicitly separated, these equations account for the dominant contribution of valence quarks (long-lived quarks that define the hadron's quantum numbers) as well as the smaller contribution of sea quarks (quark-antiquark pairs arising from quantum chromodynamics (QCD) vacuum fluctuations).

2.7.3. Parity Violating Asymmetry at Leading Order

In elastic electron-proton scattering, the electromagnetic interaction, which is mediated by photon exchange, dominates. However, the parity-violating effects that arise from the neutral-weak interaction through Z-boson exchange (figure 2.7) allow probing the proton's weak charge and the weak mixing angle.

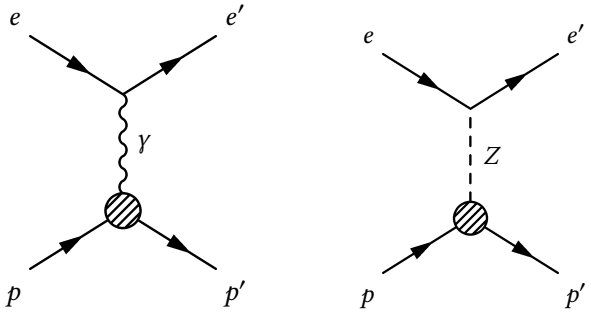

Figure 2.7.: Leading-order Feynman diagrams for elastic electron-proton scattering. The shaded blobs at the proton vertices represent the finite size of the proton. Taken from [33].

The parity transformation involves inverting spatial coordinates, as discussed in section 2.3. Helicity, which is defined (eq. 2.11) as the projection of the particle's spin along its momentum, is a pseudo-scalar and changes sign under parity. Consequently, switching the longitudinal polarization of the electron beam between being aligned and anti-aligned with its momentum in scattering on an unpolarized target is equivalent to performing a parity transformation.

The scattering cross section for elastic scattering of electrons with helicity $\pm 1/2$ on a proton is proportional to the square of the total scattering amplitude $\mathcal{M}_{ep}^{\pm}$. At leading order, this amplitude is composed of contributions via photon and Z^0 boson exchange, $\mathcal{M}_{\gamma}$ and $\mathcal{M}_{Z}$, respectively (figure 2.7):

$$\sigma \propto \left| \mathcal{M}_{ep}^{\pm} \right|^2 = \left| \mathcal{M}_{\gamma} + \mathcal{M}_{Z}^{\pm} \right|^2 . \tag{2.51}$$

While the photon exchange preserves parity, the Z boson exchange introduces a parity-violating contribution, which changes the sign based on the electron's helicity.

The parity-violating asymmetry A_{PV}^{ep} is defined as the difference between the cross sections for electrons with opposite helicities, normalized by their sum:

$$A_{\mathrm{PV}}^{ep} = \frac{\sigma_+ - \sigma_-}{\sigma_+ + \sigma_-} \,. \tag{2.52}$$

Comparing the electromagnetic and weak currents, defined by eqs. 2.17 and 2.37, reveals that only the Z-boson vertex contains a parity-violating term. Therefore, the scattering amplitudes for the left- and right-handed helicity electrons differ only in the Z-boson term

$$\mathcal{M}_{ep}^{\pm} = \mathcal{M}_\gamma \mp \mathcal{M}_Z^{\pm}, \tag{2.53}$$

with the parity-violating component of the Z-boson amplitude, which switches sign in $\mathcal{M}_Z$. Consequently,

$$\mathcal{M}_{ep}^{+} - \mathcal{M}_{ep}^{-} = 2\mathcal{M}_{\mathrm{PV}}^{Z} \tag{2.54}$$

By substituting eq. 2.53 into eq. 2.52 and considering eq. 2.51, all terms in the numerator cancel except for the $\gamma - Z$ interference cross-terms, under the approximation at low momentum transfer ($Q^2 << m_z^2 = 91.188(2)$ GeV) $|\mathcal{M}_\gamma|^2 \gg |\mathcal{M}_Z|^2$ [52]. This yields the following estimate for A_{PV}^{ep}:

$$A_{\mathrm{PV}}^{ep} \propto \frac{\Re\left[\mathcal{M}_\gamma \mathcal{M}_Z\right]}{|\mathcal{M}_\gamma|^2} \,. \tag{2.55}$$

At very small elastic momentum transfer Q^2, the proton's internal structure is unresolved, causing both amplitudes to depend only on the proton's electric and weak charges, $e_p = +1$ (in units of the positron charge) and Q_{W}^p, respectively, [5]:

$$\mathcal{M}_\gamma \propto \frac{1}{Q^2} \tag{2.56a}$$

$$\mathcal{M}_Z \propto -\frac{Q_{\mathrm{W}}^p}{16\sin^2\theta_w \cos^2\theta_w} \frac{1}{Q^2 + m_Z^2}, \tag{2.56b}$$

with $Q_{\mathrm{W}}^p = 1 - 4\sin^2\theta_w$ at tree-level (eq. 2.40).

Evaluating eq. 2.55 using eq. 2.56 for very low Q^2 and introducing the Fermi coupling constant

$$G_F = \frac{\pi\alpha}{\sqrt{2} m_w^2 \sin^2\theta_w}, \tag{2.57}$$

where α is the fine-structure constant and $m_w = m_z \cos\theta_w$ (eq. 2.33), parity-violating asymmetry simplifies to [5]:

$$A_{\mathrm{PV}}^{ep}(Q^2 \to 0) = -\frac{G_F Q^2}{4\sqrt{2}\pi\alpha} Q_{\mathrm{W}}^p \,. \tag{2.58}$$

Thus, the direct proportionality between the parity-violating asymmetry and the proton's weak charge provides the basis of the P2 experiment [5].

At non-zero momentum transfer, the full hadronic structure of the nucleon, including contributions from both proton and neutron form factors, which is parametrized by the Q^2 value and energy-dependent function $F(E_i, Q^2)$, must be taken into account:

$$A_{\mathrm{PV}}^{ep} = -\frac{G_F Q^2}{4\sqrt{2}\pi\alpha}\left[Q_{\mathrm{W}}^p - F(E_i, Q^2)\right] \equiv A_0 \left[Q_{\mathrm{W}}^p - F(E_i, Q^2)\right] \,. \tag{2.59}$$

This hadronic structure function includes contributions from electric, magnetic, axial, and strange nucleon form factors [5]:

$$F(Q^2) \equiv F_{\mathrm{EM}}(Q^2) + F_{\mathrm{A}}(Q^2) + F_{\mathrm{S}}(Q^2)\ . \tag{2.60}$$

The following kinematic factors:

$$\epsilon \equiv \left[1 + 2\,(1+\tau)\tan^2\left(\frac{\theta}{2}\right)\right]^{-1}, \quad \epsilon' \equiv \sqrt{\tau(1+\tau)(1-\epsilon^2)} \tag{2.61}$$

together with the previously defined τ (eq. 2.45) can be used to express the terms in eq. 2.60 as following:

$$F_{\mathrm{EM}}(Q^2) = \frac{\epsilon\, G_{\mathrm{E}}^{\gamma,p} G_{\mathrm{E}}^{\gamma,n} + \tau\, G_{\mathrm{M}}^{\gamma,p} G_{\mathrm{M}}^{\gamma,n}}{\epsilon\,(G_{\mathrm{E}}^{\gamma,p})^2 + \tau\,(G_{\mathrm{M}}^{\gamma,p})^2}\ ; \tag{2.62a}$$

$$F_{\mathrm{A}}(Q^2) = \frac{(1-4\sin^2\theta_w)\sqrt{1-\epsilon^2}\,\sqrt{\tau(1-\tau)}\; G_{\mathrm{M}}^{\gamma,p}\, G_{\mathrm{A}}^{Z,p}}{\epsilon\,(G_{\mathrm{E}}^{\gamma,p})^2 + \tau\,(G_{\mathrm{M}}^{\gamma,p})^2}\ ; \tag{2.62b}$$

$$F_{\mathrm{S}}(Q^2) = \frac{\epsilon\, G_{\mathrm{E}}^{\gamma,p} G_{\mathrm{E}}^{s} + \tau\, G_{\mathrm{M}}^{\gamma,p} G_{\mathrm{M}}^{s}}{\epsilon\,(G_{\mathrm{E}}^{\gamma,p})^2 + \tau\,(G_{\mathrm{M}}^{\gamma,p})^2} + \frac{\epsilon\, G_{\mathrm{E}}^{\gamma,p} G_{\mathrm{E}}^{u,d} + \tau\, G_{\mathrm{M}}^{\gamma,p} G_{\mathrm{M}}^{u,d}}{\epsilon\,(G_{\mathrm{E}}^{\gamma,p})^2 + \tau\,(G_{\mathrm{M}}^{\gamma,p})^2}\ . \tag{2.62c}$$

The first term $F_{\mathrm{EM}}(Q^2)$ represents the contributions from the proton and neutron's electric and magnetic form factors. The second term $F_{\mathrm{A}}(Q^2)$ accounts for the axial form factors associated with the neutral weak current interaction. The third term $F_{\mathrm{S}}(Q^2)$ incorporates the strange electric and magnetic form factors $G_{\mathrm{E,M}}^{s}$, as well as the isospin-breaking form factors $G_{\mathrm{E,M}}^{u,d}$.

As shown in eq. 2.46, the momentum transfer Q^2 depends on the incident electron energy and the scattering angle. Optimizing these initial experimental parameters is crucial since the average Q^2 determines which terms in A_{PV}^{ep} dominate and, consequently, to which contributions the experiment is most sensitive.

Figure 2.8 shows the dependence of the parity-violating asymmetry in the elastic electron-proton scattering A_{PV}^{ep} and its constituent contributions

$$A_{Q_{\mathrm{W}}} = -C \cdot Q_{\mathrm{W}}^{p}\,, \quad A_{\mathrm{EM}} = C \cdot F_{\mathrm{EM}}\,, \quad A_{\mathrm{A}} = C \cdot F_{\mathrm{A}}\,, \quad \text{and} \quad A_{\mathrm{S}} = C \cdot F_{\mathrm{S}}\,,$$

with

$$C \equiv \frac{G_F Q^2}{4\pi\alpha\sqrt{2}}\,,$$

where on the electron scattering angle θ_f for the electron beam energy chosen for the P2 experiment. At low Q^2, which corresponds to the forward angle limit ($\theta \to 0$), the contribution of the proton weak charge (line with $A_{Q_{\mathrm{W}}}$ label in figure 2.8) dominates over the other hadronic contributions. Therefore, measuring A_{PV}^{ep} is sensitive to the proton's weak charge Q_{W}^{p} at low four-momentum transfer Q^2. However, the overall value of A_{PV}^{ep} reduces as the scattering angle decreases, making the measurement at small scattering angles difficult.

Based on the extensive optimization of the expected precision of the weak mixing angle determination [5, 50], the P2 experiment is intended to run with an electron beam with energy of 155 MeV and a central scattering angle of 35°, resulting in $A_{\mathrm{PV}}^{ep} = -67.34$ ppb [1]. The choice of

[1] The ppb (parts-per-billion) notation represents one part per billion, equivalent to a fraction of 10^{-9}.

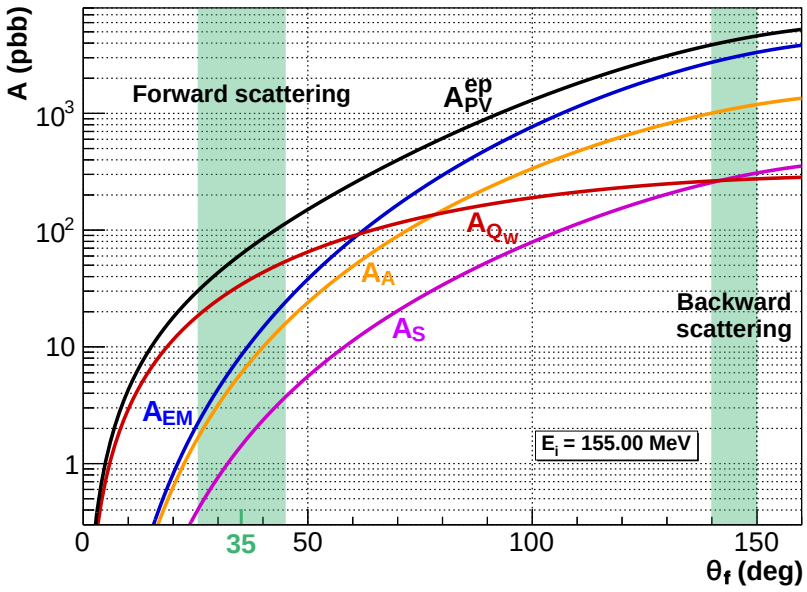

Figure 2.8.: Dependence of A_{PV}^{ep} on the electron scattering angle (θ_f) for the P2 experiment. The absolute value of the asymmetry, along with contributions from the proton weak charge (A_{Q_W}) and the nucleon form factors—electromagnetic (A_{EM}), axial (A_A), and strange quark (A_S)—are plotted. The highlighted backward scattering angle range corresponds to the planned auxiliary measurements (see section 3.7).

relatively low beam energy—compared to the typical GeV level in such experiments (figure 2.5)—is driven by the intended low four-momentum transfer Q^2 in this case (eq. 2.47) and box diagram corrections (discussed in the following section) which scale with energy and, therefore, are better controlled at low Q^2.

2.7.4. Radiative Corrections

To achieve the high precision targeted by the P2 experiment's measurement of the parity-violating asymmetry A_{PV}^{ep}, it's necessary to go beyond the tree-level approximation. This requires accounting for higher-order processes. Similarly to the discussion in section 2.5, theoretical predictions with sufficient precision can be obtained by including one-loop radiative corrections to the tree-level approximation of A_{PV}^{ep} (eq. 2.58) [5]:

$$A_{\mathrm{PV}}^{ep} = A_0 \left[Q_{\mathrm{W\,(1\text{-}loop)}}^{p} - F(E_i, Q^2) + \Delta_{\square}(E_i, Q^2) - \Delta_{\square}(0,0) \right] . \tag{2.64}$$

Here $Q_{\mathrm{W\,(1\text{-}loop)}}^{p}$ replaces the tree-level proton weak charge Q_{W}^{p}, and the $\Delta_{\square}$ terms represent contributions from processes described by box diagrams which are shown in figure 2.9.

The one-loop weak charge is given by

$$Q_{\mathrm{W\,(1\text{-}loop)}}^{p} = (\rho_{nc} + \Delta_e) \left(1 - 4 \sin^2\theta_w(\mu)_{\overline{\mathrm{MS}}} + \Delta_e^{'} \right) + \Delta_{\square}(0) , \tag{2.65}$$

where Δ_e and $\Delta_e^{'}$ account for contributions to the electron vertex, and ρ_{nc} is a renormalization factor for the neutral and charged current strengths.

The terms presented above constitute the complete set of next-to-leading order (NLO) corrections to the parity-violating asymmetry. At this order, no additional theoretical uncertainties

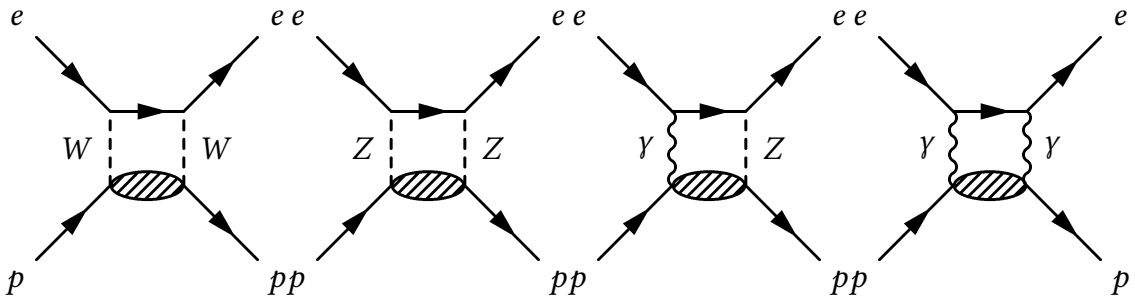

Figure 2.9.: Box diagrams for electron-proton scattering. The diagrams depict WW-, ZZ-, γZ- and $\gamma\gamma$-exchange (from left to right). The shaded blob at the lower part of each diagram indicates possible excited intermediate proton states. Picture is taken from [33].

will limit the interpretation of A_{PV}^{ep} measurement in terms of the weak mixing angle $\sin^2\theta_w$ with a precision beyond the order of 10^{-4}. However, to perform a conclusive test of the Standard Model (SM) and to analyze the anticipated P2 experiment results in the context of New Physics, it's essential to include two-loop electroweak corrections and the corresponding next-to-next-to-leading order (NNLO) calculations. The computation of these corrections is an active part of ongoing research, with a brief overview of the current status provided in [5].

3 The P2 Experiment

The Mainz Energy-Recovering Superconducting Accelerator (MESA), currently in its final construction phase, will host the P2 experiment. This experiment is dedicated to the precise measurement of the parity-violating asymmetry in elastic scattering of right- and left-handed electrons on an unpolarized proton target (section 2.7.1), contributing to a broader physics program that probes potential New Physics through an improved determination of the proton's weak charge. The first measurements for P2 are set to begin in the near future, with significant research and development progress already achieved. A major milestone is the recent delivery and installation of the superconducting magnet coil—the experiment's central component—at the Johannes Gutenberg University (JGU) campus within the MESA facility. This chapter briefly introduces the P2 experiment and overviews the design and key challenges. A more detailed description of the P2 experiment can be found in [5].

3.1. Physics Motivation

Despite the success of the Standard Model of Elementary Particle Physics (SM) in describing electromagnetic, strong, and weak interactions, it remains an incomplete description of nature. Moreover, it relies on a large set of adjustable parameters—such as masses, coupling constants, and mixing angles—which challenges the notion of a simple and elegant fundamental theory. Ideally, a more complete framework would emerge with fewer input parameters, potentially governed by a single unifying principle.

Electron scattering has been a crucial tool for studying nuclear structure for over five decades. Among various techniques, measuring parity asymmetries created by weak interactions in electron scattering has played a key role in testing the SM. It has been instrumental in probing strangeness contributions in the nucleon, refining the determination of the proton's weak charge, and strengthening the search for physics beyond the SM—New Physics. Recent technological advancements enable measurements with unprecedented precision, allowing higher-order effects to be explored in greater detail.

One of the most significant aspects of these studies is the determination of the proton's weak charge, which is highly suppressed in the SM. This makes it a sensitive probe for potential deviations that could hint at New Physics. The Q_{weak} experiment recently provided the most precise measurement of the parity-violating asymmetry [42, 43]:

$$A_{\text{PV}}^{ep} = -226.6 \pm 9.3\,\text{ppb}$$

at an incident beam energy of 1.16 GeV and momentum transfer of $Q^2 = 0.025\,\text{GeV}^2$, leading to an extracted proton weak charge of

$$Q_{\text{W}}^{p} = 0.0719 \pm 0.0045.$$

While this result is in good agreement with the SM prediction (0.0708 ± 0.0003), the P2 experiment aims to refine this measurement with significantly improved precision, providing an independent

cross-check of the Q_{weak} result.

The weak mixing angle ($\sin^2\theta_w$) is a fundamental parameter of the SM that governs the mixing of electromagnetic and weak interactions. As discussed in section 2.4.3, it is related to the masses of the charged $W^{\pm}$ and neutral Z^0 bosons, as given by eq. 2.33. However, its exact value is not predicted and must be measured experimentally. The electroweak theory does predict that $\sin^2\theta_w$ varies with scale (momentum transfer Q^2), a phenomenon known as the running of the weak mixing angle (figure 2.5; discussed in section 2.5.1). High-precision parity-violating electron scattering experiments are particularly well-suited to test this prediction. In this regard, the P2 experiment intends to measure $\sin^2\theta_w$ at lower momentum transfer with three times greater precision than Q_{weak}, further improving constraints on electroweak interactions. Additionally, complementary measurements at different energy scales are planned in the proposed MOLLER and SoLid [53] experiments (figure 2.5).

Beyond verifying SM predictions, the results of the P2 experiment, combined with results from the experiments mentioned above, can reveal New Physics. In addition to the scale-dependence of the weak mixing angle (variation of weak mixing angle with energy scale) discussed in section 2.5.1, loop contributions from new particles—like composite fermions, leptoquarks, or heavy Z' bosons—may cause an observable shift in $\sin^2\theta_w$. As reviewed in [54, 55], if new physics exists at a large energy scale ($\Lambda \gg Q^2$), small deviations from SM predictions could appear at the electroweak scale. This enables detecting or constraining these deviations from the Standard Model (SM) in high-precision parity-violating electron scattering experiments, like P2, using an effective Lagrangian approach [54]. This method allows New Physics to be probed up to the multi-TeV scale [54, 55], making it competitive with collider searches.

3.2. MESA Facility

Measuring parity-violating asymmetry A_{PV}^{ep} with high precision requires a dedicated facility. The requirement for high beam availability and precise fluctuation control from the P2 experiment cannot be met by the existing Mainz Microtron (MAMI) accelerator at the Institute of Nuclear Physics, Johannes Gutenberg University Mainz [56–58]. Therefore, a concept of a compact superconducting linear accelerator, the Mainz Energy-recovering Superconducting Accelerator, abbreviated as MESA (figure 3.1), which will fulfill all the above requirements, was developed. The MESA facility is currently in the final stages of construction, and the first measurements should start in 2026.

MESA will operate in two different modes. The first, energy recovery mode, will provide a world-first high-intensity unpolarized beam, enabling high collision rates and low energy consumption by recycling electron energy within the accelerator system. In this mode, used by the MAGIX experiment [59], the electrons that pass through a thin gas jet target with minimal deflection are redirected back to the superconducting radio frequency acceleration modules (SRF cryomodules) with a 180-degree phase shift, which will lead to deceleration, instead of acceleration. After up to two turns, the beam is decelerated to 5 MeV, returning up to 25 MeV per pass to the accelerating structures, and finally stopped in a small, remote beam dump located in a considerable distance from the experimental setup. This allows for very high beam currents of 1 mA (eventually 10 mA) with energy up to 105 MeV at a low background and reduced energy consumption. These conditions are ideal for precise measurements of the proton radius, contribute to the resolution of the so-called proton radius puzzle, in the MAGIX experiment.

However, most of the runtime (>4000 h/year out of a total of ~7000 h/year) will be done in the

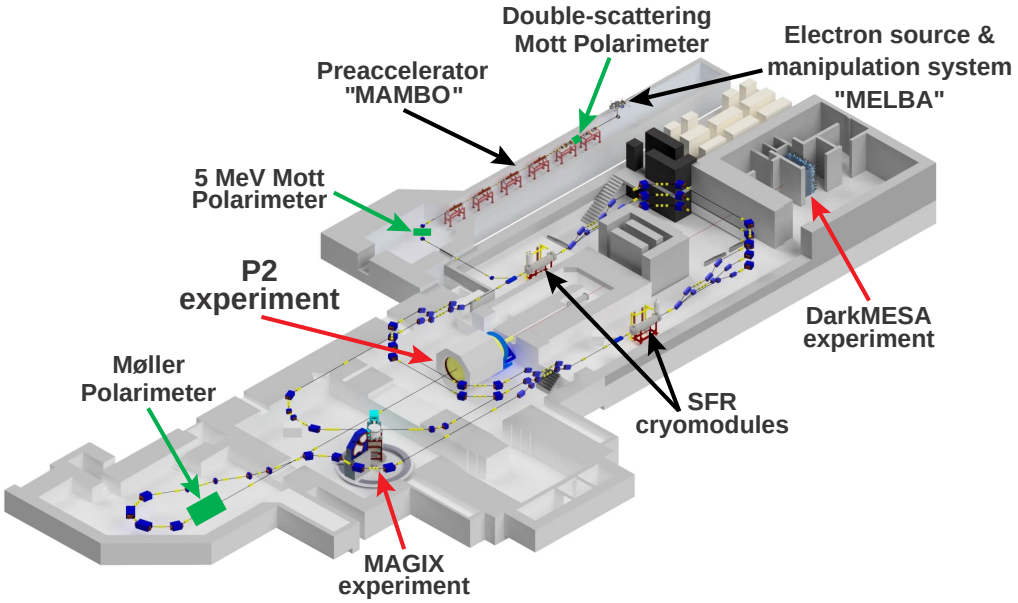

Figure 3.1.: View of the MESA facility with labeled experimental setups and polarimetry chain.

extracted beam operation mode. In this mode, MESA provides a beam of electrons emitted from a 100 keV GaAs photo-cathode at lower currents (150 µA), but with a polarization approaching 85 − 90 % and the possibility of fast ($\mathcal{O}$(1 kHz)) helicity flips. The P2 experiment [5] will use this mode to study parity violation using a variety of targets. Electrons from the source are injected into the MESA Low-Energy Beam Apparatus (MELBA), where their spin is manipulated before being guided by an α-magnet to the bunching and collimation system. The following MAMBO (MilliAmpereBooster) pre-accelerator [60, 61] boosts their energy to 5 MeV at room temperature. After this, the beam recirculates three times through two SRF cryomodules, each of which contains two cavities [62]. Each cavity, in turn, provides a 12.5 MeV energy gain, for a total of 50 MeV boost per turn, which finally results in energy of 155 MeV. The beam can be directed to the P2 experiment setup at this stage. Following interaction with the P2 target, the remaining electrons are stopped by a heavily shielded beam dump. During the P2 experiment, MESA will operate only in this mode since the $l\mathrm{H}_2$ target will make the beam quality unsuitable for further use in the energy recovery mode [63]. Another experiment, DarkMESA [59], located behind the P2 beam dump, searches for light dark matter and related particles potentially produced there.

The P2 experiment aims to achieve a world-leading measurement of the weak mixing angle through electron-hydrogen scattering. In addition, the P2 physics program includes measuring the weak charge of ^{12}C and determining the neutron skin—a region at the surface of the nucleus where a concentration of neutrons is higher compared to protons—of ^{208}Pb (see section 3.7). All of these measurements require precise knowledge of the beam polarization.

3.3. Beam Polarization at MESA. Polarimetry Chain

Continuous measurements in the P2 experiment are primarily limited by the approximately 12-day lifespan of the MESA source strained GaAs photocathodes, during which they maintain sufficient quantum efficiency for the required beam polarization and current [5]. A series of observations at the MAMI facility showed that the beam polarization can vary up to 10 % (relative) within this run time [64]. Therefore, regular beam polarization monitoring using

advanced techniques is crucial to keep the measurement error below 0.5 % during the total measurement time of the P2 experiment. Ideally, the polarization measurements should be done online to avoid additional errors due to the data interpolation between the measurements.

To achieve the stated accuracy of beam polarization, a concept employing a chain of three polarimeters for cross-validation was developed [5, 65]. It includes two polarimeters operating at the early stages of the beam production (see figure 3.1). The first one, a double scattering Mott polarimeter (DSP) [66, 67], is integrated in the injection system of MESA and operates at the electron source energy of 100 keV. The second measurement is provided by a single scattering Mott polarimeter placed behind the MESA pre-accelerator at the stage with a beam energy of 5 MeV, with an expected accuracy below 1 % [68]. This polarimeter's design is based on the similar high precision 5 MeV Mott polarimeter one used at Jefferson Lab [69]. In both cases, the beam polarization will be extracted from the measured asymmetry of Mott scattering on a thin solid target. Accurate polarization determination requires precise knowledge of the polarimeter's effective analyzing power, which is restricted by background contributions, multiple scattering, and theoretical uncertainties in the analyzing power. This calibration can be performed using a series of targets with varying thicknesses for a single-scattering Mott polarimeter. The DSP uses two targets for internal analyzing power calibration, minimizing uncertainties related to target thickness and theoretical analyzing power. After the calibration, further measurements can be done using single scattering. Both polarimetry techniques are invasive but offer rapid polarization measurements. The double Mott polarimeter requires beam currents of few nA, while a wider dynamic range in the Mott polarimeter case allows measurements near P2 beam intensity, verifying polarization stability relative to the double Mott measurement.

The final polarimeter must be placed just before the P2 setup, measuring beam polarization at its final energy of 155 MeV. Finding a suitable option for this energy is complicated because it should allow non-destructive and precise measurements. Møller scattering (section 7.2.1) on a polarized low-density atomic hydrogen gaseous target (*not to be confused with the P2 setup target*) meets all requirements (table 7.1) but poses significant technological challenges [65]. While using a thin metal foil in this setup prevents online measurements and introduces additional systematic errors, initially, it will allow for swift commissioning of the accelerator and the experimental setups and be sufficient for early, limited-statistics parity violation data taking.

The Hydro-Møller polarimeter, using a polarized gaseous atomic hydrogen target, avoids limitations associated with conventional iron targets, such as target polarization, high-current extrapolation, and the Levchuk effect. These issues can significantly increase systematic uncertainties. For example, they contributed up to ∼70 % of the total systematic uncertainty in previous cases of the Møller polarimetry based on targets made of pure iron or iron-based alloys (listed in table 7.2).

Part III of this work is devoted to a detailed overview of polarimetry techniques and Møller scattering theory (chapter 7) and the design and simulation results of the Møller polarimeter (chapter 8).

3.4. Measurement Method in the P2 Experiment

The P2 experiment will measure the parity-violating asymmetry in elastic electron-proton scattering using the *longitudinally polarized electron beam* with energy $E_{\text{beam}} = 155$ MeV provided by the MESA facility. With the current of $I_{\text{beam}} = 150\,\mu\text{A}$ and a helicity flipped at a frequency of $f \sim 1$ kHz, this beam will interact with a long *unpolarized target* made of liquid molecular

hydrogen ($l\mathrm{H}_2$) with a length of $L = 60\,\mathrm{cm}$. This results in an instantaneous luminosity

$$\mathcal{L} = I_{\mathrm{beam}}/e \cdot \rho_p \cdot L = 2.38 \times 10^{39}\,\mathrm{cm}^{-2}\,\mathrm{s}^{-1},$$

where e is the elementary charge and ρ_p is the proton density in $l\mathrm{H}_2$.

Figure 3.2 illustrates the measuring principle of the P2 experiment. The P2 spectrometer selects electrons scattered within an angular acceptance of $25 - 45°$ (the choice of central polar scattering angle and its range is discussed in section 3.6), which are then deflected toward the detector system by the solenoid's magnetic field. Electrons scattered at higher angles will strike the inner wall of the solenoid, while those that remain unscattered or scatter at angles below the acceptance threshold will be dumped.

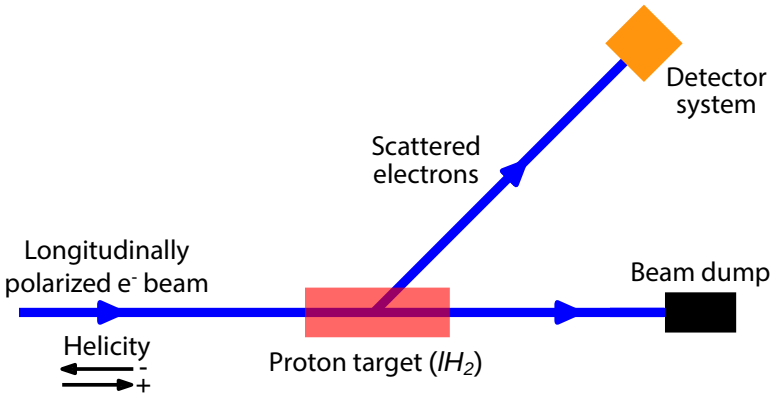

Figure 3.2.: Sketch of the measurement principle in the P2 experiment. The illustrated scattered electron track and detector system do not represent the actual azimuthal coverage or design. Modified from [5].

Within the chosen angular acceptance, the asymmetry A_{PV}^{ep} is expected to be between 30 – 100 ppb, which is significantly smaller than in the Q_{weak} experiment. This requires high statistics and strict control of systematic uncertainties to achieve sub-percent precision in measuring such a small parity-violating asymmetry in the P2 experiment case. Therefore, the total runtime at MESA is scheduled to be ~10 000 h, resulting in statistical uncertainty being the dominant factor in the overall measurement precision. The detection rate is expected to be in the order of ~0.1 THz, requiring an integrating measurement approach. The associated radiation dose must be carefully considered when choosing and designing the detector components.

In the experiment, the arising parity violating asymmetry can be measured by the integrated number of detected scattered electrons of interest for each helicity cycle at MESA according to eq. 2.52. At leading order, the value of the weak mixing angle can be finally extracted from the measured asymmetry (as follows from combining eqs. 2.40 and 2.59):

$$A_{\mathrm{PV}}^{ep} = \frac{\sigma_R - \sigma_L}{\sigma_R + \sigma_L} = -\frac{G_F Q^2}{4\sqrt{2}\pi\alpha}\left[Q_{\mathrm{W}}^p - F(Q^2)\right] = A_0\left[\left(1 - 4\boxed{\sin^2\theta_w}\right) - F(Q^2)\right]. \tag{3.1}$$

In the SM the proton's weak charge is suppressed by the weak mixing angle. Applying Gaussian error propagation for eq. 2.52 yields:

$$\frac{\Delta \sin^2\theta_w}{\sin^2\theta_w} = \frac{1 - 4\sin^2\theta_w}{4\sin^2\theta_w} \cdot \frac{\Delta Q_{\mathrm{W}}^p}{Q_{\mathrm{W}}^p} \approx 0.09 \cdot \frac{\Delta Q_{\mathrm{W}}^p}{Q_{\mathrm{W}}^p} \text{ for } \sin^2\theta_w \approx 0.23\,. \tag{3.2}$$

As this expression shows, the proton's weak charge is highly sensitive to the electroweak mixing angle. Thus, as evident from the rightmost term, a precise measurement of Q_W^p will give an almost tenfold improvement in the precision of $\sin^2\theta_w$.

It is important to note that eqs. 2.40 and 2.59 represents a leading-order approximation. As mentioned in section 2.7.4, higher-order corrections must be taken into account when analyzing actual experimental data.

3.5. The P2 Experiment Setup

The P2 setup (figure 3.3) consists of three main elements: the high-power unpolarized liquid hydrogen target, the solenoid spectrometer, including Cherenkov detectors, for measuring the electron scattering asymmetry, and the tracking system that reconstructs the momentum transfer within the target. This section provides an overview of the target and spectrometer and briefly introduces the tracking detector. A detailed description of the tracking detector's design and used sensor technology (chapter 4), together with the sensors' cooling system (chapter 6) is addressed further in part II.

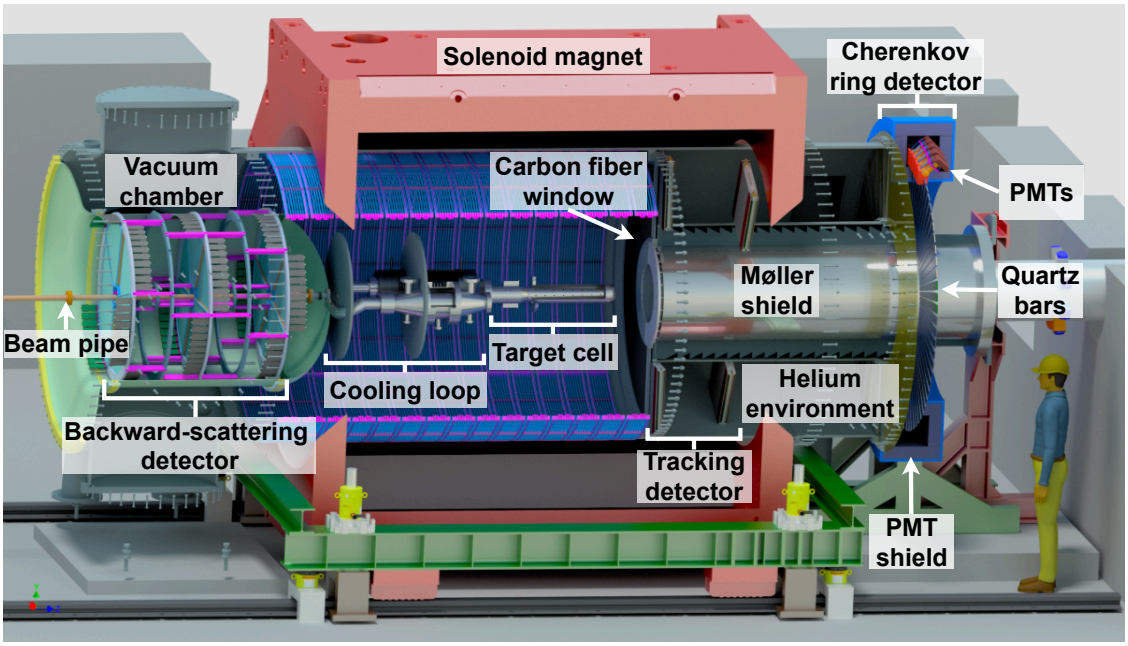

Figure 3.3.: Rendering of the P2 experiment main setup.

3.5.1. High Power Liquid Hydrogen Target

The P2 experiment requires a liquid hydrogen target, which has become common experimental equipment in particle physics experiments. A closed-loop recirculating cryogenic $l\mathrm{H}_2$ target system with a 60 cm long target cell is currently under development. This length ensures that all electrons scattered within the target and within polar angles between 20° and 45° can reach the detector system.

The target design is based on experience from the G0 experiment [70, 71], focusing on minimizing the material budget in the path of scattered electrons and maintaining azimuthal

symmetry. The current target cell design is shown in figure 3.4b. The cylindrical target cell and manifold, which connects it to the cryogenic loop, are made of an aluminum alloy. An upstream 125 µm thick aluminum vacuum window and a downstream aluminum hemispherical cell window close the cell from both sides. The target diameter is expected to be 10 – 15 cm, with a 250 µm thick cell wall, ensuring structural integrity and self-support at the given dimensions. Inside the cell, a 75 µm aluminum foil forms an internal conical flow diverter which separates the inlet $l\mathrm{H}_2$ flow entering the cell from the outlet flow.

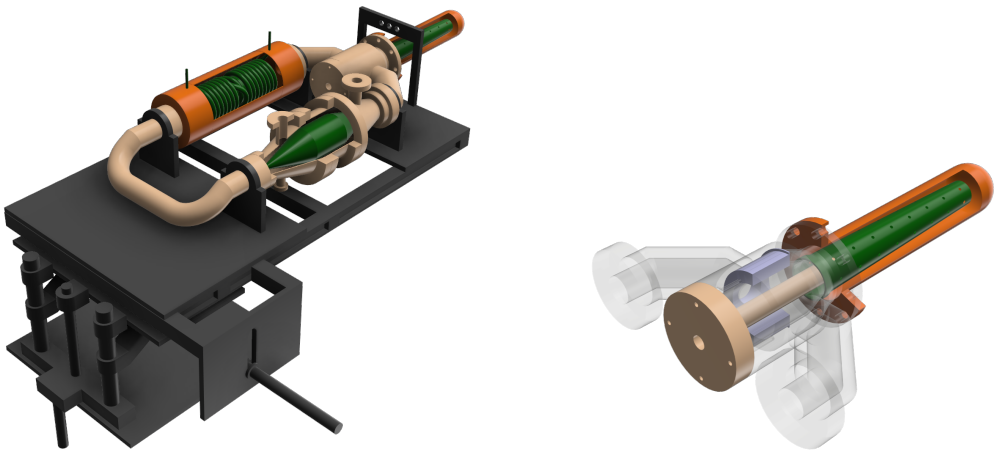

(a) The P2 target and cooling loop. **(b)** The P2 target cell.

Figure 3.4.: Rendering of the P2 high power liquid hydrogen target setup.

Figure 3.4a illustrates the P2 target loop design. The target cell and its upstream manifold are mounted on a movable table with a six-degree-of-freedom alignment mechanism for precise positioning of the upstream and downstream windows. This table is connected to a motion system, allowing target movement into the beam path. Additionally, a solid target ladder will be integrated with the hydrogen cell for beam calibration using thick aluminum alloy foils and optics studies using several carbon targets.

The target loop also includes additional external components necessary for the liquid hydrogen target operation, such as centrifugal pumps, a heat exchanger, and a high-power heater [5]. The entire target loop will be housed inside the P2 vacuum chamber, with only the target cell positioned within the P2 solenoid (see section 3.5.2).

Due to the high luminosity, approximately 4 kW of heat will be deposited into the target cell materials—twice the heat load of the Q_{weak} experiment [72], the current highest power $l\mathrm{H}_2$ target. This heat will be removed using liquid helium supplied by the MESA refrigerator, which will cool the hydrogen target loop via the heat exchanger. The P2 target loop will operate under a constant heat load regime, independent of beam presence, maintaining the $l\mathrm{H}_2$ temperature at 20 K. This stability is achieved through a high-power heater regulated by a feedback loop with temperature sensors within the target.

Extensive Computational Fluid Dynamics (CFD) simulation predicts an average $l\mathrm{H}_2$ density loss of 3 % due to beam heating, with localized losses potentially reaching 6.7 %, causing $l\mathrm{H}_2$ boiling at 23.7 K. This results in boiling noise, a critical source of density fluctuations on the electron helicity flip timescale, which could impact asymmetry measurement precision. The P2 experiment aims to limit boiling noise to below 10 ppm—a five-fold improvement compared to the Q_{weak} target [72] and half the projected noise of the MOLLER target [46]. This sets the most stringent stability requirement ever imposed on a liquid hydrogen target.

3.5.2. The P2 Spectrometer

The P2 spectrometer is primarily designed to detect large-angle electron events that scatter within the target for each helicity period. A key challenge is optimizing the detector geometry to efficiently distinguish signal electrons from background processes, particularly Møller scattering (covered in section 7.2.1 within the theoretical base for Møller polarimetry) and bremsstrahlung photons from the target. The spectrometer, shown in figure 3.5, incorporates a superconducting solenoid magnet that directs scattered electrons of interest onto the Cherenkov ring detector and a lead shielding to reduce background from low-angle scattered electrons.

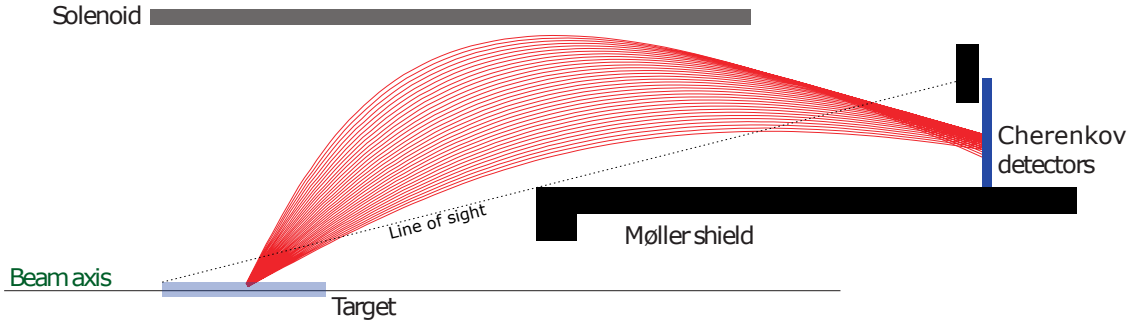

Figure 3.5.: Schematic side view of the P2 spectrometer geometry (not to scale). Auxiliary and not essential for understanding the spectrometer design parts, as well as tracking detector (addressed further in part II), are omitted. Electron tracks (in red) are for illustration and do not represent physical tracks. Taken from [33] with original from [5].

The detection principle of electrons is based on the Cherenkov effect, which occurs when a charged particle exceeds the phase velocity of electromagnetic waves in a dielectric medium. As the particle moves through the medium, it temporarily polarizes nearby atoms, emitting electromagnetic radiation. Due to the particle's velocity, this radiation forms a characteristic cone-shaped wavefront, as illustrated in figure 3.6. The Cherenkov angle, θ_C, which is the angle between the particle's momentum and the emitted Cherenkov photons, is given by:

$$\cos\theta_C = \frac{1}{n\beta}, \tag{3.3}$$

where n is the refractive index of the medium, and $\beta = v/c$ is the particle's velocity v normalized by the speed of light in a vacuum c. These Cherenkov photons can be detected using photosensitive detectors.

An electron hit rate of approximately $20\,\mathrm{MHz/cm^2}$ is expected on the Cherenkov detector, which will result in an estimated total radiation dose of 80 Mrad over the experiment's runtime. The latter requires using radiation-hard materials and components to ensure the spectrometer's reliable long-term performance. The scattered events will be detected by the produced Cherenkov light in fused silica bars chosen for their minimal response to photon backgrounds and high radiation hardness. The design optimization involves detailed Geant4 [73–75] simulation, material studies, and prototype testing at MAMI.

The spectrometer geometry is designed to focus electrons scattered in the target within the angular acceptance range of $20 - 45^\circ$ onto the Cherenkov detectors. This focusing is achieved using a large superconducting solenoid, which generates a magnetic field of up to 0.7 T along the beam axis (B_z). The solenoid field strength and geometry are adopted from the magnet used for the FOPI [76] experiment. Electrons scattered at angles exceeding this range impact the magnet's inner wall, while those scattered at smaller angles either proceed to the beam dump

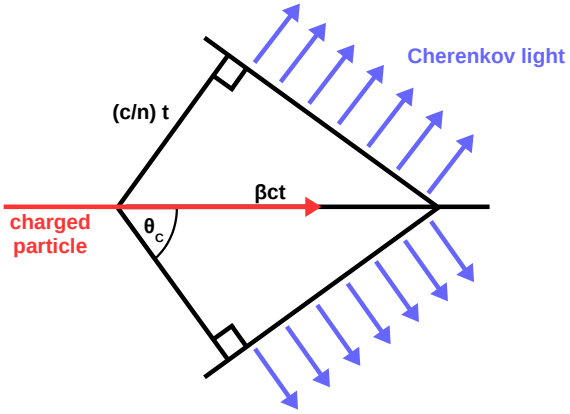

Figure 3.6.: Wavefront of Cherenkov radiation produced by a charged particle moving through a medium with refractive index n in the ideal case of no dispersion. The wavefront is geometrically defined by two right triangles with sides βct and $(c/n)\,t$, representing the distances traveled by the particle and the emitted electromagnetic wave, respectively, over time t.

or are suppressed by the Møller lead shield. The solenoid field only affects charged particles. Consequently, photons that emerge from the target are geometrically prevented from directly reaching the Cherenkov detectors via a straight path, as illustrated by the line of sight from the beginning of the target to the barrel shield in figure 3.5. This design effectively reduces background noise and enhances signal detection.

The liquid hydrogen target is housed within the solenoid in a vacuum chamber. However, the tracking detector operates in a helium atmosphere to meet cooling requirements. The transition between these environments necessitates a robust, low-mass gas window to minimize additional scattering. For this, a thin carbon fiber-based window (figure 3.3), inspired by the Kevlar® window used in the NA48 experiment, with a thickness of ~1 cm and a similar diameter of 2.3 m [77], is being developed. However, based on detailed estimations, the initial concept of using windows made of the same material [5] was ultimately rejected due to concerns about potential rupture and explosion risks when depressurizing the vacuum chamber.

The current design of the Cherenkov detector comprises 72 (revised from 82 planned initially [5]) wedged fused silica (quartz, SiO_2) bars arranged in a circular configuration, as shown in figure 3.7, to ensure maximum azimuthal coverage.

Since Cherenkov light production is enhanced at shorter UV wavelengths, the bar material is chosen to provide high UV light transparency. The emitted Cherenkov photons will be detected by photomultiplier tubes (PMTs) optimized for UV sensitivity. Each quartz bar is wrapped in highly reflective aluminum foil and coupled to a PMT at its outer end. The fused silica material not only serves as the Cherenkov medium but also efficiently guides light to the PMTs through total internal reflection (figure 3.8). The quartz bars have a length of 110 cm, of which 45 cm is the active detecting area. The outer 20 cm segment and the PMTs are shielded by a 10 cm thick lead cover to minimize background interference.

Despite optimized shielding, simulation results indicate that the photon background exceeds the signal electron rate by over one order of magnitude. However, electron-positron pair conversion must occur before producing Cherenkov light for a photon-induced signal to appear in the detector. The produced electron or positron, in turn, must have energy above the threshold energy

$$E_{\text{th}} = \frac{mc^2}{\sqrt{1-(1/n^2)}}\,. \tag{3.4}$$

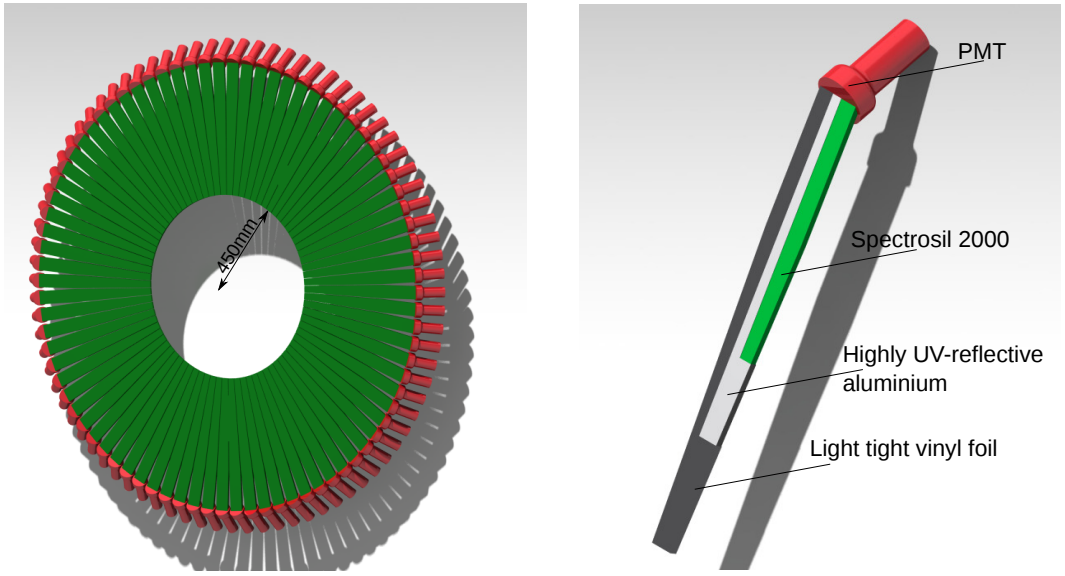

(a) Rendering of the Cherenkov detector geometry. **(b)** Rendering of a Cherenkov detector element.

Figure 3.7.: Rendering of the Cherenkov ring detector design and an individual detector element. Both pictures are taken from [5].

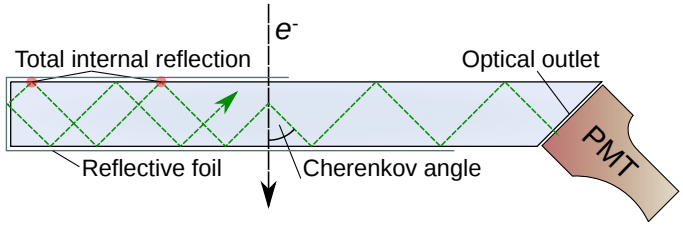

Figure 3.8.: Illustration depicting Cherenkov light (green dashed line) produced by an electron traversing a quartz bar. The light propagates to a photomultiplier tube (PMT) via total internal reflection within the quartz bar and reflection from a surrounding reflective foil. Modified from [5].

The bars are manufactured from Heraeus Spectrosil 2000 [78]—a highly pure form of amorphous silicon dioxide. For this material ($n \approx 1.475$ at $\lambda = 365\,\text{nm}$) $E_{\text{th}} \approx 0.7\,\text{MeV}$. Since most bremsstrahlung photons in the P2 experiment have energies smaller than this threshold value [5], the Cherenkov detector will significantly suppress this photon-induced background. This suppression is evident in figure 3.9, which compares the contribution of photons to the total hit rate with their relative contribution to the total photo-electron rate.

Due to the high electron rate ($\sim 20\,\text{MHz/cm}^2$), PMTs will operate in charge-integrating mode instead of single-electron mode, as Cherenkov-based single-electron detection is unsuitable for precise charge measurements. In this mode, pulses merge into a continuous current, requiring PMTs to handle high cathode currents, maintain linearity at low bias voltages, and enable fast charge collection at high gain. These factors were carefully considered when selecting a suitable PMT type. The signal readout system is adapted from the Q_{weak} experiment [79].

A high helicity reversal rate ($\sim 1\,\text{kHz}$) minimizes drift-induced false asymmetries, while helicity quartets (e.g., $+--+$ and $-++-$) and pseudo-random initial states ($\pm$) suppress systematic drifts. The integrating detector signal is normalized to the MESA beam current monitor signal to correct the drift and fluctuations of the beam current. This optimized detection system enables high-statistics data collection for precise measurement of parity-violating asymmetry in electron-proton scattering.

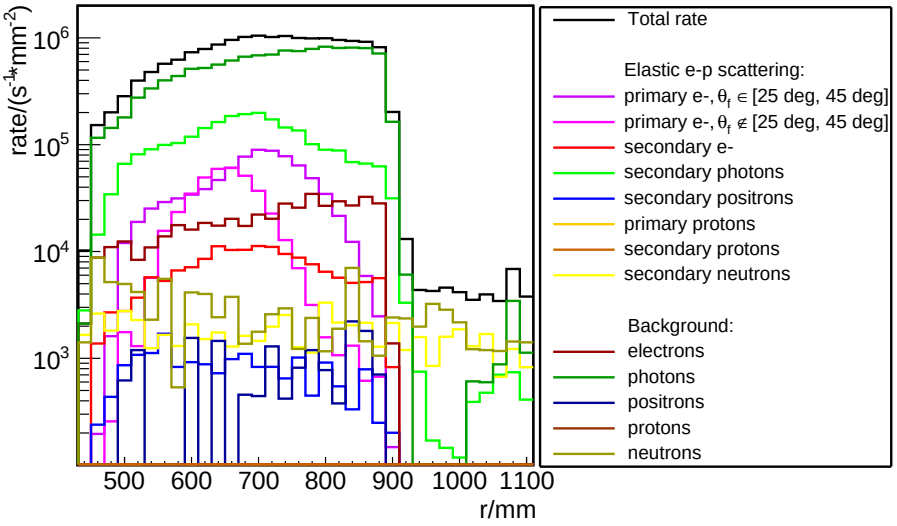

(a) Simulated rate distribution.

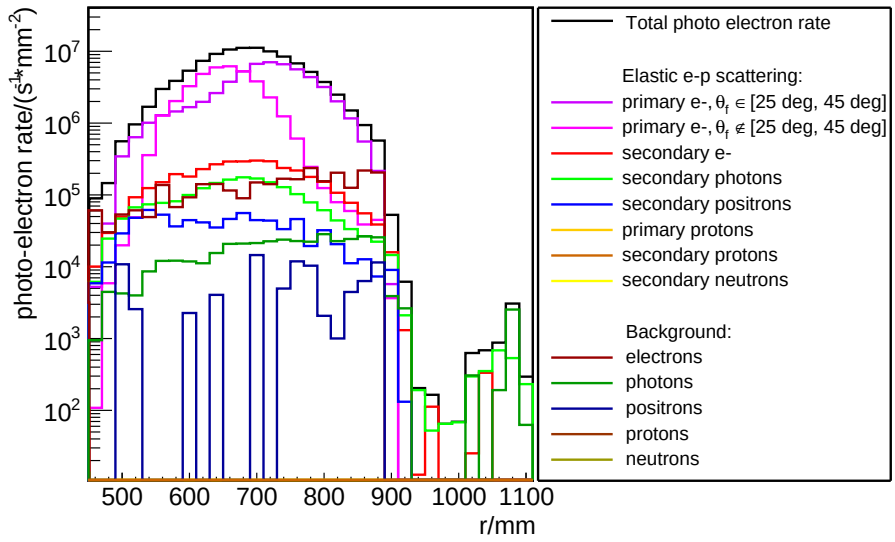

(b) Photo-electron rate distribution.

Figure 3.9.: Comparison of the simulated rate distribution (a) with photo-electron rate distributions after applying the detector response parametrization (b). Both distributions are shown on the surface of the Cherenkov ring detector as a function of the radial distance r from the beam axis. The rates are normalized by the area of the corresponding ring segments, which match the bin width in the r-direction. Plots are taken from [5].

3.5.3. The P2 Tracking Detector

Depending on the scattering position along the target, the solenoidal magnetic field maps different scattering angles into the acceptance of the integrating Cherenkov detector in asymmetry measurements. Analysis and interpretation of the obtained results require precise determination of the average momentum transfer $\langle Q^2 \rangle$ of the electrons entering the asymmetry determination. This information will be obtained from a silicon pixel sensor-based tracking detector, or 'tracker,' located within the solenoid's magnetic volume but housed in a separate gas volume with a helium atmosphere for cooling purposes, as shown in figure 3.3.

The tracker will provide detailed kinematic information for electrons reaching the Cherenkov detectors by reconstructing the scattering angles and energies of these electrons from their

trajectories. The $\langle Q^2 \rangle$ value determined from the tracker measurements will position the P2 experimental results for the running weak mixing angle alongside the data from other experiments given in figure 2.5. However, these measurements require strict requirements on the material budget limit within the detecting area to minimize multiple scattering. Furthermore, the high-resolution tracking capability enables the study of background and systematic effects dependent on position and momentum.

The tracking detector will operate in two different modes. In the first mode, the Cherenkov detector will function in a single-electron continuous tracking detection mode at a reduced beam current, allowing coincidence correlations with the tracker data. This operation mode requires the tracker acceptance to cover all electrons that reach a single fused silica bar with high efficiency. The second operation mode will study rate, position, and momentum-dependent systematic effects at high beam currents. In this high-rate scenario, the tracker will be operated in a gated mode to manage data acquisition rates, acquiring data only during selected time intervals. This mode requires radiation-hard sensor technology, electronics, and infrastructure within the solenoid.

The tracker geometry, sensor technology, and track reconstruction algorithms have been developed through extensive simulations and studies, with detailed results presented in [33]. These include Geant4 simulation of the tracking detector, signal and background studies, and pixel response to photons studies. A brief overview of these studies and a detailed description of the tracker module's technical design, sensor technology, cooling system design and simulation, and current status and results are provided in the subsequent sections of part II.

3.6. Measurement Precision of the Weak Mixing Angle in the P2 Experiment

To determine the achievable precision of the weak mixing angle $\sin^2\theta_w$ value, which will be obtained in the experiment, an extensive parameter scan was conducted in [50] to identify optimal values for the P2 experiment. After finalizing the beam energy and detector parameters for the experiment, error propagation calculations were performed to estimate the uncertainty $\Delta \sin^2\theta_w$ as a function of beam energy E_{beam}, the central electron scattering angle θ_f, and the detector acceptance $\delta\theta_f$. Analytical calculations in this context are challenging because they involve solving numerical integrals involved in relations between different sources of uncertainty. Therefore, the uncertainty calculations were performed using the Monte Carlo method, which involves generating randomized pseudo-experiments for each possible source of uncertainty. These sources include statistical uncertainties— such as false asymmetries, beam polarization, nucleon form factors (see sections 2.7.2 and 2.7.4)—and theoretical uncertainties, all considered independent. The weak mixing angle $\sin^2\theta_w$ was then computed for each pseudo-experiment, and the uncertainty $\Delta \sin^2\theta_w$ was derived from the distribution of these results.

The analysis revealed that the optimal P2 experiment configuration consists of a beam energy of 155 MeV, a central scattering angle $\theta_f = 35°$ (where $\Delta \sin^2\theta_w$ is minimized), and a detector acceptance of $\delta\theta = 20°$. As seen in figure 3.10, the statistical uncertainty dominates within the selected acceptance. Increasing the detector acceptance decreases the impact of statistical uncertainties on $\Delta \sin^2\theta_w$, as the number of events will increase in this case. However, at scattering angles $\theta_f \leq 15°$, the total uncertainty grows due to the contribution of helicity-correlated beam fluctuations (A_{false}), while at $\theta_f \geq 55°$, contributions from form factors become significant.

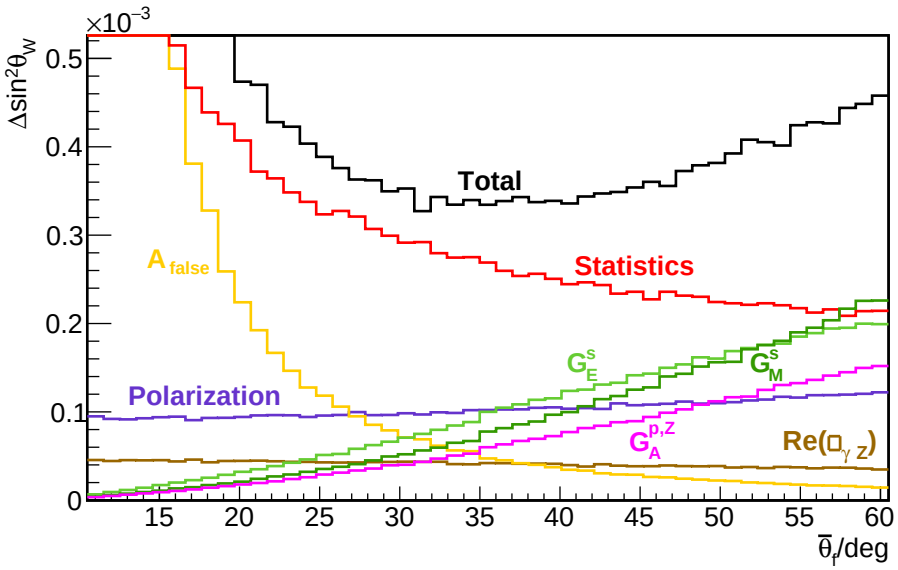

Figure 3.10.: Dependence of the total uncertainty $\Delta \sin^2\theta_w$ and dominating error contributions to it on the central scattering angle $\bar{\theta}_f$ for $E_{\text{beam}} = 155\,\text{MeV}$ and $\delta\theta_f = 20°$ ($\theta_f \pm 10°$). The statistical uncertainty is calculated for a running period of 10 000 h. Modified from [50].

Further analysis with a full Geant4 simulation model for the P2 detector, accounting for realistic detector effects and background events, refined the expected parity-violating asymmetry. The uncorrected asymmetry for signal events was determined to be $A_{\text{PV}}^{\text{sig}} = -39.94 \pm 0.56\,\text{ppb}$, with a relative uncertainty of 0.14 % for the weak mixing angle. After incorporating realistic detector effects, the expected asymmetry was reduced to $A_{\text{PV}}^{\text{exp}} = -24.03 \pm 0.57\,\text{ppb}$, and the corresponding uncertainty was adjusted for the scheduled running time of ~11 000 h. Finally, the following relative precision for the weak mixing angle $\sin^2\theta_w$ in the P2 experiment was determined:

$$\left.\frac{\Delta \sin^2\theta_w}{\sin^2\theta_w}\right|_{\text{exp}} = 0.15\,\%.$$

The measurements with such precision are sensitivity for Physics beyond the Standard Model with mass scales ranging from 70 MeV up to 50 TeV and complementary to the New Physics searches at the LHC [5].

A more detailed discussion and summary can also be found in [5, 50].

3.7. Auxiliary Measurements and Further Physics Program

Beyond its primary goal of precisely determining the weak mixing angle, the P2 experimental facility in Mainz is designed to execute an expanded measurement program utilizing parity-violating electron scattering. This program includes auxiliary backward-angle measurements and studies with different nuclear targets, aiming to conduct an even more sensitive and extensive search for New Physics.

Backward-angle measurements, conducted for the polar scattering angles of $140° \leq \theta_f \leq 150°$, are particularly sensitive to the axial form factor $G_{\text{A}}^{Z,p}$ and the strange magnetic form factor G_{M}^{s} form factors (see figure 2.8), making it an essential complement to the forward-angle P2 experiment. This approach does not require additional beam time if performed in parallel with

the main experiment. Dedicated backward-angle measurements are planned with hydrogen and deuterium targets to enhance precision further, requiring 1000 h of data each. For this, an additional set of Micromegas detectors, positioned before the target opposite the tracking detector (figure 3.3), will be used to reconstruct the momentum and vertex positions of back-scattered electrons within the specified angular range. The axial and the strange magnetic form factors have relatively large uncertainties such that corresponding terms F_A and F_S in the hadronic structure function (eqs. 2.60 and 2.62) make a non-negligible contribution to the total uncertainty in parity-violating asymmetry measurements (eq. 2.59). The backward-angle measurements will reduce this uncertainty contribution by a factor of 4 [5]. Furthermore, separate measurements on hydrogen and deuterium targets will yield the most precise determination of the axial and the strange magnetic form factors at low momentum transfer.

The P2 experiment's program also includes auxiliary measurements with a carbon (^{12}C) target. As a spin-zero nucleus, ^{12}C provides a clean probe of the weak charge, free from magnetic form factor complications [80]. This enables a more sensitive search for physics beyond the Standard Model, achieving a 0.3 % relative precision in the weak mixing angle and constraining CP-allowed (interactions respecting charge-parity symmetry) interactions up to 60 TeV [55].

Additionally, parity-violating electron scattering on a lead (^{208}Pb) target will be conducted to determine the neutron skin thickness with twice the precision of current measurements. This will significantly improve constraints on the nuclear Equation of State (EoS), impacting a better understanding of the physics of neutron stars. [5, 81]. Moreover, studies of transverse asymmetries and two-photon exchange amplitudes in heavy nuclei will be undertaken, contributing to a deeper understanding of nuclear structure and interactions [82, 83].

More details on the P2 experiment's auxiliary backward-angle measurements and further physics program can be found in [5, 84].

Part II.

The P2 Particle Tracking Detector

4 The P2 Tracker Design Highlights

This part of the thesis continues the outline of the tracking detector, initially given in section 3.5.3, providing more detailed requirements and concepts, the used sensor technology, the readout, and the track reconstruction. The initial concept of the tracker design, tracking reconstruction, and signal and background studies were described in [33]. The results presented in this work rely on these studies and continue them based on the recent updates and changes in the design and technologies used. The sections about signal and background and pixel sensor response to photons give a general overview of the studies done in [33].

4.1. General Requirements and Geometry

As outlined in section 3.5.3, the tracker supplements measurements for the electrons reaching the Cherenkov detectors by reconstructing their momentum and scattering angle. The P2 experiment requires a tracking detector system that minimizes systematic uncertainties through optimized sensor technology and geometry to achieve optimal resolution. Given the relatively low beam energy of 155 MeV, the possible momentum range of scattered electrons is limited to relatively low values, making multiple Coulomb scattering the dominant source of uncertainty in tracking resolution.

When passing through matter, electrons experience consecutive small-angle Coulomb scatterings, resulting in an effective scattering angle. A key parameter in this process is the projected root-mean-square (rms) scattering angle, θ_0^{rms}, for a material with thickness x and radiation length X_0, follows a Gaussian distribution with a width given by [17, 85, 86]:

$$\theta_0^{\text{rms}} = \frac{13.6\,\text{MeV}}{\beta c, p}\sqrt{\frac{x}{X_0}}\left[1 + 0.038\ln\left(\frac{x}{X_0}\right)\right] \sim \frac{1}{p}\sqrt{\frac{x}{X_0}}, \tag{4.1}$$

where p and βc are the momentum and velocity of the electron, respectively. This expression neglects non-Gaussian tails. The right-most equation part highlights the importance of minimizing the detector's material budget to reduce multiple scattering, thereby preventing false asymmetries introduced by unwanted interactions.

Gaseous detectors are the most obvious choice when the material budget is the main concern. Traditional gaseous detector technologies, however, suffer from low timing resolution, which is typically on the order of microseconds. Recent advancements in Micro-Mesh Gaseous Structure detectors (MicroMegas) have demonstrated excellent timing resolution, below 10 ns, without compromising spatial resolution, which remains under 70 µm, while maintaining a material budget below 0.35 % of the radiation length [87]. Despite these improvements, the rate capability of MicroMegas detectors is still limited to $O(10\,\text{MHz/cm}^2)$ [88], which is below the P2 experiment's expected rate of $20\,\text{MHz/cm}^2$. Moreover, a readout for large-area gaseous detectors with high granularity presents significant challenges due to the substantial number of required analog channels.

The latest silicon pixel sensor technology is an alternative solution that meets all requirements.

Silicon-based detectors typically introduce secondary scattering due to their relatively large material budget. However, a novel High Voltage Monolithic Active Pixel Sensors (HV-MAPS) technology offers both high-rate detection capability—up to 100 MHz/cm^2—and a very low thickness of 70 µm silicon, with only additional thin aluminum or copper traces for signal traces and power connectors [89–94]. For the P2 tracker, sensors based on HV-MAPS technology are mounted on polyimide flexprints with copper traces, resulting in a low material budget in the active tracker area of a total radiation length of approximately $X/X_0 \sim 0.2\,\%$ per layer.

Since these pixel sensors are active electronics requiring external power, they will generate and dissipate heat. This heat must be removed in limited space conditions to prevent sensors and flexprints from overheating and possible damage or breakdown. Therefore, the tracking detector modules will be placed in a gaseous atmosphere for cooling, supplemented by forced gas flow. Material budget constraints must also be considered when selecting the coolant. Further details on this pixel technology are provided in the next section, while the cooling system is presented later within the P2 tracker module mechanical design in chapter 5.

The determination of electron momentum by the tracking system relies on the curvature of electron paths, which requires an external magnetic field. As mentioned, the tracker will be placed inside the solenoid's magnetic field. Unlike in the Cherenkov ring detector case (section 3.5.2), this placement does not allow for complete geometric shielding of bremsstrahlung photons emerging from the target in this design, as shown in figure 4.1. Consequently, as shown in [5, 33], the first tracker planes are exposed to a photon rate up to six orders of magnitude higher than the signal electron rate. Therefore, ensuring a low detection probability for photons of various energies is critical for the chosen sensor technology. These studies and a detailed discussion of the results are available in [33].

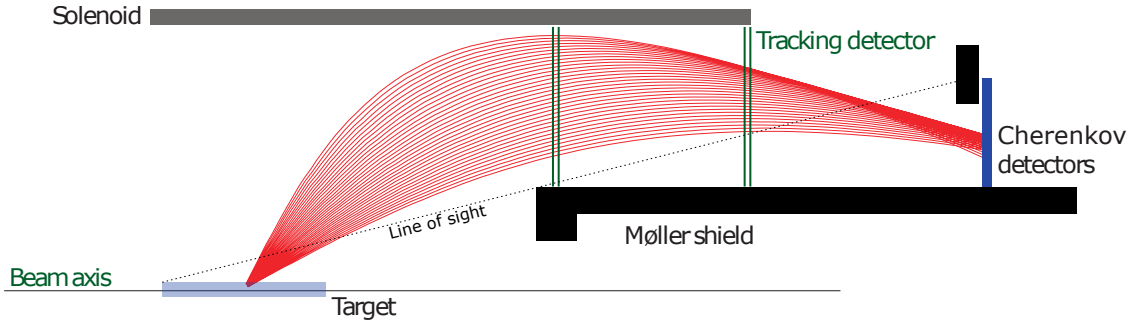

Figure 4.1.: Schematic side view of the P2 tracker geometry within the spectrometer (not to scale). Two dual-pair tracker planes are placed within the solenoid and separated by a wide drift region. Auxiliary and not essential parts are omitted. Electron tracks (in red) are added for illustration and do not represent physical tracks. Taken from [33].

For effective track reconstruction, the P2 tracking detector employs two pairs of closely spaced tracking planes. This dual-pair configuration enables precise directional measurements at two distinct points along the electron trajectory. An identical detector module design is used for both plane pairs to simplify development and assembly. The optimal spacing between the planes is approximately $1 - 2$ cm, corresponding to the typical separation of two hits on a single plane at full occupancy at a high interaction rate [5, 33]. However, the final detector design features slightly larger spacing due to mechanical constraints.

Ideally, the first position and direction measurement should be taken as close as possible to the scattering vertex. However, placing the tracking detector directly around the target is infeasible due to the extreme bremsstrahlung photon background, which would obstruct electron track identification. Increasing the distance between tracking planes enhances transverse momentum resolution. Specifically, the relative momentum resolution scales with the ratio of the

multiple scattering angle θ_{MS} to the track deflection angle Ω (figure 4.2) between two position measurements [95]:

$$\sigma_p/p \sim \theta^{\mathrm{MS}}/\Omega\,. \tag{4.2}$$

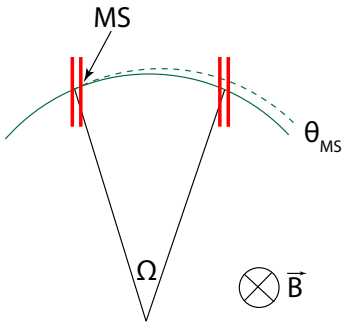

Figure 4.2.: Effect of multiple scattering (MS) on a charged particle's trajectory (green lines) in a magnetic field ($\vec{B}$). Tracker planes are shown as red lines. The deflection angle θ_{MS} at the first detector plane impacts curvature measurement precision. Modified from [33].

Thus, maximizing the deflection angle Ω between tracking planes will reduce a relative uncertainty on the curvature measurement, improving momentum reconstruction accuracy. The extensive Monte Carlo simulations [5, 33] indicated that placing one pair of tracker planes at the beginning of the Møller barrel shield and the other at the solenoid end ensures robust track reconstruction (figure 4.1 and section 4.4).

Although full azimuthal coverage is not necessary for precise $\langle Q^2 \rangle$ determination, the active tracking area must be sufficient to cover virtually all electrons directed toward a Cherenkov detector element. This requirement is met by tracker segments covering approximately 15° in azimuthal acceptance. The current design consists of 2 sets of 2 tracking detector modules (revised from initially planned four modules per set [5]), arranged diagonally symmetrically (figure 3.3). The optimal rotation angle between the module pairs, accounting for the curvature of the electron tracks, was chosen to be around 17° along the z-axis (figure 4.3) [33]. Additionally, a rotation system to enable changing the azimuthal position of modules is currently considered for covering up/down and left/right asymmetries in measurements.

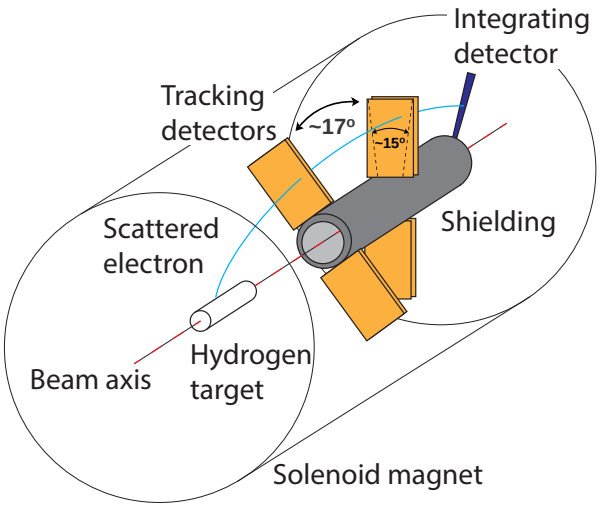

Figure 4.3.: Schematic view of the tracking detector. The electron track (in blue) is added for illustration and does not represent physical tracks.

4.2. High-Voltage Monolithic Active Pixel Sensors

Semiconductors like silicon have a crystalline structure where atoms are bonded through covalent interactions. Their electrical properties are defined by the band gap—the energy difference between the valence and conduction bands. This gap enables precise control over conductivity through doping—the process of introducing impurity atoms to modify charge carrier concentrations. Silicon pixel sensors exist in many variations, each optimized for factors such as low material budget, high detection efficiency, fast signal processing, and radiation hardness. Despite their differences, all rely on the fundamental principle of the p–n junction, schematically shown in figure 4.4.

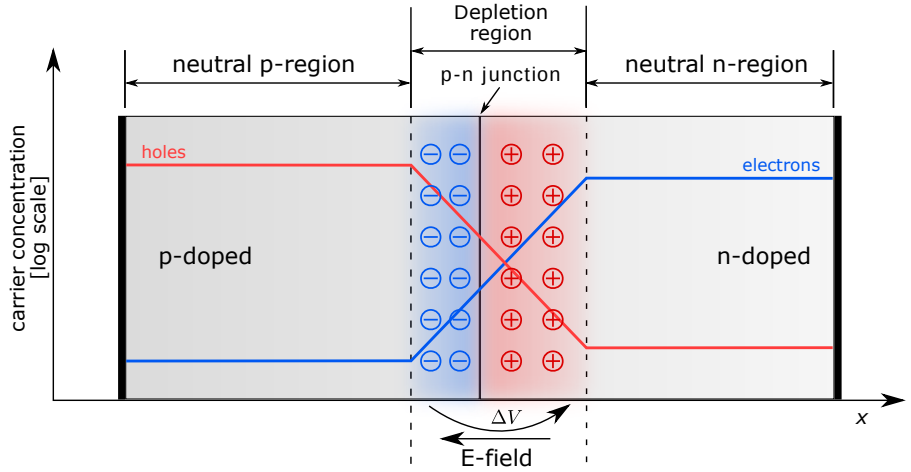

Figure 4.4.: Schematic representation of the p-n-junction region, illustrating the formation of the depletion region in the presence of the electric field (E-field) and potential difference (ΔV). Taken from [96] with modified annotation.

At thermal equilibrium, some electrons gain enough energy to move from the valence band to the conduction band, leaving behind holes. This continuous generation and recombination of electron-hole pairs occurs naturally. Doping silicon with donor atoms (with five valence electrons) creates n-type material, while doping with acceptor atoms (with three valence electrons) results in p-type material. Bringing n-type and p-type regions into contact leads to carrier diffusion and recombination, forming a depletion region (also called the space charge region) where free charge carriers are largely absent. This depletion process continues until the built-up electric field prevents further diffusion.

Applying a reverse bias voltage by connecting the positive terminal to the n-doped region and the negative to the p-doped region widens the depletion region. This extended depleted volume becomes the active region of the sensor. When an energetic particle interacts with the sensor material, it deposits energy via ionization or photon absorption, generating additional electron-hole pairs. In the depletion region, these charge carriers experience the electric field and drift toward the electrodes, producing a measurable signal. Electron–hole pairs generated outside the depletion region usually recombine, though some may still diffuse in and contribute to a slower signal component. Sensor performance can be fine-tuned by optimizing thickness, pixel size, bias voltage, and substrate resistivity. Fine segmentation enables precise position measurements, leading to strip or pixel sensors.

Sensor readout can be implemented in two architecture approaches: hybrid and monolithic. Compared to standard hybrid pixel sensors (figure 4.5a), where the separate detection and readout parts are connected via bump bonds, monolithic pixel sensors (figure 4.5b) integrate both the

sensor matrix and readout electronics onto a single silicon substrate, significantly reducing the material budget in the active area.

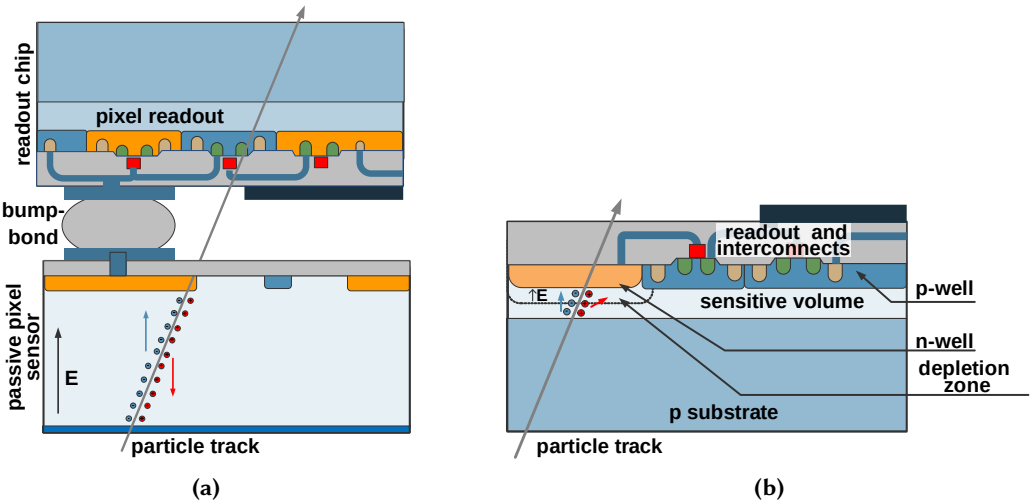

Figure 4.5.: Comparison of cross-section diagrams of standard hybrid (a) and fully depleted monolithic active pixels (b) (not to scale). Both pictures are taken from [97] with modified notation.

There are also active hybrid pixels, which differ from the standard hybrid ones by integrating amplification circuits within each pixel, which enables sub-pixel encoding. However, this technology still contains a separate readout chip connected via bump bonding, leading to a material budget comparable to standard hybrid sensors.

The P2 tracking detector will employ High-Voltage Monolithic Active Pixel Sensors (HV-MAPS; figure 4.6), which combine high-voltage Complementary Metal-Oxide-Semiconductor (CMOS) technology with standard CMOS transistors for complex readout electronics. These sensors offer several advantages. HV-MAP sensors are built on a p-type substrate with CMOS logic embedded in deep n-wells, which isolate the pixel electronics from the depletion voltage. A high reverse bias ($60 - 90\,\mathrm{V}$) creates a depletion region at the order of $30\,\mu\mathrm{m}$ thick, ensuring fast charge collection via electron drift. A key advantage of HV-MAPS is that they do not require a thick p-substrate on the backside, allowing thinning down to $50\,\mu\mathrm{m}$ and, as a result, improving momentum resolution. Overall, HV-MAPS technology offers cost-effective fabrication and minimal material usage, though at the cost of higher power consumption and reduced integration density. Furthermore, radiation hardness of HV-MAPS of 100 Mrad has been demonstrated with very high doses of protons and neutrons [98], which exceeds the estimated total radiation dose of 80 Mrad over the P2 experiment's runtime.

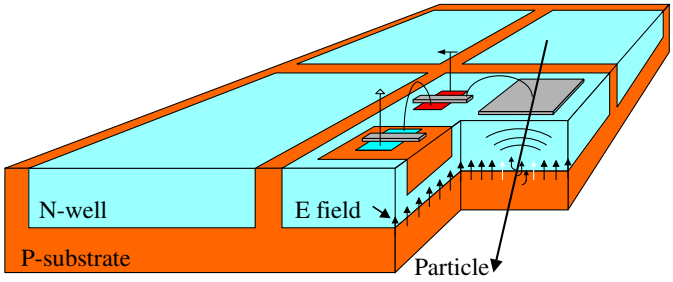

Figure 4.6.: Schematic illustration of an HV-MAPS: four high-voltage pixels with electronic readout circuitry integrated within deep N-wells. Taken from [99].

The sensors that will be used in the P2 tracking detector—the P2Pix sensors (figure 4.7)—are based on the HV-MAPS technology developed for the Mu3e experiment [100]. This development builds upon several prototype iterations—the MuPix chip series [94, 101–104]. The latest MuPix11 is a fully monolithic device with an active matrix size of $20.48 \times 20\,\mathrm{mm}^2$ and the pixel size of $80 \times 80\,\mu\mathrm{m}^2$ produced in the 180 nm HV-CMOS process [94, 105, 106]. The integration of amplification and line drivers within each pixel is a key feature of these designs, with subsequent signal processing occurring in the sensor periphery. The P2Pix sensor is an evolution of the MuPix sensor series with a set of modifications, including adjustments to pixel and matrix size, in-pixel amplification, discriminator in pixel, gated operation for handling high interaction rates in the P2 experiment, and clocking modifications for compatibility with serializers (discussed in the following section). Thus, the overall sensor performance and characteristics will not be affected. Main P2Pix specifications are presented in table 4.1.

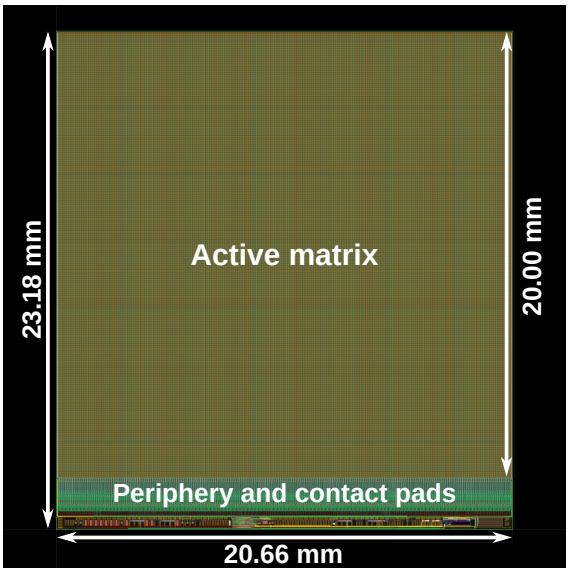

Figure 4.7.: The P2Pix layout.

Parameter	Specification
Nominal sensor thickness [µm]	70
Sensor size [mm^2]	20.66×23.18
Active area [mm^2]	20.66×20.00
Pixel size [$\mu\mathrm{m}^2$]	84×84
Pixel matrix [pixels]	244×240
Power consumption [$\mathrm{mW/cm}^2$]	$200 - 250$
Low voltage power [V]	2
Bias voltage [V]	60
CMOS amplifier	in pixel
NMOS comparator	in pixel
LVDS links	3 + 1
Clock	160 MHz
Maximum bandwidth [Gbit/s]	3×1.28

Table 4.1.: P2Pix specifications.

MuPix sensors have already undergone extensive studies and tests, demonstrating successful performance in efficiency, photon response, and radiation hardness. These tests included beam experiments at Deutsches Elektronen-Synchrotron (DESY), Mainz Microtron (MAMI), and Paul Scherrer Institute (PSI) [33, 107–110]. Results from the commissioning test beam for a 100 µm MuPix11 prototype show a hit efficiency of 99 % and a time resolution below 20 ns [110]. The achievable spatial resolution is ~23 µm [94, 100, 111]. Furthermore, MuPix sensors have demonstrated excellent radiation hardness in dedicated irradiation studies [107]. In particular, test beam results indicated that the MuPix10 chip can withstand high rates up to 200 Gy (0.2 Mrad) [109], fulfilling the requirements for the P2 experiment. In addition, a detector prototype using PCB-based support, instead of the aluminum-polyimide laminates, equipped with MuPix10 chips, was successfully operated as the first active pixel detector with gaseous helium cooling [108, 109].

4.3. Powering and Readout

The data rate depends on the tracker and Cherenkov detector's operating mode (section 3.5.3). However, at the full beam rate, the sensors in the tracker modules are expected to generate data exceeding 1 Tbit/s [5, 33], which surpasses the capacity of any affordable readout system. If full beam rate track reconstruction is attempted, the pixel sensors must operate in a gated mode, collecting data only during short intervals and then remaining inactive. However, for tasks such as reconstructing Q^2 in the target or for systematic studies, a representative subset of particles is sufficient since systematic uncertainties dominate. In contrast, the continuous tracking mode, in which the Cherenkov detector records single electrons that can be matched to reconstructed tracks, requires a reduced beam rate for uninterrupted data acquisition.

The P2Pix chips, similar to MuPix10 chips, incorporate an on-chip state machine that collects and serializes hit information [94]. Each sensor transmits triggerless, fully digital, zero-suppressed hit data, providing the column and row positions of each hit along with a sensor-generated timestamp, via a Low Voltage Differential Signaling (LVDS) links at 1.28 Gbit/s.

The operation environment in the P2 experiment requires radiation hardness, magnetic field tolerance, and compactness of the readout system components. Standard off-the-shelf readout electronics and optical modules are incompatible with on-detector applications due to their form factor and lack of radiation tolerance. Therefore, the P2 tracker readout system relies on specialized components developed by the Electronic Systems for Experiments group (EP-ESE) specifically for experiments at CERN. These include the low-power GigaBit Transceiver (lpGBT) [112], a highly configurable CMOS ASIC designed to handle high radiation doses and mitigate single-event effects, ensuring reliable short-distance data transmission. Another key component is the Versatile Link Plus Transceiver (VTRx+) [113], an optical module with a compact $20x10x4$ mm form factor that supports high-speed data transfer via multi-mode fiber. Both the lpGBT and VTRx+ are designed to withstand high radiation doses of up to $1 - 2$ MGy ($100 - 200$ Mrad) and operate in strong magnetic fields up to 4 T.

The P2Pix sensors receive a 160 MHz clock from the lpGBTs, which is scaled by a factor of four to 640 MHz by an on-board Phase-Locked Loop. The serializer outputs one bit per clock edge, producing a data stream of 1.28 Gbit/s. Since the sensor chips cannot drive signals over long distances, additional signal conditioning is necessary through LVDS repeaters or radiation-hard optical links. Given the radiation environment, the latter option is implemented in the P2 tracker modules via the VTRx+ module's electrical I/O, which is fully compatible with lpGBT high-speed interfaces. Then, the sensor data stream is routed via VTRx+ modules to back-end boards outside

the detector to minimize radiation exposure. Field Programmable Gate Arrays (FPGAs) on these boards synchronize incoming data and reduce its rate by identifying hit pairs consistent with particle tracks while discarding unmatched hits. This approach will efficiently eliminate single-hit events caused by absorbed photons. The remaining data, consisting of one or more matching hits, is then transferred to computers where sophisticated offline track-finding and reconstruction algorithms are executed.

The P2 tracker will be powered by commercial off-the-shelf power supplies placed out of the radiation environment in the counting room. The remote sensing will compensate for the voltage drop over the supply cables and regulate the voltage on the front end. The P2Pix requires a high-voltage supply of 60 V and a low-voltage supply of 2 V. To optimize space, minimize noise sources in the detector area, and prevent excessive heat generation at the front end, a remote-sensing approach was chosen over local regulation via on-detector DC-DC converters. In this case, rack-mounted Module Power Supply Units (Mod-PSUs) will provide power to the P2 tracker, supplying both bias voltage and low-voltage power to the P2Pix sensors, as well as the lpGBT chip and VTRx+ module with 1.2 V and 2.5 V, respectively.

This approach requires careful cable design and monitoring, as the cables directly affect power supply control, transient response, and voltage stability. A key challenge is the reduced efficiency caused by additional losses from high-current transmission. Nonetheless, this method has already been successfully implemented in multiple experiments, including, for example, the silicon strip tracker of the CMS experiment [114].

According to the current design, the P2 tracker comprises a total of 2160 P2Pix sensors (see chapter 5), requiring 320 lpGBT chips and 80 VTRx+ modules. Based on the expected P2Pix sensor configurations (table 4.1) and provided lpGBT chip and VTRx+ module specifications ([112] and [113], respectively). Assuming the maximum power consumption of the P2Pix sensors of 250 $\mathrm{mW/cm^2}$, this configuration results in an estimated nominal power consumption between $2.31 - 2.77$ kW for the P2 tracker. The P2Pix sensors alone will consume between $2.18 - 2.62$ kW, which corresponds to $544.5 - 656.0$ W per module. The final power distribution design and specifications are still being optimized.

4.4. Track Reconstruction

Reconstructing electron tracks in the P2 experiment is a challenging task due to the high occupancy of the tracking detector at the nominal beam current. This high occupancy means multiple particles can strike the detector simultaneously. Consequently, the numerous possible hit combinations make it computationally impractical to isolate the actual electron track using a straightforward combinatorial method. Beyond the challenges of high occupancy, the reconstruction must account for multiple scattering in the detector material, energy loss in the extended hydrogen target, and deviations from an ideal helical trajectory due to the inhomogeneous magnetic field. This section gives only a general overview of the track reconstruction algorithm concept. A more in-depth description and discussion can be found in [5, 33, 115].

Figure 4.8 presents a simplified overview of the track reconstruction process, assuming an ideal electron helical trajectory in a uniform magnetic field. This process combines efficient track finding with a robust fitting procedure, allowing for precisely determining track parameters.

Track Finding. To efficiently identify hit pairs, the developed parametrization-based algorithm [115] employs a strategy of progressing from low-occupancy to high-occupancy regions using

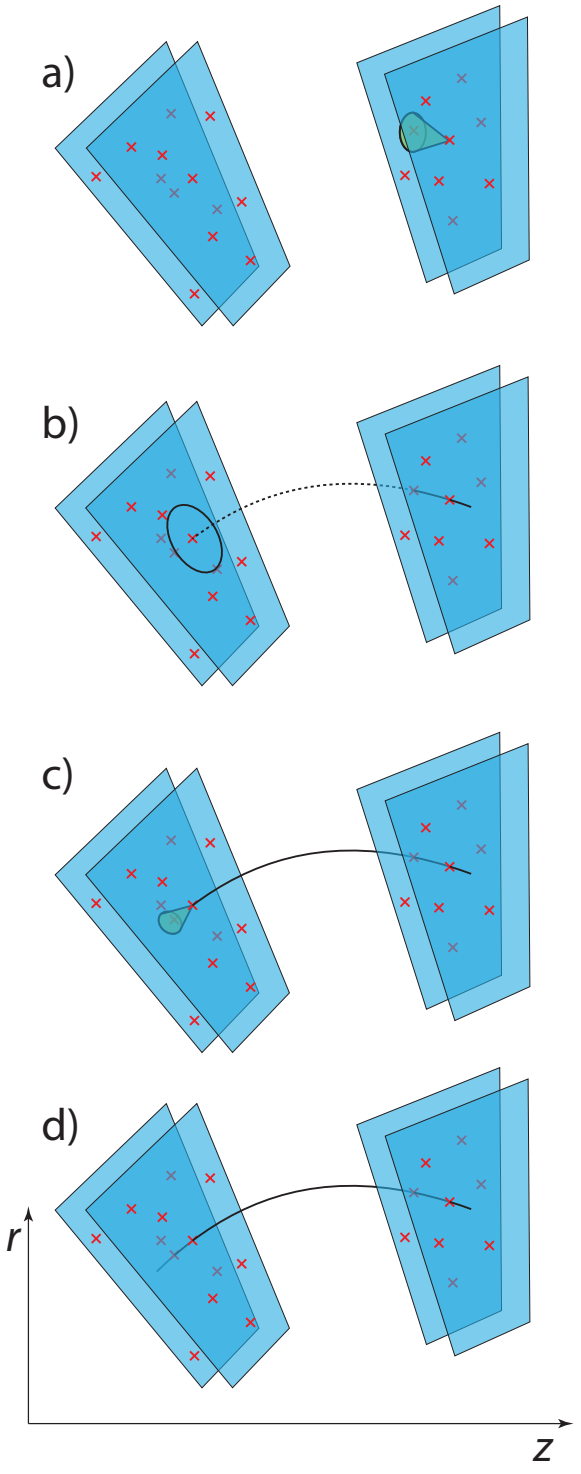

Figure 4.8.: Schematic representation of the parametrization-based track finding algorithm used in the P2 experiment, which includes the following steps (are discussed in this section): a) identifying hit pairs in the back module (low occupancy region); b) extrapolating to the front module using the target constraint; c) validating matching hits using the first plane; d) performing a track fit to accept or reject the track candidate. Taken from [5].

optimized track-dependent search windows. Rather than exhaustively testing all hit combinations, the algorithm defines search windows based on precomputed Monte Carlo simulations. In the first step (step 'a' in figure 4.8), a track candidate is initiated from a hit pair in the back (the closest to the Cherenkov detector) tracking module, where occupancy is lower. Using the target constraint and the connection vector between these hits, the algorithm defines a region of interest (ROI) on the second plane of the front module (step 'b' in figure 4.8). After matching hits within this ROI, a final validation is performed using the frontmost tracking plane (step 'c' in figure 4.8), where only candidates passing a track fit quality criterion are accepted. This approach significantly reduces the number of false track candidates, enabling efficient track reconstruction even at the full beam rate. The algorithm achieves a signal-to-background ratio exceeding 10 and an efficiency of approximately 85 % [5, 115], making it well-suited for the high-occupancy environment in the P2 experiment.

Track Fitting. Once track candidates are identified, a fitting procedure (step 'd' in figure 4.8) refines the track parameters. Initially, a rough estimate is obtained by assuming a helix track in a uniform magnetic field and fitting a circular trajectory through the centers of gravity of the first two and last two tracker hits. This initial track serves as the seed for a more precise fit using the General Broken Lines method [116, 117]. This advanced technique accounts for hit uncertainties, multiple Coulomb scattering in the detector material, and deviations from an ideal helical trajectory due to the inhomogeneous magnetic field. Track propagation between detector planes is performed using a Runge-Kutta-Nyström integration [118–121] of the realistic magnetic field map. The fit determines global track parameters, such as momentum and polar angle, while simultaneously correcting for measurement plane misalignments and scattering effects.

As shown in figure 4.9, the achieved momentum resolution is approximately 2 MeV, while the polar angle resolution is around 3 mrad, demonstrating the effectiveness of the fitting procedure.

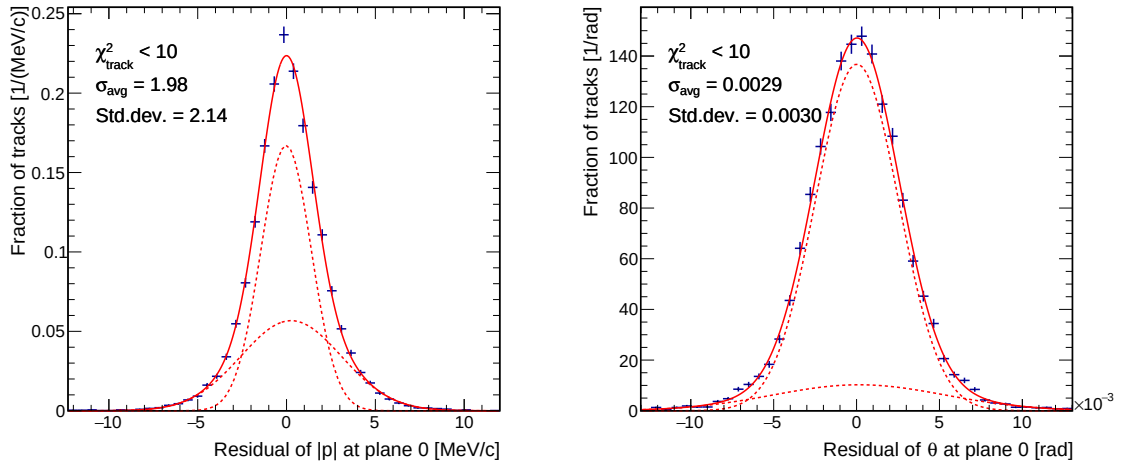

(a) Absolute momentum

(b) Polar angle

Figure 4.9.: Resolution of reconstructed track parameters at the first tracking plane. (a) Absolute momentum and (b) polar angle residuals, shown as reconstructed minus simulated values, with a requirement on the track fit $\chi^2 \leq 10$. The red curve represents the fit to the residuals (sum of two Gaussians), and σ indicates the area-weighted mean resolution. Both plots are taken from [5].

The Four-Momentum Transfer Reconstruction. The accurate determination of $\langle Q^2 \rangle$ relies on precise knowledge of the electron's momentum or scattering angle after interacting with the target. However, energy loss, multiple scattering, and detector acceptance introduce biases with non-Gaussian distributions into the reconstructed parameters. Furthermore, energy loss in the target further complicates the extraction of the initial electron momentum, potentially leading to additional reconstruction biases. To mitigate this, an iterative correction procedure using Monte Carlo simulations is employed. The simulation is carefully tuned to match observed distributions of track parameters, ensuring consistency between the reconstructed and true distributions. The currently achieved resolution of the reconstructed $\langle Q^2 \rangle$ per track (figure 4.10) is approximately $3 \times 10^{-4}\,\mathrm{GeV}^2$, corresponding to an uncertainty of around 4 %. The overall measurement precision is limited by systematic uncertainties, with multiple scattering models in the target representing the dominant contribution. Further improvements in detector alignment and refined modeling of the target interactions are ongoing efforts aimed at reducing systematic uncertainties below 1 %.

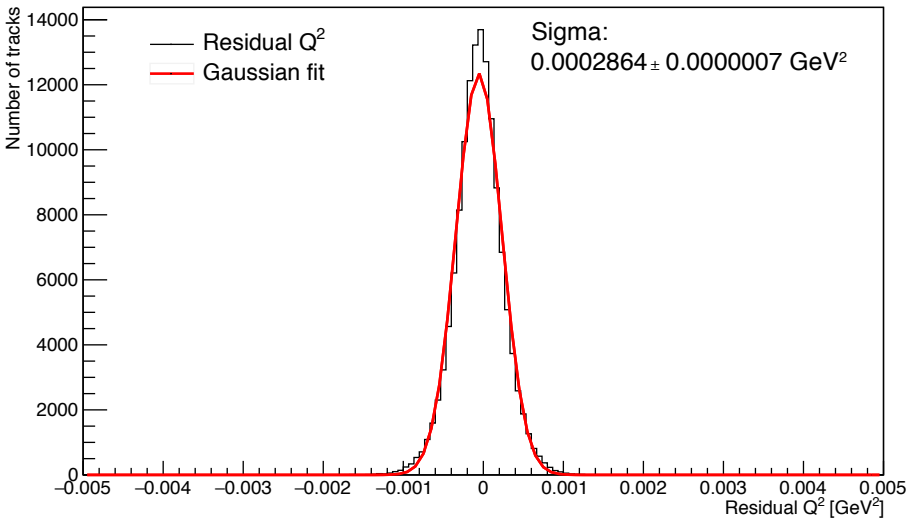

Figure 4.10.: Resolution of reconstructed momentum transfer Q^2 for simulated electron tracks. The histogram shows the residual—reconstructed minus simulated—Q^2 distribution. Taken from [5].

A further complication arises from detector misalignment. Even with high-precision mechanical alignment, residual misalignments on the order of $O(100\,\mu\mathrm{m})$ are expected. These must be corrected using track-based alignment techniques, which refine sensor positions iteratively by minimizing residuals from reconstructed tracks. The track-based alignment for the P2 tracking detector will use the alignment software developed for the Mu3e experiment [122] based on the Millepede II framework [116, 123].

5 Tracker Module Mechanics and Cooling System

One of the main parts of the work done in the scope of this thesis is refining the P2 tracking detector mechanics to address unforeseen challenges and updated requirements alongside cooling system studies. This chapter details the mechanical implementation of the tracking detector modules for the P2 experiment and the cooling system of the P2Pix sensors. The updates to the module design and the laboratory measurements for the cooling system, presented in this chapter, were carried out as part of this thesis, refining the initial concept and results outlined in [33]. Mechanical design updates and cooling system analysis were done using the Autodesk® software products: Inventor® and Fusion 360® for Computer-Aided Design (CAD) and Autodesk CFD® for CFD simulations.

It is important to note that the most recent design version includes modifications introduced after the cooling system studies were conducted. However, these changes primarily involve adjusting the front-end Printed Circuit board (PCB) dimensions to accommodate transmission lines and electronic components. The core cooling system concept remains unchanged, ensuring that the presented cooling system studies and results remain valid for guiding further optimizations and finalizing the tracker module design. Once the updated design is complete, new CFD simulations will be performed. A summary of the recent key design updates is provided at the end of this chapter in section 5.5.

Due to the ongoing development of the PCB layouts, electrical components for the power and readout systems are not depicted or discussed in the module design. This chapter is focused on the mechanical aspect of the module design and provides a general overview of the cooling system.

5.1. Technical Design

As mentioned, building a tracking detector with full azimuthal coverage between the barrel shield and the solenoid magnet body is not feasible due to cost constraints. In its current configuration, the P2 tracker consists of four modules arranged in two pairs of sensor planes. Consequently, the tracking detector consists of eight plane segments, each with about 15° of azimuthal coverage. One pair of tracker modules is positioned at the beginning of the barrel shield, just beyond the carbon fiber-reinforced plastic vacuum window, while the downstream pair of modules is placed at the end of the magnet and rotated clockwise by ~17° along the z-axis (see figure 4.3).

This section is structured first to define the essential mechanical design requirements. Subsequently, the overall tracker module concept is provided, followed by in-depth descriptions of individual parts and the complete module assembly.

5.1.1. Requirements

The technical design of the P2 tracking detector modules must satisfy multiple requirements. As highlighted in the previous chapter, minimizing the material budget within the tracker volume

is critical to reducing multiple scattering—one of the primary sources of error in reconstructing signal electron track parameters. This constraint is particularly important in the sensor's active area but also extends to mechanical support structures, even if they are located outside the active tracking region.

At the same time, the tracker module design must balance sufficient mechanical robustness with a high degree of modularity. Robust construction ensures the stability of the modules during operation and the precise positioning of sensor submodules. Modularity, on the other hand, facilitates maintenance or the replacement of faulty or malfunctioning submodules. However, this must be achieved while maintaining a minimal material budget within the detector volume. Submodules should be easily replaceable, ensuring a reliable mounting system, electrical connections, and precise positioning. The mechanical alignment of the silicon sensors requires a precision of approximately 100 µm. The silicon sensors, with a thickness of 50 µm, are minimally stiff and prone to bending. At the same time, they are rather fragile, which requires careful handling during mounting and assembly. The support structure must, therefore, provide sufficient stability, primarily managing its own weight and that of the electronic components, as the sensors themselves contribute negligible mass.

Radiation hardness is another critical factor in the module design, as discussed in section 3.5 and chapter 4. While the specific radiation tolerance requirements depend on the final measurement program, it is essential to ensure that all module components, especially electronic parts and structural materials like plastics and composites, can withstand radiation exposure. This also influences the development of the powering and readout infrastructure.

Furthermore, the P2Pix sensor includes both an active matrix and an inactive region containing digital electronics and contact pads (figure 4.7). The active area measures approximately 21 mm × 20 mm, while the overall physical size is about 21 mm × 23 mm. This results in some detection efficiency loss. To mitigate this, the mechanical module design must allow for overlapping inactive sensor regions by active regions of adjacent sensors.

Each pixel sensor requires power and readout capabilities, necessitating at least one fast readout link and one power line. While the detailed development of these systems is ongoing, the module design must integrate transmission lines and effectively accommodate electronic components.

Thermal management is another crucial aspect. The P2Pix sensors will be cooled using gaseous helium, requiring an efficient cooling system to ensure optimal heat transfer by directing helium flow precisely near the sensors. Computational Fluid Dynamics (CFD) simulations, discussed in the next chapter, have played a key role in refining the module's technical design. These simulations determined the necessary helium gas flow volume and established gas supply and cooling system requirements. By evaluating different scenarios, including varying P2Pix sensor power consumption, helium flow rates, and initial temperatures, CFD simulations enabled refinements in the mechanical design and provided more accurate estimations of the cooling system's performance while setting a reasonable safety margin. Additionally, all materials used in the module must withstand temperature variations from about −20 °C to 70 °C without damage. Thermal resistance and expansion properties must be carefully considered to maintain structural integrity.

5.1.2. General Concept

The pixel sensor coverage area on each tracker module, as depicted in figure 5.1, has the shape of an isosceles trapezoid, with dimensions corresponding to the earlier specified 15° azimuthal coverage.

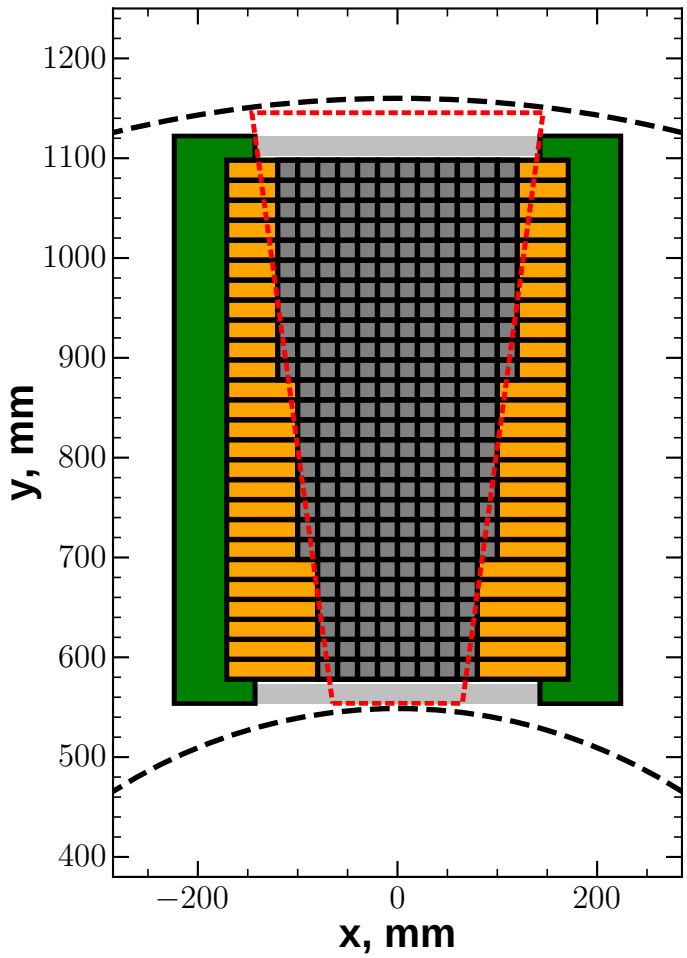

Figure 5.1.: Schematic of the tracker module. The given axes represent the module position in an upright orientation. Only the main components discussed in this section are shown: the support frame composed of front-end PCBs (green) from both sides and a mechanical connection mechanism (light gray), flex PCBs (orange), and P2Pix sensors (gray). Dashed circular segments indicate the boundaries of the gas chamber, defined by the barrel shield (inner) and solenoid magnet (outer) dimensions. The red-dashed trapezoid indicates the target sensor coverage for the full 15° azimuthal and radial coverage area. Reproduced from [33] with modifications based on the updates in the module design.

Structural Design. The support and electrical connections must contribute less material than the 70 µm-thick pixel sensors to maintain the minimal material budget in the active sensor area. This is achieved by directly adhering and bonding the sensors onto a flexible printed circuit board (*flex PCB*, also known as FPC), hereinafter also referred to as *flexprint*. The flexprint is a circuit board built on a flexible substrate, such as polyimide, with embedded copper or aluminum traces for sensor readout and powering. In this case, polyimide flexprint with copper traces will be utilized. This modular approach allows for flexible configurations, with rows of 8, 10, or 12 P2Pix sensors placed on a single flexprint.

A polyimide film structure (discussed in the next section) applied to the opposite side of the flex print provides structural support and additional cooling of sensors. Together with electrical and mechanical connection components (not depicted in figure 5.1), this assembly forms a unified mechanical structure called a "*ladder*." The detailed technical design of the ladder (figure 5.3) will be discussed in the following section.

Each ladder must be mechanically and electrically connected to a support frame at each end. As a solution, a front-end (frame) PCB at each frame side serves multiple functions: electrical connectivity for readout and power components, mechanical support, and integration of gas channels for the sensor cooling system. A tracker module frame has two sides, each formed by two *frame-PCBs*. These, in turn, are connected by additional support and gas distribution components, held together using a mechanical connection mechanism, as discussed in section 5.1.4.

Tracker Module Configuration The current design features 26 ladders with a variable number of sensors arranged per tracker plane as illustrated in figure 5.1. One plane contains 270 chips integrated onto a single sensor layer, covering an area of approximately 0.11 m^2.

Due to the mechanical constraints from the frame-PCBs and additional support structures, the actual pixel sensor coverage is slightly smaller than the targeted area (area indicated by the red-dashed trapezoid in figure 5.1). To standardize construction and assembly, fixed flexprint and ladder lengths were chosen, independent of the number of chips per ladder. This results in a rectangular frame design, ensuring a uniform rigid-flex PCB layout, consistent placement of electrical connections and elements on the frame-PCB, and simplified module assembly and operation. This modular approach also allows for flexibility in adjusting the number of ladders and overall module width, both refined during the design iterations presented here based on updated power consumption and spatial constraints.

Each tracker module consists of two tracker layers, with the second layer being a mirrored version of the first, rotated by 180° around the vertical middle axis. Thus, each tracker module comprises 540 P2Pix sensors, resulting in a total of 2160 sensors across the four-module P2 tracking detector. The combined active sensor area covers approximately 0.86 m^2.

Rotating system. Due to the reduction in the number of modules—from the initially planned eight to four [5, 33]—and the partial azimuthal coverage, a rotation system is being considered to cover up/down and left/right asymmetries in measurements. This system would allow simultaneous changing of the azimuthal position of all modules, with independent adjusting of the azimuthal position of the downstream tracker modules. However, as the technical design of this rotation system is still under development, it is not discussed further in this thesis.

5.1.3. Pixel Sensor Ladder

The ladder's technical design incorporates a flexprint layer stack adapted to the geometry and electrical connections of the P2 tracker module. Pixel sensors are mounted on polyimide flexprints with copper traces. Aluminum traces would normally be preferred due to their lower atomic number, which reduces multiple scattering. However, current global infrastructure and supply chain limitations prevent the production of flexible PCBs with aluminum traces that meet the required specifications. Consequently, copper-traced flexprints were chosen as the only viable option. The flexprint design features a two-layer stack with a total thickness of 100 µm. With mounted P2Pix sensors and a gluing gap, it will lead to the total ladder thickness of ~230 µm. This

results in a total radiation length per tracking detector module layer of approximately $X/X_0 \sim 0.2\,\%$ (figure 5.2). In comparison, the Mu3e experiment employs aluminum-traced flex PCBs, achieving a lower radiation length of $\sim 0.1\,\%$ [100, 110]. The flexprint integrates both power and signal lines for the sensor chips. However, the final design is still under development.

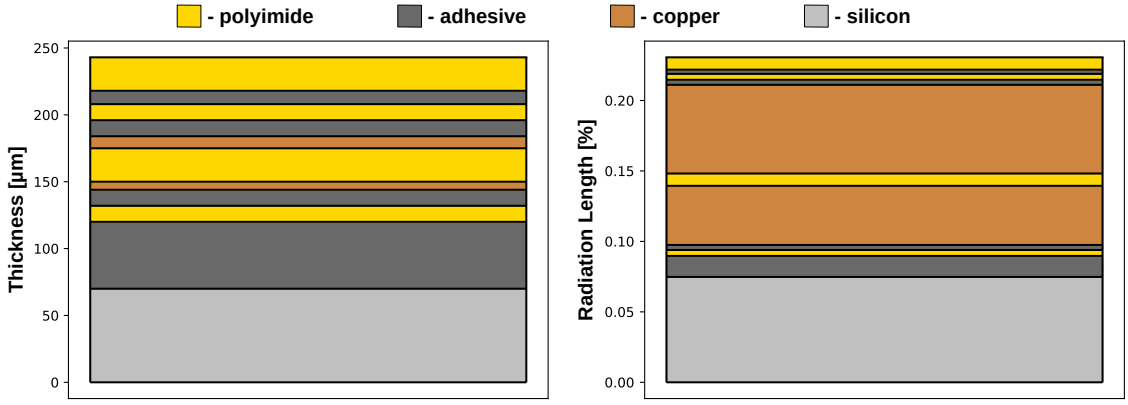

Figure 5.2.: Cross-sectional view of the flexprint layout (left) and corresponding contribution of each material to the overall radiation length (right), including silicone sensor and polyimide v-fold layers.

To ensure reliable electrical connections while keeping the material budget low, wire bonding will be used to electrically connect the P2Pix sensors to the flex PCBs. However, the switch to copper traces necessitated a change in bonding technology. The initially planned "Single-point Tape Automated Bonding" (SpTAB) technology [124] is incompatible with copper. Consequently, "Fine Wire Bonding" technology from Hesse GmbH[1] will be used instead. This technology uses thin aluminum bonding wires ($\sim 25\,\mu m$) to connect pads on the flex PCB to corresponding pads on the sensors. The connection is mechanically formed through cold welding, induced by longitudinal ultrasonic oscillations of the bondhead. This method is particularly well-suited for bonding on very thin substrates. Furthermore, compared to the initially planned SpTAB method, Fine Wire Bonding eases sensor positioning requirements on the flexprints, as overlapping and perfect pad alignment are unnecessary. This allows for better inspection of electrical connections and repair of broken ones, if any. Initial bonding trials using MuPix sensors and P2 flex PCB prototypes have already shown promising results. However, introducing wire bonding loops requires wider spacing between adjacent ladder overlaps. Consequently, the overlap design is being revised, potentially leading to removing v-folds (see section 5.5).

Figure 5.3 shows eplxoded view of the P2 tracking detector ladder. The base flexprint length in the P2 tracker design is 350 mm, independent of the number of mounted chips. The chips are arranged in a single row and centered along the ladder, as depicted in figure 5.1. As mentioned before, due to an inactive peripheral region, one edge of each sensor measures 23.18 mm instead of 20 mm (figure 4.7). The P2Pix sensors are mounted on the flexprints so that the inactive periphery parts are located along the flex PCBs. This configuration allows the ladders to be mounted on the tracker module frame in such a pattern that the inactive areas of the sensors are overlapped by the active areas of adjacent ladders, thereby providing uniform tracker area coverage (see section 5.1.5).

The flexprint design is electrically divided into two halves, with each sensor chip powered and read out from the closest frame-PCB. Only even numbers of chips per ladder are used for symmetric powering and readout. Depending on the number of mounted sensors, there are three ladder variations: ladders with 12, 10, or 8 P2Pix sensors. More ladder variations could improve

[1] https://www.hesse-mechatronics.com/en/bondjet-bj855-bj885/

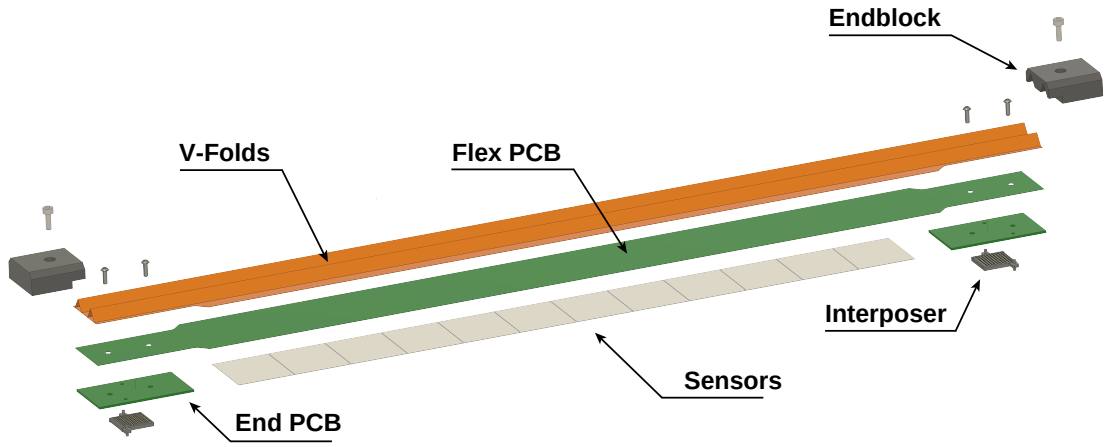

Figure 5.3.: CAD-generated exploded view of the 12-sensor P2Pix ladder configuration.

sensor coverage, especially with uneven sensor numbers. However, this would significantly complicate the fabrication and operational complexity.

Rigid end-PCBs (35 mm × 20 mm) are mounted at both ends of the flexprints, providing mechanical reinforcement and simplifying signal distribution. It has both mechanical and electrical functionality, reinforcing the ladder submodule at its ends. In addition, signal distribution is simpler on a rigid PCB than on a flexprint, as it allows more complex layer setups and vias. Signal and power traces are routed to a 10×10 pad array on each end-PCB. Electrical connection to the frame-PCBs is achieved using Samtec GMI SUPERNOVA® low-profile compression interposers [125] (figure 5.4). Two end-PCB thicknesses (0.8 mm and 1.55 mm) are used to allow the overlap of sensor inactive areas, as previously described. These two end-PCB variations, combined with the three flexprint variations, result in six different ladder variations.

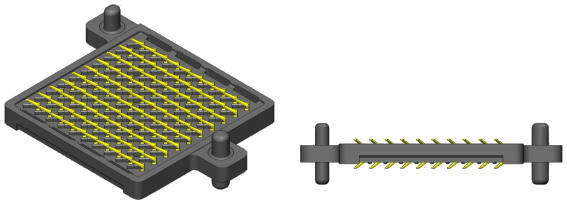

Figure 5.4.: Rendering of the Samtec GMI-10-2-1.27-G-10 interposer.

Triangularly folded polyimide structures, so-called "*v-folds*" due to their "v"-shaped cross-section (figure 5.3), are glued to the back of the flex print opposite the sensor mounting side. This additional polyimide layer is approximately 25 µm thick. The triangular cross-section of the v-folds provides self-supporting geometry, preventing flexprint sagging when handled horizontally from one side and further reinforcing each ladder. Although the modules will be mounted vertically in the P2 setup, this self-supporting feature is beneficial during tracker assembly. In addition, the v-folds serve as channels for helium cooling gas, enabling efficient heat transfer near the sensor chips. Tests have shown helium flow velocities up to 20 m/s are possible within the v-fold channels, with induced vibrations below 10 µm as shown for the Mu3e geometry in [126, 127] and for measurements using a simplified P2 ladder prototype in section 5.4, which is considered acceptable. The fold geometry was designed to provide space between the v-folds for connecting the flexprint and end-PCBs to the frame-PCBs using screws and thread inserts or nuts and screw inserts (see figure 5.3).

To distribute helium gas into the v-folds and further secure the polyimide ladder, plastic *endblocks* (figure 5.5) will be mounted at both ends. The polyimide can be glued directly to the endblock grooves for a gas-tight connection, replicating the v-fold shape. The endblock directs helium from frame-PCB openings to the v-folds through internal channels. Helium openings include notches for O-ring seals. Two endblock variants are needed to accommodate the different end-PCB thicknesses, as the interposer fixes the distance between the end-PCB and frame-PCB. Each endblock is mechanically secured to the frame-PCB with a single screw. Since radiation hardness and temperature resistance are required, polyether ether ketone (PEEK) is chosen as the material for any plastic parts in the P2 tracker module design, including the ladder sub-module endblocks.

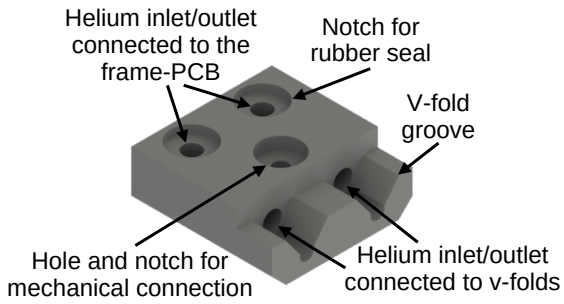

Figure 5.5.: Ladder endblock design.

5.1.4. Module Frame

Figure 5.6 illustrates the view of the complete module frame, which represents the mechanical foundation of the tracker module. It is composed of two frame sides connected by a connection mechanism.

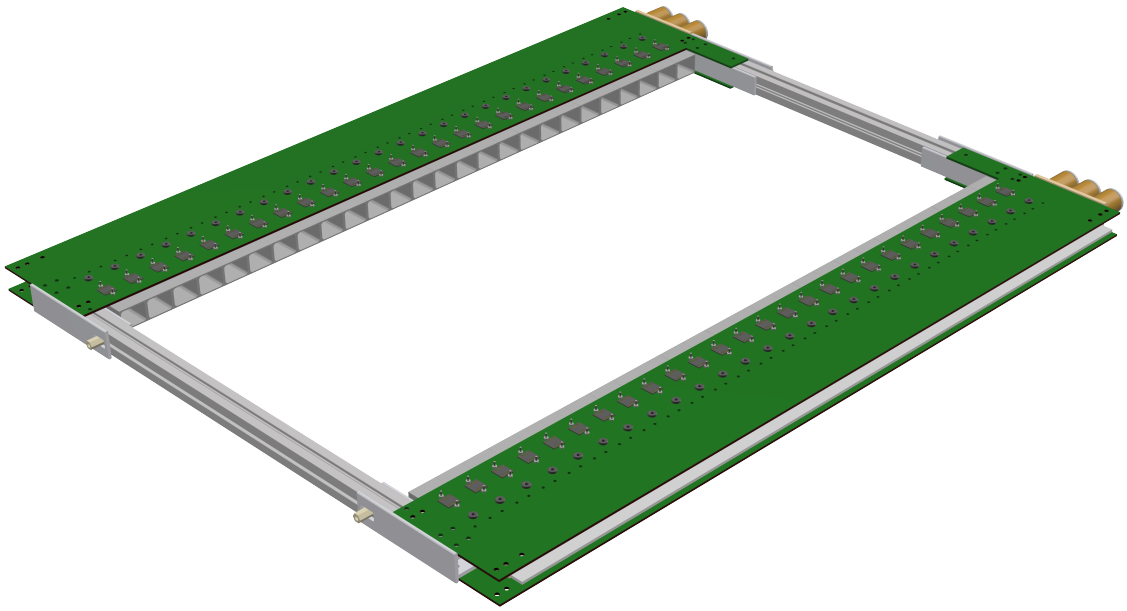

Figure 5.6.: Rendering of the module frame. Frame-PCBs include only mechanical parts for mounting the ladders and interposer connectors.

Frame Side. The tracker module frame provides mechanical support for the tracker module. It includes two identical side modules joined by an aluminum profile-based connection mechanism. Figure 5.7 shows the assembly stages of the frame side. The design concept is based on plastic profiles and diffusers sandwiched between two parallel large frame PCBs. These PCBs not only support and interconnect electronic components but also contribute to the frame's mechanical structure and gas distribution system. C-shaped plastic profiles separate the volume between frame PCBs, creating dedicated gas distribution channels for internal flow between the tracker planes and v-fold flows.

The dimensions of the frame PCB are 560 mm × 85 mm, with additional mechanical extension of approximately 19 mm×45 mm at top end. Bonded with Araldite® 2011 epoxy adhesive—widely used in accelerator physics due to its excellent radiation hard and mechanical properties —, frame PCBs and plastic gas distribution parts create a gas-tight and mechanically robust structure.

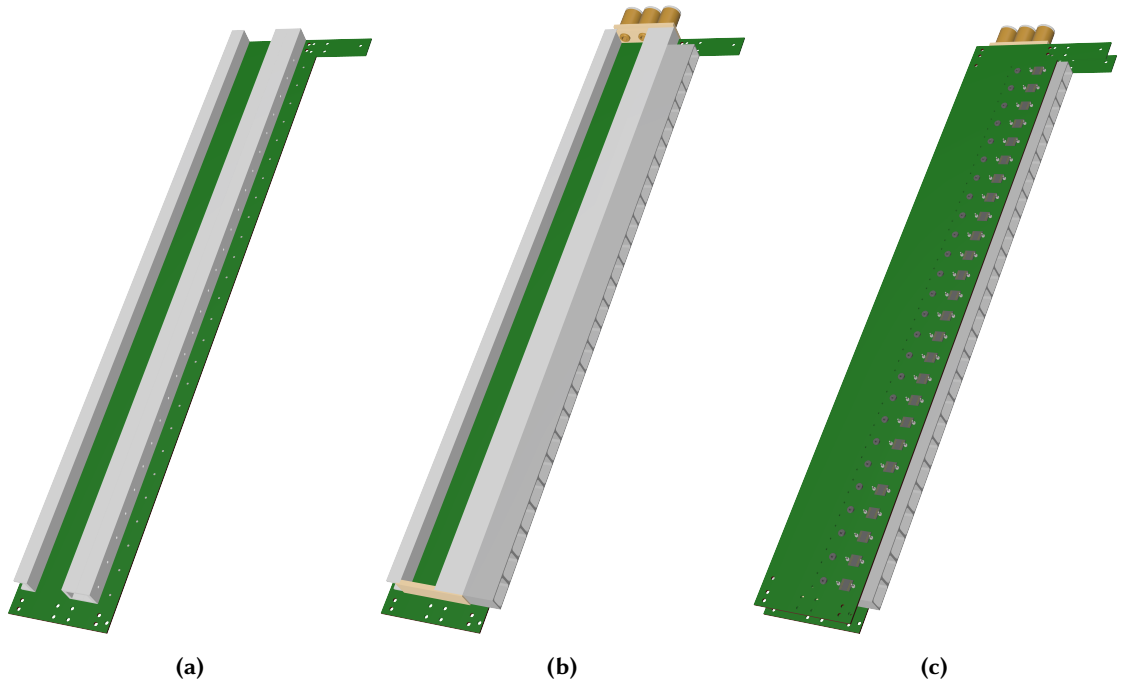

Figure 5.7.: CAD generated views of different assembly stages of one frame side: (a) Frame-PCB with plastic C-profiles for mechanical support and separating different gas flows; (b) Frame-PCB with complete gas distribution system for inner flow, including diffusers and gas connectors; (c) Fully assembled frame side. Frame-PCBs include only mechanical parts for mounting the ladders and interposer connectors.

Cooling Gas Channels. Figure 5.8 shows a cross-section of the cooling gas channels between the frame PCBs. The left channel, with a larger cross-section, distributes helium gas to the ladder v-folds, while the right channel, with a smaller cross-section, distributes helium for the gas flow between the sensor planes. After entering the frame gas distribution channels on the frame sides, helium is directed through the corresponding hole openings.

For v-fold channel flow, helium passes through a series of vertical inlet holes along both frame PCBs. Each opening is tightly connected to its counterpart in the endblock using O-rings (see figure 5.5). Two channels inside each endblock then direct helium into polyimide v-folds. Once v-folds are glued to the grooves in the endblocks (see figure 5.5), the helium flow through the v-folds becomes a closed system. Cold helium gas enters one frame side module, is distributed to the v-folds, and exits the v-folds at the other end of the ladder through vertical outlet holes

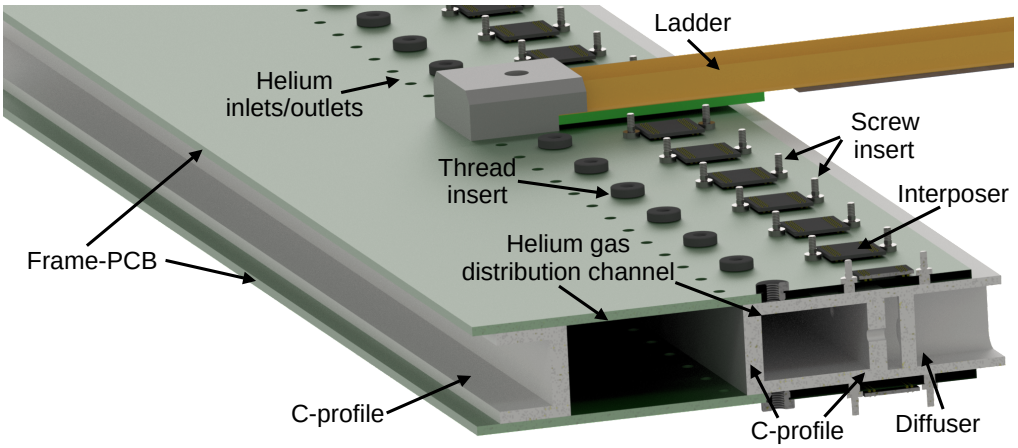

Figure 5.8.: CAD-generated view of frame side section with one mounted ladder mounting and labeled components. Frame-PCBs include only mechanical parts for mounting the ladders and interposer connectors. Taken from [33] with modified labeling.

in frame PCBs on the opposite frame side. More details on the cooling system are given in section 5.3.

Helium in the second gas channel between the frame PCBs is distributed through openings along the rightmost C-profile. After passing through these holes, helium enters diffusers (figure 5.9), designed to achieve a steady helium gas flow—*inner flow*—between the tracker planes along the ladders from one frame side module to the other. The inner flow is opposite to the v-fold flow. Due to the overlapping of adjacent ladders, which are mounted at varying distances from the frame PCB to prevent sensor interference with neighboring ladder v-folds (see figure 5.12), the volume between sensor planes is not gas-tight. Therefore, the helium flow between the tracker planes is not closed. Helium is supplied to one frame side module with overpressure, forcing it between the tracker planes. At the opposite frame side module, the same amount of helium gas is drawn in by lower pressure. Figure 5.9 shows a rendering of the diffuser design based on fluid dynamic simulations discussed in the following chapter.

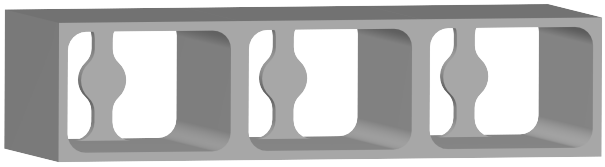

Figure 5.9.: Diffuser system on the example of rendering of the section consisting 3 diffusers.

Connection Mechanism. As outlined in section 4.1, optimal track reconstruction requires sensor planes spaced between $1 - 2$ cm. However, mechanical constraints from the connection mechanism result in a larger spacing of approximately 22 mm, with 15 mm between frame PCBs. The latter dimension is determined by the metal profiles used for the mechanical joining of the frame sides, providing construction with a simple and modular design and reasonable rigidity.

A fixed connection of the frame sides is not possible due to the thermal expansion of the ladder modules. With the cooling system, operating temperatures within the tracking detector volume are determined by two key factors: the initial coolant temperature and the temperature upper limit of the adhesive used for mounting the sensor on flexprints. In this specific case, this results in an approximate operating temperature range of $-20\,°\mathrm{C}$ to $70\,°\mathrm{C}$. For example, the thermal

expansion of 25 µm Kapton® polyimide film within this temperature range is on the order of $\mathcal{O}(20\,\text{ppm}/^\circ\text{C})$ [128]. Consequently, the 350 mm long polyimide can expands by ~0.6 mm for an 80 °C temperature difference. However, the thermal expansion of flex PCBs, a complex structure consisting of polyimide and copper traces joined together with adhesive, and its impact on reconstruction performance require further investigation. Therefore, the frame side connection mechanism is designed to compensate for potential ladder thermal expansion after initial module assembly, installation inside the tacking detector volume, and establishing a temperature gradient during operation. A rigid connection would force the ladders to deform, potentially leading to unpredictable and temperature-dependent sensor misalignment uncertainties. This, in turn, would increase uncertainty in the track reconstruction. The developed connection mechanism allows for an adjustable distance between the frame sides to accommodate thermal expansion. However, the actual impact of ladder thermal expansion on track reconstruction performance requires further investigation.

Figure 5.10 illustrates the prototype of the connection mechanism consisting of an aluminum profile and plastic fasteners from both sides. A 15 mm × 15 mm MakerBeamXL®[2] aluminum

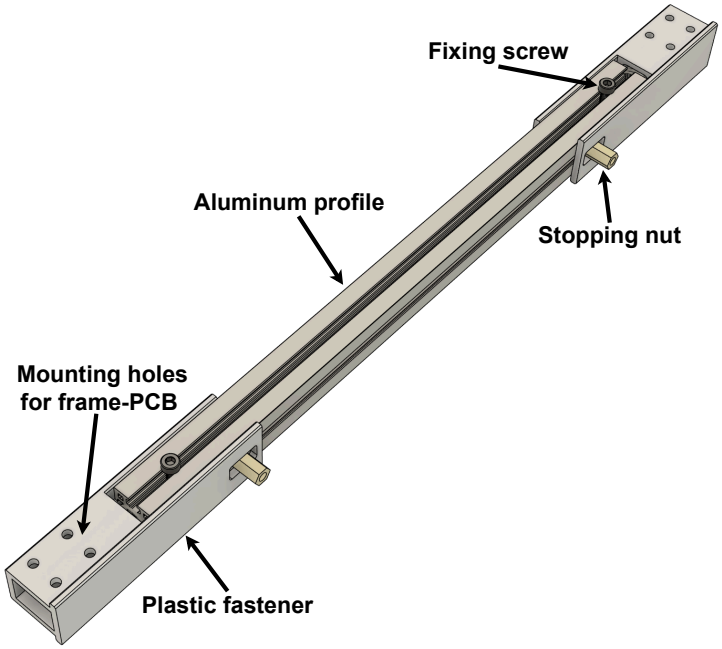

Figure 5.10.: CAD-generated view of the module frame connection mechanism with labeled components.

profile made was chosen primarily as an off-the-shelf option, well self-established in prior prototyping. While the profiles with lower dimensions are available, this particular size was chosen to ensure sufficient mechanical rigidity of the complete module based on the preliminary measurements. The final dimensions and material of the profile are still not fixed and might potentially be switched to titanium or carbon fiber-reinforced plastics. However, this option provides an excellent and affordable initial design and has performed well in the module prototype (see section 5.2).

Plastic fasteners are rigidly connected to the frame PCBs, while the aluminum profile can move on guidance rails on the fastener inside, as shown in figure 5.11, matching the profile's groove shape. To prevent ladder sagging and accommodate thermal expansion, two compression springs are added at each end of the aluminum profile, located between the profile's end face and

[2] https://www.makerbeam.com/makerbeamxl/

the fastener surfaces. These springs create a force, pushing the two frame sides slightly apart and thus creating tension on the ladders.

The adjustable distance between the frame sides prevents the ladder from sagging and accommodates its possible thermal expansion. This adjustment is limited by a stop nut moving along a slot in the fastener's side in the order of a few centimeters (figure 5.10). During frame assembly, fixing screws can lock the aluminum profile in its initial position, preventing unwanted movement during ladder mounting.

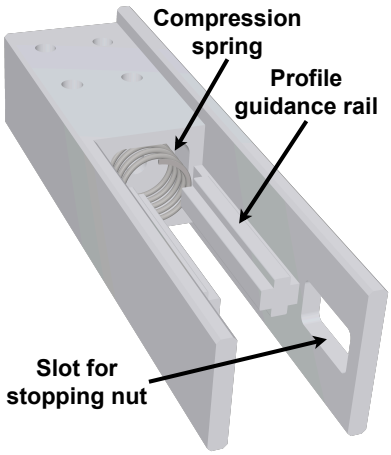

Figure 5.11.: Rendering of the plastic fastener with compression spring.

Ladder Mounting. Figure 5.12 shows the overlapping pattern of ladders mounted on the frame PCBs. The mounting system is designed to provide rigid fastening at both ladder's ends using screws and corresponding thread inserts in the frame PCBs. This ensures stability and reliable electrical connection. On the other hand, the use of screws and thread inserts allows for easy removal and replacement of individual ladders if necessary.

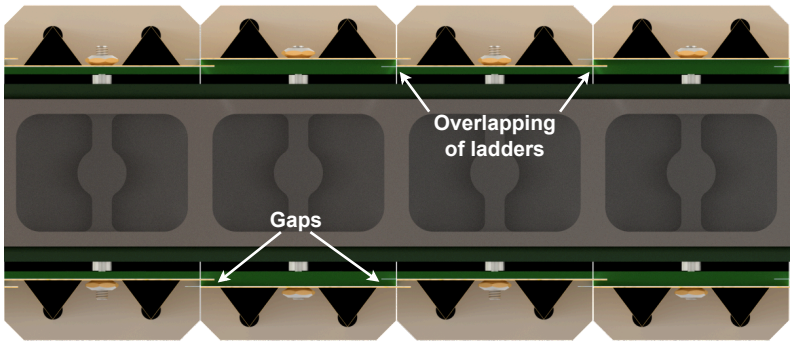

Figure 5.12.: CAD-generated side cut view of neighboring ladders mounted on both sides of the tracker module, visualizing the plane offset and sensors overlapping. Taken from [33] with added notation.

Rigid end PCBs provide electrical connections via interposers (figure 5.3). The varying thickness of the end PCBs allows overlapping via the variable pitch of the adjacent ladders. Each endblock is also secured with screws and thread inserts in the frame PCBs for ensuring gas-tight connection with v-fold flow inlets/outlets in the frame PCBs and further pressing each ladder to guarantee a reliable electrical connection via the interposer.

The electrical connection via interposers, successfully tested in [33] using a slightly different type of connectors, has undergone significant revisions (see section 5.5). However, the underlying mounting principle remains almost the same. In both cases, the electrical connection system is designed to meet the powering and readout requirements of the P2Pix sensors, listed table 4.1.

Figure 5.13 shows the frame with mounted ladders.

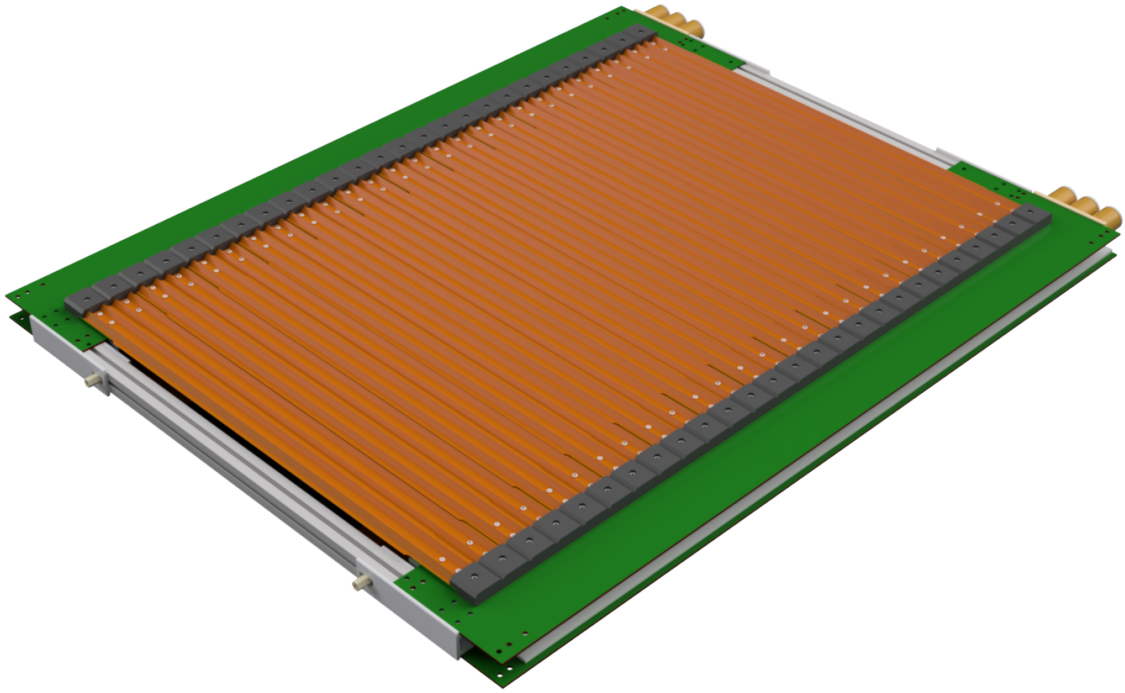

Figure 5.13.: CAD representation of the tracker frame with mounted ladders.

5.1.5. Tracking Detector Module

Figure 5.14 shows the rendered layout and main dimensions of the tacking detector module with one ladder plane mounted on the backside.

In addition to the helium flow between the module planes (*inner flow*), two flows are introduced on the outer sides of both planes (*outer flows*). The outer flow serves two important purposes: it provides additional cooling to the sensors and v-folds and compensates the pressure difference around the ladders and in the inner flow volume. The latter is necessary because the volume between the planes is not gas-tight due to the overlapping ladders (see figure 5.12). Otherwise, gas escaping from the inner frame volume due to the pressure gradient could induce ladder vibrations.

Figure 5.15 shows a rendering of the module cover, which can utilize the same gas distribution plastic parts and connectors as the inner flow.

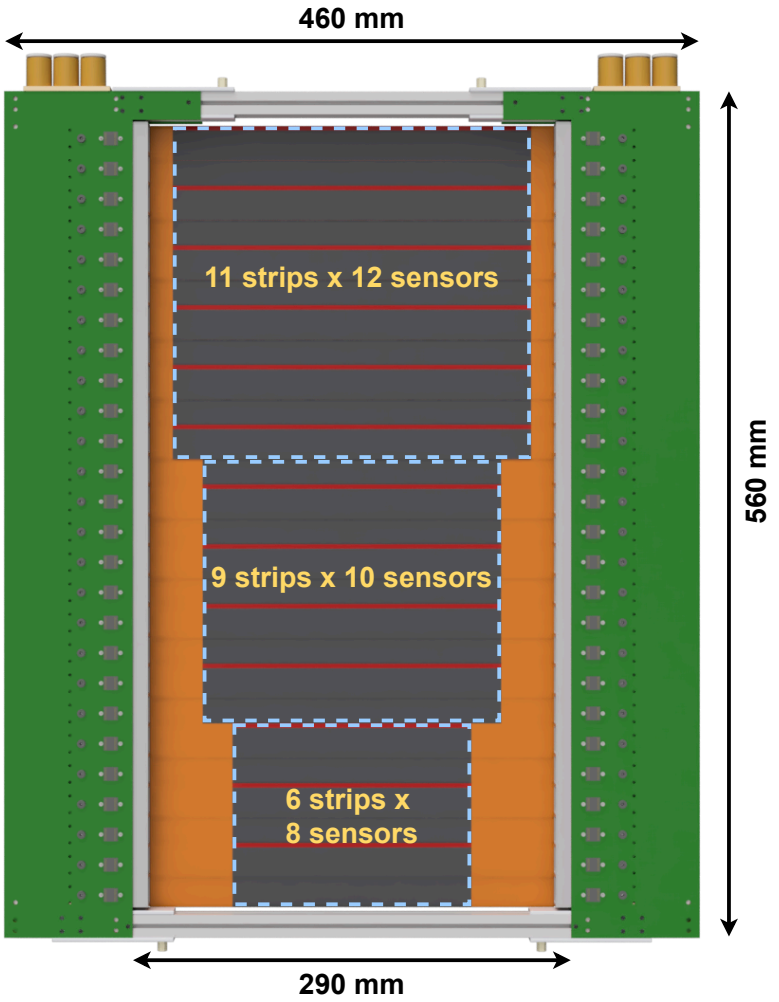

Figure 5.14.: CAD-generated tracker module layout. Only the backside ladder plane is shown to illustrate the sensors' pattern. The red area on the sensors indicates the inactive periphery part.

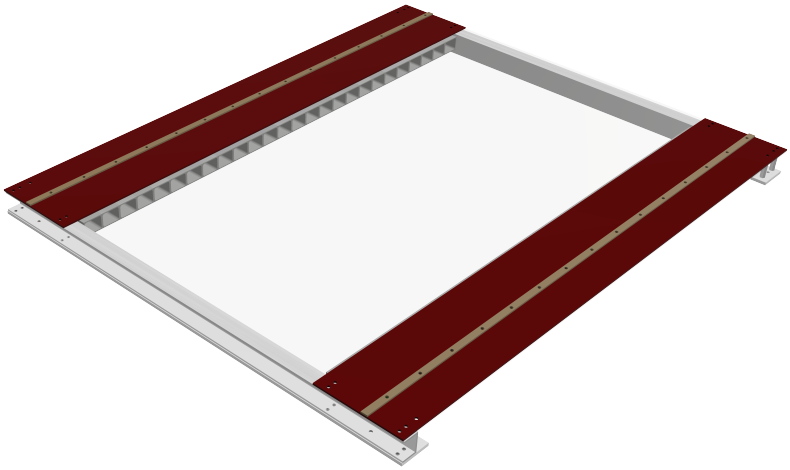

Figure 5.15.: Rendering of the module cover.

An additional cover with its own mounting system is added to house the outer gas distribution system and create a closed gas volume within a module volume.

Figure 5.16 illustrates different assembly stages of the tracking detector module. A more detailed module assembly procedure is described in [33].

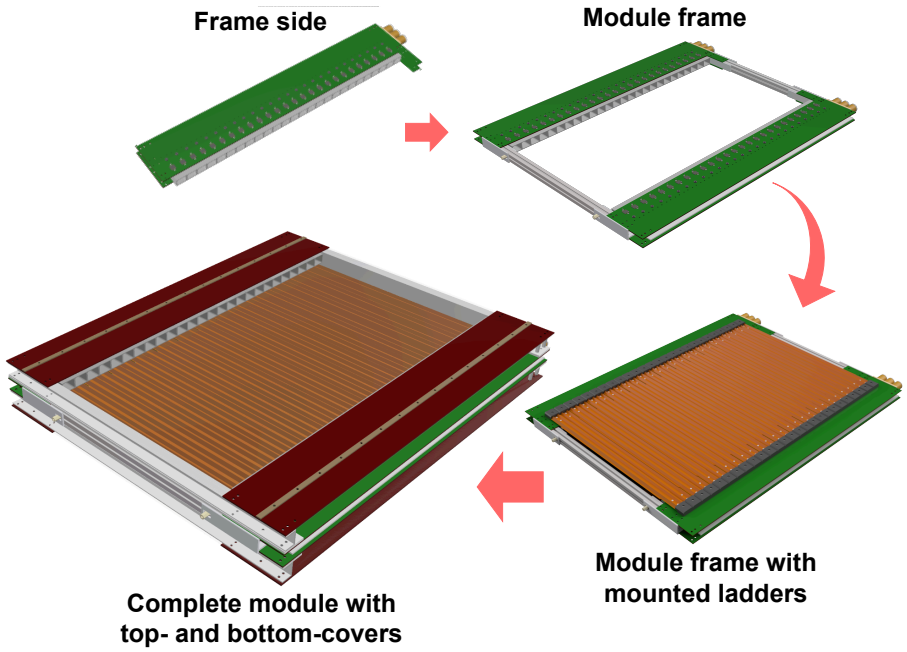

Figure 5.16.: CAD-generated representation of different assembly stages of the tacking detector module (shown at different scales).

Figure 5.17 illustrates an exploded view of all tracker module components.

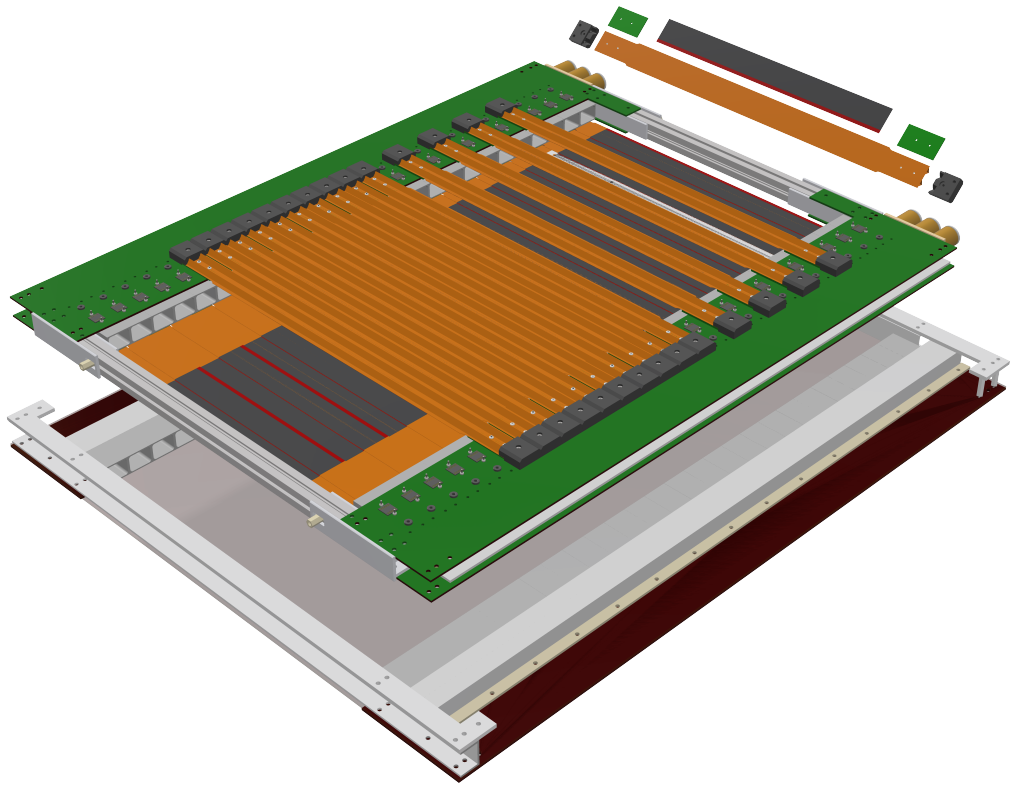

Figure 5.17.: CAD-generated exploded view of all tracker module parts.

5.2. Tracker Module Prototype

A full-size tracker module prototype with 36 dummy ladders, shown in figure 5.18, was already built. The detailed mechanical and electrical designs are provided in [33].

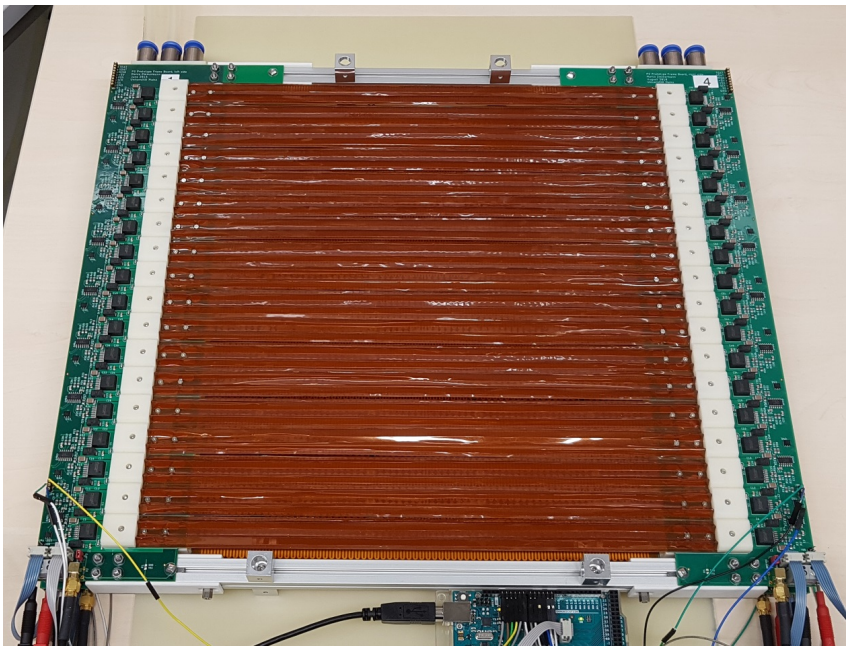

Figure 5.18.: Picture of the module prototype. The image is taken from [33].

This prototype was initially designed for electrical and cooling studies. It does not include actual HV-MAPS sensors but instead features heatable ladder prototypes—flex-PCBs with zigzagged conductive traces that simulate the heat dissipation of real sensors. Each ladder also features a set of digital temperature sensors along the flexprint for precise thermal monitoring. Figure 5.19 presents the flex-PCB design and an image of the flexprint used in this prototype. With known resistance of heating traces, the heat generation can be controlled by adjusting the supplied voltage through implemented control and data acquisition software [33]. For prototyping purposes, all plastic components were fabricated from Acrylonitrile Butadiene Styrene (ABS) instead of the more expensive and difficult-to-machine PEEK plastic. Cooling performance tests were successfully conducted using pressurized air and helium gas as coolants [33, 129, 130], demonstrating proof-of-concept for both the module and cooling system.

(a) Flex-PCB design

(b) Picture of a flexprint copy

Figure 5.19.: Design and implementation of the heatable flexprint used in the prototype. Flexprint dimensions: 360 mm × 19.90 mm. Both images from [33].

Initially, the prototype lacked outer flow channels and an additional cover (figures 5.16 and 5.17). Therefore, all cooling tests were performed with the module enclosed in a plexiglass housing, as shown in figure 5.20, to create a closed volume with a helium atmosphere.

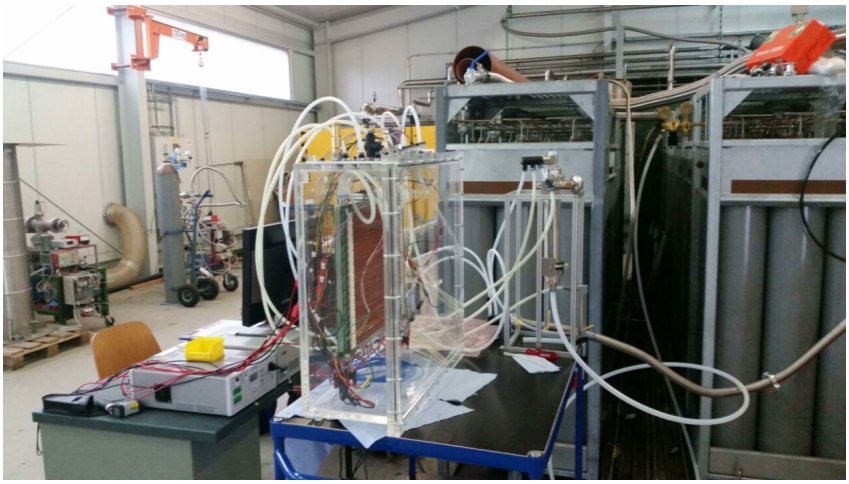

Figure 5.20.: Cooling setup with tracker module prototype and plexiglass enclosure. Image is taken from [130].

All gas distribution components were designed for conventional milling to simplify manufacturing, avoiding reliance on 3D printing [33]. As a first step towards integrating outer flow channels, the possibility of producing the gas distribution system using Selective Laser Sintering (SLS) 3D-printing technology for the given geometry was investigated in the framework of this thesis. This 3D-printing approach might allow for greater customization and design complexity while reducing assembly steps, such as gluing, which could otherwise introduce gas leakage in case of insufficient local gluing.

Figure 5.21 shows the produced gas distribution parts made of ABS plastic for outer flow.

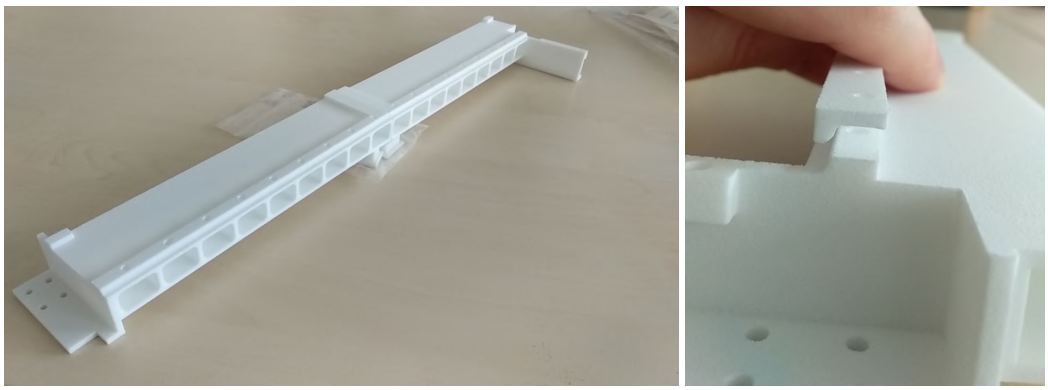

Figure 5.21.: 3D-printed components for the prototype of the outer flow gas distribution system, featuring integrated parts for connection with frame PCBs and a cover clamping mechanism (right).

Figure 5.22 shows the first assembled version of the outer top flow, covered with a large polyamide film secured by the clamping mechanism (figure 5.21).

These results confirm the feasibility of producing the gas distribution elements— only for outer flows or complete systems—using SLS 3D printing since PEEK can also be used as a printing material. However, the roughness of the printed surfaces requires post-processing to ensure gas-tight connections. Therefore, the feasibility of this approach for producing gas system parts

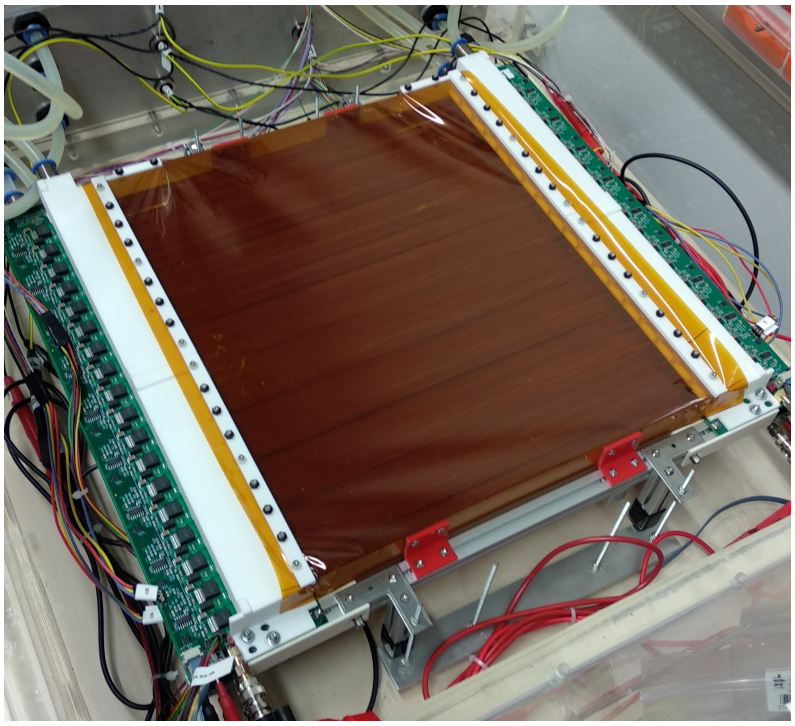

Figure 5.22.: Picture of the cooling setup showing gas distribution parts for outer flow and a module cover assembled and mounted on top.

remains under evaluation. Further incorporating outer flows and covers on both sides of the module and further cooling system measurements require a full prototype redesign. Once the final design updates are completed, the next iteration of the module prototype and the following measurements are planned. The key focus will be on the outer performance, particularly to evaluate the impact of potentially removing v-folds and their corresponding gas supply system elements (see sections 5.1.3 and 5.5).

5.3. Cooling System

Cooling the silicon pixel sensors is a significant challenge in developing the P2 tracking detector. The P2Pix sensors are expected to generate heat similar to MuPix sensors (as referenced in [94]), with the heat density (flux) between 200 $\mathrm{mW/cm^2}$ and 300 $\mathrm{mW/cm^2}$. Based on the recent refinements, the power consumption of MuPix11 chips is estimated to be around 215 $\mathrm{mW/cm^2}$ [94, 110]. The power consumption of P2Pix sensors is expected to be slightly lower than the latter value. Currently, cooling system studies consider two power consumption scenarios for P2Pix sensors: a *moderate* scenario with the heat density of 200 $\mathrm{mW/cm^2}$ and a *high-power* scenario with the heat density of 250 $\mathrm{mW/cm^2}$.

In Computational Fluid Dynamics (CFD) simulations, it is assumed that all electrical power consumed by the sensors is converted to heat and released into the environment, accurately reflecting real-world conditions. Therefore, given the current design, one module can produce excess heat of around 1 kW. A continuous helium flow must remove this heat through channels along the sensor surface in each module, as natural convection will not be sufficient to dissipate this heat.

As reported in [105], the HV-MAPS technology, which is utilized in P2Pix and MuPix sensor architectures, demonstrated successful operation stability for ambient temperature range from −20 °C to 80 °C. The maximum working temperature of 70 °C was already exceeded at the ambient temperature of 45 °C, and at higher ambient temperatures, the supply voltage was lowered not to exceed the sensor temperature further. However, the performance criteria for the cooling system are defined by the requirement of maintaining the maximum temperature of P2Pix sensors below 70 °C. This limit is determined by the glass-transition temperature of the adhesives used for mounting the sensors on the flexprints.

Minimizing the material budget in the active area restricts coolant choices, favoring gases with low atomic numbers and low radiation lengths to reduce secondary scattering and increase the tracking reconstruction performance. The obvious choice could be Hydrogen since it has the lowest atomic number and density and good cooling properties, as shown in table 5.1. However, hydrogen's explosiveness when mixed with air and the resulting safety hazards from potential gas supply-system leakage led to its rejection. Helium, being chemically stable and free of such safety concerns, was chosen instead. It also has a low density and heat conductivity comparable to hydrogen, making it an optimal gaseous coolant. Nevertheless, gaseous helium's low density results in a low volumetric heat capacity (heat capacity per unit volume; not to be confused with the specific heat capacity at constant volume) compared to liquid coolants, requiring higher volume flow rates.

	Hydrogen	**Helium**	**Air**
Radiation lenght X_0/m	0.028 %	0.018 %	0.046 %
Density ρ [kg/m^3]	0.0819	0.1625	1.177
Specific heat capacity c_p [kJ kg^{-1} K^{-1}]	14.31	5.19	1.01
volumetric heat capacity [J m^{-3} K^{-1}]	1172	844	1185
Heat conductivity k [W m^{-1} K^{-1}]	0.187	0.156	0.02623
Kinematic viscosity ν [cm^2/s]	109.2	1.23	1.575
Prandtl number Pr	0.685	0.664	0.713
Speed of sound v_s [m/s]	1270	1019	347

Table 5.1.: Main thermophysical properties of different gases (at $T = 300$ K and normal pressure $p = 1$ atm) [131].

5.3.1. General Concept

Given the module design and overall dimensions, several gas channels must be implemented to effectively cool the sensors with gaseous helium. Additionally, the opposing direction of different gas flows should be considered to mitigate the potential overheating of sensors at the ladder ends. Ideally, the tracker module would be a closed, gas-tight system. However, complete gas tightness is unnecessary since the tracker operates within a helium atmosphere gas chamber.

The base design, initially presented in [33], incorporates three distinct gas flow types within a tracker module, as shown in figure 5.23: an *inner flow* between the two tracker planes, *channel flows* inside the v-folds on each ladder, and two *outer flows* at the module's top and bottom (from the given perspective, as modules will be vertically installed). The channel flow direction opposes the inner and outer flows, reducing temperature gradients and preventing sensor overheating at the ladder ends furthest from the inner and outer flow entrances.

As previously mentioned, the top covers are needed to ensure the inner flow direction is

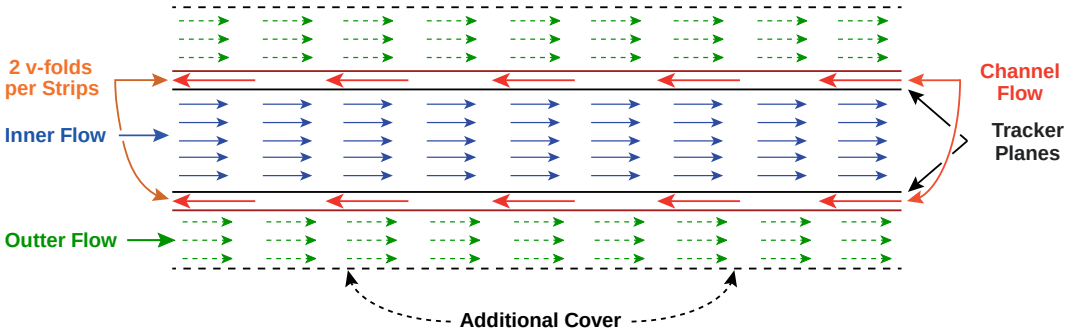

Figure 5.23.: Schematic section view of the helium cooling system within a tracker module, showing the different flow types. Diagram not to scale. Reproduced from [33].

strictly along the ladders, preventing the perpendicular helium mass movement throughout gaps between ladders in the overlapping regions (figure 5.12) due to pressure difference. Updated simulation results and the consideration of removing v-folds (see section 5.5) due to revised spacing requirements between adjacent ladders (section 5.1.3) have led to the current design incorporating fixed outer flows, in contrast to their initial optional status in [33].

The pipes connecting the gas supply system to the tracker modules will be placed at the outer magnet wall and, therefore, enter the modules from the top (as illustrated in figure 3.3). However, the technical design of the complete gas supply infrastructure is not covered in this thesis since it is still being designed. Only some remarks regarding the suitable compressor options for providing estimated flows based on the simulation results are provided in section 6.3.3.

The helium will circulate through a closed loop with the P2 tracking detector and a heat exchanger. Pipes connecting the gas supply system to the tracker modules will be located at the outer wall of the solenoid magnet, entering the modules from the top. The concept of the gas distribution system within a module is outlined in the following section. While the detailed technical design of the complete gas supply infrastructure for the whole tracking detector is still under development and is not covered in this thesis, some aspects, such as suitable compressor options for achieving the necessary flow rates based on simulation results, will be addressed in section 6.3.3.

5.3.2. Gas Distribution System Within a Module

The primary goal in developing the helium gas distribution system is to maintain a uniform, steady laminar flow along the ladders and avoid turbulence in all flow regions to minimize ladder vibrations induced by gas flows and pressure drops in the module.

Once cold helium enters a module's gas distribution system, it is routed through a series of channels toward the sensors, as illustrated in figure 5.24.

A key challenge is ensuring that each channel along the module receives equal gas flow. At the same time, the maximum flow velocity must remain below the speed of sound v_s in helium (table 5.1) to preserve the laminar flow regime. An even stricter requirement is maintaining near-incompressible flow, which, in a less restrictive definition [132], demands flow velocities below $0.3v_s$. This condition minimizes density variations due to pressure changes and was therefore imposed as the main criterion in most CFD simulations, with only minor local violations in the distribution channels before the gas enters the sensor volume. Consequently, the flow rates were chosen, given this requirement.

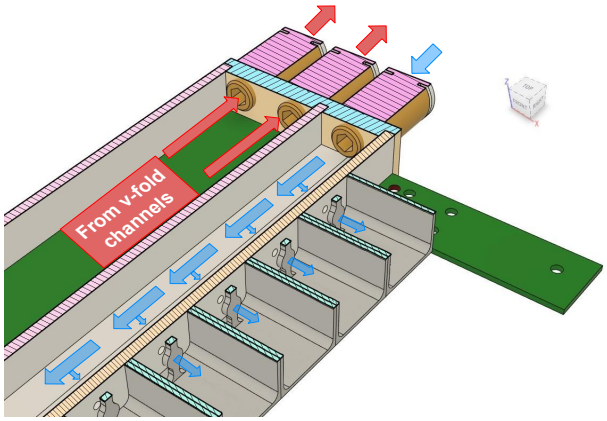

(a) Section view of the gas supply system within frame side.

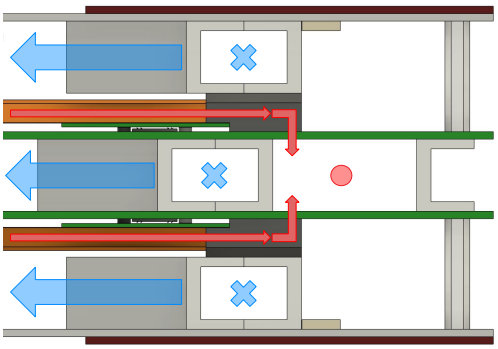

(b) Side view of different gas flows.

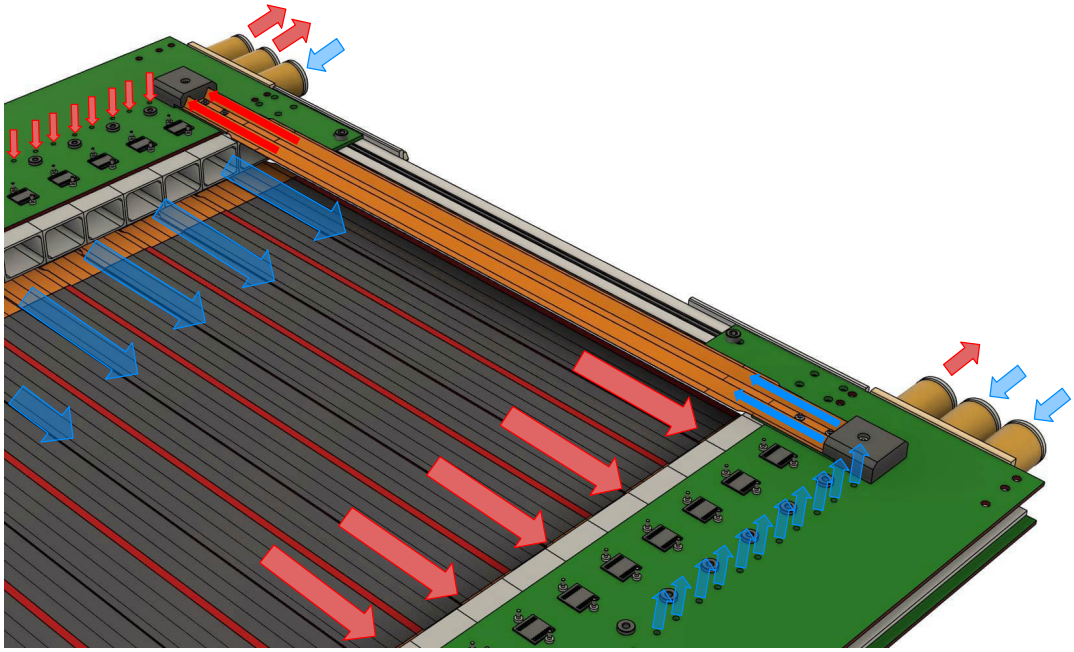

(c) General view of different gas flows within the module frame.

Figure 5.24.: CAD-generated views for demonstration of the module gas distribution system. The arrow direction indicates the direction of the corresponding flow. The arrow color indicates helium temperature: blue corresponds to the initial gas temperature, while red corresponds to increased gas temperature after taking heat produced by sensors.

Additionally, in the case of the Mu3e experiment, it was estimated that local velocities inside the v-folds should not exceed approximately ~20 m/s [100]. Since the v-fold geometry in this design is almost identical, the same criterion was adopted to optimize the v-fold flows. For the inner and outer flows, the diameters and spacing of the outlet openings along the C-profiles were optimized to ensure a uniform flow in the sensor volume between the two module sides. However, because these openings are relatively small (1.5 cm; discussed in the following chapter), diffusers were added by incorporating small "bridge" structures immediately downstream of each opening to prevent inhomogeneity in inner and outer flows, as shown in figure 5.25. These bridges help diffuse the jet flow exiting the holes in the C-profiles, making the inner and outer helium flows more uniform and, therefore, enhancing sensor cooling effectiveness.

The main points of the decisions made while implementing the module cooling system will be further covered in the following chapter 6. Some additional details can also be found in [33].

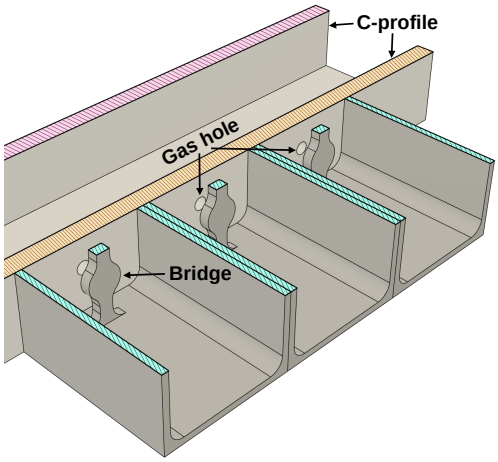

Figure 5.25.: CAD-generated section view of diffusers with the gas channel formed by 2 C-profiles.

5.4. Ladder Vibrations Induced by Channel Gas Flow

Laboratory studies conducted within this thesis include the evaluation of potential ladder vibrations induced by gas flow inside v-fold channels. A test setup, shown in figure 5.26, was assembled. This measurement also aimed to reproduce and compare results with previous vibration measurements conducted for the Mu3e experiment and presented in [126, 127] since the design of the P2 experiment shared the base concept of the ladder design with the Mu3e experiment. In those studies, it was shown that helium flow velocities of up to 20 m/s induce vibrations of ladders prototype below 10 µm. A simple measuring stand, which can be seen in figure 5.26, was assembled. The test bench consists of a dummy ladder heating prototype mounted on a PCB using a secure mounting system, with a gas connection and tensioning mechanism provided by a compression spring, as described previously in this chapter. This setup also included a digital flow meter [133] and a high-precision laser distance sensor with a resolution of $0.7 - 1$ µm and repeat accuracy of ~0.3 µm [134]. The laser sensor was positioned to measure the displacement of the flexprint at its midpoint, where the vibration amplitude was expected to be maximal.

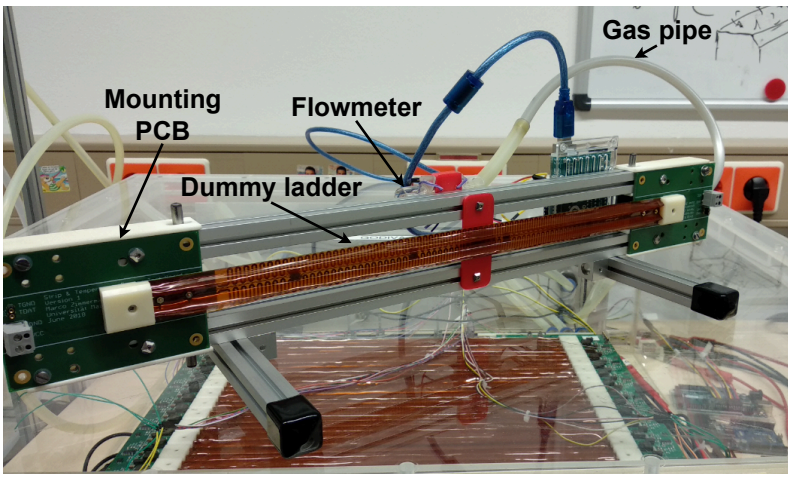

Figure 5.26.: Picture of the test bench for ladder vibration measurements induced by v-fold channel flow along the ladder. The laser distance sensor is not presented.

Due to constraints in the availability of helium gas at the time of measurement, pressurized air was used instead. Therefore, air flow rates were estimated using Computational Fluid Dynamics (CFD) simulations to replicate the conditions of helium flow at 20 m/s. Based on these simulations, the air flow rates corresponding to the target helium velocity for this measurement setup were estimated to be within the range of 13 – 20 slm (standard liters per minute).

Figure 5.27 summarizes the obtained results for the measured vibration amplitude. Based on the simulation results, the recalculated air flow, which corresponds to the helium flow inside the v-folds with an average helium velocity of 20 m/s, is around 13 – 20 slm (standard liter per minute). As can be seen, with applied tension to the ladder ("Spring Tension" data points), even at air flow rates exceeding the above-mentioned estimated range, the observed vibration amplitude remained close to the resolution limit of the laser sensor. However, when no tension was applied to the ladder ("No Tension" data points), the vibration amplitude start exceeding 10 µm at flow rates equivalent to helium velocities of 20 m/s. Measurement accuracy was limited by difficulties in ensuring the gas-tightness of the ladder prototype and the mounting system. Therefore, more measurements were impossible. Also, the tension force created by the compression springs was not measured.

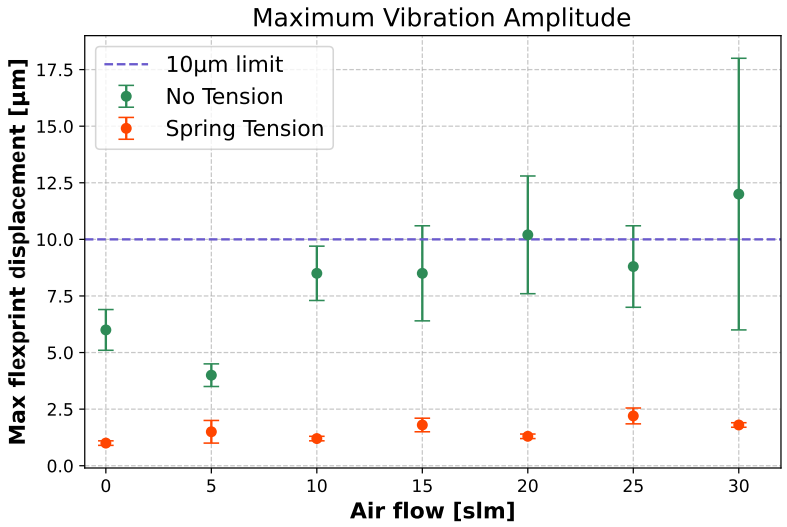

Figure 5.27.: Measured vibration amplitudes induced by v-fold channel gas flow. Data was collected for a horizontally positioned ladder, both with and without applied tension from the compression springs.

The obtained results are consistent with prior Mu3e experiment measurements, confirming that controlled gas flow within v-fold channels induces minimal ladder vibrations when sufficient tension, which prevents an initial ladder sag, is applied. However, further detailed investigations are necessary due to the preliminary nature of this study and limitations in measurement conditions. Future studies should employ a dedicated test stand, conduct measurements under varying tension forces, and use helium to reproduce experimental conditions relevant to actual detector operation more accurately.

5.5. Recent Updates in the Module Design

The tacker module design described in this chapter, used for CFD simulations (discussed in the following chapter), is an updated version of the initial design presented in [33]. Since then, several modifications have been made to the module design. However, these updates fall outside the scope of the work done within this thesis and are only briefly summarized in this section.

Figure 5.28 illustrates the latest version of the inner module design, which is still undergoing refinements. The primary tracker module design updates not covered in this work include:

- Replacement of flex PCBs with rigid end-PCBs for electrical connection via interposers and plastic endblocks for mechanical connection and helium supply. The new design uses flexible PCBs with composite stiffeners on both sides for mechanical support and Flexible Printed Circuits (FPC) connectors instead of interposers;
- A complete revision of the endblock design;
- Consideration of negative inlet gas temperatures of $\gtrsim -20\,^{\circ}\mathrm{C}$ for dehumidified helium gas;
- Optimization of frame-PCB dimensions and layout to accommodate the electronics for sensor power and readout (not shown in figure 5.28);
- Modification of flex PCB dimensions due to the change of binding technology for electrical connections of P2Pix sensors (see section 5.1.3) to flex PCBs. The flexprint is now slightly larger than the actual sensor size (27 mm compared to 23.18 mm) to accommodate additional space for pads and bonding wires;
- Possible removal of v-folds and the corresponding part of the gas supply system is being considered due to additional requirements from bonding technology to the ladder overlap design (section 5.1.3). In this case, sensors can be mounted on the opposite flexprint sides for adjacent ladders for better cooling.

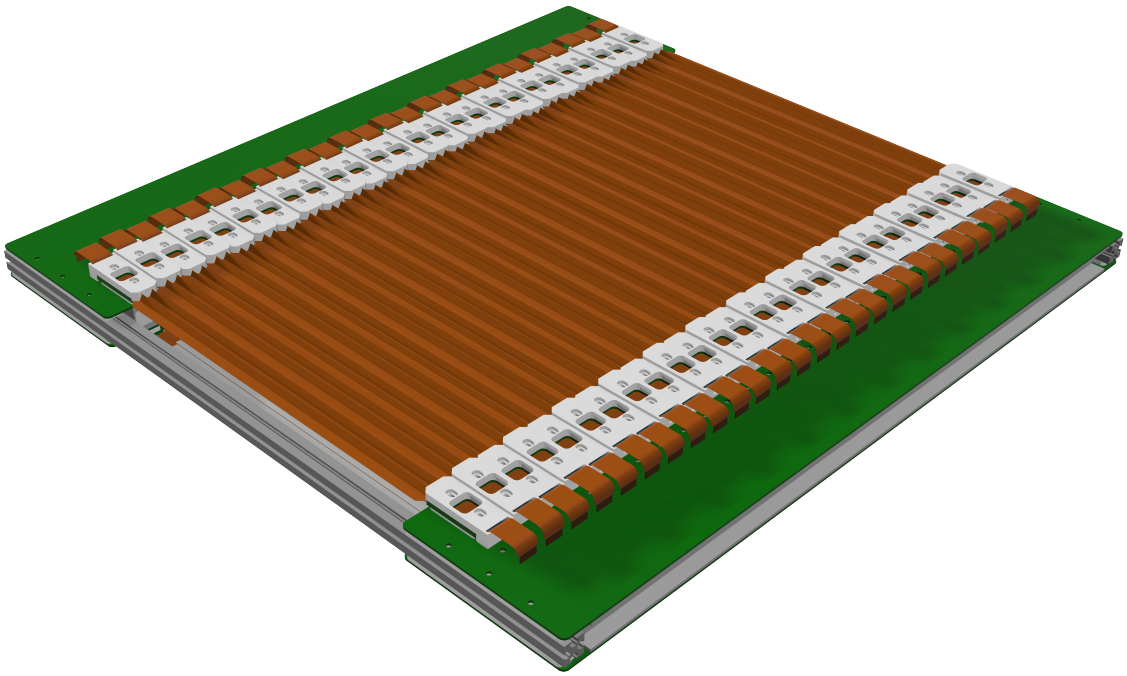

Figure 5.28.: Rendering of the updated design of the module frame.

Also, it is important to note that only recently, the P2Pix sensor thickness was revised to 70 µm from the initially planned 50 µm [5, 33] and used in all CFD simulations presented in this thesis (discussed in the following chapter). This adopts the change of the MuPix11 sensor design [105, 106], driven by increased sensor substrate thickness to avoid physical damage, which was found to be one of the most common sources of sensor failures. Furthermore, in this case, the thicker depletion zone enables a signal increase and, as a result, improves the signal-to-noise ratio.

Despite these significant updates, the overall cooling system concept remains largely unchanged. As a result, the CFD simulation results presented in the next chapter remain relevant for guiding further optimizations and finalizing the tracker module design.

6 Tracker Module Cooling System Studies

As presented in the previous chapter, developing the cooling system for the P2 tracking detector is challenging due to the strict material budget requirements for the modules and the constraints on the coolant option. Section 5.3 introduced the cooling system's concept and design, along with the expected heat level produced by P2Pix sensors. Additionally, the rationale for selecting helium as the coolant was discussed.

This chapter provides a brief theoretical background on fluid dynamics and presents the results of Computational Fluid Dynamics (CFD) simulations of the cooling system for the P2 tracking detector module conducted as a part of this thesis. The simulation method was used to optimize flow distribution within the module, estimate flow and pressure drop for each flow, and the total values throughout the modules and the entire tracker. Additionally, based on the results, the feasibility of the obtained values and the efficiency of the gas supply system can be assessed. The cooling studies conducted within this thesis and the CFD simulation results presented in this chapter refine and build upon the work in [33]. However, the obtained results are intermediate, given the recent updates and refinements in the module design (section 5.5).

All simulations discussed in this section were conducted using Autodesk CFD® software.

6.1. Fluid Dynamics and Heat Transfer

This section outlines the theoretical foundation of fluid dynamics and heat transfer. The structure and content of this section are based on the corresponding section in [33], with additional clarifications on modeling assumptions and practical considerations.

Minimum Helium Flow Rate Estimation. The initial estimate of the required coolant flow rate can be obtained using simplified calculations based on the specific heat capacity of gaseous helium (c_p). Under the assumption of ideal heat transfer—i.e., the entire helium flow is uniformly heated by the maximum allowed temperature difference (ΔT_{max})—the minimum volume flow rate $\dot{V}_{\text{min}}$ needed to maintain steady-state thermal equilibrium is given by

$$\dot{V}_{\text{min}} = \frac{N_{\text{sensor}} A_{\text{sensor}} \phi_q}{c_p \rho \Delta T_{\text{max}}}, \tag{6.1}$$

where:

- N_{sensor} is the total number of sensors to be cooled,
- A_{sensor} denotes the surface area of one sensor,
- ϕ_q represents the heat flux of the silicon pixel sensors,
- ρ is the density of the coolant,
- ΔT_{max} is the maximum temperature difference between the inlet and outlet gas.

The P2 tracking detector module contains 540 sensors, each approximately 20 mm × 23 mm in size. Assuming a maximum operating temperature of 70 °C with the initially planned inlet helium temperature of ~0° [33], the maximum possible temperature rise is $\Delta T_{\max} \approx 70\,^{\circ}\mathrm{C}$.

Table 6.1 summarizes the total estimated heat dissipation $\dot{Q}$ and the corresponding helium volumetric flow rate $\dot{V}$ for maintaining steady-state thermal equilibrium under different assumptions for sensor power dissipation. The values calculated in table 6.1 align well with the estimated

Sensor ϕ_q [mW/cm^2]	Tracker Module		Full Tracker	
	$\dot{Q}$ [W]	$\dot{V}$ [L/s]	$\dot{Q}$ [kW]	$\dot{V}$ [L/s]
200	496.8	7.66	1.99	30.63
250	621.0	9.57	2.48	38.28
300	745.2	11.5	2.98	45.94
350	869.4	13.4	3.48	53.60

Table 6.1.: Estimated total heat dissipation $\dot{Q}$ and the lower bound on the helium volume flow rate $\dot{V}$ for various sensor power dissipation levels. In the calculations, $\Delta T = 70\,^{\circ}\mathrm{C}$ and a helium density $\rho = 0.1785\,\mathrm{kg/m^3}$ at 0 °C are assumed. The minimum heat flux represents the mean power consumption of the P2Pix sensor (table 4.1). The maximum value of 350 mW/cm^2 represents the maximum allowed on-chip heat load for the pixel detectors, based on MuPix specifications [94, 110]. Results are provided for both a single module and the full four-module tracker.

power consumption of the P2Pix sensors, as discussed in section 4.3 based on their electrical specifications (table 4.1).

Flow and Heat Transfer Analysis. A detailed evaluation of the helium flow's temperature and velocity profiles is necessary for a more precise flow and heat transfer analysis. A set of partial differential equations governs the behavior of the fluids.

First, the continuity equation for incompressible flow, describing the velocity field $\vec{v}$, is given as

$$\nabla \cdot \vec{v} = 0, \tag{6.2}$$

ensuring flow mass conservation. Secondly, the Navier–Stokes equation, which describes the motion of the fluid, is expressed as

$$\rho \left(\frac{\partial \vec{v}}{\partial t} + (\vec{v} \cdot \nabla)\vec{v} \right) = -\nabla p + \mu \, \Delta \vec{v} + \vec{g}, \tag{6.3}$$

where μ is the dynamic viscosity and $\vec{g}$ represents external forces (e.g., gravity). Under steady-state conditions, the time derivative $\frac{\partial \vec{v}}{\partial t}$ vanishes. While gravitational force becomes significant in natural convection scenarios, the Coriolis force can typically be neglected in this context.

Incompressible flow, valid for moderate velocities and forced convection, simplifies the analysis by neglecting density variations. However, when natural convection is substantial, buoyancy effects from temperature-induced density changes become significant. In some contexts, the Mach number, which is defined as

$$M = \frac{u}{c}, \tag{6.4}$$

where u is the local mean flow velocity, and c is the speed of sound in the medium used to estimate whether compressible effects and density variations due to temperature can be expected for the given flow. A flow is considered incompressible with $M < 0.3$ since the density changes are negligible [135].

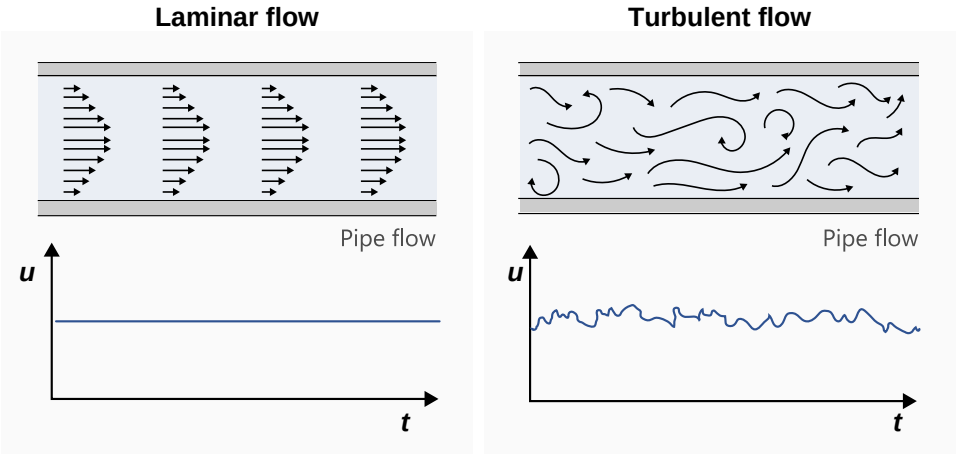

Figure 6.1.: Comparison of laminar and turbulent flow within a pipe, illustrating velocity profiles and local velocity fluctuations over time. Taken from [136] with edits.

Due to the non-linear nature of the Navier–Stokes equation, turbulent behavior may arise within the flow. A practical parameter to determine whether turbulence should be considered is the Reynolds number, defined by

$$\mathrm{Re} = \frac{u\,L}{\nu}, \tag{6.5}$$

where L denotes a characteristic length scale of the flow geometry (diameter in the pipe case), and ν represents the kinematic viscosity. In a turbulent regime, the flow velocity profile is not uniform, and local flow velocities are not constant, as illustrated in figure 6.1, leading to chaotic velocity fluctuations. Therefore, this flow regime is undesirable within the gas supply systems because it can induce mechanical vibrations within the gas supply systems. A flow remains laminar below a critical Reynolds number $\mathrm{Re}_{\mathrm{crit}}$, the exact value of which depends on the specific geometry. Generally, flow in pipes is considered in a laminar regime for $\mathrm{Re} \lesssim 2000$ [131].

Neglecting viscous heating, the energy equation for an incompressible fluid, expressed in terms of the static temperature T, is given by

$$\rho\, c_p \left(\frac{\partial T}{\partial t} + \vec{v} \cdot \nabla T \right) = \nabla \cdot (k\, \nabla T) + q_V, \tag{6.6}$$

where k is the thermal conductivity, and q_V represents any volumetric heat source. In steady-state conditions, $\partial T / \partial t = 0$. Combined together, eqs. 6.2, 6.3 and 6.6 involve five unknowns: the three spatial components of $\vec{v}$, the pressure p, and the temperature T.

Analytical Solutions. Computational Fluid Dynamics. Analytical results can be derived in simplified configurations by further approximating the relevant equations. However, analytical solutions are impractical for complex geometries such as the helium cooling channels in the P2 tracker module, and, therefore, the CFD approach becomes necessary.

The typical CFD workflow includes:

- **Model Preparation:** Simplifying the geometry to capture only essential features of the flow domain and the surrounding solid components where heat conduction occurs.
- **Boundary Conditions:** Defining inlet velocities, pressure, and temperature constraints.
- **Meshing:** Discretizing the model geometry into a finite element mesh.

- **Physical Modeling:** Specifying relevant simulation parameters, including compressibility, radiation, and gravitational effects.
- **Iterative Simulation:** Perform iterative simulations until convergence is achieved for the velocity, pressure, and temperature fields.

Due to discretization limitations imposed by computational resources, CFD simulations include inherent uncertainties. In practice, several factors can affect the accuracy of CFD simulation results:

- **Mesh Quality and Convergence:** Finer meshes improve accuracy but at higher computational costs.
- **Turbulence Modeling:** While simplified turbulence models often suffice, advanced approaches may be considered for detailed analyses.
- **Boundary Conditions:** It is crucial to represent inlet/outlet conditions and heat sources accurately.
- **Experimental Validation:** CFD results should be validated against experimental measurements and studies. For instance, the results of CFD simulation made for the Mu3e experiment were validated with recent cooling studies using a mock-up that matches the Mu3e detector's materials and dimensions, demonstrating good agreement with experimental measurements [110, 137].

6.2. Optimization of Gas Distribution System

This section provides a brief overview of the initial optimization of the gas distribution system within the tracker module, as detailed in [33].

The most critical part of the gas distribution system within the tracker module is represented by channel flows inside the v-folds because of their small cross-section (figure 6.2). According to the test results reported in [126, 127], velocities in the v-folds should remain below 20 m/s to limit strip vibrations to an average amplitude of ~10 µm.

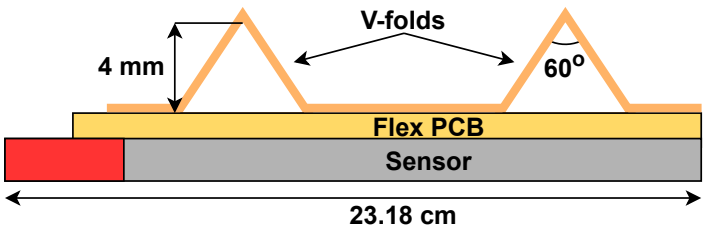

Figure 6.2.: Section view of the ladder. Not to scale.

The main task in developing the helium distribution system for the channel flow is to provide uniform flow rates across all flows. In particular, each v-fold channel should receive a similar share of the total channel flow, ensuring even cooling performance. To accomplish this, the inlet hole diameters in the C-profile and frame-PCB were chosen to balance flow among all outlets along the frame side, thereby guiding the helium uniformly to the cooling volume.

Figure 6.3 illustrates the simulated results of the dependence of volume flow through outlets along a pipe on the hole diameter. The example shows a rectangular pipe with a cross section of 8 mm × 8 mm and 29 holes spaced at 20 mm. As the figure shows, adjusting the outlet diameter

can yield an almost uniform flow rate from each opening. In the same way, the diameter of flow openings in the frame PCBs for channel flow was optimized.

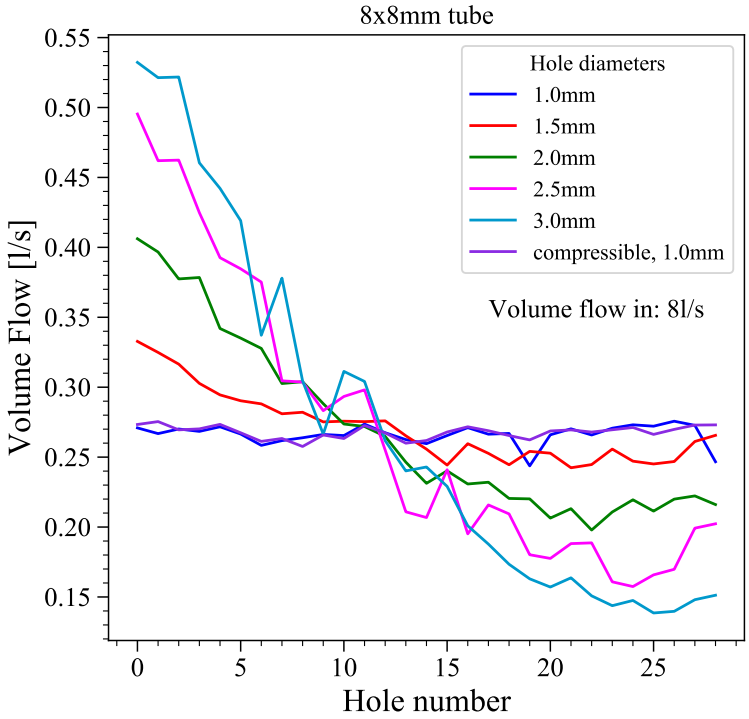

Figure 6.3.: Helium flow through openings in a gas channel depending on the hole diameter. A pipe with a rectangular cross section of 8 mm × 8 mm with 29 holes spaced by 20 mm was simulated. Taken from [33].

In the case of inner and outer flows, the module volume with ladders is not separated. Therefore, the helium velocity along the strips should be rather uniformly distributed. In this case, helium enters the volume with ladders through diffuser sections placed directly behind the inlet holes along C-profiles (figure 5.25). After leaving the opening, the helium may form a narrow jet flow, resulting in high local velocities and potentially uneven cooling. To mitigate this, a bridge—an internal obstacle—was added to each diffuser (figure 5.25). This component helps spread the helium flow laterally before it enters volume with ladders, thus improving cooling efficiency, especially for the sensors closest to the diffusers, the maximum local velocity, and the risk of chaotic flow near the ladders. Figure 6.4 compares simulations of the diffuser outlets with and without bridges. In both cases, the total helium flow is the same (6 L/s), but, as can be seen, bridges noticeably decrease the strong directional component of the flow.

Once helium exits the diffuser, it spreads into the volume containing the ladders. Figure 6.5 shows a top view of the x-component of the velocity field at the midplane between the two tracker planes. The flow from neighboring diffusers merges and slows rapidly, resulting in more uniform velocities across the plane. This uniformity is essential for ensuring even cooling of all sensors and minimizing vibration effects on the ladders induced by inner and outer flows.

More details on the implemented flow optimizations within the module can be found in [33].

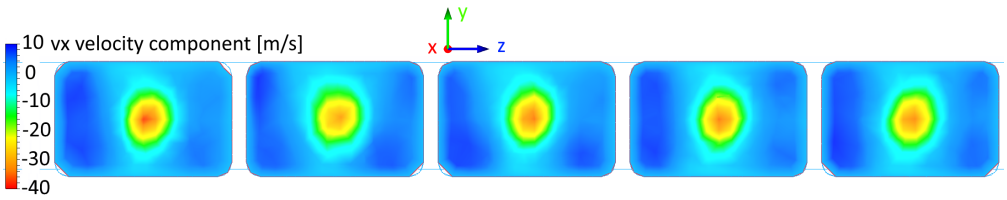

(a) Simulation without bridges in the diffuser part.

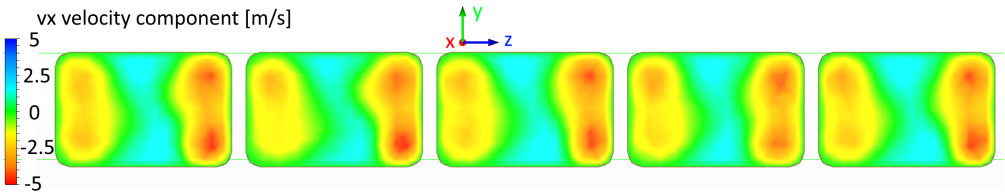

(b) Simulation with complete diffuser part.

Figure 6.4.: Comparison of diffuser outlet flow for the inner flow, each with a total helium flow of 6 L/s. In (a), the bridge is absent, allowing a more narrowly directed jet; in (b), the full diffuser design reduces the flow velocity immediately after the opening. Negative velocities indicate helium exiting the diffuser region. The helium flow in the distributing channel is in the positive z-direction. Taken from [33]

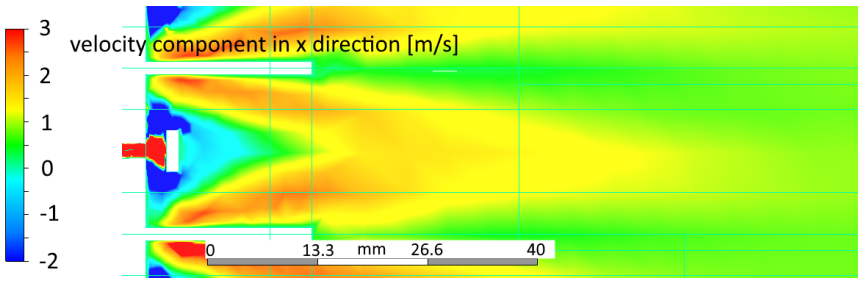

Figure 6.5.: Profile of the velocity x-component in the midplane between the tracker planes downstream of the diffuser outlets. The color scale covers the velocity range outside the diffuser chamber; the color scale does not fully cover some higher velocities within the diffuser. Taken from [33].

6.3. CFD Simulation

6.3.1. Simulation Setup

P2Pix sensor thickness. Helium gas temperature. Due to recent updates in the module design listed in section 5.5, a few remarks should be made.

First, all CFD simulations presented here were conducted assuming a sensor thickness of 50 µm, as this was the intended value at the time of the simulations. However, the heat generated by the sensor was set based on the volumetric heat generation rate, calculated for a given heat flux, which does not depend on sensor size, for each considered simulation scenario (see table 6.3).

Second, the helium gas temperature was set to 5 °C, planned initially, to avoid issues in the helium distribution system and prevent ice formation on detector components and in actual operation due to residual moisture in the helium. Currently, the possibility of further cooling the sensors by lowering the temperature of dehumidified helium to subzero values ($\gtrsim -20$ °C) is being explored, provided that almost all moisture is removed from the gas.

Simulation model. A simulation input consists of a simplified mechanical model of the tracked module, omitting irrelevant components and features such as screws or connectors or replacing them with simplified geometries. The gas volume is then incorporated into the simulation model, as illustrated in figure 6.6.

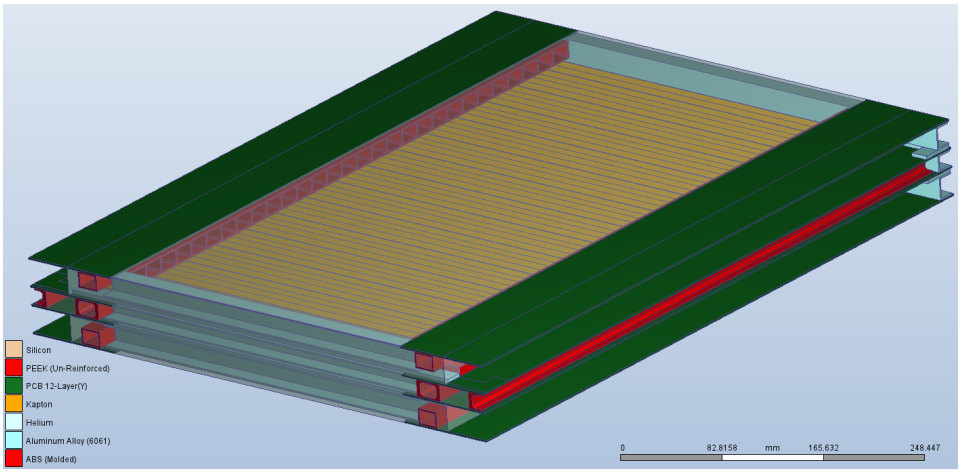

Figure 6.6.: Rendering of the tracker module model used for CFD simulations.

The gas distribution system in each module operates as a closed-flow circuit. The design and optimization of this system are complex due to the varying cross-sectional dimensions of different components, such as pipes, gas connectors, and internal channels, as well as the required flow rates for effective cooling. In all cases, the gas is initially supplied to the module through connectors and channels formed by PCBs and internal partitions.

To further simplify the simulation model and reduce computational time, only critical components involved in heat generation and cooling can be included, as shown in figure 6.7. In this case, the included elements are the P2Pix sensors, flex print, v-folds (limited to regions in direct contact with the sensors), and gas volumes. Since no other components in the system generate heat, their exclusion has a negligible impact on the results. The gas volumes inside flow path parts represent negative copies of the inner volume of these parts, preserving the correct geometry.

Before running the simulation, the appropriate material properties must be assigned to each component, and all initial and boundary conditions must be defined. Next, the model mesh must be reasonably optimized. Once these steps are complete, the simulation parameters can be set, and the simulation can be started. To simulate the worst-case scenario, all heat generated by the sensors is assumed to be transferred entirely to the surrounding gas volume for each heat dissipation level.

Meshing and simulation parameters. Before running the CFD analysis, the simulation geometry is discretized into finite elements, with nodes at each element's corners where calculations are performed. An example of the resulting mesh structure is shown in figure 6.7.

Table 6.2 lists the mesh size and key simulation parameters used for modeling the full tracker module. The results of these simulations are presented further in section 6.3.3.

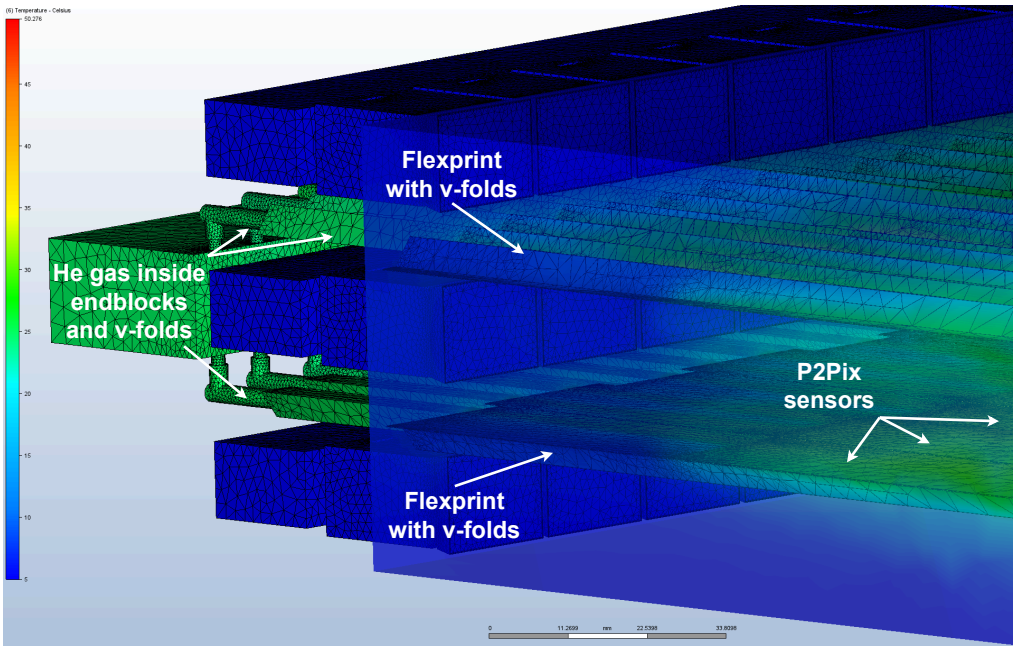

Figure 6.7.: Simplified CFD simulation model, including only critical for simulation components. Volume colors indicate temperature distribution, and surfaces are overlaid with the mesh used for the simulation discretization.

Parameter	Value
Model mesh:	
- Fluid elements	15 293 130
- Fluid nodes	4 687 456
- Solid elements	1 731 357
- Solid nodes	85 619
Physics:	
- Flow	Incompressible
- Heat transfer	Enabled, no radiation
- Turbulence model	k-epsilon

Table 6.2.: Key CFD simulation parameters.

It is important to note that heat transfer was enabled in these simulations, though thermal radiation was excluded due to its high computational cost. For the global temperature differentials below 70 – 80 °C, the effect of radiation is generally negligible [138]. It is important to note that this temperature threshold is a rule of thumb, as the significance of radiative heat transfer also depends on factors such as pipe or channel geometry, flow velocity, pressure drop, and surface emissivity. As demonstrated in [33], simulations that initially consider only forced convection and incorporate thermal radiation at later simulation steps typically show a maximum sensor temperature change of less than 1.5 % toward reducing the temperature values. Given this small effect, thermal radiation was not enabled in this interim module design simulations. Consequently, the presented results provide an approximate estimate of the cooling performance. However, the impact of thermal radiation needs to be evaluated more precisely, and it may be enabled at later design stages for more accurate simulations.

6.3.2. Unequal Heat Dissipation by Sensors

As presented in [33], initial simulation results assumed uniform heat dissipation throughout the sensor volume. However, as discussed in [100, 139], MuPix sensors are expected to dissipate heat unevenly, with up to approximately 50 % of the power being generated in the periphery and the remaining half in the active matrix region. CFD simulations incorporating this non-uniform heat dissipation demonstrated that the increased heat generation in the periphery could lead to local sensor temperature increases of up to 30 °C, particularly in overlapping sensor regions [139]. Although the detectors in P2 and Mu3e experiments have different geometries, these results clearly show that without considering non-uniform heat dissipation by the sensor, the maximum sensor temperature might be significantly underestimated in the simulation. In real operation, such underestimation could result in local sensor overheating. This situation must be excluded since if the sensor's temperature exceeds the 70 °C limit determined by mechanical properties of the adhesive used to mount the sensors onto flex prints (section 5.3), partial delamination or, in the worst case, sensor failure may occur. In both cases, the track reconstruction performance might be seriously affected. Therefore, the simulation model was refined to account for the non-uniform heat generation in P2Pix sensors.

Figure 6.8 shows the chip model used in the CFD simulation, which explicitly incorporates the unequal heat dissipation by different sensor parts.

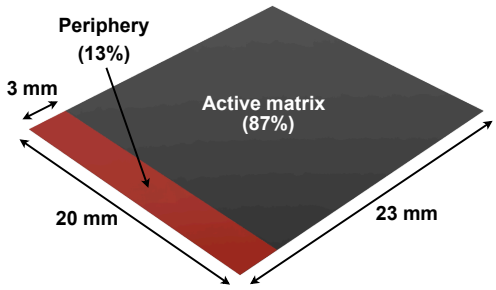

Figure 6.8.: P2Pix sensor model used in the CFD simulations. 50 % of the total dissipated heat is generated in the periphery, which takes ~13 % of the sensor's area.

Based on these estimates, the volumetric heat generation rates for active and periphery sensor regions were computed for different heat flux densities, as summarized in table 6.3.

Notably, under the given heat dissipation assumptions for the sensor and the size of its periphery region, the volumetric heat generation in the periphery part is approximately 8.7 times higher than in the active part. These volumetric values were used as boundary conditions for all CFD simulations presented in this section.

Heat flux, mW/cm^2	**Volumetric heat generation rate,** W/cm^3		
	Total*	**Active area (87%)**	**Periphery area* (13%)**
400	80	40	346
350	70	35	304
250	50	25	217
200	40	20	174

*The periphery area contributes up to 50 % of the total heat dissipation.

Table 6.3.: Comparison of P2Pix sensor heat fluxes and corresponding volumetric heat generation rates, distinguishing between active and periphery sensor parts.

Figure 6.9 shows the effect of non-uniform heat dissipation by P2Pix sensors for the initial module design presented in [33]. The design consists of 29 ladders with an increased number of sensors. To reproduce a high-power scenario, as defined in [33], the following simulation parameters were applied:

- Total sensors heat flux of 400 mW/cm^2. For the non-uniform heat dissipation case, the corresponding volumetric values from table 6.3 were used;
- Inlet helium temperature of 5 °C. The flow rates were chosen to have helium average velocity of 17.2 m/s in v-folds and 0.5 m/s in inner and outer flows.

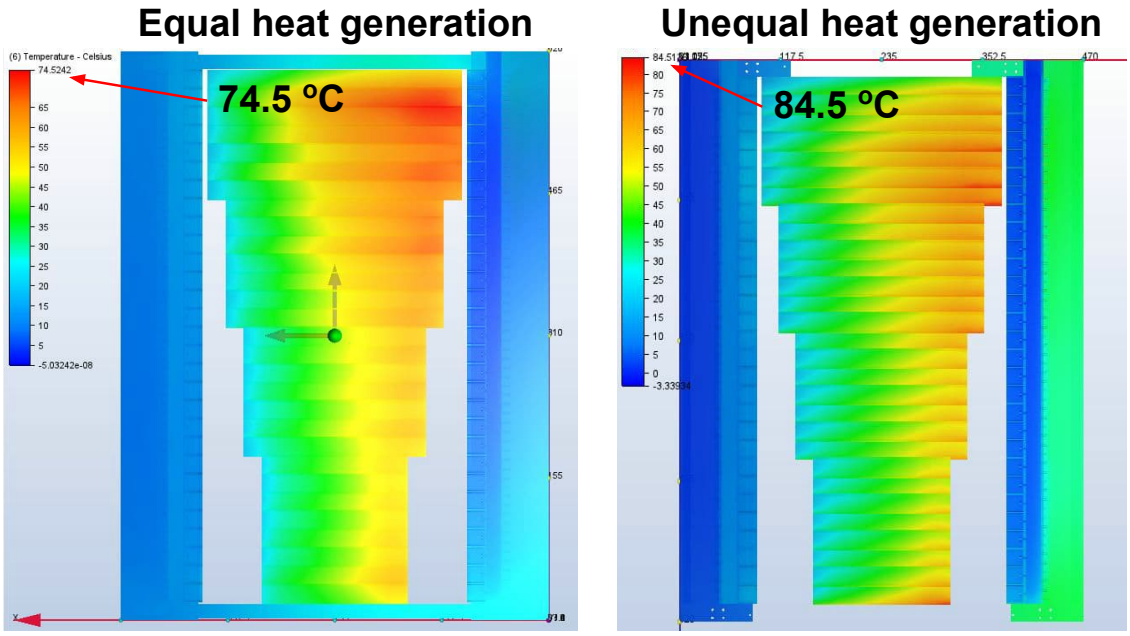

Figure 6.9.: Comparison of simulated temperature distributions in the complete module with the design used in [33], illustrating the difference between uniform and non-uniform heat generation in sensors. Note: temperature ranges differ between distributions.

While the average sensor temperature remains nearly unchanged, the non-uniform heat dissipation leads to a significant local increase in maximum temperature in the sensor's periphery regions by up to 10 °C. This result demonstrates the importance of incorporating non-uniform heat generation of P2Pix sensors in CFD simulations to avoid underestimating the sensors' maximum temperature and potential overheating.

6.3.3. Simulation Results for the Complete Tracker Module

As already mentioned in section 5.3, based on the recent refinement of power consumption estimates for MuPix11 sensors and projections for P2Pix sensors, two primary power consumption scenarios are considered: the moderate scenario and the high-power scenario, corresponding to heat fluxes of 200 mW/cm^2 and 250 mW/cm^2, respectively. Flow rates were initially optimized in this series of simulations to ensure a laminar and incompressible regime in all channels. Furthermore, the thermal design requirements were extended to maintain the temperature below the specified limit of 70 °C, even under the maximum allowed on-chip heat load of 350 mW/cm^2 specified for MuPix sensors, representing the *worst case power scenario*. This additional requirement maximally ensures a sufficient initial safety margin against overheating since it exceeds the moderate power scenario by 75 % in dissipated heat.

Thermal Results. Figure 6.10 presents the temperature distribution results for different heat dissipation scenarios within the range mentioned above under the following *base flow configuration*:

- Channel flow: 15 L/s;
- Inner and outer flows: 8.5 L/s each.

These flows satisfy the stated thermal constraints, preventing overheating even in the worst-case scenario.

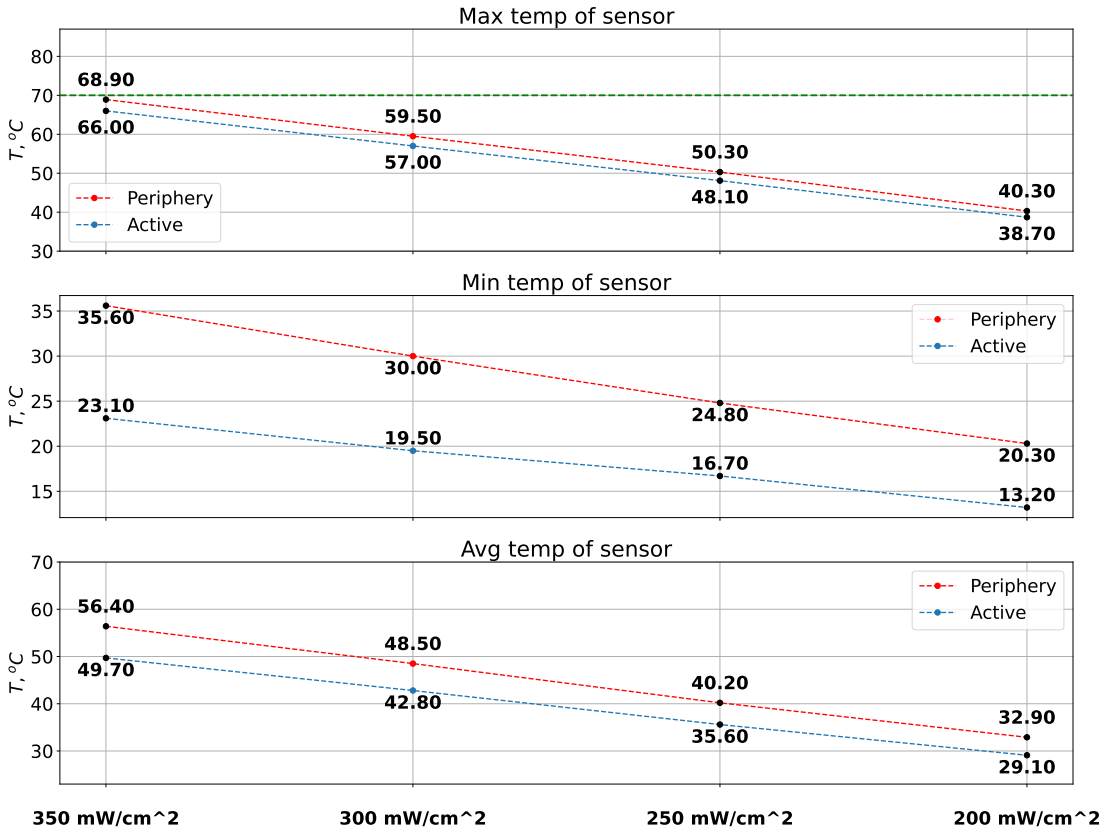

Figure 6.10.: Maximum, average, and minimum temperatures of sensors along the ladders for different power generation scenarios **under the same base flow configuration**. The y-axis represents different levels of heat generation (non-uniform) by sensors, from the expected level of 200 $\mathrm{mW/cm^2}$ (moderate power scenario) up to the maximum allowed on-chip heat load for the pixel detectors of 350 $\mathrm{mW/cm^2}$.

The observed linear dependence between heat dissipation and chip temperature from the above results is consistent with the results from the Mu3e experiment, where similar dependencies were also found in simulations and studies [110, 137, 139]. This allows temperature profiles to be estimated for lower or higher sensor powering scenarios if needed.

Figure 6.11 demonstrates the temperature distribution within the tracking detector module for the high-power scenario under the base flow configuration. As expected, the maximum sensor temperature has a clear safety margin, allowing further flow optimization.

The considerable safety margin of nearly 30 °C in the moderate power scenario with the base flow configuration indicates the potential for reducing flow rates. Table 6.4 summarizes the thermal results for the primary sensor power scenarios, with a refined configuration for the moderate power scenario to almost match the performance of the high-power scenario.

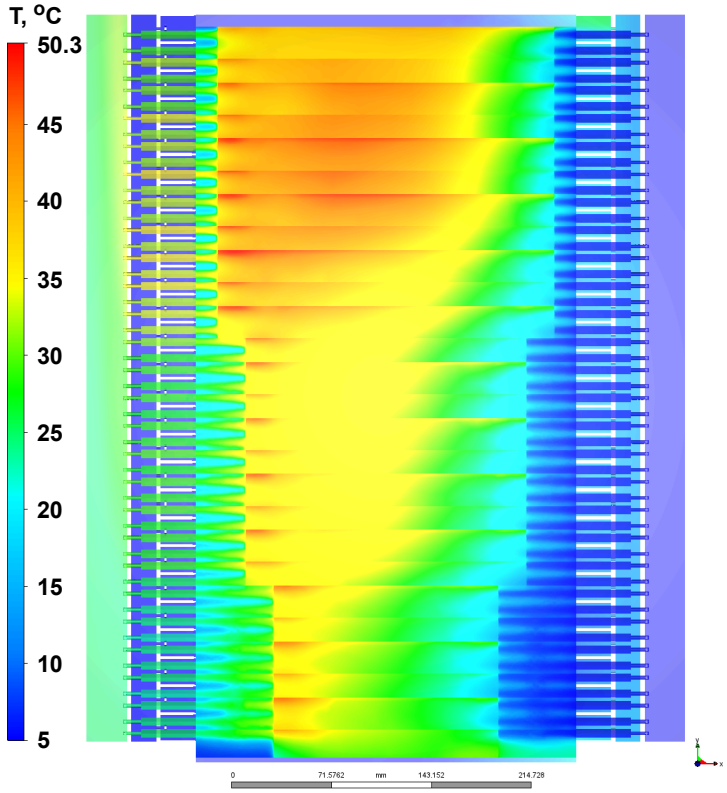

Figure 6.11.: Temperature distribution within the tracking detector module for high-power scenario (250 $\mathrm{mW/cm^2}$) under the base flow configuration. For visibility, the tracker module is sectioned in the xz-plane, showing the sensors of one tracker plane. The inner and outer flows are directed in the positive x-direction (from the left to the right), and the channel flow is directed in the negative x-direction.

	moderate power scenario	**high power scenario**
Sensor heat load [$\mathrm{mW/cm^2}$]	200	250
Total generated heat [W]	496.8	621.0
Flow configuration:		
- channel flow [L/s]	10	15
- inner flow [L/s]	6	8.5
- outer flows [L/s]	2×6	2×8.5
Inlet helium temperature [°C]	**5**	
Maximum sensor temperature [°C]	**54.9**	**50.3**

Table 6.4.: Summary table of thermal results for different scenarios of heat generated by P2Pix **under different flow configurations**.

A temperature gradient exceeding 20 °C can be observed along the ladder sides, even in the moderate power scenario. Despite the demonstrated operational stability of HV-MAPS technology within a temperature range of −20 °C to 80 °C, as mentioned in section 5.3, this temperature difference for sensors at both sides of the ladders must be considered in further cooling system optimization. Specifically, in the case of removing the v-fold channel flow, a configuration featuring opposing inner and outer flows might be considered to mitigate this temperature gradient.

Flows and Pressure Drop. Table 6.5 provides detailed parameters for different flows within the tracking detector cooling system for primary P2Pix powering scenarios.

	moderate power scenario	**high power scenario**
Sensor heat load [mW/cm^2]	200	250
Mass (Volumetric) flow rates [g/s] ([L/s]):		
- channel flow	1.7 (10)	2.6 (15)
- inner flow	1.1 (6)	1.5 (8.5)
- outer flows	2×1.1 (6)	2×1.5 (8.5)
Total mass (volumetric) flow per module [L/s] ([g/s])	5 (28)	7.1 (40.5)
Pressure drop* [mbar]:		
- channel flow	15	30
- inner and outer flows (per flow)	28	53
Mass (Volumetric) flow per v-fold [g/s] ([L/s])	0.016 (0.10)	0.025 (0.14)
Average He velocity [m/s]:		
- inside v-folds	~15	~18
- within the volume with sensors	~1.3	~2
Reynolds number:		
- inside v-folds	~300-600	~450–1000
- within the volume with sensors	$\lesssim$30	$\lesssim$50
Mach number:		
- inside v-folds	~0.015	~0.019
- within the volume with sensors	~0.001	~0.002

*A pressure boundary condition of 0 bar was applied at all flow outlets.

Table 6.5.: Parameters of flows of the sensors scenarios **with different flow configurations**.

For the helium flow rates considered in the P2 tracking detector cooling simulations, the Reynolds numbers remain below the critical threshold ($R_{\text{crit}} \sim 2000$), ensuring laminar flow, particularly in the v-folds. Furthermore, Mach number analysis confirms that all flows remain in the subsonic and incompressible regime. Consequently, the main cooling system design requirements are satisfied.

Based on specifications of commercially available compressors [100, 110, 137], helium supply to the module can be efficiently managed using available gas-bearing radial turbo-compressors. Table 6.6 lists the relevant specifications.

	Celeroton CT-NG-2000
Type	Miniature turbo-compressor
Maximum mass flow [g/s]	18.5
Maximum pressure ratio	1.17
Pressure drop [mbar]	up to ~100

Table 6.6.: Characteristics of possible options for compressors for supplying helium to the tracker module helium at the inlet of the compressor with $T = 20\,^{\circ}\text{C}$ and absolute pressure $p_{in} = 1.013\,\text{bar}$ [100, 110, 137, 140].

As can be seen after comparing the specifications of this compressor with flow parameters in table 6.5, a combination of 2 Celeroton compressors per module will allow sufficient helium

supply for both moderate and high-power scenarios: 1 compressor for channel flows and 1 for inner and outer flows combined.

6.4. Conclusions and Outlook on the Tracker Module Cooling System

The obtained CFD simulation results confirm that the current cooling system design ensures effective cooling of the P2Pix sensors, even under the high-power scenario with a heat flux of 250 mW/cm^2 and an inlet helium temperature of 5°. A substantial safety margin of approximately 20 °C in maximum sensor temperature for all sensor powering scenarios demonstrates the robustness of the cooling approach.

These studies represent a preliminary evaluation of the interim updated module design. Given the available thermal safety margin, there is potential for further optimization of the cooling system while maintaining sufficient helium flow rates within the limits of commercially available turbo-compressors. Key areas for future studies and design refinement include:

- Further flow optimization to reduce helium consumption while maintaining efficient heat dissipation.
- Simulations incorporating actual pixel sizes and negative inlet helium temperatures, considering dehumidified helium as an option for further reducing flow requirements.
- Additional simulations for assessment of v-fold removal, potentially simplifying the gas distribution system.
- Optimization of the gas distribution system, particularly for outer flows, with a possible unification of components with the inner flow system.
- Experimental validation of outer flows using prototype modules to refine the cooling performance under realistic conditions.
- Additional experimental evaluation of cooling efficiency and mechanical stability, including vibration measurements with updated prototypes.
- Validation of CFD results through direct comparison with real measurement data to refine modeling accuracy.

These steps will ensure the final cooling system configuration is efficient and mechanically stable while minimizing helium flows. The upcoming experimental phase with updated prototypes will provide critical insights into the system's final implementation and operational performance. Since this study is limited to the cooling system within the tracker modules, the complete design of a global closed-loop helium distribution system, including a heat exchanger, should follow next.

Part III.

A Møller Polarimeter for the P2 Experiment

7 Electron Beam Polarimetry

Polarized electron beams play a crucial role in high-energy particle physics, enabling tests of the Standard Model and searches for New Physics. Unfortunately, due to engineering and physics constraints, it is not possible to produce 100% polarized electrons. As discussed in section 3.3, the degradation of the source photocathodes can introduce errors associated with relative change of the beam polarization, making them the leading contribution to the total experiment systematic error budget. Therefore, a precise polarimetry technique is essential for monitoring and correcting polarization changes throughout the experiment to fully exploit a highly polarized electron beam.

7.1. Polarimetry Principles and Techniques

Fundamentally, electron beam polarization can be determined by measuring the asymmetry in a scattering process (*not to be confused with parity-violating asymmetry measured in the P2 setup*). The asymmetry, in turn, is characterized by the analyzing power - a degree to which the measured cross-section changes due to variations in the polarization of the beam or target, with the electrons initially polarized along the same direction. Therefore, it is often called the *double-spin asymmetry*. Table 7.1 shows and summarizes a comparison of the existing polarimetry techniques.

Scattering process	Physics	Pros	Cons
Mott	$\vec{e^-} + Z \rightarrow e^- + Z$	Rapid, precise	Beam destructive, suitable for lower energies ($\lesssim$1 MeV)
Laser-Compton	$\vec{\gamma} + \vec{e^-} \rightarrow \gamma + e^-$	Non-destructive	Suitable for higher energies ($\geq$1 GeV)
Møller	$\vec{e^-} + \vec{e^-} \rightarrow e^- + e^-$	Rapid, precise; analyzing power is energy-independent*	Beam destructive (but: **concept of a low-density gaseous H target**)

*In the limit of relatively high energies of $\geq$100 MeV.

Table 7.1.: Comparison of the available/existing polarimetry techniques.

The first common technique is based on electron-nucleus or Mott scattering (covered in section 2.7.1). Mott polarimetry relies on the polarization-dependent asymmetry due to the spin-orbit coupling in a polarized electron beam interacting with the thin unpolarized target made of high-Z material (like gold, platinum, lead, etc.). Despite being rapid and relatively precise, it is a beam-destructive technique due to the use of a solid target. More importantly, it is primarily used for energies below 1 MeV, where the spin-orbit interaction dominates, and the analyzing power is significant. Although the cross-section remains large at higher energies, the spin-orbit asymmetry decreases, making Mott polarimetry impractical. Therefore, this technique

is primarily used to measure polarization before injecting electrons into the main accelerator [141] and is typically combined with other methods, as in the polarimetry chain at MESA (section 3.2).

In the case of laser-Compton polarimetry, the beam polarization is measured via/through the asymmetry induced when circularly polarized photons from a laser (typically in the visible or infrared range) collide with polarized electrons in the beam, undergoing Compton scattering. This is a non-destructive technique. However, it yields a very low rate of backward-scattered photons, the typical detection signal. In contrast to the previous technique, this method is suitable for higher energies, typically above 1 GeV, where sufficient interaction rates, acceptable measurement precision, and larger, more sensitive asymmetries are achievable.

The last technique of measuring high-energy electron polarization is based on Møller scattering polarized electrons on a magnetized thin ferromagnetic foil target, typically made of iron or iron-based alloys. Table 7.2 provides an overview of past Møller polarimetry measurements. As can be seen, it is an established technique with possible sub-percent accuracy. For the Møller scattering, in the limit of relatively high energies of ≥100 MeV, the analyzing power is energy-independent and can be determined with high precision (figure 7.2). On top of that, the signature of the signal event is represented by two electrons, allowing background suppression using coincidence detection. Conventionally, Møller polarimeters use solid targets, making this technique beam-destructive. However, there is a concept of using a low-density gaseous atomic hydrogen target [142] (discussed in section 8.1), which is almost transparent for the incident beam, therefore allowing the online measurements and thereby meeting all the requirements of the P2 experiment.

Year	Facility	E_{beam}	Source of limitations*	Coinc. scheme	$\Delta P/P$
1975	SLAC [143]	19.4 GeV	foil/stat/BG	✗	4%
1982	SLAC (E130) [144]	22.7 GeV	foil/stat	✓	4%
1984	Bonn [145]	2.0 GeV	stat	✓	12%
1990	MAMI [146]	185 MeV	foil/BG	✓	4%
1995	SLAC (E143) [147]	29 GeV	foil	✓	2%
2001	JLAB Hall C [148]	1 − 6 GeV	foil	✓	≲1%
2012	JLAB Hall A (Qweak) [149]	1.165 GeV	stat/BG	✓	~0.6%
2019	JLAB Hall A (CREX) [150]	2 − 11 GeV	foil	✓	0.85%

*"foil" = target polarization; "stat" = statistics; "BG" = background.

Table 7.2.: Examples of previous polarization measurements made using Møller polarimeters with thin metal foil targets (adopted and extended from [141]).

7.2. Møller Polarimetry

Møller polarimetry is based on the spin-dependent elastic electron-electron scattering process named after the Danish physicist Christian Møller (1932) [151]. A significant advantage is that

Møller scattering has a larger cross-section and asymmetry than, for example, Compton scattering, particularly at high energies, making it well-suited for precise polarization measurements.

7.2.1. Møller Scattering

In general, the differential cross-section of Møller scattering in the center-of-mass (CM) frame is given by [152]

$$\frac{d\sigma_{\text{Møller}}}{d\Omega} = \frac{d\sigma_0}{d\Omega}\left(1 - \sum_{i,j=x,y,z} P^i_{beam} A_{ij} P^j_{\text{target}}\right), \tag{7.1}$$

where $\frac{d\sigma_0}{d\Omega}$ is the unpolarized differential cross-section, P^i_{beam} and P^j_{target} are the components of the beam and target polatization, A_{ij} are the analizing power components.

The unpolarized differential cross-section depends on the scattering angle in the CM frame θ_{CM} but is independent of the azimuthal angle ϕ_{CM}. In the ultrarelativistic limit (where the Lorentz factor $\gamma \gg 1$) is can be approximated as [152, 153]

$$\frac{d\sigma_0}{d\Omega} \approx \left(\frac{\alpha(3 + \cos^2\theta_{\text{CM}})}{\sqrt{s}\sin^2\theta_{\text{CM}}}\right)^2, \tag{7.2}$$

where α is the fine structure constant, $\sqrt{s} = E_{\text{CM}}$ is the center-of-mass energy, representing the total available energy in the system.

In the P2 experiment case, $\sqrt{s} \approx \sqrt{2E_{beam}m_e} \approx 12.6\,\text{MeV}$ ($E_{beam} = 155\,\text{MeV}$) is much lower than the mass of the Z^0 boson (≈91 GeV). Consequently, direct Z boson exchange contribution (figure 7.1b) is strongly suppressed due to the low center-of-mass energy. At this energy, the scattering process is dominated by electromagnetic interactions, mediated by photon exchange via the lowest-order t- and u-channel diagrams (figure 7.1a).

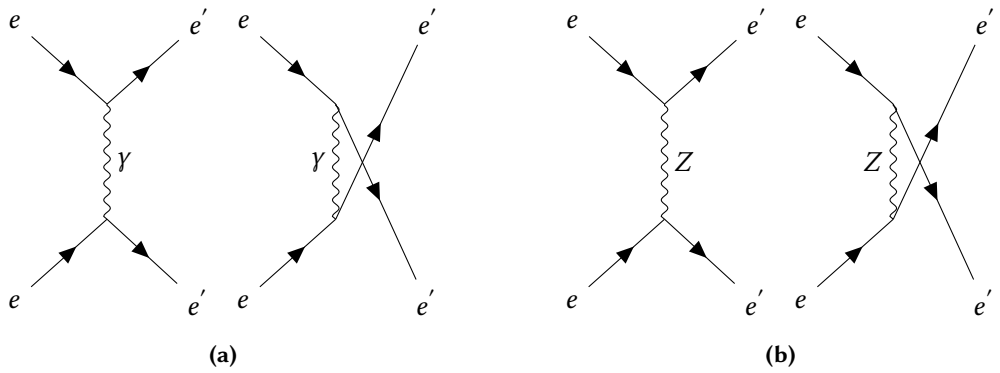

Figure 7.1.: Feynman diagrams for Møller scattering with photon (a) and Z boson (b) exchange at tree level (reproduced and adapted from [154]).

The initial electrons can have two spin configurations: parallel and anti-parallel to the direction of the beam. In the case of the anti-parallel spin configuration, the scattered spins also remain anti-parallel. According to Fermi-Dirac statistics, this spin state includes an additional negative phase between the two possible orientations of the outgoing spins. This causes the amplitudes to combine, resulting in a larger cross-section for the anti-parallel spin configuration. This cross-section difference between parallel and anti-parallel spin configurations generates a non-zero asymmetry in Møller scattering.

In the coordinate system where the z-axis coincides with the direction of the beam, the x-axis is perpendicular to the scattering plane, and $\vec{y} = [\vec{x} \times \vec{z}]$, the analyzing power components can be expressed (following the [152] with some modifications) as

$$A_{xx} = \tau(\gamma, \theta_{\mathrm{CM}}) \left[4\gamma + (\gamma - 1)(\gamma + 3) \sin^2 \theta_{\mathrm{CM}}\right] \tag{7.3a}$$
$$A_{yy} = \tau(\gamma, \theta_{\mathrm{CM}}) \left[4\gamma(2\gamma - 1) - (\gamma - 1)^2 \sin^2 \theta_{\mathrm{CM}}\right] \tag{7.3b}$$
$$A_{zz} = \tau(\gamma, \theta_{\mathrm{CM}}) \left[4\gamma(2\gamma - 1) - (\gamma - 1)(\gamma + 3) \sin^2 \theta_{\mathrm{CM}}\right] \tag{7.3c}$$
$$A_{xz} = A_{zx} = \tau(\gamma, \theta_{\mathrm{CM}}) \, (\gamma - 1)\sqrt{2(\gamma + 1)} \sin 2\theta_{\mathrm{CM}} \tag{7.3d}$$
$$A_{xy} = A_{yx} = A_{yz} = A_{zy} = 0\,, \tag{7.3e}$$

where

$$\tau(\gamma, \theta_{\mathrm{CM}}) = \frac{\sin^2 \theta_{\mathrm{CM}}}{4\gamma^2(1 + 3\cos^2 \theta_{\mathrm{CM}}) + (\gamma - 1)^2(4 + \sin^2 \theta_{\mathrm{CM}}) \sin^2 \theta_{\mathrm{CM}}}\,. \tag{7.3f}$$

In the ultrarelativistic limit ($\gamma \gg 1$), terms of order γ^2 become dominant over the lower order terms, therefore eqs. 7.3 can be approximated as [152]

$$A_{xx} \approx -A_{yy} = \tau(\gamma, \theta_{\mathrm{CM}}) \, \gamma^2 \sin^2 \theta_{\mathrm{CM}} \tag{7.4a}$$
$$A_{zz} \approx \tau(\gamma, \theta_{\mathrm{CM}}) \, \gamma^2 (7 + \cos^2 \theta_{\mathrm{CM}}) \tag{7.4b}$$
$$A_{xz} \approx A_{zx} = \tau(\gamma, \theta_{\mathrm{CM}}) \, 2\gamma \sin \theta_{\mathrm{CM}} \cos \theta_{\mathrm{CM}} \tag{7.4c}$$
$$A_{xy} \approx A_{yx} = A_{yz} = A_{zy} = 0\,, \tag{7.4d}$$

with

$$\tau(\gamma, \theta_{\mathrm{CM}}) \approx \frac{\sin^2 \theta_{\mathrm{CM}}}{\gamma^2 (3 + \cos^2 \theta_{\mathrm{CM}})^2}\,. \tag{7.4e}$$

In this high-energy region, the transverse component of the polarization is suppressed by the Lorentz factor $1/\gamma$ [155], while relativistic effects do not diminish longitudinal polarization. In addition, from the analysis of eqs. 7.4, it can be seen that in the case of perfectly symmetric Møller scattering when $\theta_{\mathrm{CM}} = 90^\circ$ the longitudinal (A_{zz}) and transverse (A_{xx} and A_{yy}) components of analyzing power have maximum absolute values (figure 7.2). However, the latter is a factor of 7 lower. Considering all this, the beam and target are typically polarized longitudinally in experiments with polarized electrons for more reliable measurements. Consequently, only one relevant asymmetry term A_{zz} remains in the cross-section (initially given by eq. 7.1):

$$\frac{d\sigma_{\mathrm{Møller}}}{d\Omega} \approx \frac{d\sigma_0}{d\Omega}\Big(1 - P_{beam} P_{\mathrm{target}} A_{zz}(\theta_{\mathrm{CM}})\Big)\,, \tag{7.5}$$

where in this case P_{beam}, P_{target} are the beam and target longitudinal polarization respectively.

It is important to note that the analyzing power A_{zz}, which can be finally expressed as

$$A_{zz}(\theta) = sin^2(\theta)(7 + cos^2(\theta))/(3 + cos^2(\theta))^2, \tag{7.6}$$

is independent of the beam energy, which is an important advantage of Møller polarimeters.

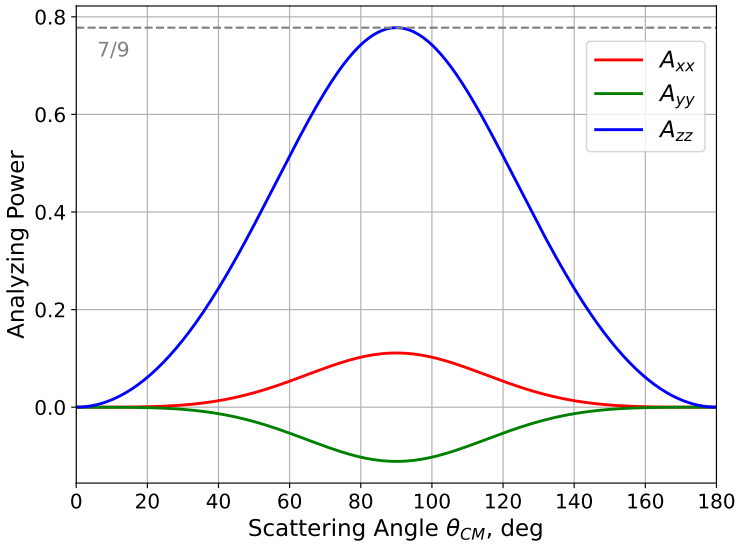

Figure 7.2.: Longitudinal and transverse components of the analyzing power in the case of Møller scattering given by eqs. 7.4a and 7.4b.

7.2.2. Møller Asymmetry Measurement

The arising asymmetry can be effectively determined by comparing the cross-section asymmetry measured in the experiment for the beam and target spins aligned parallel and anti-parallel:

$$A_{\text{Møller}} := A_{\text{exp}} = \frac{\sigma_{\uparrow\uparrow} - \sigma_{\uparrow\downarrow}}{\sigma_{\uparrow\uparrow} + \sigma_{\uparrow\downarrow}} = \frac{R_{\uparrow\uparrow} - R_{\uparrow\downarrow}}{R_{\uparrow\uparrow} + R_{\uparrow\downarrow}} = \boxed{P_{beam}} P_{\text{target}} \langle A_{zz} \rangle, \tag{7.7}$$

where $\sigma_{\uparrow\uparrow}$ and $\sigma_{\uparrow\downarrow}$ ($R_{\uparrow\uparrow}$ and $R_{\uparrow\downarrow}$) are the cross-sections (coincidence scattering rates) for parallel and anti-parallel spin alignments of the beam and target electrons, respectively; $\langle A_{zz} \rangle$ is the average over the instrumental acceptance value of the longitudinal analyzing power of the polarimeter $A_{zz}(\theta)$ by integrating over the angular acceptance of the detector system (see explanation and eq. 8.9 in section 8.4). Since the target polarization P_{target} might be independently estimated or measured, this expression can be used to extract the beam longitudinal polarization P_{beam} (section 8.4). The precision is mainly limited by the accuracy of determining the target polarization P_{target}.

As mentioned earlier, at the scattering angle $\theta_{\text{CM}} = 90°$, which corresponds to the perfectly symmetric scattering case, the analyzing power is maximum: $A_{zz} = 7/9$ (eq. 7.6, figure 7.2). Hence, polarimeters based on Møller scattering are typically designed with acceptance around this angle where the performance is optimal.

In contrast to the main measurements in the P2 setup (see discussion in the following section), the elastic electron-proton scattering (outlined in section 2.7.1) represents the background in this case.

7.3. Signal and Background in the P2 experiment and Møller Polarimetry

While both the P2 experiment and Møller polarimetry involve elastic ep and Møller scattering, the roles of these processes as signal and background are reversed. As discussed in section 2.6, parity-

violating asymmetry is inherent to both ep and Møller scattering. However, the experimental design and objectives determine which process is used to probe this asymmetry. In the P2 experiment, the primary goal is precisely determining the electroweak mixing angle extracted from the measured tiny parity-violating asymmetry in elastic ep scattering. Experimental parameters, such as kinematics, target, and detector configuration, are optimized to maximize sensitivity to weak neutral current contributions. Operating at low momentum transfer (Q^2) minimizes hadronic uncertainties and allows for better control of radiative corrections, leading to a more precise extraction of electroweak parameters. In this kinematic regime, the parity-violating effects in Møller scattering are suppressed. Therefore, it is a secondary process in this case. Møller events typically have different angular and energy distributions that can be kinematically separated from the dominant ep signal. In addition, a dense, unpolarized liquid molecular hydrogen target is employed to provide high luminosity, which is crucial for high statistics. Despite contributions from hydrogen electrons, this target closely approximates an ideal proton target.

In contrast, the Møller polarimeter is designed to measure the beam polarization via doubly-polarized Møller scattering. Here, the arising asymmetry depends directly on the product of beam and target polarizations. The high polarization of both the beam and target enhances the asymmetry. A low-density gaseous atomic hydrogen target is chosen to ensure near-complete transparency to the beam, enabling non-destructive measurements, and because it can be almost perfectly polarized, as each hydrogen atom contains a single electron in its outer orbital. Consequently, in this setup, Møller scattering is the signal, while ep scattering, which is insensitive to the double-spin asymmetry, contributes to the background.

7.4. Radiative Corrections in Møller and ep Scattering

Similarly to the main measurement at the P2 setup, radiative corrections (RC) are also crucial in high-precision polarimetry measurements. In this case, these corrections arise from Quantum Electrodynamics (QED) and account for contributions from virtual loop corrections, soft photon emission, and hard photon bremsstrahlung. Properly incorporating these effects is necessary for accurate data analysis in high-precision experiments. This section provides a general overview of radiation corrections beyond the ultrarelativistic approximation (URA) for Møller and ep scattering, which are detailed in [156–158]. These corrections were incorporated into the Geant4 simulations, as discussed in section 9.2.

7.4.1. Lowest-Order Contributions and Radiative Processes

Radiative corrections (RC) are theoretical adjustments applied to account for the emission of photons during scattering processes. The lower-order contributions to the observable cross sections of Møller and ep scattering are

$$e(k_i, \xi_L) + e(l_i, \eta_L) \rightarrow e^{'}(k_f) + e^{'}(l_f)$$

and

$$e(k_i) + p(p_i) \rightarrow e^{'}(k_f) + p^{'}(p_f),$$

respectively. Here k, l, and p are four-momentum vectors of the corresponding particles, with subscripts i and f indicating the initial and final states, respectively, and ξ_L and η_L represent initial polarization vectors of electrons in Møller scattering.

For radiative processes involving real photon emission, the corresponding scattering processes are complemented as

$$e(k_i, \xi_L) + e(l_i, \eta_L) \rightarrow e^{'}(k_f) + e^{'}(l_f) + \gamma(k_\gamma)$$

and

$$e(k_i) + p(p_i) \rightarrow e^{'}(k_f) + p^{'}(p_f) + \gamma(k_\gamma),$$

where k_γ represents the four-momentum of the emitted photon.

7.4.2. Structure of the Observed Cross Section

To maintain consistency with the referenced sources, the following notation is used for both the Møller and ep scattering processes:

$$\sigma \equiv \frac{d\sigma}{dQ^2\, d\phi},$$

where kinematic variable Q^2 is the negative four-momentum transfer squared, defined as:

$$Q^2 = -(k_i - k_f)^2. \tag{7.8}$$

The experimentally observed scattering cross section, σ_{obs}, can be expressed as a sum of the non-radiative and radiative contributions:

$$\sigma_{\text{obs}} = \sigma_{\text{BSV}}(v_{\text{min}}) + \sigma_{\text{rad}}(v_{\text{min}}, v_{\text{max}}). \tag{7.9}$$

Here, v represents the inelasticity of the scattering process. The parameter v_{min} defines a cutoff, splitting soft-photon emission (with $v < v_{\text{min}}$) and hard-photon emission (with $v \geq v_{\text{min}}$), while v_{max} is the kinematic upper bound of the inelasticity determined by the kinematic constraints of the process. The first term, $\sigma_{\text{BSV}}(v_{\text{min}})$, includes the contributions from the Born cross section, soft-photon emission, and virtual corrections. The second one, $\sigma_{\text{rad}}(v_{\text{min}}, v_{\text{max}})$, accounts for cross section contribution with an additional hard photon emission. This formulation applies for both Møller and ep scattering, provided that the infrared divergences are canceled by appropriate treatment of the virtual and soft photon contributions.

For the total cross-section of the non-radiative part, the integration is performed over different cross-section components, which account for virtual loop corrections, vacuum polarization effects, the infrared contribution from soft photons, and additional corrections depending on the inelasticity cutoffs. For the radiative part, integration extends over the inelasticity range $v_{\text{min}} \leq v \leq v_{\text{max}}$ and further includes integration over the real photon phase space for the corresponding cross-section components and, in the ep scattering case, for nucleon form factors.

The Feynman diagrams contributing to the non-radiative and radiative correction cross sections are depicted in figures 7.1a and 7.3 for Møller scattering and in figures 2.7a and 7.4 for ep scattering.

These corrections play a crucial role in ensuring the accuracy of cross-section calculation and must be carefully accounted for in the Monte Carlo simulations. A more detailed discussion of these radiation corrections is beyond the scope of this thesis. More details can be found in [156–158].

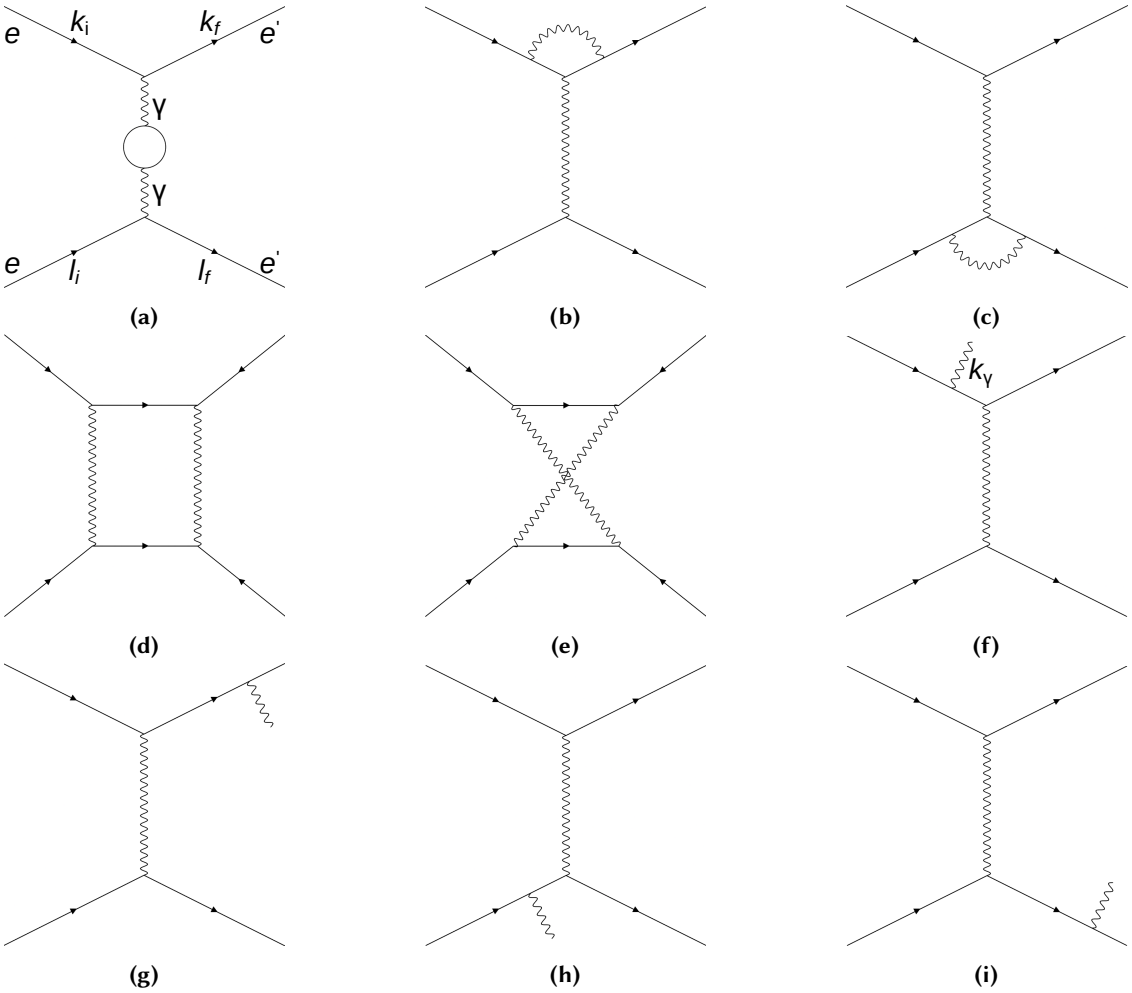

Figure 7.3.: Feynman diagrams contributing to radiative corrections (only t-channel is shown) cross section for Møller scattering. Reproduced from [156].

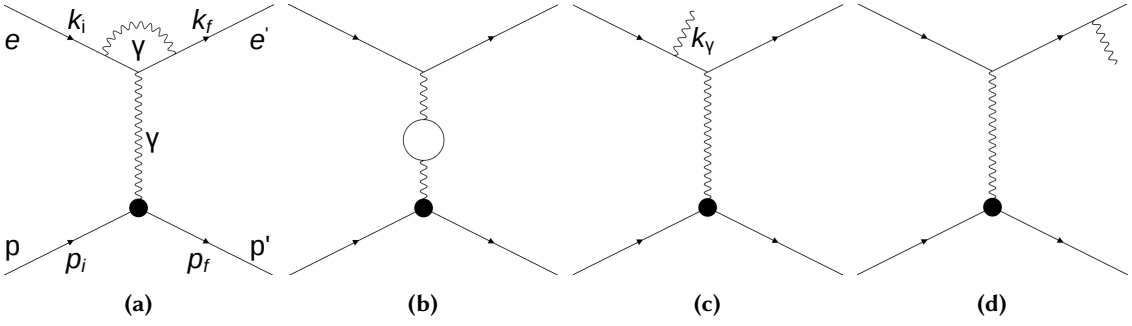

Figure 7.4.: Feynman diagrams contributing to radiative corrections cross section for ep scattering. Reproduced from [156].

8 Møller Polarimeter

The precision of beam polarization is typically limited by the knowledge of the target polarization, P_{target}, which depends heavily on the target material, specifically the electron configuration of the atoms.

Atomic hydrogen (H) is the simplest atomic system with only one shell electron, ideally suited for achieving a high polarization level. However, H is a highly reactive element. Therefore, it will quickly react with another hydrogen atom once in free form, recombining to molecular hydrogen (H_2) or forming various compounds with other atoms and elements. Because of this, H_2 must be dissociated into atomic hydrogen. Once created, H atoms must be stored and polarized for a long lifetime, which is challenging due to their reactivity. As demonstrated in [159], the lifetime can be significantly extended by lowering the temperature to extremely low levels in the presence of a strong magnetic field.

This chapter presents the design of the Møller polarimeter, which was developed and optimized within the framework of this thesis. It expands upon the description and analysis in [7], providing more detailed calculations and additional estimations of the polarimeter performance.

8.1. Gaseous Atomic Hydrogen Target

As proposed by Chudakov and Luppov [142], a strong magnetic field along the beam axis created by the superconducting solenoid can trap hydrogen atoms of the desired polarization at mK temperature and expel atoms with opposing polarization along the field direction (figure 8.1). This represents a perfect target for polarimetry since almost all atoms will be almost perfectly polarized.

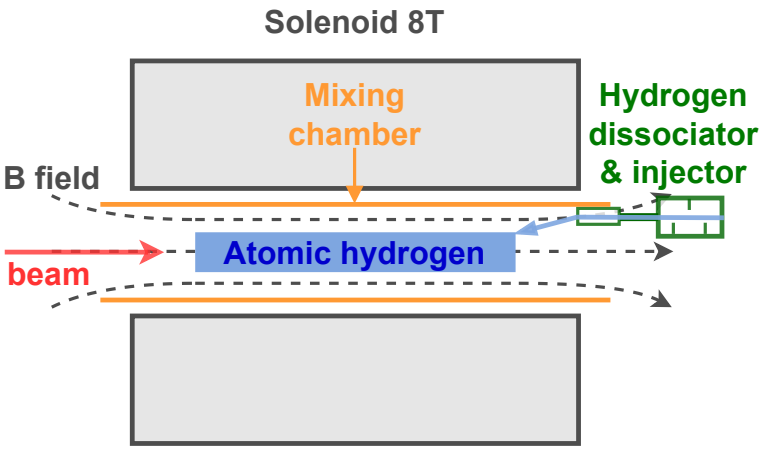

Figure 8.1.: Scheme of atomic hydrogen gas injection into the mixing chamber, followed by trapping the polarized hydrogen atoms in the strong solenoid magnetic field.

8.1.1. Polarization of Atomic Hydrogen

In the presence of a solenoid magnetic field, the hyperfine structure of the ground state of a hydrogen atom is defined by the spin Hamiltonian

$$\mathcal{H} = a\,\mathbf{S}\cdot\mathbf{I} - \hbar\,\mathbf{B}\cdot(\gamma_p\mathbf{I} - \gamma_e\mathbf{S}), \tag{8.1}$$

where a is the hyperfine coupling constant for the hydrogen atom, **S** (**I**) is the electron (proton) spin operator, $\hbar$ is the reduced Plank constant, **B** is the applied the solenoid magnetic field (along the beam the direction of the beam), and γ_e (γ_p) is the gyromagnetic ratio of the electron (proton) [160].

The static magnetic field splits the H ground state into four hyperfine levels with different energies, listed in table 8.1. For the mixed states $|a\rangle$ and $|c\rangle$, the mixing angle ε (not to be confused with the weak mixing angle) is determined as [160–162]

$$\tan 2\varepsilon = \frac{A}{\hbar\gamma_e\gamma_p B}\,. \tag{8.2}$$

State		Wave function	Energy
Energy ↓	$\|a\rangle$	$\cos\varepsilon\,\|\downarrow\Uparrow\rangle - \sin\varepsilon\,\|\uparrow\Downarrow\rangle$	$E_{a,b} = -\frac{a}{4} \mp \frac{1}{2}\sqrt{(a^2 + \hbar^2(\gamma_e+\gamma_p)^2B^2)}$
	$\|b\rangle$	$\|\downarrow\Downarrow\rangle$	
	$\|c\rangle$	$\sin\varepsilon\,\|\downarrow\Uparrow\rangle + \cos\varepsilon\,\|\uparrow\Downarrow\rangle$	$E_{c,d} = \frac{a}{4} \mp \frac{\hbar}{2}(\gamma_e+\gamma_p)B$
	$\|d\rangle$	$\|\uparrow\Uparrow\rangle$	

Note:↑ and ↓ (⇑ and ⇓) denote spins of electron (proton); ε is the mixing angle.

Table 8.1.: Hyperfine eigenstates of atomic hydrogen in the order of increasing energy [160–162].

Under a strong solenoid strong magnetic field $B = 8\,\mathrm{T}$ along the beam axis, the transverse field gradient exerts a Stern-Gerlach force $-\boldsymbol{\nabla}(\boldsymbol{\mu}_\mathrm{H}\cdot\mathbf{B})$, where $\boldsymbol{\mu}_\mathrm{H}$ is the magnetic moment of the atom [163], on the magnetic moments of the moving atoms. It deflects and, as a result, separates the lower and higher energy states of the hydrogen atoms. The H atoms with lower energy states are pulled into the center of the mixing chamber (figures 8.1 and 8.2), where the field is stronger, while the atoms with higher energy states are repelled towards the periphery [142]. At the temperature of $T = 0.3\,\mathrm{K}$ inside the mixing chamber, the polarized H atoms, trapped by the solenoid magnetic field, will end up at the point of the statistical equilibrium, following the Boltzmann distribution [142]

$$p \propto \exp\left(\frac{\mu_e B}{kT}\right), \tag{8.3}$$

where μ_e is the magnetic moment of the electron and k is the Boltzmann constant. The space near the beam axis will be mainly populated by atoms with lower energy states $|a\rangle$ and $|b\rangle$ (high-field seekers), with a negligible admixture of the states $|c\rangle$ and $|d\rangle$ (low-field seekers) approximately $exp(-2\mu_e B/kT) \approx 3\times10^{-16}$ [142].

In the given case, with $B = 8\,\mathrm{T}$ and $T = 0.3\,\mathrm{K}$: $\tan 2\theta \approx 0.00625$, hence $\cos\theta \approx 1 - 5\times10^{-6}$ and $\sin\theta \approx 0.003$. In the mixed state $|a\rangle$ (table 8.1) the probability of the electron spin being parallel (spin-up H↑) or antiparallel (spin-down H↓) to the magnetic field direction along the beam axis (z-axis), according to the Born rule, is proportional to the corresponding amplitudes

$\cos^2 \varepsilon$ and $\sin^2 \varepsilon$, respectively. Therefore, in this state, the hydrogen atom is almost completely polarized in the antiparallel configuration, with only a negligible probability ($\sin^2 \varepsilon \approx 10^{-5}$) of being in the parallel configuration.

By definition, the state $|b\rangle$ corresponds to a fully polarized antiparallel configuration. Therefore, the atomic hydrogen target around the area of interaction with the beam ($\sigma_X \approx \sigma_Y \sim 0.1\,\text{mm}$) is almost perfectly polarized in the antiparallel configuration: $P_{\text{target}} = 1 - \delta$, with $\delta \sim 10^{-5}$ [64, 142]. For comparison, in the case of iron, only 2 of 26 electrons are polarized, resulting in an effective target polarization of only ~8 % [148], which, according to eq. 7.7, significantly affects the final precision of beam polarization measurement.

Following similar reasoning, the low-field seeking states ($|c\rangle$ and $|d\rangle$) are actively expelled from the interaction region, leading to spatial separation. Consequently, the mixing chamber periphery is populated by these low-seeking states, which are almost completely polarized in the parallel configuration, ensuring a highly pure spin-down polarized target in the interaction region.

8.1.2. Atomic Hydrogen Gas Lifetime

The lifetime of the atomic hydrogen (H) gas in the target is mainly limited by the thermal escape of the atoms through the magnetic fringe field at both ends of the target, the recombination into molecular H_2 within the target volume, and the depolarization of atoms [64, 142]. Introducing a strong magnetic field and mK-level temperature can suppress the first factor. However, the latter two need to be treated additionally and separately.

In 1980, Silvera and Walraven first achieved [159] lifetime of the atomic hydrogen of almost 9 min with density $n \sim 10^{14}\,\text{cm}^{-3}$ by stabilizing it at low temperatures $\approx 270\,\text{mK}$ and in magnetic fields up to 7 T. The essential point was covering the exposed container surfaces with a thin superfluid ^{4}He film.

The recombination between polarized H atoms is suppressed since two atoms in a triplet state cannot form an H_2 molecule [160]. Although, as discussed in previous section 8.1.1, there is a negligible admixture of the electron-reversed states in both regions populated mainly by high- or low-seeking H atoms. However, it was shown that the probability of this process is significantly suppressed in comparison to the zero field recombination rate. As a result, volume recombination remains negligible up to densities of $\sim 10^{17}\,\text{cm}^{-3}$ [142, 159, 160]. The dominant process that limits the gas density and lifetime is represented by the recombination on the surface of the mixing chamber [64, 142]. That is precisely why the coating of exposed surfaces with a thin film of ^{4}He was emphasized by [159] and later by others (for example, in [162]). The helium film has a very small sticking coefficient [142] for hydrogen atoms. In contrast, ^{4}He atoms stick to the inner hydrophilic metal surface after being injected into the mixing chamber volume, forming a stable film and acting as a protective buffer layer with a thickness of ~50 nm [142, 162]. At ultracold temperatures $\lesssim 0.3\,\text{mK}$, ^{4}He has extremely low binding energy with other atoms and molecules. Therefore, the H atoms experience only weak van der Waals interactions when approaching a surface coated with the helium film, suppressing surface-catalyzed recombination [162]. In addition, in this case, helium will be in a superfluid state where it has extremely low surface tension and no viscosity, providing an additional protective effect by reducing the chance of surface recombination [142, 160, 162]. Thus, the intrinsic three-body process H + H + ^{4}He $\longrightarrow$ H_2 + ^{4}He will be significantly suppressed [162].

The following mechanisms [142] primarily cause the depolarization of hydrogen atoms:

- internally by unpolarized contamination, like H_2 and other gasses, as well as by high energy states $|c\rangle$ and $|d\rangle$ (table 8.1) and excited atomic states within the target volume around the beam axis;
- externally by the beam due to its electromagnetic field, gas ionization, and heating during the impact.

According to the calculations given in [142] with the parameters listed in table 8.2, the lifetime of the H gas is estimated to be $\sim 1\,\mathrm{h}$. However, the detailed description of all these factors is beyond the scope of this dissertation. More details can be found in [142].

8.1.3. Design of the Hydrogen Target

Figure 8.2 shows the schematic view of the atomic hydrogen target at MESA.

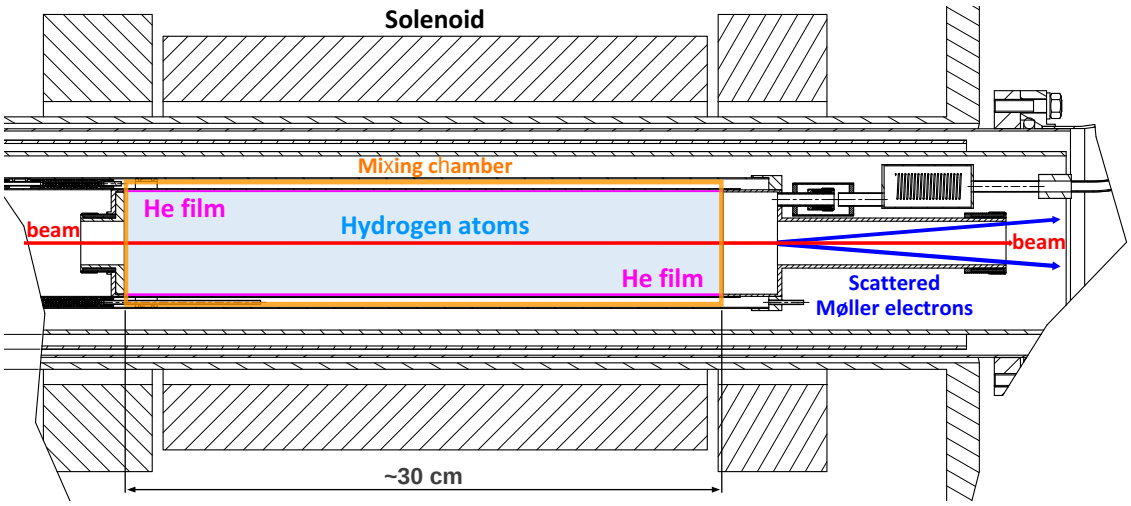

Figure 8.2.: Schematic view of the atomic hydrogen target. Based on a technical drawing [164], with edits and added elements and annotations.

The length of this target type should be significantly larger than in the case of the metal foil case because of the extremely low density and scattering rate. In the present case, the effective length, where the scattering occurs within the considered instrumental acceptance, is confined to $\sim 8\,\mathrm{cm}$ (discussed in section 9.3). However, the mixing chamber should be longer, about 30 cm in this case, to ensure consistent/uniform atomic hydrogen density within the area of the effective target length. The schematic view of the target is shown in figure 8.2. More technical details can be found in [64] and [142].

In the Geant4 simulation model, the target is implemented with a uniform density profile. However, as discussed section 9.3, in the presented case, the effective target length–from where scattered signal Møller pairs reach the detector acceptance–is confined to approximately 8 cm and slightly shifted backward from the center. However, the mixing chamber should extend beyond this region to properly account for the actual density profile while avoiding overestimating the signal rate or underestimating the background rate. Based on these considerations, the target length in the simulation was set to 20 cm, within which the density drops to half of the maximum value (figure 8.3).

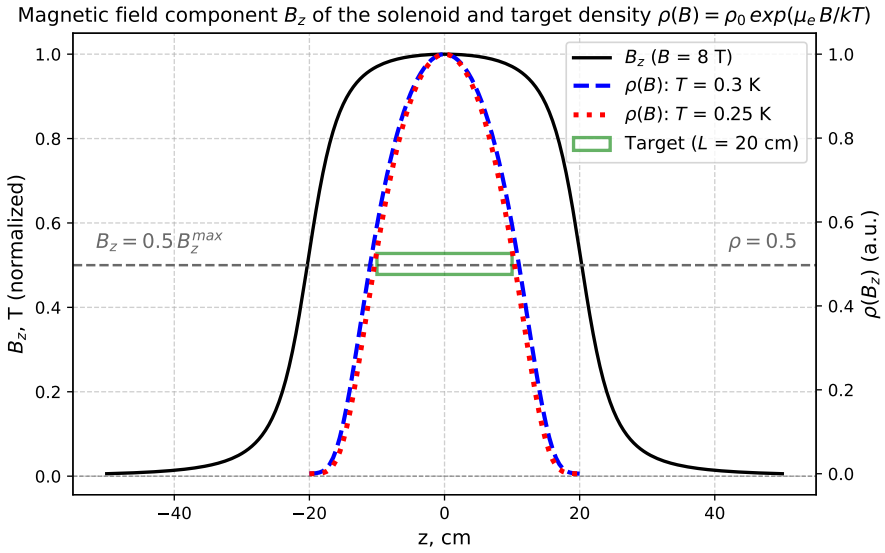

Figure 8.3.: Magnetic field of the solenoid model used in the simulation and the profile of the hydrogen target density. The green box depicts the hydrogen target position inside the solenoid (with corresponding effective length and arbitrary width). Discussed further in section 9.3.4.

Despite all the technical challenges, an atomic hydrogen target has a significant advantage over solid foil targets because it is almost transparent to the beam. This allows real-time polarization data to be taken in parallel with the main experiment at the full beam current of 150 µA and avoids uncertainties from interpolating the results between measurements. As a consequence, substantial improvements in accuracy are expected.

Table 8.2 lists the technical characteristics of the hydrogen target.

Parameter	Value
Solenoid length (L_{Sol})	40 cm
Solenoid magnetic field (B_{Sol})	8.0 T
Effective target length	20 cm
Mixing chamber length	30 cm
Inner radius of the mixing chamber	2 cm
H gas and He film temperature	0.25 − 0.3 K
Expected gas density (n)	$\sim\ 3 \times 10^{15}\,\mathrm{cm}^{-3}$
Pressure	$\sim\ 1 \times 10^{-13}$ Pa

Table 8.2.: Technical characteristics of the hydrogen target.

8.2. Solid Iron Target

The thin solid metal target will be made of pure iron foil with an approximate thickness of 5 µm to 10 µm. In a high magnetic field that considerably exceeds the saturation magnetization of iron, the target polarization can be oriented parallel to the foil normal (z-direction), allowing measurements of A_{zz} with the beam also moving in this direction.

Parameter \ Target	Hydrogen (H)	Iron (Fe)
Solenoid magnetic field	8.0 T	
Solenoid length	40 cm	
Temperature (H and He film)	0.25 − 0.3 K	-
Radius, mm	20*	∼ 10
Length l_{target}	20 cm (eff.**)	5 µm
Density ρ, g/cm^3	5×10^{-9}	7.87
$\overline{Z}/\overline{A}$, kg^{-1}	992	466
I_{beam}, µA	150	0.25
N_{beam}, e$^-$/s	9.36×10^{14}	1.56×10^{12}
Electron density ρ^e_{target}, e$^-$/cm^3	2.99×10^{15}	2.21×10^{24}
Luminosity $\mathcal{L}_{\text{eff}}$, cm^{-2} s^{-1}	2.80×10^{31}	1.72×10^{33}

*Radius of the hydrogen mixing chamber.
**Effective length of the atomic hydrogen target within which the originating Møller electron pairs reach the detecting area within the instrumental acceptance of interest (discussed in section 9.3).

Table 8.3.: Target properties and operating parameters.

The main disadvantage of this type of target is that it destructs the beam, making online measurements during the main experiment impossible. Another main concern in the iron case is that core electrons are in filled orbitals where spins are paired, leading to zero net magnetic moment and high binding energy. Therefore, magnetization properties originate mainly from the outer valence $3d$ electrons. At room temperature (300 K), the saturation magnetization for iron is $M_s \approx 1.7\,\text{T}/\mu_0$, where μ_0 is the permeability of free space. This means that almost all valence electrons in iron atoms will be polarized in a magnetic field of $\gtrsim 1.7$ T. However, considering only 2 M-shell electrons out of total $Z = 26$ electrons carry the Fe magnetization [153], the highest achievable polarization of iron targets is at the level of ~ 8 %. This, in turn, raises the requirements for higher statistics and/or systematic error control to reach the needed precision of beam polarization measurement [148, 153]. Additional challenges might be caused by inhomogeneities of the local thickness of the targets [165] and by wrinkles in the thickness of the foil $\lesssim 4$ µm [150], which can affect target polarization and overall polarimeter performance.

8.2.1. Target Polarization and Heating

The actual polarization of the target is highly dependent on temperature, which is determined by the initial working temperature. The latter depends on the ambient temperature or an applied cooling system. Furthermore, the energy deposited by the incident beam in collision with target atoms can significantly increase the target temperature, introducing intolerable errors by reducing the target polarization. In extreme cases, excessive beam current can even melt or destroy a thin metal target. Consequently, measurements must be conducted at beam currents significantly lower than the operating one in the P2 experiment, typically below $1 - 2$ µA, to minimize the foil depolarization due to heating by incident beam [149, 150]. However, this low-current measurement introduces additional errors due to the necessity of high-current extrapolation [150]. As discussed above, this extrapolation is not necessary for the hydrogen target.

Uncertainties associated with target polarization usually introduce the leading contribution to the total systematic error in such experiments. Therefore, it is essential to measure and monitor the target polarization or use a polarization technique that allows for its precise calculation. The latter can be provided using a brute force (out-of-the-foil plane) polarization technique [148, 166, 167].

A conventional polarization technique involves a ferromagnetic foil composed of alloys such as Supermendure (49 % Fe, 49 % Co, and 2 % V), which is polarized in-plane by a relatively low magnetic field (0.05 T). The target is positioned at an angle of $\alpha \sim 20^\circ$ relative to the beam and magnetic field direction, resulting in a reduction of the relevant longitudinal polarisation proportional to $\cos\alpha$ [148, 153, 166].

In contrast, the brute force technique employs a foil made of nearly pure iron (close to 99.99 %) positioned strictly perpendicular to the strong magnetic field exceeding 3.5 T [166] and to the beam direction. Once the pure iron reaches full magnetic saturation, a direct measurement of the target polarization (magnetization) becomes unnecessary, as it can be determined with high precision [168]. Together with precise alignment of the magnetic field along the beam, this technique can reduce systematic errors to ~0.9 %, compared to ~1.7 % in the conventional method case [166].

If, for example, a higher beam current will be needed, the potential decrease in target polarization can be measured online using the Kerr effect-based technique, as discussed and shown in [148, 153, 169]. However, as demonstrated in [149], during the Q_{weak} experiment in Hall C at Jefferson Lab, the heating effect of $1 - 4\,\mu\text{m}$ pure iron target by incident 1.16 GeV beam became the dominant source of systematic uncertainty in the extracted beam polarization—exceeding ~0.24 %—only at beam currents of $\geq 4.5\,\mu\text{A}$, which is significantly higher than the $0.25\,\mu\text{A}$ considered in the present case (table 9.1).

8.2.2. Levchuk Effect

One of the main problems in the iron target case is the presence of the Levchuk effect [170]. It occurs for two reasons: because only electrons in the outer atom shells, with lower binding energies, are polarized and due to the intraatomic motion of electrons (more details can be found in [170]). This leads to a potential overestimation of the measured asymmetry due to changes in the analyzing power $\langle A_{zz}\rangle$ due to the different contribution of the Møller pair that was scattered from unpolarized inner bound target electrons to the measured asymmetry at different acceptance regions [150]. As a result, these uncertainties in $\langle A_{zz}\rangle$ introduce an additional systematic error to the measured beam polarization P_{beam} (see eq. 7.7). In contrast, this effect does not exist in the case of atomic hydrogen since it has only a single electron.

The Levchuk effect can be mitigated by determining$\langle A_{zz}\rangle$ more precisely, as discussed in [150, 165, 170]. One of the simplest solutions involves instrumental adjustments. This can be achieved by either increasing the difference between energy ($\Delta E/E$) and angular ($\Delta\theta/\theta$) instrumental acceptance [170], or by restricting the angular acceptance alone [150]. However, the first approach is feasible only at much higher beam energies in the GeV range, as demonstrated in [165]. Meanwhile, the second approach is constrained by the simultaneous loss of signal.

However, due to the MESA beam energy and the impossibility of restricting angular acceptance too much, the only way of treating this effect in the present case is by using the improved atomic wave functions in calculations to predict the effective analyzing power $\langle A_{zz}\rangle$. For example, as was shown in [150], for the case of bulk iron, this method allows calculating the Levchuk effect

corrections with a level of precision when sub-percent accuracy in the further determination of the beam polarization becomes achievable.

8.2.3. Position of the Target Inside the Solenoid

Ideally, the metal foil target should be precisely positioned at the solenoid's center along the z-axis, where the magnetic field reaches its maximum. However, as discussed in section 9.3, a slight negative shift improves energy selection for the applied collimation system at the quadrupole magnet while still maintaining a strong enough solenoid field to ensure full magnetic saturation of iron (section 8.2.1). Additionally, the detector coincidence scheme can potentially be improved by optimizing the target shift to enhance energy dispersion along the quadrupole's defocusing axis and enable detector segmentation.

8.3. Design of the Møller Polarimeter

A polarimeter design should offer large, well-defined acceptance and good background suppression with either hydrogen or iron targets. Additionally, the detector system must efficiently register signal events. Due to space limitations in the MESA halls, the entire polarimetry setup should not exceed $\sim 3 - 5\,\mathrm{m}$ along the beam direction.

Design Principles. The proposed polarimeter design aims to be versatile and adaptable for both targets with minor changes, ideally affecting only the collimation system and the mounting and support system for the target. After evaluating various options, a design based on a single, large aperture quadrupole analyzing magnet and a customized collimation system was chosen. An overview of the design is shown in figure 8.4.

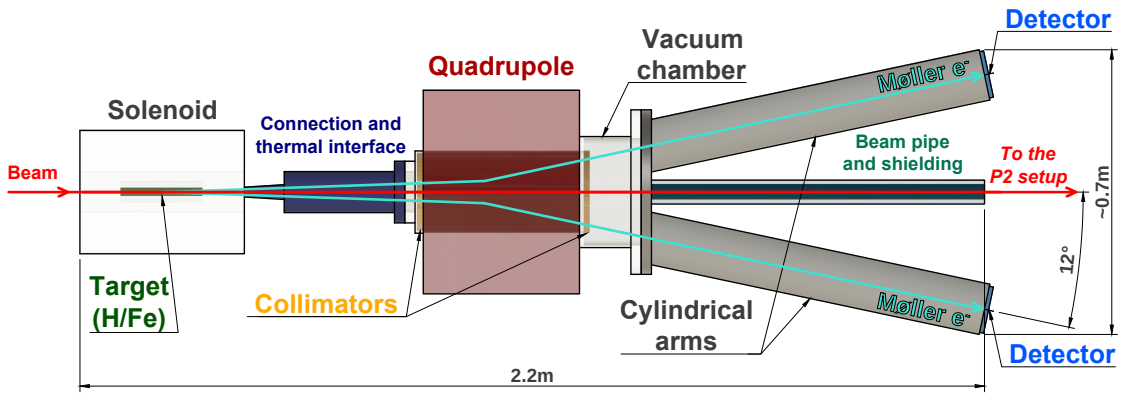

Figure 8.4.: Design diagram of the two-arm Møller polarimeter, top view – in the defocusing quadrupole plane. The tracks of scattered symmetric Møller electron pair (in cyan) are for illustration purposes and do not represent physical tracks.

The target—whether iron foil or atomic hydrogen—is placed inside a long superconducting solenoid. As discussed in section 8.2, a solenoid magnetic field strength of $\geq 3.5\,\mathrm{T}$ should be sufficient to achieve full magnetic saturation of iron. However, in the presented design, the field strength of 8 T will be used for both targets. This unified design ensures the following key moments for both targets:

- Full magnetic saturation of the iron target, even with its slight positional shift inside the solenoid;
- Effective longitudinal polarization and magnetic trapping of the hydrogen atoms while preserving the quality of the primary electron beam. To achieve this, the solenoid's parameters (length and magnetic field strength) are chosen so that the four-dimensional transfer matrix is diagonal, with all elements equal to one. This configuration eliminates any net focusing, coupling, or rotation of the electron beam as it transits the solenoid, ensuring it remains undistorted for subsequent measurements in the P2 experiment.

The design of auxiliary components, such as connection and thermal interface, connection flanges, and angle and length of arms, as well as position and aperture size of the quadrupole magnet and total length of the setup, is also unified for both targets. This configuration allows for initial technical measurements using the iron target, facilitates the positioning and alignment of the magneto-optics system, and allows for studying the dependence of the signal on the target position inside the solenoid. Since the hydrogen target can be approximated as a set of thin targets along the beam axis, these preliminary studies provide valuable insights before transitioning to the hydrogen target.

Downstream of the solenoid, a connection and thermal interface link to the vacuum chamber, which is inserted into the quadrupole magnet aperture and contains collimators before and after the quadrupole. This collimation system selects signal events within the defined instrumental acceptance based on the radial energy distribution and suppresses most of the background. The chosen acceptance covers energies in the range of $70 - 85\,\text{MeV}$ ($E_{\text{Møller}}[\theta_{\text{CM}} = 90°] \pm 7.5\,\text{MeV}$), which corresponds to the scattering angle range of $4.21 - 5.10°$ in the laboratory frame (or $90° \pm 5.55°$ in center-of-mass frame). This acceptance range is used for simulation, though the focusing effect of the solenoid magnet influences the actual instrumental angular acceptance. The energy acceptance was chosen based on preliminary calculations (presented in table 8.4) to ensure an optimal signal rate while maintaining a negligible level of analyzing power fluctuations ($(\langle A_{zz}^2\rangle - \langle A_{zz}\rangle^2)/\langle A_{zz}^2\rangle$).

θ_{CM} [degree]	90 ± 1.85	**90 ± 5.55**	90 ± 9.28
θ_{lab} [degree]	4.49–4.79	**4.21–5.10**	3.94–5.45
$E_{\text{Møller}}$ [MeV]	75–80	**70–85**	65–90
	(77.5 ± 2.5)	**(77.5 ± 7.5)**	(77.5 ± 12.5)
$[x_{\text{min}}, x_{\text{max}}]$	[0.93, 1.07]	**[0.90, 1.10]**	[0.83, 1.17]
$\langle A_{zz}\rangle$	0.776	**0.774**	0.767
$\langle A_{zz}^2\rangle$	0.602	**0.599**	0.588
$(\langle A_{zz}^2\rangle - \langle A_{zz}\rangle^2)/\langle A_{zz}^2\rangle$	$< 2 \times 10^{-5}$ %	**0.002%**	0.02 %

Table 8.4.: The characteristic unpolarised cross-sections and averaged analyzing power for Møller scattering calculated for an idealized Møller polarimeter with a detection efficiency of 100 % and $E_{\text{beam}} = 155\,\text{MeV}$. The boldfaced values represent the optimal instrumental acceptance based on the aperture of the quadrupole magnet and collimation. Reproduced, adapted, and calculated for the given case from [153].

Collimation System. The first collimator at the quadrupole magnet entrance suppresses scattered Møller electrons outside the above defined energy range and high-rate background events scattered at low angles. As shown in figure 8.5a, this collimator is designed to be transparent only to electrons within the angular range corresponding to the instrumental energy acceptance of interest. The quadrupole magnetic field then further separates the selected electrons in the

defocusing plane. After passing through the second collimator at the end of the quadrupole (figure 8.5b), the remaining electrons leave the chamber and travel further through two symmetrical cylindrical arms until they hit detectors located symmetrically on both sides of the beam axis at the focal distance of the quadrupole. This setup effectively suppresses the background and separates scattered events into two symmetric arms, allowing the selected signal events to be detected in coincidence. Both collimators are made from ~4.3 radiation lengths of tungsten (1.5 cm).

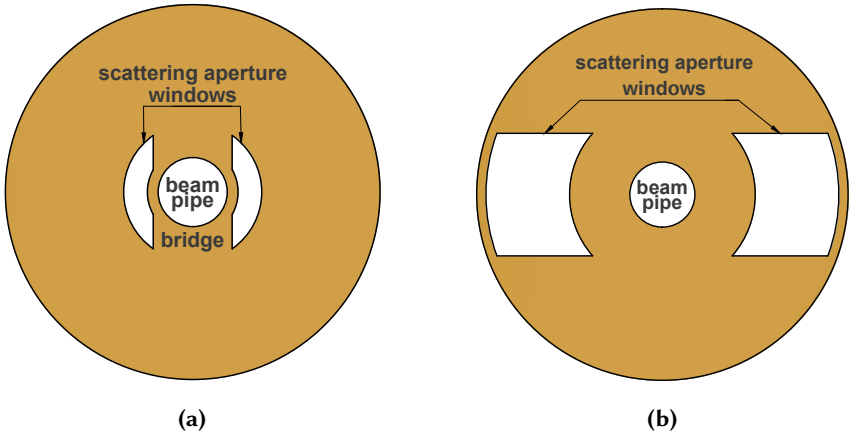

Figure 8.5.: The cross-section view of the collimators (for hydrogen target) at the (a) entrance and (b) end of the quadrupole magnet entrance implemented in the simulation.

The gradient of the quadrupole magnetic field was chosen such that the distance between the detectors is sufficiently large compared to the aperture of the quadrupole. The rotation angle of the cylindrical arms and detector relative to the beam axis was set to the average value of 12° for both targets. This ensures a unified design that suppresses single-bounced Bremsstrahlung photons from the target from reaching the detectors. That leaves the radiative parts of ep and Møller scatterings and secondary electrons scattered in the space after the first collimator as a primary source of background. This remaining background can be strongly suppressed by applying a coincidence requirement for the signal events detected in both arms, since the signature of the signal event is represented by a pair of scattered and target recoil Møller electrons.

In the hydrogen target case, the unscattered part of the beam passes the quadrupole through the central holes in both collimators (figure 8.5) and transports further to the P2 setup inside the beam pipe. Measurements with the iron target can be done between the main experiment runs. In this case, the beam passing through the polarimeter has to be directed to a beam dump immediately afterward. Once the measurement is completed, the iron target should be removed from the beam path before the P2 experiment resumes. In addition, the beam pipe is shielded with lead to ensure maximum suppression of potential background.

Detector. Given the relatively narrow instrumental energy acceptance—$E_{\text{Møller}}[\theta_{\text{CM}} = 90°] \pm 7.5\,\text{MeV}$—and the estimated signal and background rates (calculated values in table 9.2), plastic scintillators coupled with photomultiplier tubes (PMTs) provide a cost-effective, reliable, and easy-to-implement detector option that is well-suited for this case. The fast time resolution on the order of 1 ns, combined with the coincidence logic, should effectively suppress background noise and significantly reduce the pile-up effect. As previously mentioned, adjusting the quadrupole magnetic field configuration can enable decent detector segmentation, which, in turn, will

enhance coincidence detection and narrow the detectable energy range within each segment.

8.4. Measurement of the Beam Polarization

As shown in section 7.2.1, the beam polarization can be extracted from eq. 7.7 after the asymmetry $A_{\text{Møller}}$ is measured based on a difference in Møller scattering rates for two configurations with different relative orientations of the beam and target polarizations. Depending on the implemented detection system, polarization measurement can be performed in two ways: integrated and differential. The content of this section is based on the corresponding section in [153], with several adaptations and modifications.

8.4.1. Integrated Measurement

In the experiments, measurable quantities often involve energies and momenta rather than the angular distribution. Therefore, transitioning from the angular-based (θ) to energy-based acceptance better aligns theoretical calculations with experimental observables. It can be done using the following re-parametrization:

$$x = 2p_{\text{lab}}/p_{\text{beam}}\,, \tag{8.4}$$

where p_{lab} and p_{beam} are the momentum of the scattered electron and incident beam in the laboratory frame, respectively. Polarization measurements are conducted for two different beam-target longitudinal polarization configurations: $(+\vec{P}_{\text{beam}}, \vec{P}_{\text{target}})$ and $(-\vec{P}_{\text{beam}}, \vec{P}_{\text{target}})$. The number of Møller scattering events detected within the acceptance range $[x_{\text{min}}, x_{\text{max}}]$ over the measurement time t is given by

$$N_{\pm} = \mathcal{L}_{\pm}\, t_{\pm} \int_{\phi_{\text{min}}}^{\phi_{\text{max}}} d\phi \int_{x_{\text{min}}}^{x_{\text{max}}} \epsilon_{\pm}(x)\, \frac{d\sigma_0}{dx} \left(1 \pm P_{\text{beam}} P_{\text{target}} A_{zz}(x)\right) dx, \tag{8.5}$$

where the sign in '±' corresponds to the sign of the beam polarization, $\mathcal{L}$ is the instantaneous beam luminosity, and $\epsilon(x)$ is the acceptance function of the polarimeter that takes into account the detector efficiency.

Given the connection of the laboratory momentum of the scattered electron to the initial momentum of the electron in the beam, the parameter x given in eq. 8.4 can be expressed as

$$p_{\text{lab}} = \frac{p_{\text{beam}}}{2}(1 + \cos\theta_{\text{CM}}) \implies x = 1 + \cos\theta. \tag{8.6}$$

Substituting the latter in eqs. 7.2 and 7.6 yields the unpolarized differential cross-section $d\sigma_0/dx$ and analyzing power $A_{zz}(x)$ as [153]

$$\frac{d\sigma_0}{dx} = \frac{\alpha^2}{s} \frac{[3 + (x-1)^2]^2}{[1 - (x-1)^2]^2}\,; \tag{8.7a}$$

$$A_{zz}(x) = \frac{[7 + (x-1)^2]\,[1 - (x-1)^2]}{[3 + (x-1)^2)]^2}\,. \tag{8.7b}$$

Next, following eq. 7.7, the experimentally measured asymmetry can be expressed in terms of detected event counts given by eq. 8.5 (for simplicity, assuming $\mathcal{L}_+ t_+ = \mathcal{L}_- t_- = \mathcal{L}\, t$ and

$\epsilon_+(x) = \epsilon_-(x) = \epsilon(x)$):

$$A_{\text{Møller}} := A_{\text{exp}} = \frac{N_+ - N_-}{N_+ + N_-} = P_{\text{beam}} P_{\text{target}} \langle A_{zz} \rangle \,, \tag{8.8}$$

where $\langle A_{zz} \rangle$ is the integrated average analyzing power, which is defined by the corresponding remaining parts from eq. 8.5 as

$$\langle A_{zz} \rangle = \frac{\int \epsilon(x) \frac{d\sigma_0}{dx} A_{zz}(x)\, dx}{\int \epsilon(x) \frac{d\sigma_0}{dx}\, dx} \,. \tag{8.9}$$

Since the target polarization P_{target} can be independently estimated or measured, the beam polarization can be extracted from the experimentally measured asymmetry:

$$P_{\text{beam}} = \frac{A_{\text{exp}}}{P_{\text{target}} \langle A_{zz} \rangle} \,. \tag{8.10}$$

As follows from eq. 8.10, the relative error of the measured beam polarization is then:

$$\left(\frac{\Delta P_{\text{beam}}}{P_{\text{beam}}} \right)^2 = \left(\frac{\Delta A_{\text{exp}}}{A_{\text{exp}}} \right)^2 + \left(\frac{\Delta P_{\text{target}}}{P_{\text{target}}} \right)^2 \,. \tag{8.11}$$

Propagating the error of the asymmetry A_{exp} measured in the experiment (see appendix A.1), and using

$$\sigma_{\text{total}} = \int_{\phi_{\text{min}}}^{\phi_{\text{max}}} d\phi \int_{x_{\text{min}}}^{x_{\text{max}}} \epsilon(x)\, \frac{d\sigma_0}{dx}\, dx \,. \tag{8.12}$$

the required measurement time to achieve the given relative precision of the measured beam polarization $\Delta P_{\text{target}} / P_{\text{target}}$ can be estimated as

$$\frac{1}{t_{\text{meas}}} \simeq \mathcal{L}\, \sigma_{\text{total}} \left(\frac{\Delta A_{\text{exp}}}{A_{\text{exp}}} \right)^2 \frac{\left(P_{\text{target}}\, P_{\text{target}}\, \langle A_{zz} \rangle \right)^2}{1 - \left(P_{\text{target}}\, P_{\text{target}}\, \langle A_{zz} \rangle \right)^2} \,. \tag{8.13}$$

Finally, the corresponding needed number of events and rate are:

$$R_{\text{int}} = \mathcal{L}\, \sigma_{\text{total}} \,, \tag{8.14a}$$

$$N_{\text{int}} = \mathcal{L}\, t_{\text{meas}}\, \sigma_{\text{total}} \,. \tag{8.14b}$$

8.4.2. Differential Measurement

If the polarimeter detector system can also measure the momentum of the Møller-scattered events or if there is sufficient energy dispersion created by magnetic elements and segmentation in the detector system, the polarization measurements can be performed for a set of discrete bins x^i, corresponding to momentum bins p^i_{lab} [153].

In this case, the experimental asymmetry is measured for each bin x_i:

$$A^i_{\text{exp}} = \frac{N^i_+ - N^i_-}{N^i_+ + N^i_-} = P^i_{\text{beam}} P_{\text{target}} \langle A_{zz} \rangle^i \,. \tag{8.15}$$

Similarly, the beam polarization for each particular bin can be evaluated as

$$P^i_{\text{beam}} = \frac{A^i_{\text{exp}}}{P^i_{\text{target}} \langle A_{zz} \rangle^i} \,. \tag{8.16}$$

The total beam polarization can be calculated as the weighted mean of the set of measured polarization values P^i_{beam}:

$$P_{\text{beam}} = \sum_i \frac{P^i_{\text{beam}}}{\left(\Delta P^i_{\text{beam}}\right)^2} \Big/ \sum_i \frac{1}{\left(\Delta P^i_{\text{beam}}\right)^2} \,, \tag{8.17}$$

where ΔP^i_{beam} is the deviation of P^i_{beam} from the mean.

Measurement time and the number of events required to achieve the desired relative polarization precision can be estimated using the same approach as for the integrated measurement case discussed in section 8.4.1. However, a properly implemented differential measurement requires fewer events, leading to a shorter measurement time and improved control over systematic errors and background contributions [153]. This advantage arises because the analyzing power, with energy dispersion, acceptance of certain detector segments can be optimized for a better signal-to-background ratio, enhancing measurement accuracy. Furthermore, A_{zz} is averaged over multiple smaller acceptance ranges in this case.

8.5. Estimation of the Polarimeter Performance

Table 8.5 summarizes the estimated systematic and statistical errors for both targets.

Error source \ Target	Hydrogen (H)	Iron (Fe)
Systematic errors		
Positioning and alignment of beam, target and magneto-optical system*	~0.45 %	
Target heating by the beam	-	up to 0.24 %
Target spin polarization	10^{-3} %	0.25 %
Levchuk effect	-	0.33 %
High-current extrapolation	-	up to 0.5 %
Monte Carlo statistics	0.14 %	
Total	~0.47 %	~0.67 − 0.84 %**
Statistical error (maximum)***	$\lesssim$0.17 %	-

*Combines values for all relevant sources listed in [149, 171].
**The lower bound value does not include high current extrapolation.
***Maximum possible value needed to achieve the required polarization error $\leq$ 0.5 %.

Table 8.5.: Estimated systematic and statistical errors for both targets. Values of systematic errors are taken for evaluative purposes from [149, 171]. The statistical error is not provided for the iron target, as the systematic uncertainties alone result, in this case, in a total systematic error exceeding the required beam polarization measurement precision of 0.5 %.

The systematic error values are taken from [149, 171], where they were originally determined for the Q_{weak} experiment using an iron foil target of comparable thickness $1 - 4\,\mu\text{m}$, though at a higher electron beam energy of 1.16 GeV and currents up to $4.5\,\mu\text{A}$. Therefore, these values are only provided here for the initial evaluation of systematic and statistical errors for the given case. Due to differences in beam energy, current, and the stricter requirements for beam position and angle stability in the P2 experiment [63], these estimates serve as a conservative upper limit for the total systematic uncertainty in the polarization measurement.

The primary possible source of systematic errors in both cases is the positioning and alignment accuracy of the beam and magneto-optical system. These requirements are particularly strict for the iron target when the brute force technique is used for target polarization (see section 8.2.1). For the iron target, additional systematic contributions from target heating, the Levchuk effect, and high-current extrapolation lead to a total systematic error exceeding the 0.5 % requirement. However, this remains consistent with the intended purpose of the initial measurements using this target. The maximum possible statistical uncertainty is given for the hydrogen target to estimate the measurement time needed to achieve the required precision provided in table 9.3. However, over the full P2 experiment duration of ~10 000 h, the measurement error will ultimately be determined only by systematic uncertainties.

Table 8.6 compares estimated measurement parameters for a Møller polarimeter with the hydrogen and iron targets to meet the required beam polarization precision for the P2 experiment. Since the required measurement uncertainty is not achievable for the iron target (as shown in table 8.5), the statistical error for the hydrogen target is used as a reference for comparing the performance of the two targets.

Parameter \ Target	Hydrogen (H)	Iron (Fe)
$P_{\text{beam}} \times \langle A_{zz} \rangle$	0.85×0.774	
P_{target}	1	0.08
$\left(\Delta P_{\text{target}}/P_{\text{target}}\right)_{\text{stat}}$	0.017*	
t_{meas}, min	~0.46	~3.80
$R_{\text{Møller}}$, Hz	1.65×10^4	5.48×10^5
$N_{\text{Møller}}$	4.54×10^5	1.25×10^8

*The measurement uncertainty of 0.17 % from table 8.5 is used as a reference value for comparison of the performance of two targets.

Table 8.6.: Comparison of estimated measurement parameters for a Møller polarimeter using different targets to meet the required beam polarization precision for the P2 experiment. For simplicity, the detection efficiency of 100 % is assumed ($\epsilon(x) = 1$ in eqs. 8.9 and 8.12). The calculations are performed within the optimal energy acceptance, corresponding to an angular acceptance of $\theta \in 90\,\text{deg} \pm 5\,\text{deg}$ (see table 8.4).

Table 8.7 compares the characteristics and performance of various Møller polarimeter designs with the proposed configuration for the P2 experiment.

Parameter \ Facility	JLAB [148]	TESLA [153]	MESA (P2)	
Target	Fe	Fe	H	Fe
E_{beam}	1 − 6 GeV	250 GeV	155 MeV	
θ_{lab}, deg	1.83-0.74	0.11	4.63	
p_{lab}	0.5 − 3 GeV	125 GeV	77.5 MeV	
$(\Delta P_{\text{target}}/P_{\text{target}})_{\text{syst}}$	0.5 %	≃1.3 %	∼0.47 %*	∼0.67 − 0.84 %*
$\Delta P_{\text{target}}/P_{\text{target}}$	≃1.1 %	≃1.4 %	≲0.5 %*	-

*Estimated values from table 8.5.

Table 8.7.: Comparison of characteristics and performance of various Møller polarimeter designs with the proposed configuration for the P2 experiment at MESA. The given values of θ_{lab} and p_{lab} correspond to the symmetric Møller scattering case ($\theta_{\text{CM}} = 90°$). Reproduced and adapted from [153].

8.6. Expected Counting Rates

The electron density of the target is given by

$$\rho^e_{\text{target}} = N_A \, \rho \, \frac{\overline{Z}}{\overline{A}}, \tag{8.18}$$

where N_A is the Avogadro number, ρ is the density of the target material, $\overline{Z}$ and $\overline{A}$ are the mean atomic number and atomic mass, respectively.

The number of electrons hitting the target per second is related to the beam current I_{beam} as

$$N^e_{\text{beam}} = \frac{I_{\text{beam}}}{q_e}, \tag{8.19}$$

where q_e is the electron charge.

The counting rate, defined as the number of scattering events per second, is given by

$$R = l_{\text{target}} \, \rho^e_{\text{target}} \, N^e_{\text{beam}} \, \sigma_{\text{Møller}} = \mathcal{L}_{\text{eff}} \, \sigma_{\text{total}}, \tag{8.20}$$

where l is the target length, $\mathcal{L}_{\text{eff}} = l_{\text{target}} \, \rho^e_{\text{target}} \, N^e_{\text{beam}}$ is effective luminosity, and σ_{total} is the total cross-section of corresponding scattering process defined by integrating the differential cross section over the acceptance.

The expected Møller scattering rate in the experiment can be estimated based on the non-polarized differential cross section σ_0 defined by eq. 7.2 as

$$\sigma_{\text{Møller}} = \int_{\phi_{\min}}^{\phi_{\max}} d\phi \int_{\theta_{\min}}^{\theta_{\max}} \frac{\alpha^2}{2 \, E_B \, m_e} \frac{(3 + \cos^2 \theta_{\text{CM}})^2}{\sin^4 \theta_{\text{CM}}} \, d\theta. \tag{8.21}$$

For the ep scattering, the expected scattering rate can be estimated using the Mott differential cross section from eq. 2.43:

$$\sigma_{\text{Mott}} = \int_{\phi_{\min}}^{\phi_{\max}} d\phi \int_{\theta_{\min}}^{\theta_{\max}} \frac{\alpha^2}{4E^2 \sin^4\left(\frac{\theta}{2}\right)} \cos^2\left(\frac{\theta}{2}\right) d\theta. \tag{8.22}$$

The calculated values of the expected scattering rates are summarized in table 9.2 (section 9.3), providing a comparison with the simulation results for different acceptances.

9 Geant4 Simulation

This chapter details the simulation conducted in the framework of this thesis for the Møller polarimeter design presented in the previous chapter. The content represents a more comprehensive analysis of the results in [7]. All simulations were conducted using the Geant4 toolkit (version 11.2) [73–75]. The simulation project code is available at [172].

9.1. Simulation Model

The simulation model, shown in figure 9.1, includes all the relevant components described in section 8.3 to consider all possible sources of secondary scattering within the polarimeter, with simplification of certain auxiliary elements, such as connection flanges, etc. All components were implemented with slightly simplified geometries using the solids (geometrical shapes) supported natively by GEANT4. Additionally, a series of virtual detector planes is added to monitor the distribution of scattered events at different stages of passing through the simulation model.

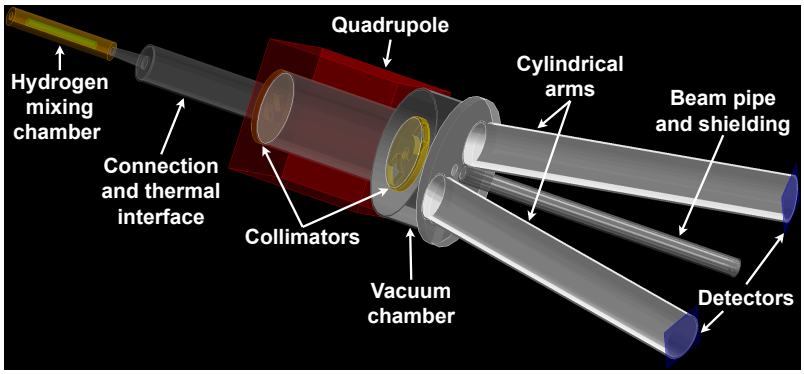

Figure 9.1.: Rendering of the implemented GEANT4 simulation model with hydrogen target.

Table 9.1 shows the main simulation parameters used in the GEANT4 simulation. It is worth mentioning again that the beam current needs to be significantly decreased during the measurement with the iron target.

The simulated angular range was chosen to exceed the acceptance of the polarimeter with reasonable extension to exclude background underestimation while avoiding excessive increases in simulation time. For Møller scattering, the simulated range was set to cover the maximum achievable energy range of $1 - 154\,\mathrm{MeV}$, based on limitations in numerical integration over the phase space arising from the rapid growth of cross-section components at low scattering angles. This corresponds to a polar scattering angle range of approximately $4.21 - 5.10°$. The angular acceptance for ep scattering was chosen to be the same, as further extending the range significantly decreases the fraction of generated events reaching the detector area, leading to longer simulation times without significantly impacting the event rate at the detectors. These limits ensure coverage of all polarimeter components, from the inner radius of the beam pipe to the edges of the quadrupole body (figure 8.4).

Parameter	Value	
	H target	**Fe target**
Target length	20 cm (effective[a])	5 µm
Z-offset relative to the solenoid center	-	−4.25 cm
Beam energy	$E_{\text{beam}} = 155$ MeV	
Møller acceptance of interest	$70 - 85$ MeV ($E_{\text{Møller}}[\theta^{\text{CM}} = 90°] \pm 7.5$ MeV); $\theta^{\text{lab}}_{\text{Møller}} \sim 4.21 - 5.10°$ [b]	
Polar angle collimation at the quadrupole entrance[c]	$\theta^{\text{lab}}_{\text{instr}} \sim 1.8 - 3.2°$	
Simulated Møller range	$1 - 154$ MeV ($\theta^{\text{lab}}_{\text{Møller, sim}} \sim 0.4 - 45°$)	
Simulated ep range	$\theta^{\text{Møller, sim}}_{\text{lab}} \sim 0.4 - 45°$	
Simulated azimuthal range	$\phi_{\text{sim}} \in [0, 2\pi]$ rad	
Azimutal collimation at the quadrupole entrance[d]	$\Delta\phi_{\text{instr}} \approx 177.4°$	$\Delta\phi_{\text{instr}} \approx 76.8°$
Target density	5.0×10^{-9} g/cm^3	7.87 g/cm^3
Target areal density	$\sim 10^{-7}$ g/cm^2	$\sim 10^{-3}$ g/cm^2
Target electron density	2.99×10^{15} e$^-$/cm^3	2.21×10^{24} e$^-$/cm^3
Beam current	150 µA $\sim 10^{15}$ e$^-$/s	0.25 µA $\sim 10^{12}$ e$^-$/s
Solenoid magnet	$B = 8.0$ T, $R_{\text{aperture}} = 5$ cm, $L = 40$ cm	
Quadrupole magnet	$G = 1.5$ T/m, $R_{\text{aperture}} = 10$ cm, $L \approx 40$ cm	

[a] Based on the atomic hydrogen density profile (see figure 8.3 and discussion in section 9.3).
[b] Scattering angles not affected by the solenoid focusing effect.
[c] Corresponds to the Møller angular acceptance of interest at the quadrupole magnet entrance in the presence of the solenoid focusing effect.
[d] Averaged value based on the shape of the collimator at the quadrupole entrance (figure 8.5a).

Table 9.1.: Polarimeter operating parameters used in the simulation.

The solenoid and quadrupole magnetic fields are implemented as pre-calculated field maps throughout the entire simulation model volume to avoid sharp discontinuities and account for distortions in focusing properties caused by fringe field components. The superconducting solenoid field was calculated for a corresponding air-core model, whereas the quadrupole field was simulated based on a realistic iron-core model. The solenoid field strength and quadrupole gradient were iteratively adjusted to balance energy acceptance of the collimation system, minimize low-angle scattered background at the quadrupole entrance, and optimize final focusing and detector area size.

The simulation time for a set number of initial particles depends on the complexity of the detector geometry and the chosen physics models. GEANT4 offers various models for the same process, balancing accuracy and computational cost. Choosing the appropriate set of physics models included in the simulation requires selecting the most relevant processes while ensuring reasonable precision since the results can depend significantly on included physics. The FTFP_BERT GEANT4 physics list, recommended for collider physics applications [173], was used in all simulations. It is well-suited for this study as it accurately models electromagnetic interactions. The included hadronic components effectively handle low-energy nuclear effects, ensuring realistic background estimations. Moreover, the physics lists provided by the GEANT4 collaboration undergo regular technical and physics validation. Additionally, all simulations were done without applying internal step length calculation limits.

9.2. Particle Generators

Due to the low probability of signal events relative to the incident beam rate, a direct simulation would require a large number of generated events to achieve statistically significant results, leading to an increase in computational time. To address this, the simulation can be biased by generating more signal events relative to background events. While GEANT4 provides built-in biasing tools, dedicated custom event generators allow for incorporating more complex processes, such as initial state radiation and simulating events within the defined acceptance. Once an event is generated, the standard GEANT4 physics libraries handle the rest of the simulation, including interaction with the material and magnetic fields within the simulation model. To maintain accuracy, the artificial enhancement of signal events is corrected by weighting them according to their cross sections in the analysis.

For these reasons, custom event generators for elastic unpolarized ep-scattering and polarized Møller scattering were used to reduce simulation time. The Møller generator produces signal events represented by pairs of Møller electrons, while the ep generator estimates the pure contribution to the background. The code for the generators, which includes the complete calculation of QED radiative corrections discussed in section 7.4, is entirely based on the corresponding implementation in the Geant4 simulation project [174] developed for the PRad experiment [175]. These generators were validated in the PRad experiment, demonstrating good performance. In that experiment, the extracted ep scattering cross section, used for measurements of electromagnetic proton form factors, was normalized to the Møller scattering cross section, measured simultaneously within the same detector acceptance. However, since the beam energy in the PRad experiment was 1.1/2.2 GeV, the generator performance for the case of lower energy, 155 MeV in the present case, was additionally checked. The previous results from the Møller polarimeter at MAMI [146] were used as reference data. After adjusting the generator parameters, such as inelasticity cuts, switching to the same beam energy, and applying similar aperture cuts, both types of generators showed good agreement with the reference results.

The Monte Carlo simulation using these custom event generators proceeds as follows:

1. **Differential Cross Section Calculation.** After initializing generator parameters based on the beam energy, both non-radiative and radiative differential cross sections are evaluated over the full polar angle acceptance using a defined step size. An interpolator (a ROOT [176] class object) is used to obtain cross-section values at intermediate scattering angles.

2. **Scattering Angle Sampling Initialization.** A self-adapting Monte Carlo event generator of the TFOAM class (part of the ROOT framework) is initialized to sample the scattering angle using the differential cross section as the probability density function.

3. **Event Type Determination and angle sampling.** The event generator selects the event type (non-radiative or radiative) based on their cross-section contributions to the total cross section and then samples the scattering angle, weighted by the corresponding cross section.

4. **Event Weight Calculation.** The corresponding event weight is calculated using the differential cross section value provided by the interpolator for the given sampled angle, as well as the beam current and target properties.

5. **Event Construction.** The final four-momenta of all particles are constructed, the effective cross-section is calculated, and the event is generated, including the production of all involved particles.

6. **Particle Tracking and Physics Interactions.** Geant4 simulates the step-by-step propagation of particles generated within an event as they traverse the defined geometry and magnetic fields. At each step, the probabilities of various physical interactions are calculated based on the included physics processes, the particle's properties, and the materials encountered. If an interaction occurs, Geant4 simulates the resulting particles and their properties.

7. **Logging.** Following each event, relevant particle parameters (scattering angle, energy, momentum components, particle type, cross section, rate, etc.) and detector hit data, hits at virtual detector planes, are logged in a ROOT file. Additionally, event rates are normalized by the total number of generated events to ensure accurate signal count representation.

After the initial execution of the first two steps, steps 3–7 are repeated for the given number of generated events. Once the simulation is complete, the ROOT file is stored for further analysis.

Figure 9.2 presents the energy spectrum and scattering angle distributions of the generated events for Møller and ep scattered events. Since events are sampled according to their cross-sections during generation, the number of events per bin provides cross-section information. The event rate, however, is determined by the product of the total cross-section integrated within the simulated acceptance and the effective target luminosity (see eq. 8.20). While both factors are constants in this case, they are target-specific.

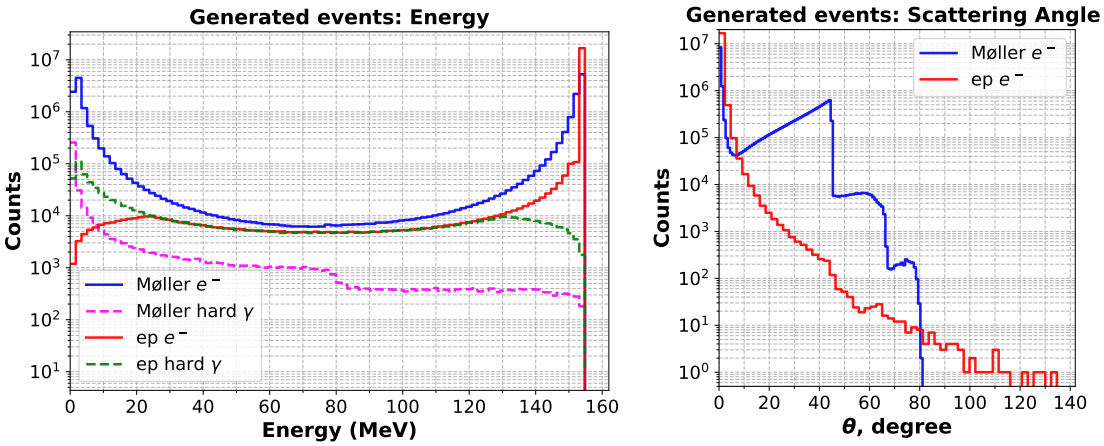

Figure 9.2.: Energy spectrum and scattering angle distributions of the generated events. The distributions for Møller and ep electrons include both non-radiative and radiative contributions. The y-axes (in logarithmic scale) represent event counts rather than rates to ensure consistency across different targets (see explanation in text).

9.3. Results and Analysis

The results below are given in the order as the polarimeter design was developed: from optimizing the collimating system to ensure the balance between maximum background suppression and minimal signal loss for both targets, as stated in section 8.3, completing with assessing/calculating the detector system parameters. For simplicity, all calculations and estimations assume an idealized detector with a detection efficiency of 100 %. To ensure reasonable statistics, 10 and 20 million events were generated by the Møller and Ep generators, respectively, in each study. In the case of the collimation system studies, reduced event samples of 5 million were used for each generator and target.

9.3.1. Collimation System

Figure 9.3 compares the radial energy distribution of simulated Møller and ep events (including radiation parts) at the quadrupole entrance with full azimuthal coverage–without any collimation or cuts applied. The differences in the results for each target are primarily caused by their different lengths. In the case of the hydrogen target, which can be considered a set of thin targets along the beam axis, the solenoid magnet focuses the electrons that emerge from different positions along the target differently. Thus, all the distributions for the hydrogen target derived from the superposition of results for a set of thin ones shifted along the mixing chamber.

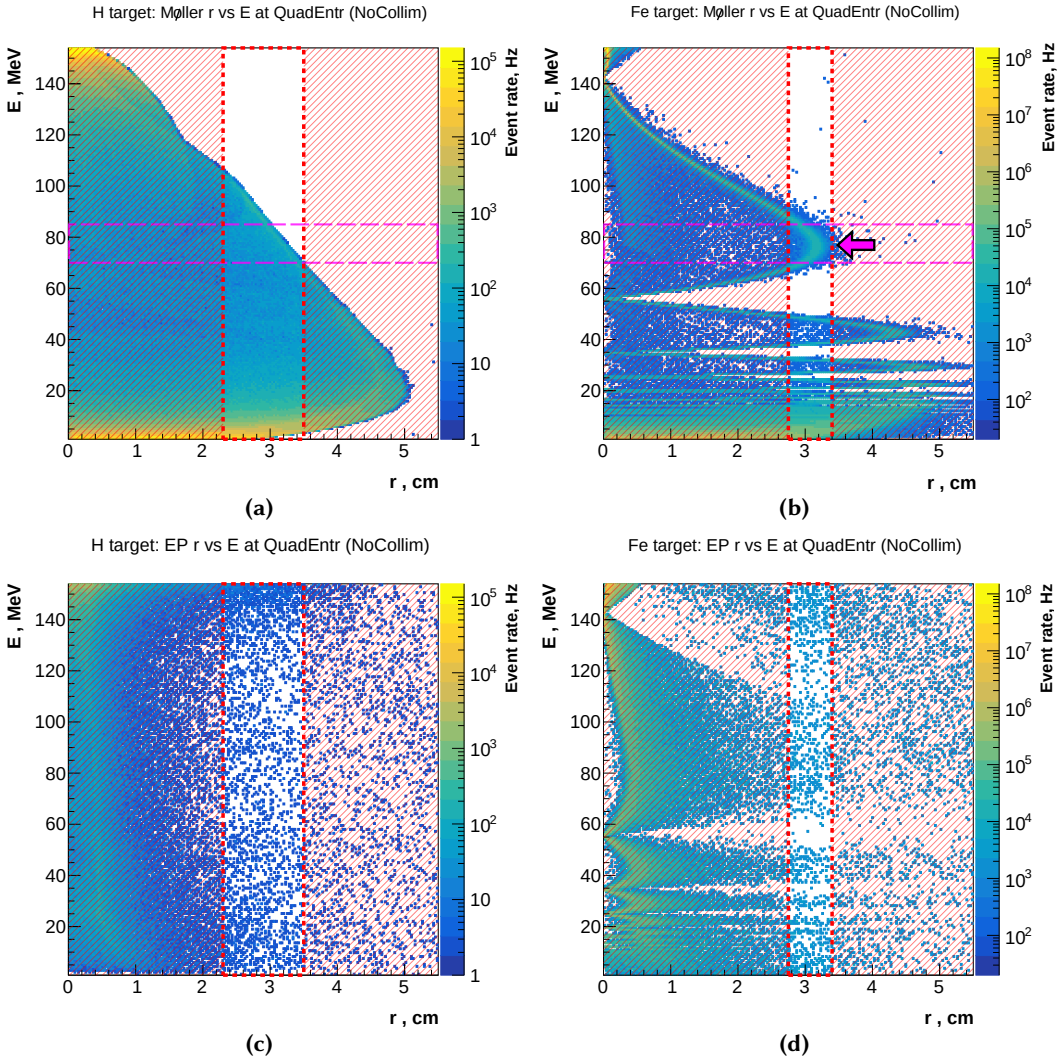

Figure 9.3.: Radial energy distribution of (a, b) Møller and (c, d) ep electrons at the quadrupole magnet entrance for the hydrogen (left group) and iron (right group) target cases. Two red hatched rectangles in each case bound inside the collimation aperture window of interest. Simulated acceptance for generators is given in table 9.1.

From the analysis and comparison of the distributions, it can be seen that in each target case, a significant part of the ep background is concentrated inside a radius of ~2 cm (figures 9.3c and 9.3d). Meanwhile, most of the Møller events (comprising both the potential signal and the radiation part, which contributes to the background) within the chosen energy acceptance of $70 - 85$ MeV scatter up to a radius of ~3.5 cm (figures 9.3a and 9.3b). Consequently, excluding all the events outside the collimation apertures (red-shaded areas in figure 9.3) will significantly

suppress the background, with acceptable signal loss. The iron target offset was optimized to align the local peak of the energy distribution (indicated by the magenta arrow in figure 9.3b) with the center of the energy acceptance of interest. This ensures symmetrical aperture cuts on the energy acceptance, minimizing the inclusion of potential background. Furthermore, the symmetric Møller electrons, for which the analyzing power is maximal (figure 7.2), are positioned radially as far from the beam as possible. The specific angular and vertical dimensions of collimation windows were optimized for each target.

Collimation System Performance. Figure 9.4 demonstrates the performance of the implemented collimation system by comparing the XY hit density distributions of Møller and ep events at the quadrupole magnet entrance, both before and after applying radial collimation.

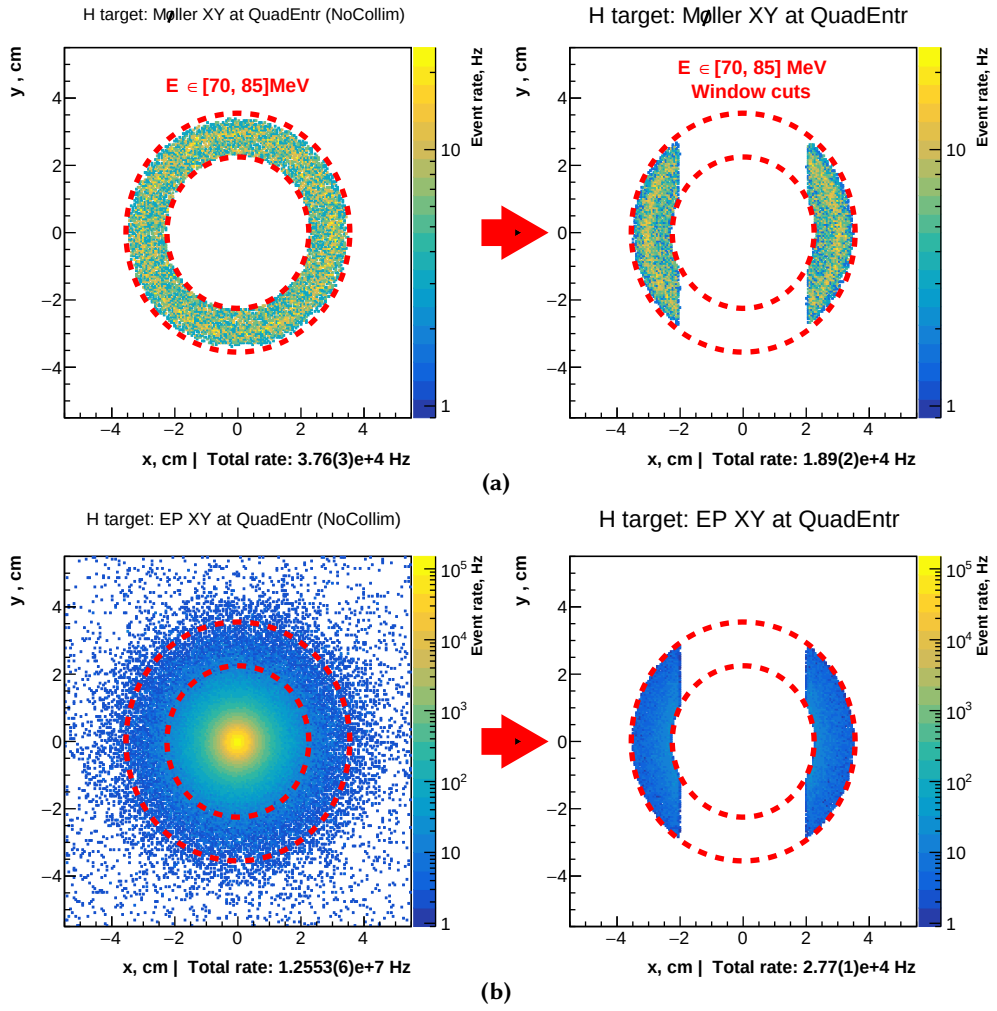

Figure 9.4.: XY hit density distributions of generated (a) Møller and (b) ep events at the quadrupole magnet entrance before and after implemented collimation at the quadrupole entrance for the hydrogen target. Dashed red circles indicate the minimum and maximum radii of scattering aperture cuts by the collimator (fig. 8.5a). Secondary scattered electrons outside the collimation region are excluded on all plots except for the ep scattering case without applied collimation for descriptive reasons.

In figure 9.4a, only Møller events within the energy acceptance of interest are selected. Without physical collimation, the left plot includes events only within the radial aperture with full azimuthal coverage. Meanwhile, the right plot–with the implemented collimator at the

quadrupole entrance–additionally excludes secondary scattered electrons outside the collimation window regions. This comparison shows how many potential signal Møller events pass through the first collimator's windows (figure 8.5a) and demonstrates an acceptable potential signal loss as seen by the relatively small drop in the rate.

Figure 9.4b evaluates the suppression of the ep background. In this case, the only additional constraint is that the right plot again presents results with the applied collimation at the quadrupole entrance and excludes secondary scattered electrons outside the collimation window regions. Therefore, this comparison reveals the fraction of background events entering the quadrupole magnet freely, thus providing a rough estimate of the level of background suppression based on the decrease in the rate of more than two orders of magnitude.

Figure 9.5 provides the same comparison of the XY hit density distributions of Møller and ep events at the quadrupole magnet entrance for the iron target. Again, the applied collimation system demonstrates an acceptable potential signal loss while effectively suppressing the background.

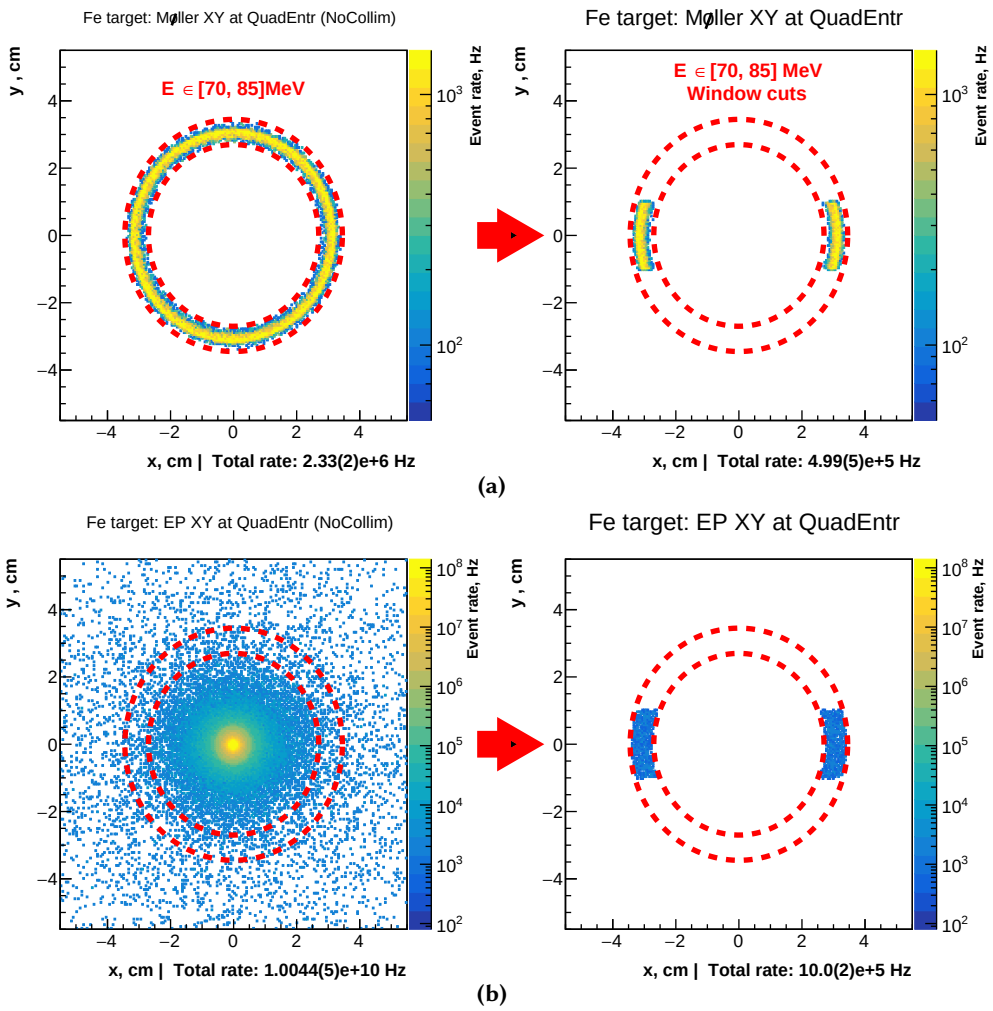

Figure 9.5.: XY hit density distributions of generated (a) Møller and (b) ep events at the quadrupole magnet entrance before and after implemented collimation at the quadrupole entrance for the iron target. Dashed red circles indicate the minimum and maximum radii of scattering aperture cuts by the collimator (fig. 8.5a). Secondary scattered electrons outside the collimation region are excluded on all plots except for the ep scattering case without applied collimation for descriptive reasons.

The size of the collimation windows at the quadrupole end (fig. 8.5b) was optimized to pass all potential signal electrons further into the cylindrical arms.

9.3.2. Energy Distribution at the Detectors

Following beam propagation, figure 9.6 shows energy distributions along the defocusing axis and rates of Møller events remaining after passing the applied collimation for both targets. The left plots include the radiative contribution, accidental single Møller electrons, and secondary electrons produced along the way, which are also classified as background. The right plots, in turn, only include signal Møller pairs selected within the expected detecting area and energy acceptance, corresponding to the pure signal under the coincidence condition (row "R_S" in table 9.3).

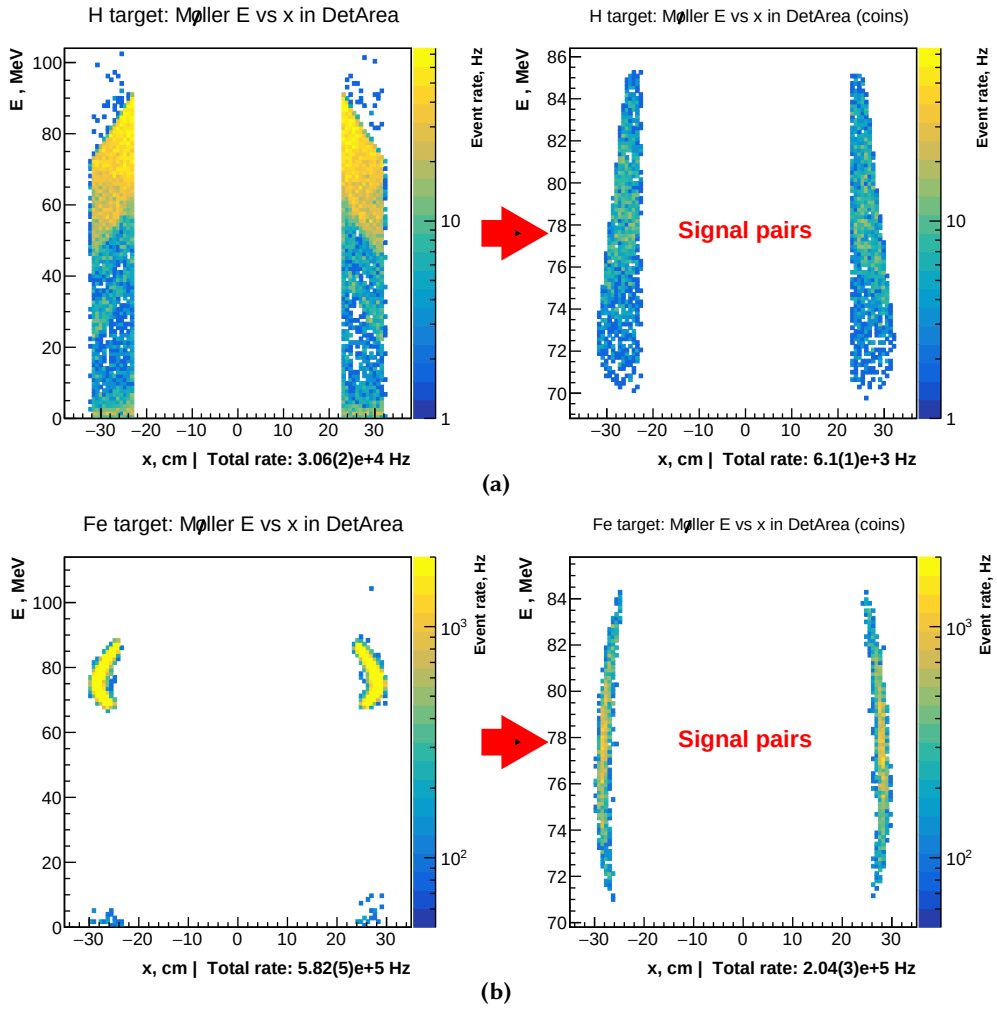

Figure 9.6.: Energy distributions along the X-axis of Møller events at the detector planes for the (a) hydrogen and (b) iron target cases. The X-coordinates are corrected for the detectors' rotation angle of 12° (figure 8.4). The left plots include the radiative contribution, accidental single Møller electrons, and secondary scattered electrons from interactions with polarimeter components, while the right plots show only selected signal events.

Figure 9.7 shows the same distributions but for the background part represented by ep events and produced along the way secondary electrons that reach the detecting region (row "R_b" in table 9.3).

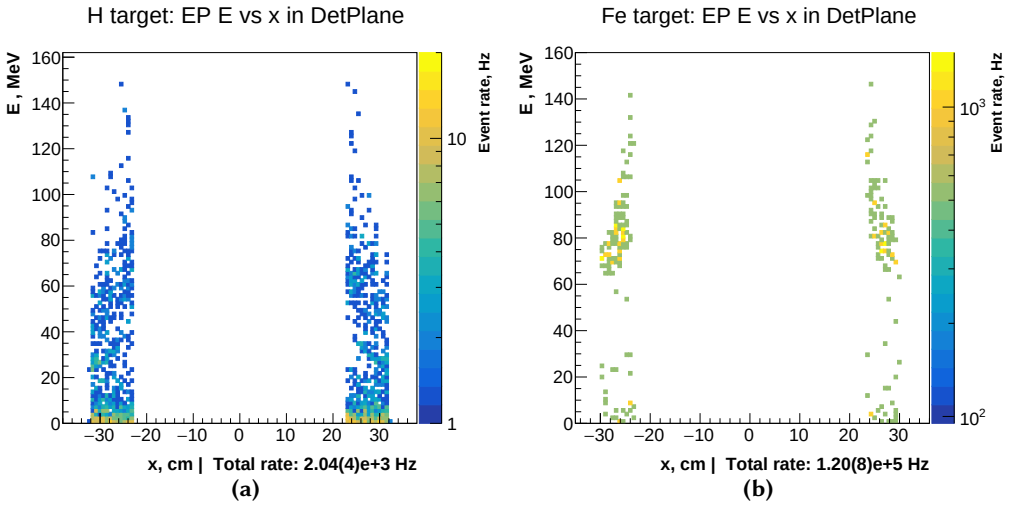

Figure 9.7.: Energy distributions along the X-axis of ep events, including the radiative part and secondary scattered electrons from interactions with polarimeter components, at the detector planes for the (a) hydrogen and (b) iron target cases. The X-coordinates are corrected for the detectors' rotation angle of 12° (figure 8.4).

9.3.3. XY Distribution at the Detectors

Figure 9.8 shows an example XY hit distribution at the end of the cylindrical arms for scattered electrons, including secondaries, remaining after passing the applied collimation.

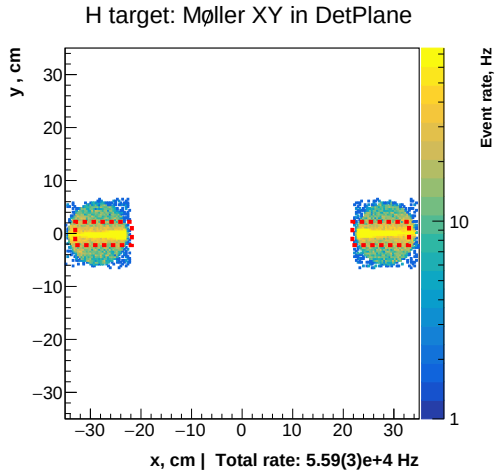

Figure 9.8.: Example of XY hit density distributions of electron hits produced by Møller generator at the detector planes with the hydrogen target. The size and location of the detecting areas, which correspond to the acceptance of interest, are delineated by red dashed rectangles in all plots.

The detection regions have approximate dimensions of approximately 10 cm × 2.5 cm for the hydrogen target and approximately 7 cm × 1 cm for the iron target.

9.3.4. Effective Length of the Hydrogen Target

Figure 9.9 shows the vertex positions of the Møller signal pairs that reach the detecting area for the hydrogen target case with the given instrumental acceptance. As seen, all pair vertices are confined within ~8 cm of the initially simulated hydrogen target length of 20 cm, with a distribution peak shifted in the negative direction relative to the center of the solenoid by about 3 cm. Although this result indicates some hydrogen target regions do not contribute to the

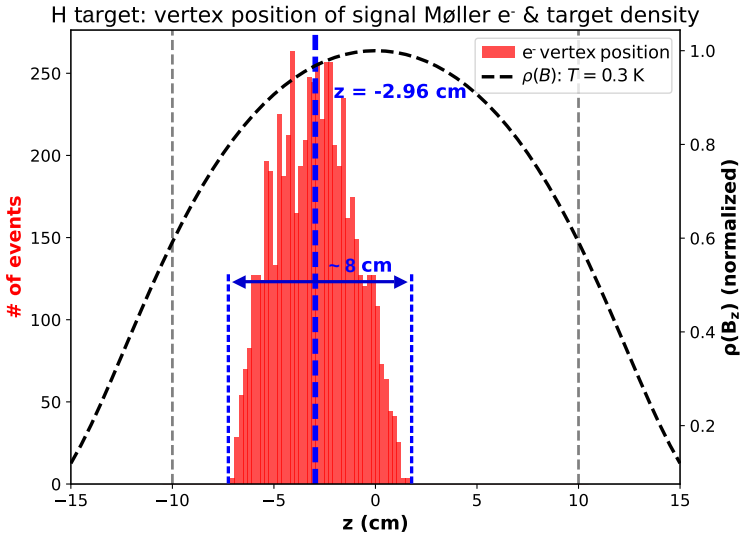

Figure 9.9.: Distribution of vertex positions of Møller signal pairs within the simulated hydrogen target length of 20 cm (indicated by dashed gray vertical lines) that reach the detectors within the instrumental acceptance of interest. For reference, the normalized hydrogen target density profile (dashed black line) from figure 8.3 is added with z-values on the right. The vertical dashed blue line marks the mean of the vertex position distribution, determined from a Gaussian fit (not shown), with a central value of $z = -2.96$ cm.

registered signal, the available signal rate remains sufficient for good performance, as shown in table 9.3. Furthermore, the observed shift in the distribution is still within the acceptable target density region (figure 8.3). However, this fact should be considered, for example, when validating the signal rate (table 9.2).

9.3.5. Comparison of Expected and Simulated Event Rates

Table 9.2 compares the expected Møller and ep scattering rates, calculated using the leading-order ultrarelativistic cross sections [177], with the results obtained in simulation for both iron and hydrogen targets for different acceptance scenarios.

As can be seen, the particle generators used show good agreement with independent calculations for cases with full azimuthal coverage—i.e., without applied collimation—within the total simulated energy acceptance ("Simulated acceptance") and energy acceptance of interest ("Møller acceptance of interest (full azimuthal coverage)"). The observed increase in the rate in these two cases is within the expected value due to radiative corrections.

In the last case, which corresponds to energy acceptance of interest and the corresponding azimuthal coverage defined by the implemented collimation system, a discrepancy that cannot be attributed to the radiation corrections arises. However, it can be explained by the rotation of scattered events due to their helical motion in the presence of the solenoid magnetic field. This effect is visible in figure 9.10 an oval-shaped halo of low-energy events ($\leq$ 10 MeV) around the

Parameter \ Target	**Hydrogen (H)**	**Iron (Fe)** (beam: 0.25 µA)
Simulated acceptance		
$\Delta\phi$, rad	2π	
$\theta^{\text{CM}}_{\text{Møller}}$, deg	$\sim 90 \pm 80.8^{*}$	
$\text{Rate}_{\text{Møller}}$, Hz	calc.: 2.85×10^{7}	8.76×10^{8}
	sim.: $3.170(1) \times 10^{7}$ ($\approx +11.2\%$)	$9.756(3) \times 10^{8}$ ($\approx +11.4\%$)
$\theta^{\text{lab}}_{\text{ep}}$, deg	$0.4 - 45$	
Rate_{ep}, Hz	calc.: 1.2467×10^{6}	9.9748×10^{9}
	sim.: $1.2541(6) \times 10^{7}$ ($\approx +0.60\%$)	$1.0029(5) \times 10^{10}$ ($\approx +0.54\%$)
Møller acceptance of interest, full azimuthal coverage		
$\Delta\phi$, rad	2π	
$\theta^{\text{CM}}_{\text{Møller}}$, deg	90 ± 5.55	
$\text{Rate}_{\text{Møller}}$, Hz	calc.: 8.05×10^{4}	2.48×10^{6}
	sim.: $9.07(5) \times 10^{4}$ ($\approx +12.7\%$)	$2.76(2) \times 10^{6}$ ($\approx +11.3\%$)
Møller detector acceptance of interest		
$\Delta\phi^{**}$, deg	≈ 177.4	≈ 76.8
$\theta^{\text{CM}}_{\text{Møller}}$, deg	90 ± 5.55	
$\text{Rate}_{\text{Møller}}$, Hz	calc.: 4.0×10^{4} ($1.6 \times 10^{4***}$)	5.28×10^{5}
	sim.: $6.1(1) \times 10^{3}$ ($\approx -84.8\%$) ($\approx -61.9\%^{***}$)	$2.04(3) \times 10^{5}$ ($\approx -61.4\%$)

*Corresponds to the simulated energy acceptance of $1 - 154$ MeV.
**Average values are taken due to the non-constant phi acceptance over the collimation windows (figure 8.5).
***For the hydrogen target length of ~8 cm within which scattered Møller electron pairs reach the detectors within the instrumental acceptance of interest (see section 9.3.4).

Table 9.2.: Calculation Møller and ep scattering rates using leading-order ultrarelativistic cross sections [177] (calc.) and simulation results obtained for iron and hydrogen targets (sim.). The uncertainties given represent statistical errors and do not contain any systematic effects. Operating parameters used in calculations can be found in table 9.1.

distribution center: the quadrupole magnetic field flattens this distribution, while the residual solenoidal field causes its tilt. In this scenario, Møller signal electrons with different energies experience rotation at varying speeds, disrupting pairwise alignment along the same diametral line. As a result, one electron from the pair may fail to enter the scattering aperture window (figure 8.5a), reducing the signal. Meanwhile, the total number of Møller electrons—including unpaired ones and radiative contribution—within the scattering aperture window remains the same.

For reference, a narrower energy acceptance of $76.5 - 78.5$ MeV ($E_{\text{Møller}}[\theta_{\text{CM}} = 90°] \pm 1$ MeV, against to ± 7.5 MeV in the present case) results in a drop in the signal of ~16 % relative to the expected values for both targets. This also implies a lower relative contribution to the background from Møller scattering. On the other hand, too narrow aperture windows needed to select signals

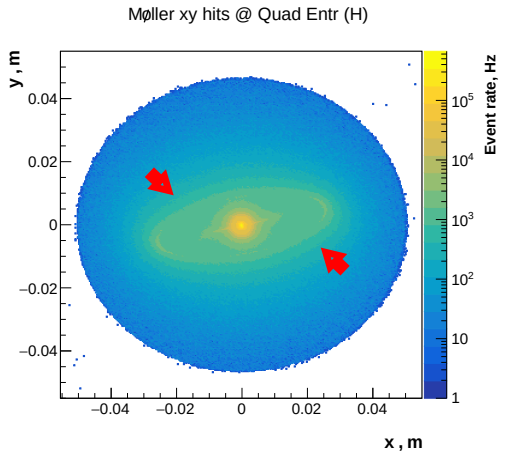

Figure 9.10.: XY hit density distributions of generated Møller events at the quadrupole magnet entrance without collimation at the quadrupole entrance for hydrogen target. The red arrows indicate a rotated oval halo of low-energy events around the beam area.

with corresponding energies (as shown in figure 9.3) would inevitably increase the sensitivity of the polarimeter performance to one of the main sources of systematic errors due to misalignment of the beam, target, and magneto-optical system. Namely, it can increase the contribution of secondary scattering at the edges of collimation windows to the background. Therefore, this approach was discarded in the preliminary analysis of the results.

For the hydrogen target, the calculated Møller rate, considering the full azimuthal coverage constrained by the applied collimation, should be additionally corrected for the effective target region of approximately 8 cm (compared to the simulated target length of 20 cm). This correction is necessary since only signal events within this region reach the detectors (see section 9.3.4). Considering this, the signal drop becomes comparable for both targets (the value in the second set of brackets for the hydrogen target in table 9.2).

9.3.6. Detector Segmentation

As discussed in section 8.4.2, the differential measurement using segmented detectors can enhance the signal-to-background ratio based on the energy dispersion induced by the analyzing quadrupole. This optimization provides better control over systematic uncertainties and background contributions, thereby reducing the required statistics to achieve the desired beam polarization measurement precision.

For the given polarimeter design, detector segmentation is feasible along the horizontal X-axis since the XZ-plane (with the beam propagating along the Z-axis) corresponds to the defocusing plane of the quadrupole magnet. However, since the detector system is considered to consist of thin plastic scintillators as counters and does not provide a direct energy measurement, the segmentation makes sense only in the case of the iron target case. Furthermore, vertical segmentation (in the Y-axis) is complicated because the detector planes are located in the averaged focal point of the quadrupole, optimized for symmetric Møller electrons.

Figure 9.11 illustrates a possible detector segmentation scheme for the iron case along the X-axis. In this simple configuration, the energy acceptance can be divided into three regions, each approximately 5 MeV wide. Given that the signal Møller electron pair hits the detector in

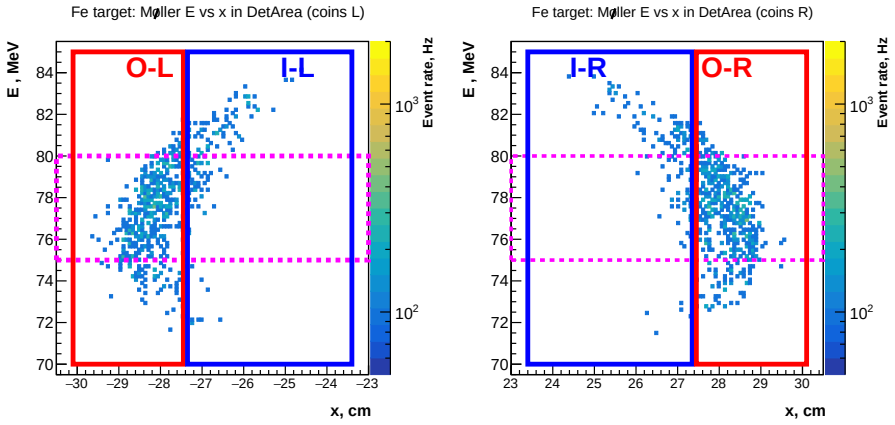

(a) C-shape E dispersion.

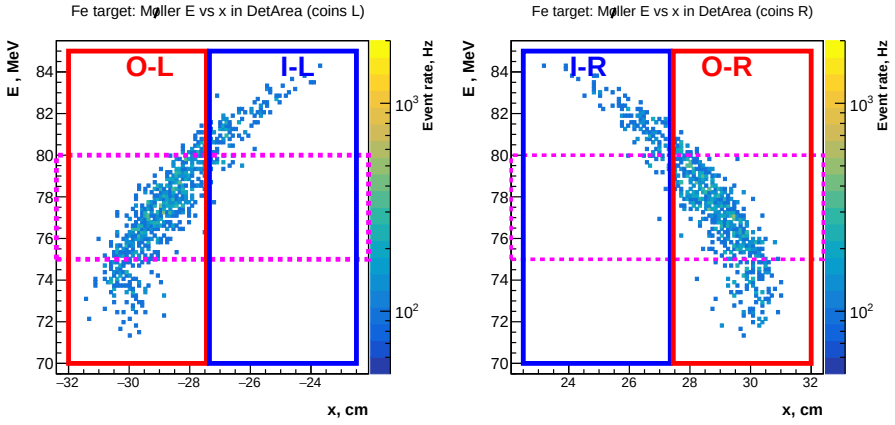

(b) Semi-linear E dispersion.

Figure 9.11.: Energy distributions along the X-axis of signal Møller events at the detector planes with the different iron target z-offsets: (a) a non-linear C-shape energy dispersion with original target offset of −4.25 cm (table 9.1) and (b) a semi-linear energy dispersion with the offset of −3 cm. The X-coordinates are corrected for the detectors' rotation angle of 12° (figure 8.4).

coincidence, with energies symmetrically distributed around 77.5 MeV—the symmetric Møller scattering energy for the beam energy of 155 MeV—an improved coincidence scheme can be implemented as follows:

- A valid event configuration for a signal electron pair with energies in the range 75 – 80 MeV requires simultaneous hits in the outer left and outer right detector segments ("O-L" and "O-R" in figure 9.11);
- Electron pairs where one electron has energy in the range of 70 – 75 MeV and its pair in the range of 80 – 85 MeV correspond to events with one hit registered in an inner or outer segment of one detector and the opposite segment of the other one (for example, the combination of "I-L" and "O-R" segments is valid in this case);
- The coincidence configuration where both electrons hit the inner segments ("I-L" and "I-R") is excluded. Therefore, the inner segments can be used for additional background evaluation.

The given iron target offset results in energy dispersion following a non-linear *"C-shape"* distribution, as shown in figure 9.11b, due to the initial radial distribution at the quadrupole entrance (see figure 9.3b). Based on the additional studies, this can be partially improved

by adjusting the Z-offset of the target from −4.25 cm to −3 cm. This adjustment results in a *semi-linear* energy dispersion at lower energies, as illustrated in figure 9.11b. However, this improvement comes at the cost of a reduced signal-to-background ratio, which worsens by nearly a factor of two (see table 9.3). This happens because the modified target position offset slightly alters the collimation condition at the quadrupole entrance for the local peak of the energy distribution being aligned with the center of the energy acceptance window, as indicated by the magenta arrow in figure 9.12, in contrast to the initial configuration, which features nearly perfect peak alignment, as shown in figure 9.3b. This results in larger radial collimations, inevitably including more low-energy non-pair Møller electrons with energies below 70 MeV.

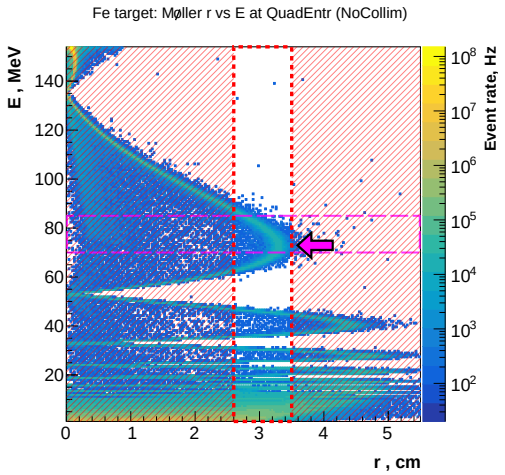

Figure 9.12.: Radial energy distribution of Møller electrons at the quadrupole magnet entrance for iron target cases with semi-linear energy dispersion. Two red hatched rectangles in each case bound inside the collimation aperture window of interest. The magenta arrow indicates the position of the local energy distribution peak.

The rate results and measurement time calculations in the following section incorporate these two segmentation configurations with adjusted iron target position and the collimation system, referred to as *C-shape* and *semi-linear* dispersion options.

9.3.7. Rates and Detector System

Table 9.3 presents the simulation results and rate and measurement time (required to achieve the stated beam polarization error) estimations calculations for the signal-to-background ratio (*SBR*) for both targets, with an assumed detector time resolution $\tau_{det} = 1$ ns. The presented values of the measurement time aim to compare the difference in performance between both targets in achieving the same precision level, which was arbitrarily chosen to be equal to the maximum possible statistical error for the hydrogen target of 0.17 % (table 8.5) in both cases. For simplicity, the following values were used in the measurement time calculations: $\langle A_{zz} \rangle = 7/9$, $P_{\text{target}}(\text{H}) = 1$, $P_{\text{target}}(\text{Fe}) \sim 0.08$, $P_{\text{beam}} = 0.8$.

The calculated measurement time required to achieve the reference statistical precision of 0.17 % (as specified in table 8.5) exceeds the initial estimates in table 8.6 for both targets. However, this increase directly correlates with the drop in the signal, which aligns with expectations based on the analysis in table 9.2, where simulated scattering rates are compared with calculated estimates for different azimuthal and polar coverages. Despite this drop in the signal, the rate values, along with the calculated SBR and measurement time, indicate good polarimeter performance and ensure sufficient statistical precision within a reasonably short measurement

Parameter	Target material		
	Hydrogen (H)	Iron (Fe) (0.25 μA)	
		C-shape[1]	semi-linear[1]
τ_{det}	1 ns		
$R_{Møller}$, Hz	$3.06(2) \times 10^4$	$5.82(5) \times 10^5$	$8.01(6) \times 10^5$
R_S[2], Hz	$6.1(1) \times 10^3$	$2.04(3) \times 10^5$	$2.16(3) \times 10^5$
R_{ep}, Hz	$2.04(4) \times 10^3$	$1.20(8) \times 10^5$	$2.2(1) \times 10^5$
R_B[3], Hz	$2.65(2) \times 10^4$	$5.0(1) \times 10^5$	$8.1(1) \times 10^5$
$R_B[\tau_{det}]$[4], Hz	$7.0(1) \times 10^{-1}$	$2.5(1) \times 10^2$	$6.4(2) \times 10^2$
$SBR[\tau_{det}]$[4]	~8665	~824	~334
t_{meas}[5], min	~1.3	~10.2	~9.6

[1]The energy dispersion configuration for the iron target (see section 9.3.6).
[2]Møller signal pairs only.
[3]The total background rate, including the contribution of Møller and ep radiation parts.
[4]Within the detecting time window $\tau = 1$ ns.
[5]To achieve the statistical precision of 0.17 % (see table 8.5 and the discussion in this section). The details of calculations are given in appendix A.2.

Table 9.3.: The obtained rates from simulation and evaluated signal-to-background ratio (*SBR*) and measurement time for both targets. The Møller and ep scattering rates include the radiative part and secondary scattered electrons from interactions with polarimeter components.

time with both hydrogen and iron targets. This, together with the size of detection regions (section 9.3.3), defines scintillation detectors made of polystyrene, each with dimensions of approximately 10 cm × 2.5 cm and a thickness of ~1 cm, as a suitable option for both targets.

9.3.8. Photons and Secondary Electrons

The key challenge in developing a particle scattering setup is creating a suitable design that effectively isolates the signal from large-angle scattered electrons while suppressing various background processes at the detector system. Bremsstrahlung photons, secondary scattered electrons, and secondary emitted photons are the main sources of secondary contributions to the background in Møller polarimetry. They are produced when primary particles and, subsequently, secondary particles interact with polarimeter components, particularly at the collimator edges and with components in the region close to the detectors, like the cylindrical arms in the present design (figure 8.4). Figure 9.13 shows the vertex positions of all electrons produced in the ep scattering that reach the detector in the hydrogen target case.

Hard photons emitted in radiative processes from particle generators and bremsstrahlung photons emerging from the target represent additional potential background sources. However, the polarimeter geometry suppresses these photons from reaching the detectors. While the quadrupole magnet introduces additional deflection for the electrons in the defocusing plane (figure 8.4), the tracks of electrically neutral photons remain straight, preventing them from reaching the detectors. A detailed simulation of the detector system is beyond the scope of this study. However, preliminary simulations confirmed the efficient geometrical suppression of bremsstrahlung photons that emerged from the target. Furthermore, simulations using the built-in GEANT4 beam generator (G4PARTICLEGUN) demonstrated that the contribution of secondary gamma particles [1] reaching the detectors is negligible.

[1]In the GEANT4 toolkit, a gamma particle (G4GAMMA class) represents photons that may originate from various

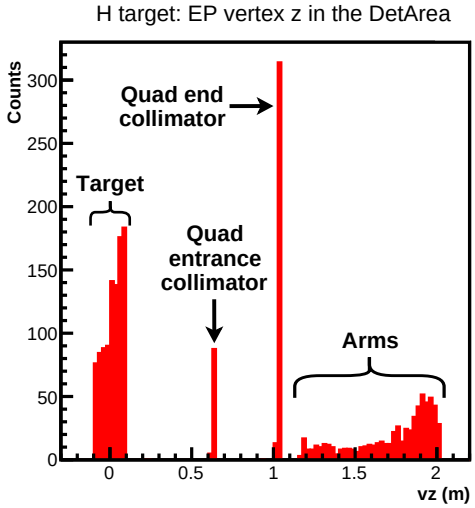

Figure 9.13.: Example vertex distribution of electrons produced by the ep generator with a hydrogen target, including radiative contributions and secondary scattered electrons from interactions with polarimeter components at the detector planes.

The impact of secondary gamma particles reaching the detectors was omitted from these studies based on the following considerations:

- Although the gamma event rates are 2-3 orders of magnitude higher compared to signal rates for each target configuration, most of these gamma photons have energies below 10 MeV, as shown in figure 9.14 on the example of ep scattering with an iron target.
- In a plastic scintillator of approximately 1 cm thickness, the direct energy deposited by a gamma photon through ionization is negligible. Additionally, the probability of a gamma photon interaction, primarily through Compton scattering or pair production, is significantly lower than in the electron case. Moreover, signal threshold discrimination techniques can further suppress the gamma-induced background.

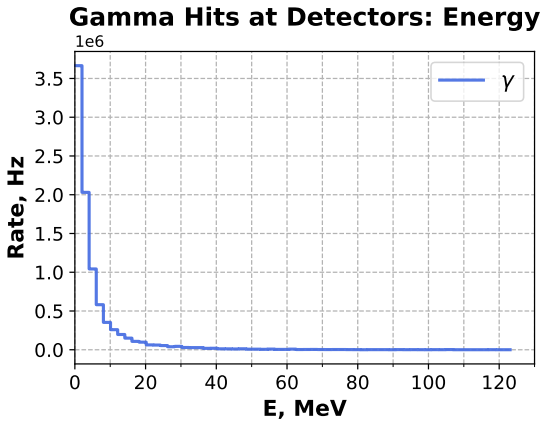

Figure 9.14.: Energy spectrum of secondary gamma photons reaching the detectors in the case of ep scattering with the iron target.

However, further studies will incorporate more detailed detector simulations to further assess the potential impact of gamma photons on the detector system.

physical processes, including bremsstrahlung, scattering, nuclear decay, and annihilation.

9.4. Conclusions and Outlook on the Møller Polarimeter

The simulation results presented in this chapter validate the proof of concept for the double-arm Møller polarimeter design with a magneto-optical system consisting of the long superconducting solenoid magnet and the large-aperture quadrupole analyzing magnet developed in this thesis. The collimation system effectively suppresses background while optimizing signal acceptance, demonstrating compatibility of this design with both iron and hydrogen targets through a simple collimator exchange without requiring modifications to the magneto-optical system.

A preliminary assessment of the uncertainty sources indicates that the required beam measurement precision can be achieved with the hydrogen target. Even though the iron target might not provide the needed precision, it remains important for the intended initial measurements. Simulations using custom event generators that incorporate radiative corrections crucial in high-precision polarimetry measurements demonstrated good agreement with estimated values, confirming the consistency of the results and ensuring that background contributions are not underestimated.

These results demonstrate the feasibility of the proposed design while identifying the potential for further improvements. Future studies will focus on enhancing simulation accuracy. One of the main aspects includes incorporating the Levchuk effect into the simulation for the iron target case to mitigate its impact as one of the main sources of systematic uncertainty. The next steps for the detector system will focus on conducting more detailed simulations, including the response of scintillators with realistic detector efficiency factors to improve simulation precision. Additionally, a more detailed investigation of detector segmentation for the iron target is needed to further optimize the signal-to-background ratio by refining event selection across different segments. For the hydrogen target case, incorporating the target density profile in event sampling and extending the target to its full length may improve accuracy by addressing potential signal overestimation or background underestimation.

Furthermore, consideration should be given to reducing the contribution of secondary scattered electrons after exiting the quadrupole. Additionally, a combined field map calculated simultaneously for both the solenoid and quadrupole could improve the accuracy of the fringe field components and enhance the overall simulation framework.

Beyond these refinements, the possibility of operating the entire polarimetry chain at MESA under a stable intermediate beam current might be examined. If feasible, this approach could eliminate uncertainties associated with high-current extrapolation, thereby improving the robustness of polarization measurements.

Part IV.

Conclusion

10 Summary and outlook

This thesis presents the results of developments and studies done for the P2 experiment in two domains. The first involves refining the tracking detector module design and its cooling system for silicon HV-MAP sensors, which are key components of the detector. The second focuses on developing the design of a double-arm Møller polarimeter with a magneto-optical system that includes a long superconducting solenoid magnet for target polarization and a large-aperture quadrupole analyzing magnet.

The first part of this thesis presents the theoretical framework and an overview design of the P2 experiment. The P2 experiment aims to test the Standard Model of Elementary Particle Physics at the low-energy frontier by precisely determining the weak mixing angle, a fundamental parameter in the SM. This will be achieved by measuring the parity-violating asymmetry in elastic electron-proton scattering at the upcoming MESA facility in Mainz. The experiment is designed to measure the parity-violating cross-section asymmetry in electron scattering on the order of 10×10^{-8}, the smallest ever measured in electron scattering. Given the planned run time of ~11 000 h and projected instantaneous luminosity of approximately $2.38 \times 10^{39}\,\mathrm{cm}^{-2}\,\mathrm{s}^{-1}$, the parity-violating asymmetry A_{PV} can be measured with the expected value of −33.94 ppb [1] and absolute accuracy of 0.56 ppb. This level of precision enables an extraction of the weak mixing angle $\sin^2\theta_w$ at a low momentum transfer $Q^2 = 4.5 \times 10^{-3}\,\mathrm{GeV}^2$ with a relative precision of 0.15 %. Achieving these goals requires advanced experimental techniques, including P2Pix sensors based on HV-MAP technology and a novel atomic hydrogen gaseous target for the Møller polarimeter.

The MESA facility, currently in its final construction phase, will host the P2 experiment and provide the required high beam availability and precise fluctuation control. The first measurements are set to begin in the near future, with significant research and development progress already achieved, including the recent delivery and installation of the superconducting magnet coil at the MESA facility as a major milestone. Furthermore, the P2 experimental has a broad physics program that covers both particle physics and nuclear physics.

The P2 tracking detector is critical in reconstructing individual electron tracks and determining the momentum Q^2 at the target. The P2Pix sensors, based on the novel HV-MAP technology, integrate the readout chip on the sensor substrate, minimizing the material budget while providing high spatial and good time resolution. These features make the sensors ideal for high-rate electron tracking with momenta at which multiple scattering significantly affects the resolution of reconstructed track parameters.

A major design challenge is managing the heat dissipation at the level of ~600 W per module due to the large number of sensors required to achieve 15° azimuthal coverage. To address this, the tracker module incorporates a cooling system with helium gas as a coolant to minimize the material budget in the active area and increase the tracking reconstruction performance.

The second part of the thesis addresses the studies on refining the tracker module design and conducting a detailed assessment of the cooling system's performance, accounting for the non-uniform heat dissipation of P2Pix sensors. CFD simulation results confirm that the current

[1] ppb (parts-per-billion) ≡ 10^{-9}.

cooling system design ensures effective cooling of the P2Pix sensors, even under the high-power consumption scenario. A substantial safety margin of approximately 20 °C in maximum sensor temperature of 70 °C, determined by the glass-transition temperature of the adhesives used for mounting the sensors on the tracker ladders, demonstrates the robustness of the cooling approach. Although the complete global gas distribution system for the tracking detector is still under development, simulation results indicate that commercially available turbo-compressors can maintain sufficient helium flow rates. Further studies and design refinements are ongoing, with planned experimental tests with the thermo-mechanical prototype of the tracker module.

Long-term scattering asymmetry measurements at the Mainz Microtron MAMI have shown that beam polarization can fluctuate by up to 10 % during a typical run. Since the measured asymmetry is directly proportional to the beam polarization, the latter must be monitored continuously with a precision of $\leq$0.5 % to meet the required accuracy in the asymmetry measurements in the P2 experiment. To achieve this, MESA employs a chain of three polarimeters for cross-validation, with the final polarimeter located immediately after the last beam acceleration stage before the P2 setup.

A Møller polarimeter using a low-density gaseous atomic hydrogen target is the only suitable option to meet these stringent requirements, enabling online, non-destructive beam monitoring. However, this novel gaseous target introduces significant technological challenges that must be addressed. A Møller polarimeter, which will initially use a conventional solid iron target and operate in discontinuous mode until the hydrogen target is ready, is currently under consideration as an interim solution.

The third part of this work focuses on the design and Monte Carlo simulations for the Møller polarimeter for the P2 experiment. The simulation results validate the proof of concept for the proposed Møller polarimeter design and demonstrate the desired compatibility with both target types. The analysis of the results also demonstrates the good performance of the intended detecting system based on signal and background rates, signal-to-background ratio, and measurement times for both targets. The iron target is intended for initial technical measurements and design validation. After this step, the target will be replaced with the gaseous atomic hydrogen target, finalizing the Hydro-Møller polarimeter. The next steps will focus on more detailed simulations of the polarimeter detector system, enhancing the simulation model to improve accuracy and addressing potential sources of signal overestimation or background underestimation.

The advancements achieved in this thesis and the presented results show considerable progress in developing the P2 tracking detector and cooling system. The progress made in the Møller polarimeter design and the promising simulation results ensure the feasibility of achieving the required precision of the beam polarization monitoring. These improvements and developments are essential for successfully running the P2 experiment and achieving its ambitious physics goals.

Part V.

Appendix

A Beam Polarization Measurement Time

A.1. Measurement Time Estimation Based on Polarimeter Parameters

The calculations given here follow the ones in [153] with some adaptations and in more detail.

In section 8.4.1, the relative error of the measured polarization was given by eq. 8.11. Using

$$N = N_+ + N_- = \mathcal{L}\, t\, \sigma_{\text{total}} \tag{A.1}$$

the left part of eq. 8.8 can be written as

$$A_{\text{exp}} = \frac{N_+ - N_-}{N}\,. \tag{A.2}$$

Here, $N_\pm$ are discrete counts of the signal events. Therefore, their distribution can be modeled using the binomial distribution with probabilities

$$p_\pm = \frac{1 \pm A_{\text{exp}}}{2}\,. \tag{A.3}$$

The variance of the Møller asymmetry is

$$Var(A_{\text{exp}}) = Var\left(\frac{N_+ - N_-}{N}\right). \tag{A.4}$$

When N is large, fluctuations in N_+ and N_- are small relative to N. Therefore, N can be treated as constant in eq. A.4. Then, using that

$$Var(a\,X) = a^2\, Var(X) \text{ for } \{a = const\}, \tag{A.5}$$

eq. A.4 can be expressed as

$$Var(A_{\text{exp}}) \approx \frac{Var\,(N_+ - N_-)}{N^2}\,. \tag{A.6}$$

Considering eq. A.5:

$$Var\,(N_+ - N_-) = Var\,(2\,N_\pm) = 4\,Var\,(\,N_\pm)\,. \tag{A.7}$$

Then, given that

$$Var\,(\,N_\pm) = N\,p_+\,p_- = N\,\frac{1 - A_{\text{exp}}^2}{4}\,, \tag{A.8}$$

$Var(A_{exp})$ can be written as

$$Var(A_{exp}) = \Delta A_{exp}^2 = \frac{1 - A_{exp}^2}{N} . \tag{A.9}$$

Combining eqs. 8.8 and A.1 and substituting into eq. A.9, the statistical error of the measured Møller asymmetry can be expressed as

$$\Delta A_{exp}^2 = \frac{1}{\mathcal{L} T \sigma_{total}} \left[1 - \left(P_{beam} P_{target} \langle A_{zz} \rangle \right)^2 \right] . \tag{A.10}$$

Next, by using eqs. 8.8 and A.10 eq. 8.11 can be rewritten as

$$\left(\frac{\Delta P_{beam}}{P_{beam}} \right)^2 - \left(\frac{\Delta P_{target}}{P_{target}} \right)^2 = \left(\frac{\Delta A_{exp}}{A_{exp}} \right)^2 = \frac{1}{\mathcal{L}\, t\, \sigma_{total}} \frac{1 - (P_{beam} P_{target} \langle A_{zz} \rangle)^2}{(P_{beam} P_{target} \langle A_{zz} \rangle)^2} . \tag{A.11}$$

Finally, the desired eq. 8.13 for the estimated measurement time can be directly expressed from here.

A.2. Measurement Time Based on Simulation Results

For a rough estimation, 100% detection efficiency is assumed here.

The total beam polarization measured error consists of statistical (measurement) uncertainty and systematic uncertainty:

$$\left(\frac{\Delta P_{beam}}{P_{beam}} \right)^2 = \sigma_{stat}^2 + \sigma_{sys}^2 . \tag{A.12}$$

The systematic errors introduced by the accuracy of determining the longitudinal analyzing power and target polarization are ignored here (eq. 8.16) for the current estimation. From eqs. A.1 and A.11 the idealized—without the presence of background—uncertainty in the asymmetry measurement is

$$\left(\frac{\Delta A_{exp}}{A_{exp}} \right)^2 = \frac{1}{N_S} \frac{1 - (P_{beam} P_{target} \langle A_{zz} \rangle)^2}{(P_{beam} P_{target} \langle A_{zz} \rangle)^2} = (\sigma_{stat}^{ideal})^2, \tag{A.13}$$

where N_S = is the total number of signal events that must be registered to achieve the required uncertainty.

In the presence of background, the number of background events expected within the detection resolution window τ per signal event is:

$$N_B^{per\ signal} = R_B\, \tau. \tag{A.14}$$

The total number of background events expected within the registered events N_S is

$$N_b^{total} = (R_b\, \tau)\, N_S , \tag{A.15}$$

the actual–effective–registered signal will be reduced by the following dilution factor:

$$D = \frac{N_S}{N_S + N_b} = \frac{N_S}{N_S + R_B\,\tau\,N_S} = \frac{1}{1 + R_B\,\tau}\,. \tag{A.16}$$

Therefore, the actual statistical precision becomes

$$\sigma_{stat} = \sigma_{stat}^{ideal} \cdot D\,, \tag{A.17}$$

and the effective number of events that needed to be registered to achieve this prevision is

$$N_S \geq \frac{(1 + R_B\,\tau)^2\ \left[1 - (P_{beam}\,P_{target}\,\langle A_{zz}\rangle)^2\right]}{\sigma_{stat}^2\left(\langle A_{zz}\rangle P_{target} P_{beam}\right)^2}\,. \tag{A.18}$$

To estimate the lower limit of the number of events that need to be detected, the following values are used:

- For the given energy acceptance, the averaged polarimeter analyzing power: $\langle A_{zz}\rangle = 0.774$ (table 8.4);
- Hydrogen target can be assumed to be perfectly polarized, therefore $P_{target}(\mathrm{H}) = 1$;
- Typical value of the polarization for the thin solid iron target case is $P_{target}(\mathrm{Fe})) \sim 0.08$;
- At MESA: $P_{beam} = 0.85$.

Given the maximum possible value needed to achieve the required precision in the beam polarization measurements of $\leq 0.5\,\%$ for the hydrogen target case of $\approx 0.17\,\%$ (table 8.5), the numbers of Møller pairs needed to achieve this uncertainty of beam polarization are $N_S^{\mathrm{H}} \geq 4.53 \times 10^5$ and $N_S^{\mathrm{Fe}} \geq 1.25 \times 10^8$ (for both C-shape and semi-linear energy desperation configurations). Finally, the corresponding measurement time can be calculated based on the signal rate R_S from the simulation as

$$t_{meas} = \frac{N_S}{R_S}\,, \tag{A.19}$$

which gives $t_{meas}^{\mathrm{H}} \geq 1.3\,\mathrm{min}$ and $t_{meas}^{\mathrm{Fe}} \geq 10.2\,\mathrm{min}$ (9.6 min) with C-shape (semi-linear) energy dispersion configuration.

References

[1] E. Rutherford. "The scattering of alpha and beta particles by matter and the structure of the atom." *Phil. Mag. Ser. 6* 21 (1911), 669–688. DOI: 10.1080/14786440508637080.

[2] CDF Collaboration. "High-precision measurement of the W boson mass with the CDF II detector." *Science* 376.6589 (2022), 170–176. DOI: 10.1126/science.abk1781.

[3] G. Aad et al. "Observation of a new particle in the search for the Standard Model Higgs boson with the ATLAS detector at the LHC." *Phys.Lett.* B716 (2012), 1–29. DOI: 10.1016/j.physletb.2012.08.020.

[4] S. Chatrchyan et al. "Observation of a new boson at a mass of 125 GeV with the CMS experiment at the LHC." *Phys.Lett.* B716 (2012), 30–61. DOI: 10.1016/j.physletb.2012.08.021.

[5] D. Becker et al. "The P2 experiment." *The European Physical Journal A* 54.11 (2018), 208. ISSN: 1434-601X. DOI: 10.1140/epja/i2018-12611-6.

[6] N. Berger et al. "Measuring the weak mixing angle with the P2 experiment at MESA." *J. Univ. Sci. Tech. China* 46.6 (2016), 481–487. DOI: 10.3969/j.issn.0253-2778.2016.06.006.

[7] M. Kravchenko et al. "A Møller polarimeter for the Mainz Energy-Recovering Superconducting Accelerator (MESA)." *JINST* (2025). Forthcoming.

[8] C. Burgess and G. Moore. *The Standard Model: A Primer*. Cambridge University Press, 2006. ISBN: 9780511819698.

[9] M. Thomson. *Modern Particle Physics*. Modern Particle Physics. Cambridge University Press, 2013. ISBN: 9781107034266.

[10] M. Peskin and D. Schroeder. *An Introduction to Quantum Field Theory*. Advanced book classics. Addison-Wesley Publishing Company, 1995. ISBN: 9780201503975.

[11] G. Aruldhas. *Quantum mechanics*. PHI Learning, 2008. ISBN: 9788120336353. URL: https://books.google.de/books?id=4HLB6884s9IC.

[12] F. Halzen and A. D. Martin. *Quarks and leptons: An introductory course in modern particle physics*. John Wiley & Sons Inc, 1984. ISBN: 978-0-471-88741-6.

[13] P. Schmüser. *Feynman - Graphen und Eichtheorien Für Experimentalphysiker*. Lecture notes in physics. Springer Berlin Heidelberg, 1995. ISBN: 9783540584865.

[14] D. Griffiths. *Introduction to Elementary Particles*. Physics Textbook. Wiley, 2008. ISBN: 9783527406012.

[15] G. Malle and D. Testerman. *Linear Algebraic Groups and Finite Groups of Lie Type*. Cambridge Studies in Advanced Mathematics. Cambridge University Press, 2011.

[16] W. Fulton and J. Harris. *Representation Theory: A First Course*. Graduate texts in mathematics. Springer, 1991. ISBN: 9783540974956. DOI: https://doi.org/10.1007/978-1-4612-0979-9.

[17] S. Navas et al. "Review of particle physics." *Phys. Rev. D* 110.3 (2024), 030001. DOI: 10.1103/PhysRevD.110.030001.

[18] D. Galbraith. *Ux: Standard Model of the Standard Model*. CERN Webfest 2012, 2017. URL: https://davidgalbraith.org/portfolio/ux-standard-model-of-the-standard-model/ (visited on 11/11/2024).

[19] P. W. Higgs. "Broken Symmetries and the Masses of Gauge Bosons." *Phys. Rev. Lett.* 13 (16 Oct. 1964), 508–509. DOI: 10.1103/PhysRevLett.13.508.

[20] P. W. Higgs. "Spontaneous Symmetry Breakdown without Massless Bosons." *Phys. Rev.* 145 (4 May 1966), 1156–1163. DOI: 10.1103/PhysRev.145.1156.

[21] F. Englert and R. Brout. "Broken Symmetry and the Mass of Gauge Vector Mesons." *Phys. Rev. Lett.* 13 (9 Aug. 1964), 321–323. DOI: 10.1103/PhysRevLett.13.321.

[22] P. W. Anderson. "Plasmons, Gauge Invariance, and Mass." *Phys. Rev.* 130 (1 Apr. 1963), 439–442. DOI: 10.1103/PhysRev.130.439.

[23] G. S. Guralnik et al. "Global Conservation Laws and Massless Particles." *Phys. Rev. Lett.* 13 (20 Nov. 1964), 585–587. DOI: 10.1103/PhysRevLett.13.585.

[24] T. W. B. Kibble. "Symmetry Breaking in Non-Abelian Gauge Theories." *Phys. Rev.* 155 (5 Mar. 1967), 1554–1561. DOI: 10.1103/PhysRev.155.1554.

[25] Y. Fukuda et al. "Evidence for Oscillation of Atmospheric Neutrinos." *Phys. Rev. Lett.* 81 (8 Aug. 1998), 1562–1567. DOI: 10.1103/PhysRevLett.81.1562.

[26] K. G. Wilson. "Confinement of quarks." *Phys. Rev. D* 10 (8 Oct. 1974), 2445–2459. DOI: 10.1103/PhysRevD.10.2445.

[27] G. B. West. "Confinement in Quantum Chromodynamics." *Phys. Rev. Lett.* 46 (21 May 1981), 1365–1368. DOI: 10.1103/PhysRevLett.46.1365.

[28] H. Suganuma. "Quantum Chromodynamics, Quark Confinement, and Chiral Symmetry Breaking: A Bridge Between Elementary Particle Physics and Nuclear Physics." *Handbook of Nuclear Physics*. Ed. by I. Tanihata et al. Springer Nature Singapore, 2020, 1–48. ISBN: 978-981-15-8818-1. DOI: 10.1007/978-981-15-8818-1_22-1.

[29] E. Noether. "Invarianten beliebiger Differentialausdrücke." ger. *Nachrichten von der Gesellschaft der Wissenschaften zu Göttingen, Mathematisch-Physikalische Klasse* 1918 (1918), 37–44. URL: http://eudml.org/doc/59011.

[30] S. L. Glashow et al. "Weak Interactions with Lepton-Hadron Symmetry." *Phys. Rev. D* 2 (7 Oct. 1970), 1285–1292. DOI: 10.1103/PhysRevD.2.1285.

[31] A. Salam. "Weak and Electromagnetic Interactions." *Conf. Proc. C* 680519 (1968), 367–377. DOI: 10.1142/9789812795915_0034.

[32] S. Weinberg. "A Model of Leptons." *Phys. Rev. Lett.* 19 (21 Nov. 1967), 1264–1266. DOI: 10.1103/PhysRevLett.19.1264.

[33] M. Zimmermann. "Particle Rate Studies and Technical Design Development for the P2 Silicon Pixel Tracking Detector." PhD thesis. Johannes Gutenberg University of Mainz, 2019. DOI: 10.25358/openscience-2344.

[34] W. Hollik. "Renormalization of the Standard Model." *Adv. Ser. Direct. High Energy Phys.* 14 (1995), 37–116. DOI: 10.1142/9789814503662_0003.

[35] M. J. G. Veltman. "Perturbation theory of massive Yang-Mills fields." *Nucl. Phys.* B7 (1968), 637–650. DOI: 10.1016/0550-3213(68)90197-1.

[36] G. 't Hooft. "Renormalizable Lagrangians for Massive Yang-Mills Fields." *Nucl. Phys.* B35 (1971), 167–188. DOI: 10.1016/0550-3213(71)90139-8.

[37] G. 't Hooft and M. J. G. Veltman. "Regularization and Renormalization of Gauge Fields." *Nucl. Phys.* B44 (1972), 189–213. DOI: 10.1016/0550-3213(72)90279-9.

[38] G. 't Hooft and M. J. G. Veltman. "Combinatorics of gauge fields." *Nucl. Phys.* B50 (1972), 318–353. DOI: 10.1016/S0550-3213(72)80021-X.

[39] W. J. Marciano. "Radiative corrections to neutral current processes." *Adv. Ser. Direct. High Energy Phys.* 14 (1995), 170–200. DOI: 10.1142/9789814503662_0005.

[40] G. Alexander et al. "Electroweak parameters of the Z^0 resonance and the Standard Model: the LEP Collaborations." *Phys. Lett.* B276 (1992), 247–253. DOI: 10.1016/0370-2693(92)90572-L.

[41] P. Gambino and A. Sirlin. "Relation between $sin^2\hat{\theta}_W(m_Z)$ and $\sin^2\theta_{\text{eff}}^{\text{lept}}$." *Phys. Rev.* D49 (1994), 1160–1162. DOI: 10.1103/PhysRevD.49.R1160.

[42] D. Androić et al. "Precision measurement of the weak charge of the proton." *Nature* 557.7704 (2018), 207–211. DOI: 10.1038/s41586-018-0096-0.

[43] G. Smith. "Final Results from the Jefferson Lab Qweak Experiment and Constraints on Physics Beyond the Standard Model." *PoS* SPIN2018 (2019), 008. DOI: 10.22323/1.346.0008.

[44] P. L. Anthony et al. "Observation of Parity Nonconservation in Møller Scattering." *Physical Review Letters* 92.18 (May 2004). ISSN: 1079-7114. DOI: 10.1103/physrevlett.92.181602.

[45] P. L. Anthony et al. "Precision Measurement of the Weak Mixing Angle in Møller Scattering." *Physical Review Letters* 95.8 (Aug. 2005). ISSN: 1079-7114. DOI: 10.1103/physrevlett.95.081601.

[46] J. Benesch et al. "The MOLLER Experiment: An Ultra-Precise Measurement of the Weak Mixing Angle Using Møller Scattering" (2014). arXiv: 1411.4088 [nucl-ex].

[47] C. Y. Prescott et al. "Parity Nonconservation in Inelastic Electron Scattering." *Phys. Lett.* B77 (1978). [,6.31(1978)], 347–352. DOI: 10.1016/0370-2693(78)90722-0.

[48] W. Heil et al. "Improved Limits on the Weak, Neutral, Hadronic Axial Vector Coupling Constants From Quasielastic Scattering of Polarized Electrons." *Nucl. Phys.* B327 (1989), 1–31. DOI: 10.1016/0550-3213(89)90284-8.

[49] P. A. Souder et al. "Measurement of parity violation in the elastic scattering of polarized electrons from C-12." *Phys. Rev. Lett.* 65 (1990), 694–697. DOI: 10.1103/PhysRevLett.65.694.

[50] D. Becker. "Voruntersuchungen zur Messung der schwachen Ladung des Protons im Rahmen des P2-Experiments." PhD thesis. Johannes Gutenberg-Universität Mainz, 2018. DOI: 10.25358/openscience-3737.

[51] J. Arrington et al. "Nucleon electromagnetic form factors." *Journal of Physics G: Nuclear and Particle Physics* 34.7 (May 2007), S23–S51. ISSN: 1361-6471. DOI: 10.1088/0954-3899/34/7/s03.

[52] D. Armstrong and R. McKeown. "Parity-Violating Electron Scattering and the Electric and Magnetic Strange Form Factors of the Nucleon." *Annual Review of Nuclear and Particle Science* 62.1 (Nov. 2012), 337–359. ISSN: 1545-4134. DOI: 10.1146/annurev-nucl-102010-130419.

[53] J. P. Chen et al. "A White Paper on SoLID (Solenoidal Large Intensity Device)" (2014). arXiv: 1409.7741 [nucl-ex].

[54] K. S. Kumar et al. "Low Energy Measurements of the Weak Mixing Angle." *Ann. Rev. Nucl. Part. Sci.* 63 (2013), 237–267. DOI: 10.1146/annurev-nucl-102212-170556.

[55] J. Erler et al. "Weak Polarized Electron Scattering." *Annual Review of Nuclear and Particle Science* 64.1 (Oct. 2014), 269–298. ISSN: 1545-4134. DOI: 10.1146/annurev-nucl-102313-025520.

[56] H. Herminghaus et al. "The Design of a Cascaded 800-MeV Normal Conducting CW Racetrack Microtron." *Nucl. Instrum. Meth.* 138 (1976), 1–12. DOI: 10.1016/0029-554X(76)90145-2.

[57] K. H. Kaiser et al. "The 1.5-GeV harmonic double-sided microtron at Mainz University." *Nucl. Instrum. Meth.* A593 (2008), 159–170. DOI: 10.1016/j.nima.2008.05.018.

[58] M. Dehn et al. "The MAMI-C Accelerator: 25 Years of Operation and Strategies for the Next Decade." *Proceedings, 8th International Particle Accelerator Conference (IPAC 2017): Copenhagen, Denmark, May 14-19.* 2017. DOI: 10.18429/JACoW-IPAC2017-TUPIK054.

[59] S. Schlimme et al. *The MESA physics program.* 2024. arXiv: 2402.01027 [nucl-ex].

[60] R. Heine et al. "Current Status of the Milliampere Booster for the Mainz Energy-recovering Superconducting Accelerator." *Proceedings, 7th International Particle Accelerator Conference (IPAC 2016): Busan, Korea, May 8-13.* 2016. DOI: 10.18429/JACoW-IPAC2016-TUPOW002.

[61] F. Hug and R. Heine. "Injector linac stability requirements for high precision experiments at MESA." *J. Phys. Conf. Ser.* 874.1 (2017). [MOPVA014(2017)], 012012. DOI: 10.1088/1742-6596/874/1/012012.

[62] T. Stengler et al. "Modified ELBE Type Cryomodules for the Mainz Energy-Recovering Superconducting Accelerator MESA." *Proceedings, 17th International Conference on RF Superconductivity (SRF2015): Whistler, Canada, September 13-18.* 2015. DOI: 10.18429/JACoW-SRF2015-THPB116.

[63] R. Kempf et al. "Beam parameter stabilization for the P2 experiment at MESA." *Nucl. Instrum. Methods A* 982 (2020), 164554. ISSN: 0168-9002. DOI: https://doi.org/10.1016/j.nima.2020.164554.

[64] V. Tyukin and K. Aulenbacher. "Polarized Atomic Hydrogen Target at MESA." *PoS* PSTP2019 (2020), 005. DOI: 10.22323/1.379.0005.

[65] K. Aulenbacher et al. "The polarimetry chain for the P2 experiment." *Nuovo Cim.* C035N04 (2012), 186–191. DOI: 10.1393/ncc/i2012-11301-y.

[66] A. Gellrich et al. "Elimination of instrumental asymmetries in electron polarization analysis." *Review of Scientific Instruments* 61.11 (1990), 3399–3404. DOI: 10.1063/1.1141591.

[67] M. Molitor. "Double scattering polarimeter for the P2 experiment at MESA." *PoS* PSTP2015 (2016), 030. DOI: 10.22323/1.243.0030.

[68] V. Tioukine et al. "A Mott polarimeter operating at MeV electron beam energies." *Review of Scientific Instruments* 82.3 (2011), 033303. DOI: 10.1063/1.3556593.

[69] J. M. Grames et al. "High precision 5 MeV Mott polarimeter." *Phys. Rev. C* 102 (1 July 2020), 015501. DOI: 10.1103/PhysRevC.102.015501.

[70] S. D. Covrig et al. "The Cryogenic target for the G0 experiment at Jefferson Lab." *Nucl. Instrum. Meth.* A551 (2005), 218–235. DOI: 10.1016/j.nima.2005.05.074.

[71] D. Androic et al. "The G0 Experiment: Apparatus for Parity-Violating Electron Scattering Measurements at Forward and Backward Angles." *Nucl. Instrum. Meth.* A646 (2011), 59–86. DOI: 10.1016/j.nima.2011.04.031.

[72] J. Brock et al. "The Qweak high performance LH2 target." *Nucl. Instrum. Methods A* 1053 (2023), 168316. ISSN: 0168-9002. DOI: https://doi.org/10.1016/j.nima.2023.168316.

[73] J. Allison et al. "Recent developments in Geant4." *Nucl. Instrum. Methods A* 835 (2016), 186–225. ISSN: 0168-9002. DOI: https://doi.org/10.1016/j.nima.2016.06.125.

[74] J. Allison et al. "Geant4 developments and applications." *IEEE Transactions on Nuclear Science* 53.1 (2006), 270–278. DOI: 10.1109/TNS.2006.869826.

[75] S. Agostinelli et al. "Geant4—a simulation toolkit." *Nucl. Instrum. Methods A* 506.3 (2003), 250–303. ISSN: 0168-9002. DOI: https://doi.org/10.1016/S0168-9002(03)01368-8.

[76] J. Ritman. "The FOPI detector at SIS/GSI." *Nucl. Phys. Proc. Suppl.* 44 (1995), 708–715. DOI: 10.1016/0920-5632(95)00606-0.

[77] V. Fanti et al. "The Beam and detector for the NA48 neutral kaon CP violations experiment at CERN." *Nucl. Instrum. Meth.* A574 (2007), 433–471. DOI: 10.1016/j.nima.2007.01.178.

[78] UQG Ltd. *Quartz Glass for Optics Data and Properties. Datasheet.* 2024. URL: https://suddendocs.samtec.com/catalog_english/gmi.pdf.

[79] T. Allison et al. "The Qweak experimental apparatus." *Nucl. Instrum. Methods A* 781 (2015), 105–133. ISSN: 0168-9002. DOI: https://doi.org/10.1016/j.nima.2015.01.023.

[80] P. A. Souder et al. "Measurement of parity violation in the elastic scattering of polarized electrons from ^{12}C." *Phys. Rev. Lett.* 65 (6 Aug. 1990), 694–697. DOI: 10.1103/PhysRevLett.65.694.

[81] X. Roca-Maza et al. "Neutron Skin of ^{208}Pb, Nuclear Symmetry Energy, and the Parity Radius Experiment." *Physical Review Letters* 106.25 (June 2011). ISSN: 1079-7114. DOI: 10.1103/physrevlett.106.252501.

[82] M. Gorchtein et al. "Beam normal spin asymmetry in elastic lepton–nucleon scattering." *Nuclear Physics A* 741 (2004), 234–248. ISSN: 0375-9474. DOI: https://doi.org/10.1016/j.nuclphysa.2004.06.008.

[83] A. De Rújula et al. "Elastic scattering of electrons from polarized protons and inelastic electron scattering experiments." *Nuclear Physics B* 35.2 (1971), 365–389. ISSN: 0550-3213. DOI: https://doi.org/10.1016/0550-3213(71)90460-3.

[84] S. Baunack et al. "Measurement of the axial and the strangeness magnetic form factor of the proton with a P2 backward angle setup." *AIP Conf. Proc.* 1563.1 (2013). Ed. by R. Milner et al., 73–77. DOI: 10.1063/1.4829378.

[85] V. L. Highland. "Some Practical Remarks on Multiple Scattering." *Nucl. Instrum. Meth.* 129 (1975), 497. DOI: 10.1016/0029-554X(75)90743-0.

[86] G. R. Lynch and O. I. Dahl. "Approximations to multiple Coulomb scattering." *Nucl. Instrum. Meth.* B58 (1991), 6–10. DOI: 10.1016/0168-583X(91)95671-Y.

[87] A. Magnon et al. "Tracking with 40x40-cm**2 MICROMEGAS detectors in the high energy, high luminosity COMPASS experiment." *Nucl. Instrum. Meth.* A478 (2002), 210–214. DOI: 10.1016/S0168-9002(01)01759-4.

[88] J. Bortfeldt et al. "High-Rate Capable Floating Strip Micromegas." *Nucl. Part. Phys. Proc.* 273-275 (2016), 1173–1179. DOI: 10.1016/j.nuclphysbps.2015.09.184.

[89] I. Peric. "A novel monolithic pixelated particle detector implemented in high-voltage CMOS technology." *Nucl. Instrum. Meth.* A582 (2007), 876–885. DOI: 10.1016/j.nima.2007.07.115.

[90] I. Peric and C. Takacs. "Large monolithic particle pixel-detector in high-voltage CMOS technology." *Nucl. Instrum. Meth.* 624.2 (2010), 504–508. ISSN: 0168-9002. DOI: https://doi.org/10.1016/j.nima.2010.03.161.

[91] I. Peric et al. "Particle pixel detectors in high-voltage CMOS technology - New achievements." *Nucl. Instrum. Meth* 650.1 (2011), 158–162. ISSN: 0168-9002. DOI: https://doi.org/10.1016/j.nima.2010.11.090.

[92] I. Peric. "Active pixel sensors in high-voltage CMOS technologies for ATLAS." *JINST* 7 (2012), C08002. DOI: 10.1088/1748-0221/7/08/C08002.

[93] I. Perić et al. "High-voltage pixel detectors in commercial CMOS technologies for ATLAS, CLIC and Mu3e experiments." *Nucl. Instrum. Meth.* A731 (2013), 131–136. DOI: 10.1016/j.nima.2013.05.006.

[94] H. Augustin et al. *MuPix10: First Results from the Final Design*. 2019. DOI: 10.48550/ARXIV.2012.05868.

[95] A.-K. Perrevoort. "Sensitivity Studies on New Physics in the Mu3e Experiment and Development of Firmware for the Front-End of the Mu3e Pixel Detector." PhD thesis. Universität Heidelberg, 2018. DOI: 10.11588/heidok.00024585.

[96] Wikipedia. *p–n junction*. 2024. URL: https://en.wikipedia.org/wiki/P%E2%80%93n_junction (visited on 01/10/2025).

[97] T. Hemperek. "Overview and perspectives of depleted CMOS sensors for high radiation environments." *PoS* Vertex 2017 (2018), 034. DOI: 10.22323/1.309.0034.

[98] M. Benoit et al. "Testbeam results of irradiated ams H18 HV-CMOS pixel sensor prototypes." *Journal of Instrumentation* 13.02 (Feb. 2018), P02011. DOI: 10.1088/1748-0221/13/02/P02011.

[99] I. Perić. "A novel monolithic pixelated particle detector implemented in high-voltage CMOS technology." *Nucl. Instrum. Methods A* 582.3 (2007). VERTEX 2006, 876–885. ISSN: 0168-9002. DOI: https://doi.org/10.1016/j.nima.2007.07.115.

[100] K. Arndt et al. "Technical design of the phase I Mu3e experiment." *Nucl. Instrum. Methods A* 1014 (2021), 165679. DOI: 10.1016/j.nima.2021.165679.

[101] S. Shrestha. "The High-Voltage Monolithic Active Pixel Sensor for the Mu3e Experiment." *PoS* TIPP2014 (2014), 047. DOI: 10.22323/1.213.0047.

[102] H. Augustin et al. "The MuPix high voltage monolithic active pixel sensor for the Mu3e experiment." *JINST* 10.03 (2015), C03044. DOI: 10.1088/1748-0221/10/03/C03044.

[103] H. Augustin et al. "MuPix7—A fast monolithic HV-CMOS pixel chip for Mu3e." *JINST* 11.11 (2016), C11029. DOI: 10.1088/1748-0221/11/11/C11029.

[104] H. Augustin et al. "MuPix8 - Large area monolithic HVCMOS pixel detector for the Mu3e experiment." *Nucl. Instrum. Meth.* (2018). DOI: https://doi.org/10.1016/j.nima.2018.09.095.

[105] F. Schötzer. "Temperature sensitivity study & verification of the MuPix11 fast differential data links for the Mu3e experiment." Bachelor's Thesis. Universität Heidelberg, 2024. URL: http://www.physi.uni-heidelberg.de/Publications/Schloetzer_Bachelorarbeit.pdf.

[106] H. Augustin et al. "MuPix: An HV–MAPS for the Mu3e Experiment." *Journal of the Physical Society of Japan* (2024). DOI: 10.7566/JPSCP.42.011020.

[107] H. Augustin et al. "Irradiation study of a fully monolithic HV-CMOS pixel sensor design in AMS 180 nm." *Nucl. Instrum. Meth.* A905 (2018), 53–60. DOI: 10.1016/j.nima.2018.07.044.

[108] M. Köppel. "Mu3e Integration Run 2021." *Proceedings of The 22nd International Workshop on Neutrinos from Accelerators — PoS(NuFact2021)*. Vol. 402. 2022, 233. DOI: 10.22323/1.402.0233.

[109] M. Köppel. "Data Flow in the Mu3e Data Acquisition System." PhD thesis. Johannes Gutenberg University of Mainz, 2024. DOI: 10.25358/openscience-10928.

[110] T. T. Rudzki et al. *An ultra-light helium cooled pixel detector for the Mu3e experiment*. 2023. arXiv: 2307.14803 [physics.ins-det].

[111] R. M. Amarinei. *The Mu3e Experiment: Status and Short-Term Plans*. 2025. arXiv: 2501.14667 [hep-ex].

[112] lpGBT Support Team. *lpGBT Manual*. CERN. 2021. URL: https://lpgbt.web.cern.ch/lpgbt/v0/.

[113] J. Troska. *Versatile Link+ Transceiver (VTRx+)*. EDMS Document Number 1719329. CERN/EP-ESE. 2021. URL: https://edms.cern.ch/ui/file/1719329/1/VTRxPlus_spec.pdf.

[114] A. Bocci et al. "The Powering Scheme of the CMS Silicon Strip Tracker." *10th Workshop on electronics for LHC and future experiments* (2004).

[115] I. Sorokin. "Parameterization-based tracking for the P2 experiment." *EPJ Web Conf.* 150 (2017), 00012. DOI: 10.1051/epjconf/201715000012.

[116] V. Blobel et al. "Fast alignment of a complex tracking detector using advanced track models." *Comput. Phys. Commun.* 182 (2011), 1760–1763. DOI: 10.1016/j.cpc.2011.03.017.

[117] C. Kleinwort. "General Broken Lines as advanced track fitting method." *Nucl. Instrum. Meth.* A673 (2012), 107–110. DOI: 10.1016/j.nima.2012.01.024.

[118] L. Bugge and J. Myrheim. "Tracking and Track Fitting." *Nucl. Instrum. Meth.* 179 (1981), 365–381. DOI: 10.1016/0029-554X(81)90063-X.

[119] A. Strandlie and W. Wittek. "Derivation of Jacobians for the propagation of covariance matrices of track parameters in homogeneous magnetic fields." *Nucl. Instrum. Meth.* 566 (2006), 687–698. DOI: https://doi.org/10.1016/j.nima.2006.07.032.

[120] E. Lund et al. "Track parameter propagation through the application of a new adaptive Runge-Kutta-Nystroem method in the ATLAS experiment." *JINST* 4 (2009), P04001. DOI: 10.1088/1748-0221/4/04/P04001.

[121] E. Lund et al. "Transport of covariance matrices in the inhomogeneous magnetic field of the ATLAS experiment by the application of a semi-analytical method." *JINST* 4 (2009), P04016. DOI: 10.1088/1748-0221/4/04/P04016.

[122] U. Hartenstein. "Track Based Alignment for the Mu3e Pixel Detector." PhD thesis. Universität Mainz, 2018.

[123] V. Blobel. "Software alignment for tracking detectors." *Nucl. Instrum. Meth.* A566 (2006), 5–13. DOI: 10.1016/j.nima.2006.05.157.

[124] M. Oinonen et al. "ALICE Silicon Strip Detector module assembly with single-point TAB interconnections." *Proceedings, eleventh Workshop on Electronics for LHC and Future Experiments, Heidelberg, Germany, 12-16 September*. 2005. URL: https://cds.cern.ch/record/920152.

[125] Samtec. *SUPERNOVA Low Profile Compression Interposer. Catalog page.* 2019. URL: https://www.uqgoptics.com/wp-content/uploads/2019/03/Heraeus-Spectrosil-2000.pdf.

[126] R. P. Austermuhl. "Analyse von Michelson-Interferometriedaten von Vibrationsmessungen eines dünnen gasgekühlten Pixeldetektors." Bachelor's Thesis. Universität Heidelberg, 2015. URL: https://www.psi.ch/mu3e/ThesesEN/BachelorAustermuehl.pdf.

[127] L. Henkelmann. "Optical Measurements of Vibration and Deformation of the Mu3e Silicon Pixel Tracker." Bachelor's Thesis. Universität Heidelberg, 2015. URL: https://www.psi.ch/mu3e/ThesesEN/BachelorHenkelmann.pdf.

[128] DuPont Electronics & Industrial. *DuPont Kapton. Summary of Properties.* 2022. URL: https://www.dupont.com/content/dam/electronics/amer/us/en/electronics/public/documents/en/EI-10142_Kapton-Summary-of-Properties.pdf.

[129] F. J. Stieler. "Tests der Mechanik und Kühlung des Spurdetektors für das P2-Experiment." Bachelor's Thesis. Universität Mainz, 2018.

[130] F. E. A. Greiner. "Gaskühlung für den Spurdetektor des P2-Experiments." Bachelor's Thesis. Universität Mainz, 2019.

[131] J. Lienhard IV and J. Lienhard V. *A Heat Transfer Textbook.* 4th. Version 2.12. Phlogiston Press, 2018. URL: http://ahtt.mit.edu.

[132] Autodesk Inc. Documentation. *Compressible Flow.* 2025. URL: https://help.autodesk.com/view/SCDSE/2018/ENU/?guid=GUID-620F44CE-9506-4C48-9E9C-6C689345B008 (visited on 12/15/2024).

[133] SENSIRION AG. *Datasheet SFM3400-AW & SFM3400-D. Datasheet.* 2024. URL: https://sensirion.com/media/documents/9EE7E5FF/659D365C/GF_DS_SFM3400AW_SFM3400D.pdf.

[134] Baumer GmbH. *Distance sensors OM70-L0070.HH0048.EK. Datasheet.* 2022. URL: https://media.baumer.com/Baumer_OM70-L0070.HH0048.EK_EN_20220218_DS.pdf.

[135] F. White. *Viscous Fluid Flow.* McGraw-Hill international edition. McGraw-Hill Higher Education, 2006. ISBN: 9780071244930.

[136] Altair Engineering Inc. *Turbulent Flow Verses Laminar Flow.* 2025. URL: https://help.altair.com/hwcfdsolvers/acusolve/topics/acusolve/training_manual/turb_flow_vs_lam_flow_r.htm (visited on 01/20/2025).

[137] T. T. Rudzki et al. "Successful cooling of a pixel tracker using gaseous helium: Studies with a mock-up and a detector prototype." *Nucl. Instrum. Methods A* 1054 (2023), 168405. ISSN: 0168-9002. DOI: https://doi.org/10.1016/j.nima.2023.168405.

[138] Autodesk Inc. *Autodesk CFD online documentation.* URL: https://knowledge.autodesk.com/support/cfd (visited on 05/12/2024).

[139] M. Deflorin. "Helium cooling of Silicon Pixel Detector for Mu3e Experiment." Master's Thesis. University of Applied Sciences and Arts Northwestern Switzerland, 2019. URL: https://www.psi.ch/sites/default/files/import/mu3e/ThesesEN/MasterDeflorin.pdf.

[140] Celeroton AG. *CT-NG-Series. Datasheet.* 2020. URL: https://www.celeroton.com/wp-content/uploads/datasheet-ct-ng-2000gb.pdf.

[141] M. Loppacher. "Møller Polarimetry for CEBAF Hall C." Available at https://hallaweb.jlab.org/equipment/moller/docs/Loppacher__Moller_Polarimetry_for_CEBAF_Hall_C.pdf. PhD thesis. University of Basel, 1996.

[142] E. Chudakov and V. Luppov. "Møller polarimetry with atomic hydrogen targets." *The European Physical Journal A - Hadrons and Nuclei* 24.2 (2005). Eur. Phys. J.A24S2,123(2005), 123–126. ISSN: 1434-601X. DOI: 10.1140/epjad/s2005-04-028-8.

[143] P. S. Cooper et al. "Polarized Electron-Electron Scattering at GeV Energies." *Phys. Rev. Lett.* 34 (25 1975), 1589–1592. DOI: 10.1103/PhysRevLett.34.1589.

[144] G. Baum et al. "New Measurement of Deep-Inelastic $e - p$ Asymmetries." *Phys. Rev. Lett.* 51 (13 1983), 1135–1138. DOI: 10.1103/PhysRevLett.51.1135.

[145] W. Brefeld et al. "Measurement of the polarization degree of accelerated polarized electrons at the 2.5 GeV synchrotron in Bonn for energies between 0.85 and 2 GeV." *Nucl. Instrum. Methods A* 228.2 (1985), 228–235. ISSN: 0168-9002. DOI: https://doi.org/10.1016/0168-9002(85)90264-5.

[146] B. Wagner et al. "A Møller polarimeter for CW and pulsed intermediate energy electron beams." *Nucl. Instrum. Methods A* 294.3 (1990), 541–548. ISSN: 0168-9002. DOI: https://doi.org/10.1016/0168-9002(90)90296-I.

[147] A. Feltham and P. Steiner. "Recent developments in Moeller polarimetry." *7th Conference on Perspectives in Nuclear Physics at Intermediate Energies*. May 1995, 47–52.

[148] M. Hauger et al. "A high-precision polarimeter." *Nucl. Instrum. Methods A* 462.3 (2001), 382–392. ISSN: 0168-9002. DOI: https://doi.org/10.1016/S0168-9002(01)00197-8.

[149] J. Magee et al. "A novel comparison of Møller and Compton electron-beam polarimeters." *Physics Letters B* 766 (2017), 339–344. ISSN: 0370-2693. DOI: https://doi.org/10.1016/j.physletb.2017.01.026.

[150] D. King et al. "Precision Møller polarimetry for PREX-2 and CREX." *Nucl. Instrum. Methods A* 1045 (2023), 167506. ISSN: 0168-9002. DOI: https://doi.org/10.1016/j.nima.2022.167506.

[151] C. Møller. "Zur Theorie des Durchgangs schneller Elektronen durch Materie." *Annalen der Physik* 406.5 (1932), 531–585. DOI: https://doi.org/10.1002/andp.19324060506.

[152] A. Kresnin and L. Rosentsveig. "Polarization effects in the scattering of electrons and positrons by electrons." *Journ. Exp. Theor. Phys. (USSR)* 5.2 (1957), 288. URL: http://jetp.ras.ru/cgi-bin/e/index/e/5/2/p288?a=list.

[153] G. Alexander and I. Cohen. "Møller scattering polarimetry for high energy e+e− linear colliders." *Nucl. Instrum. Methods A* 486.3 (July 2002), 552–567. ISSN: 0168-9002. DOI: 10.1016/s0168-9002(01)02167-2.

[154] A. Czarnecki and W. J. Marciano. "Polarized Møller scattering asymmetries." *International Journal of Modern Physics A* 15.16 (June 2000), 2365–2375. ISSN: 1793-656X. DOI: 10.1142/s0217751x00002433.

[155] T. Donnelly and A. Raskin. "Considerations of polarization in inclusive electron scattering from nuclei." *Annals of Physics* 169.2 (1986), 247–351. ISSN: 0003-4916. DOI: https://doi.org/10.1016/0003-4916(86)90173-9.

[156] I. Akushevich et al. "Radiative corrections beyond the ultra relativistic limit in unpolarized ep elastic and Møller scatterings for the PRad Experiment at Jefferson Laboratory." *The European Physical Journal A* 51.1 (2015). ISSN: 1434-601X. DOI: 10.1140/epja/i2015-15001-8.

[157] A. Afanasev et al. "MERADGEN 1.0: Monte Carlo generator for the simulation of radiative events in parity conserving doubly-polarized Møller scattering." *Computer Physics Communications* 176.3 (2007), 218–231. ISSN: 0010-4655. DOI: https://doi.org/10.1016/j.cpc.2006.10.002.

[158] I. Akushevich et al. "Monte Carlo generator ELRADGEN 2.0 for simulation of radiative events in elastic ep-scattering of polarized particles." *Computer Physics Communications* 183.7 (2012), 1448–1467. ISSN: 0010-4655. DOI: https://doi.org/10.1016/j.cpc.2012.01.015.

[159] I. F. Silvera and J. T. M. Walraven. "Stabilization of Atomic Hydrogen at Low Temperature." *Phys. Rev. Lett.* 44 (3 Jan. 1980), 164–168. DOI: 10.1103/PhysRevLett.44.164.

[160] W. Hardy et al. "Magnetic resonance of atomic hydrogen at low temperatures." *Physica B+C* 109-110 (1982). 16th International Conference on Low Temperature Physics, Part 3, 1964–1977. ISSN: 0378-4363. DOI: https://doi.org/10.1016/0378-4363(82)90222-4.

[161] R. W. Cline et al. "Nuclear Polarization of Spin-Polarized Hydrogen." *Phys. Rev. Lett.* 47 (17 1981), 1195–1198. DOI: 10.1103/PhysRevLett.47.1195.

[162] J. Walraven and T. Hijmans. "Atomic hydrogen in magnetostatic traps." *Physica B: Condensed Matter* 197.1 (1994), 417–425. ISSN: 0921-4526. DOI: https://doi.org/10.1016/0921-4526(94)90240-2.

[163] W. Gerlach and O. Stern. "Der experimentelle Nachweis der Richtungsquantelung im Magnetfeld." *Zeitschrift für Physik* 9 (1 1922), 349–352. DOI: 10.1007/BF01326983.

[164] N. Borisov, A. Dolzhikov, A. Fedorov, I. Gorodnov, A. Neganov, A. Priladyshev, Y. Usov, V. Tyukin. Unpublished technical drawing obtained via personal communication. 2022.

[165] P. Steiner et al. "A high-rate coincidence Møller polarimeter." *Nucl. Instrum. Methods A* 419.1 (1998), 105–120. ISSN: 0168-9002. DOI: https://doi.org/10.1016/S0168-9002(98)00938-3.

[166] O. Glamazdin. "Møller (iron foils) existing techniques." *Nuovo Cimento della Societa Italiana di Fisica C* 35 (July 2012), 176–180. DOI: 10.1393/ncc/i2012-11275-8.

[167] J. Kessler. *Polarized Electrons*. Springer Berlin, Heidelberg, 2013. ISBN: 978-3-662-02434-8. DOI: https://doi.org/10.1007/978-3-662-02434-8.

[168] R. A. Reck and D. L. Fry. "Orbital and Spin Magnetization in Fe-Co, Fe-Ni, and Ni-Co." *Phys. Rev.* 184 (2 Aug. 1969), 492–495. DOI: 10.1103/PhysRev.184.492.

[169] L. de Bever et al. "A target for precise Møller polarimetry." *Nucl. Instrum. Methods A* 400.2 (1997), 379–386. ISSN: 0168-9002. DOI: https://doi.org/10.1016/S0168-9002(97)00961-3.

[170] L. Levchuk. "The intra-atomic motion of bound electrons as a possible source of the systematic error in electron beam polarization measurements by means of a Möller polarimeter." *Nucl. Instrum. Methods A* 345.3 (1994), 496–499. ISSN: 0168-9002. DOI: https://doi.org/10.1016/0168-9002(94)90505-3.

[171] J. Magee. "Sub-percent precision Møller polarimetry in experimental Hall C." *PoS* PSTP2013, 39 (Sept. 2013), 39. DOI: 10.22323/1.182.0039.

[172] P2 experiment collaboration. *P2 Møller Polarimeter Geant4 Simulation*. GitLab repository: https://gitlab.rlp.net/p2/p2-polar.

[173] Geant4 Collaboration. *Physics List Guide*. 2024. URL: https://geant4.web.cern.ch/documentation/dev/plg_html/PhysicsListGuide/physicslistguide.html (visited on 02/09/2025).

[174] Peng, Chao and Levillain, Mexime and Gu, Chao. *PRad Geant4 Simulation Package*. GitHub repository: https://github.com/JeffersonLab/PRadSim.

[175] W. Xiong et al. "A small proton charge radius from an electron–proton scattering experiment." *Nature* 575.7781 (Nov. 2019), 147–150. ISSN: 1476-4687. DOI: 10.1038/s41586-019-1721-2.

[176] R. Brun and F. Rademakers. "ROOT - An Object-Oriented Data Analysis Framework." *Nucl. Inst. & Meth. in Phys. Res. A* 389 (1997), 81–86. DOI: 10.1016/S0168-9002(97)00048-X.

[177] A. G. Minten. *Electron scattering, form factors, vector mesons*. CERN Academic Training Lecture. CERN, Geneva, 1968 - 1969. CERN, 1969. DOI: 10.5170/CERN-1969-022.

Acknowledgments

”Per aspera ad astra.”
Eng.: ”Through hardships to the stars.”

Latin proverb